Retrieval of Water Vapour and Methane from the MIPAS Satellite Instrument

A thesis submitted for the degree of Doctor of Philosophy in the

University of Oxford

Vivienne H. Payne

Atmospheric, Oceanic and Planetary Physics

Trinity Term 2005

Retrieval of Water Vapour and Methane from the MIPAS Satellite Instrument

Vivienne Helen Payne

Lady Margaret Hall

Atmospheric, Oceanic and Planetary Physics

A thesis submitted for the degree of Doctor of Philosophy in the University of Oxford

Trinity Term 2005

The Michelson Interferometer for Passive Atmospheric Sounding (MIPAS) is one of the core experiments on the European Space Agency (ESA) Envisat satellite, launched in March 2002. MIPAS measures infrared atmospheric limb emission spectra from 685–2410 cm^{-1} (wavelengths of 14.5–4.1 μm) over an altitude range 6–68 km. After suitable ground processing, these spectra allow retrieval of profiles of atmospheric temperature, pressure and numerous atmospheric trace gases. The MIPAS spectra also contain enough information to retrieve minor isotopes of many trace gases.

Profiles of pressure, temperature and six high priority species (H_2O, O_3, HNO_3, CH_4, N_2O and NO_2) are retrieved operationally by ESA. A separate retrieval scheme has been developed at Oxford in order to validate the ESA retrievals and to extend the range of products which can be retrieved from the MIPAS spectra (for example, to retrieve profiles of minor isotopes).

The focus of the thesis is water vapour and methane. The first aim of the thesis has been to assist in the validation of the ESA operational retrievals of water vapour and methane. The ESA dataset has been examined, persistent problems have been identified and possible causes of these problems have been investigated using the Oxford retrieval processor. The second aim of the thesis has been to use the Oxford processor to retrieve global distributions of $H_2^{18}O$, $H_2^{17}O$, HDO and CH_3D from the MIPAS spectra.

Acknowledgements

Many thanks to my principal supervisor, Anu Dudhia for all his help, advice and patience, and for all those lifts to and from Stansted airport at unsociable hours. Thanks to my other supervisor, Don Grainger, for his advice and for encouraging me to take a broader view.

Thanks to the MIPAS group in AOPP and to the rest of the Earth Observation group for their input and suggestions at meetings. In particular, thanks to Chiara Piccolo for help with getting hold of data, retrievals, data analysis and all manner of other things.

Thanks also to Anu, Don and Chiara for reading and commenting on drafts of this thesis.

I am glad to have been given the opportunity to attend various MIPAS meetings around Europe, at which I learned a lot. Many thanks to the members of MIPAS CalVal and Quality Working Group teams, and to all those involved in the AMIL2DA project, particularly to Victoria Jay for her help in the early stages of my DPhil.

I am grateful to David Noone at the University of Colorado, Boulder for hosting my visit there and for his input on the isotope work and to the Royal Meteorological Society's Rupert Ford Fund for making the visit possible. Thanks also to John Worden and Kevin Bowman at JPL for their interest and suggestions.

Thanks to Nicolas Lautiè, Jo Urban and the Odin team for access to the Odin data and to Nathaniel Livesey at JPL for supplying MLS data.

This DPhil project was funded by the Natural Environmental Research Council. I am also grateful to the RMetSoc, the IoP, the British Council and LMH for funding various excursions.

Thanks to Steve, Lisa, Sam, Barbara and Chiara for providing me with a roof over my head when life started to get a bit complicated. Thanks also to others who offered.

To the runners — thanks for all the guilt–free beer and crisps!

Last but not least, many thanks to my husband Mike for his contribution to the proof–reading effort, for all his support and for providing a welcome distraction from a distance throughout my time in Oxford.

Contents

List of Acronyms

ACE	Atmospheric Chemistry Experiment
AILS	Apodised Instrument Line Shape
AMIL2DA	Advanced MIPAS Level 2 Data Analysis
dfs	degrees of freedom for signal
ECMWF	European Centre for Medium–Range Weather Forecasts
ENSO	El Niño Southern Oscillation
EOS	Earth Observing System
ERS	European Remote Sensing Satellite
ESA	European Space Agency
FOV	Field of View
FTS	Fourier Transform Spectrometer
HALOE	Halogen Occultation Experiment
IFAC	Istituto Fisica Applicata della Nello Carrara
IG2	Initial Guess 2 (climatological dataset)
ILS	Instrument Line Shape
ISAMS	Improved Stratospheric and Mesospheric Sounder
LOS	Line of Sight
LTE	Local Thermodynamic Equilibrium
MIPAS	Michelson Interferometer for Passive Atmospheric Sounding
MIPAS–B	MIPAS Balloon
MIPAS–STR	MIPAS Stratospheric Aircraft
MLS	Microwave Limb Sounder
MORSE	MIPAS Orbital Retrieval using Sequential Estimation
NASA	National Aeronautics and Space Administration
NESR	Noise Equivalent Spectral Radiance
NLTE	Non–Local Thermodynamic Equilibrium

NRT	Near real time
OFL	Off–line (refers to the ESA off–line retrieval)
OFM	Optimised Forward Model
OPD	Optical Path Difference
ORM	Optimised Retrieval Model
ppbv	parts per billion by volume
ppmv	parts per million by volume
PSC	Polar Stratospheric Cloud
PV	Potential Vorticity
QBO	Quasi–Biennial Oscillation
QWG	Quality Working Group
REC	Residual and Error Correlation
RFM	Reference Forward Model
SAMS	Stratospheric and Mesospheric Sounder
SMOW	Standard Mean Ocean Water
SMR	Sub-Millimetre Radiometer
TES	Tropospheric Emission Spectrometer
TTL	Tropical Tropopause Layer
UARS	Upper Atmosphere Research Satellite
UKMO	United Kingdon Meteorological Office
UTLS	Upper Troposphere and Lower Stratosphere
VMR	Volume Mixing Ratio

Chapter 1

Water vapour and methane

1.1 Introduction

The focus of this thesis is the retrieval of H_2O and CH_4 from the MIPAS satellite instrument.

There are many motivations to measure water vapour in the atmosphere. Water vapour in the upper troposphere and stratosphere plays a major role in the balance of planetary radiation (Harries, 1997; Forster and Shine, 1999). It exhibits strong absorption and emission in the infrared, making it an important greenhouse gas. Its importance in the planetary radiation budget means that an accurate representation of water vapour is of great importance in climate models. Water vapour distributions are strongly influenced by atmospheric dynamics, and so serve as useful diagnostics of the atmospheric circulation. In turn, atmospheric dynamics are influenced by the water vapour distribution, since the condensation of water vapour provides a substantial reservoir of heat in the atmosphere (WMO (2000) and references therein). Furthermore, water vapour plays a key role in many aspects of atmospheric chemistry. It is a primary source of OH radicals, and so is strongly coupled with ozone and nitrogen chemistry.

Methane is also an important greenhouse gas and a useful tracer of dynamical motions. However, in addition to methane being useful/interesting in its own right, it is also an important source of water vapour in the stratosphere, with methane oxidation producing approximately two molecules of water vapour for every methane molecule destroyed. Water vapour and methane, along with molecular hydrogen, account for most of the hydrogen budget in the stratosphere. If the hydrogen held in other species is assumed to be negligible, then the total hydrogen can be expressed as

$$\mathrm{H_{total}} = [\mathrm{H_2}] + 2[\mathrm{CH_4}] + [\mathrm{H_2O}], \tag{1.1}$$

where $[X]$ denotes the volume mixing ratio (VMR) of gas X. The total hydrogen in the stratosphere and mesosphere is generally assumed to be a conserved quantity. The mixing ratio of molecular hydrogen is expected to remain reasonably constant in the lower stratosphere, with a value of around 0.5 ppmv (Le Texier et al., 1988). So the quantity H_2O+$2CH_4$ (often referred to as "equivalent water" (McCarthy et al., 2003b)) is expected to be a conserved quantity in the lower stratosphere (Engel et al., 1996) except where water is lost, for example due to ice formation and gravitational settling in the winter vortices.

Since methane is a significant source of water vapour in the stratosphere, changes in water vapour are linked to changes in methane. Simultaneous measurements of water vapour and methane are therefore important in the study of causes of long–term changes in water vapour. Also, from the point of view of validation of measurements, the expected correlation between water vapour and methane can provide a useful internal validation test for the individual gases.

The Michelson Interferometer for Passive Atmospheric Sounding (MIPAS) is one of the core experiments on the European Space Agency's Envisat satellite, launched on 1^{st} March 2002. MIPAS measures infrared limb emission spectra in the spectral range 685–2410 cm^{-1} (wavelengths of 14.5–4.1 μm) over an altitude range 6–68 km. After suitable ground processing, these spectra allow retrievals of atmospheric pressure, temperature and numerous trace gases. The distribution of aerosol particles, tropospheric cirrus and stratospheric ice clouds (including polar stratospheric clouds) can also be derived from MIPAS data.

The European Space Agency (ESA) has been retrieving pressure, temperature and six high priority species (H_2O, O_3, HNO_3, CH_4, N_2O and NO_2) from the MIPAS spectra operationally. In addition, separate retrieval schemes have been developed at various European institutions, including Oxford (under the EU–funded 'AMIL2DA' project (AMIL2DA, 2002a)), both to validate the operational retrievals and to extend the range of products which can be obtained from the MIPAS spectra. For example, the MIPAS spectra contain sufficient information to distinguish between minor isotopes of many trace gases.

Both water vapour and methane provide the potential of additional information through measurements of their isotopic composition. Due to its high spectral resolution, broad spectral range and good global coverage, MIPAS is the first instrument capable of making simultaneous measurements of isotopes of water vapour and methane on a global scale for an extended period of time.

1.2 Thesis outline

The aims of the thesis are:

- To contribute to the validation of the ESA operational retrievals of these gases.
- To retrieve global distributions of the isotopic composition of these gases using the Oxford retrieval scheme.

Before describing the work which has been performed towards achieving these aims, it is useful to provide some background information. This chapter outlines the current understanding of water vapour and methane in the Earth's atmosphere. A brief summary of the relevant large–scale dynamics and chemistry which affect the global–scale distributions of water vapour and methane is provided, along with descriptions of the expected distributions. The focus is on the MIPAS altitude measurement range (the upper troposphere to the lower mesosphere.) Chapter 2 provides an introduction to the principles of remote sounding and to the MIPAS instrument. Chapter 3 provides an introduction to the retrieval terminology and to certain specific applications of retrieval theory which will be used and referred to in the later chapters.

Chapter 4 describes work that has been done towards the validation of the ESA retrievals of water vapour and methane in terms of internal consistency checks and comparisons with other data sources. In Chapter 5, possible causes of the problems with the ESA MIPAS water vapour and methane products which have been identified in Chapter 4 are examined.

Chapter 6 covers the work that has been done on retrievals of the isotopic composition of water vapour and methane using the retrieval software developed at Oxford. Chapter 7 reflects on conclusions and outlines possible future work which might stem from the work described in this thesis.

1.3 Previous measurements and measurement techniques

A great deal is known already about the global distributions of water vapour and methane. This knowledge has been built up over a number of years using data from many instruments on numerous platforms, using various *in situ* and remote sounding techniques. In this section, the aim is to put MIPAS measurements into the context of past measurements which have led to the present–day understanding of the global–scale distribution of water vapour and methane in the MIPAS altitude measurement range.

There has been somewhat more controversy in the history of water vapour measurements than in that of methane. A detailed review of *in situ* and remote sounding measurement techniques used in the measurement of atmospheric water vapour can be found in the SPARC Water Vapour Assessment (WMO, 2000). A brief overview is provided here.

Measurements of water vapour in the troposphere have been of interest for a long time, due to the role of water vapour in weather forecasting. The first measurements of water vapour in the stratosphere were made from aircraft, over the south of England, using a manually operated frost–

point hygrometer (Brewer, 1949). The first flights reported mixing ratios as low as 1.6 ppmv at an altitude around 2 km above the tropopause, providing the first indication that the stratosphere was extremely dry compared to the troposphere. The earliest measurements were later corrected to account for a temperature error, bringing the measured values up to around 4 ppmv (Roscoe, 2005). Established values for stratospheric water vapour mixing ratios were in the region of 3 ppmv in the 1950s and around 5 ppmv in the 1970s, based on ongoing frost–point hygrometer measurements from aircraft.

Balloon–borne *in situ* and remote measurements of stratospheric water vapour were first reported in the literature in the 1960s. Results were mixed with some measurements indicating a considerable increase of water vapour mixing ratio with altitude above the tropopause and others showing little or no change (Gutnik, 1961). The debate at this time was not as to whether there was a slight increase in the water vapour mixing ratio with altitude, but whether or not there were order of magnitude changes in the mixing ratio in the stratosphere. It was later understood that out–gassing of water vapour from the balloon skin during ascent caused water vapour contamination of the *in situ* sensors or of the atmosphere in the vicinity of the balloon.

Measurements from frost–point hygrometers on balloons were begun in the 1960s. A long and valuable set of water vapour measurements were made, first by Mastenbrook (mainly over Washington DC) and later by Oltmans (mainly over Boulder, Colorado) (see, for example, Mastenbrook and Oltmans (1990)). These measurements were used to establish that the dryness of the stratosphere did extend up to at least 28 km, and did not just apply to the altitude region just above the tropopause.

Measurements in the late 1970s made using the newly developed Lyman–α hygrometer (Kley et al., 1979) showed a slight increase of water vapour mixing ratio in the stratosphere with altitude in the stratosphere. Tropical soundings revealed an absolute minimum in water vapour mixing ratio (the "hygropause") located 2–3 km above the tropical tropopause. Minimum values of 2.3 ppmv were reported.

Satellite measurements of water vapour in the stratosphere began in the 1970s with instruments on board the Nimbus satellites (see Tables 1.1, 1.2 and 1.3). Satellite measurements provided confirmation of the increase of water vapour mixing ratio with altitude in the stratosphere.

The SAMS instrument on Nimbus 7 offered the first satellite measurements of CH_4. Before this, measurements were limited to somewhat sparse individual profiles obtained by *in situ* sampling (see the summary in WMO (1982)).

Coincident measurements of water vapour and methane from LIMS and SAMS on the Nimbus 7 satellite allowed the first global view of the total hydrogen variability (Jones et al., 1986). These findings were confirmed by the ATMOS space shuttle missions (Gunson et al., 1990).

Satellite instruments measuring water vapour and methane from the early Nimbus satellites through to the present day are listed in Tables 1.1, 1.2 and 1.3. These, in conjunction with ongoing shuttle–borne, balloon, aircraft and ground–based measurements, have allowed a reasonable idea of what to expect in terms of the global distribution of water vapour and methane. Even so, the atmosphere is continually changing with time, and so present and future measurements are important in refining and developing current knowledge and understanding of the atmosphere.

There are still outstanding issues in the understanding of water vapour in particular. Satellite measurements of water vapour in the upper troposphere and lower stratosphere, where many of the unresolved issues lie, are difficult to interpret due to fine vertical structure at the tropopause and the large vertical gradients of water vapour in the upper troposphere. Measurements at low altitudes are difficult to make, especially in the presence of cirrus clouds, which may bias results in the upper troposphere and lower stratosphere (UTLS) region towards dry values.

Table 1.1: Satellite nadir sounding measurements of H_2O and CH_4

Launch	Satellite	Instrument		Technique†	H_2O	CH_4
1969,70	Nimbus 3,4	IRIS	Infrared Interferometer Spectrometer	MI	●	●
1970,72	Nimbus 5	SCR	Selective Chopper Radiometer	GC	●	
1972	Nimbus 5	NEMS	Nimbus E Microwave Spectrometer	MW	●	
1975	Nimbus 6	HIRS	High Resolution Infrared Radiation Sounder	FR	●	
		SCAMS	Scanning Microwave Spectrometer	MW	●	
1974–94	NOAA 6–14	*TOVS*	[a] *TIROS Operational Vertical Sounder*		●	
		HIRS/2	High Resolution Infrared Radiation Sounder/2	FR	●	
1980–96	GOES 4–7	VAS	VISSR Atmospheric Sounder	FR	●	
1994–	GOES 8–		(sounders with similar channels to HIRS)	FR	●	
1998–	NOAA 15–	*ATOVS*	[a] *Advanced TOVS*		●	
1999	EOS Terra	MOPITT	Measurements of Pollution in the Troposphere	GC		●
2001	Aqua	AIRS	Atmospheric Infrared Sounder	GS	●	●
2002	Envisat	SCIAMACHY	Scanning Imaging Absorption Spectrometer for Atmospheric Chartography	GS	●	●
2004	Aura	TES	[b] Tropospheric Emission Spectrometer	MI	●	●
2005	Metop	IASI	Infrared Atmospheric Sounding Interferometer	MI	●	●
		ATOVS	*(as above)*	FR/MW	●	

†FR=Filter Radiometer, MI=Michelson Interferometer, GC=Gas Correlation Radiometer, MW=Microwave Radiometer, GS=Grating Spectrometer

Table 1.2: Satellite limb sounding measurements of H_2O and CH_4

Launch	Satellite	Instrument		Technique†	H_2O	CH_4
1978	Nimbus 7	LIMS	Limb Infrared Monitoring of the Stratosphere	FR	●	
		SAMS	Stratospheric and Mesospheric Sounder	GC	●	●
1981	SME		Solar Mesosphere Explorer	RS	●	
1991	UARS	ISAMS	Improved Stratospheric and Mesospheric Sounder	GC	●	●
		CLAES	Cryogenic Limb Array Etalon Spectrometer	FP	●	●
		MLS	Microwave Limb Sounder	MW	●	
1994,97	Shuttle	CRISTA	Cryogenic Infrared Spectrometers and Telescopes for the Atmosphere	GS	●	●
2001	Odin	SMR	Sub-Millimeter Radiometer	MW	●	
2002	Envisat	MIPAS	Michelson Interferometer for Passive Atmospheric Sounding	MI	●	●
		SCIAMACHY	[b] Scanning Imaging Absorption Spectrometer for Atmospheric Chartography	GS	●	●
2001	TIMED	SABER	Sounding of the Atmosphere using Broadband Emission Radiometry	FR	●	
2004	Aura	HIRDLS	High Resolution Dynamics Limb Sounder	FR	●	●
		MLS	Microwave Limb Sounder	MW	●	
		TES	[a] Tropospheric Emission Spectrometer	MI	●	●

†FR=Filter Radiometer, GC=Gas Correlation Radiometer, FP=Fabry-Perot Spectrometer, MI=Michelson Interferometer, MW=Microwave Radiometer, GS=Grating Spectrometer, RS=Rayleigh Scattering [a] See also Table 1.1 [b] See also Table 1.3

Table 1.3: Satellite occultation measurements of H_2O and CH_4

Launch	Satellite	Instrument		Technique†	H_2O	CH_4
1984	ERBS	SAGE II	Stratospheric Aerosol Gas Experiment II	FR	●	
1985	Spacelab 3	ATMOS	Atmospheric Trace Molecule Spectroscopy	MI	●	●
1991	UARS	HALOE	Halogen Occultation Experiment	GC/FR	●	●
1996	ADEOS	ILAS	Improved Limb Atmospheric Spectrometer	GS	●	●
1998	SPOT-4	POAM III	Polar Ozone and Aerosol Measurement III	FR	●	
2001	Envisat	GOMOS	Global Ozone Monitoring by Occultation of Stars	GS	●	
		SCIAMACHY	[a]Scanning Imaging Absorption Spectrometer for Atmospheric Chartography	GS	●	●
2001	Meteor-3M	SAGE III	Stratospheric Aerosol Gas Experiment III	GS	●	
2003	SCISAT	ACE	Atmospheric Chemistry Explorer	MI	●	●
2005	Metop	GRAS	GPS Receiver for Atmospheric Sounding	RO	●	

†FR=Filter Radiometer, MI=Michelson Interferometer, GC=Gas Correlation Radiometer, RO=Radio Occultation, GS=Grating Spectrometer

[a] See also Table 1.2

1.4 Distributions

The aim in this section is to provide an overview of the current knowledge of the global distribution of water vapour and methane which has been built up over the years.

Figure 1.1 shows expected shapes of mid–latitude profiles of temperature, water vapour, methane and equivalent water (H_2O + $2CH_4$) (Remedios, 1999). The temperature profile is shown here in order to relate the approximate altitude ranges of the different temperature layers (troposphere, stratosphere and mesosphere) to changes in the gas concentration profiles. The MIPAS altitude measurement range is also shown. It can be seen that MIPAS measurements extend from the upper troposphere to the lower mesosphere. Water vapour mixing ratios are extremely high in the troposphere, dropping off sharply in the stratosphere, with minimum values slightly above the tropopause. The water vapour profile then increases with height in the stratosphere. At some point in the upper stratosphere, the water vapour mixing ratio begins to decrease with height. Methane is well–mixed in the troposphere, with a mixing ratio that decreases with altitude in the stratosphere. The expected profile of equivalent water can be seen to be reasonably constant with altitude throughout the stratosphere, starting to decrease with altitude at the point where water vapour starts to decrease with altitude.

The mid–latitude climatological profiles in Figure 1.1 give a general picture of the expected variation with height of temperature, water vapour and methane. Variations in the profiles in location

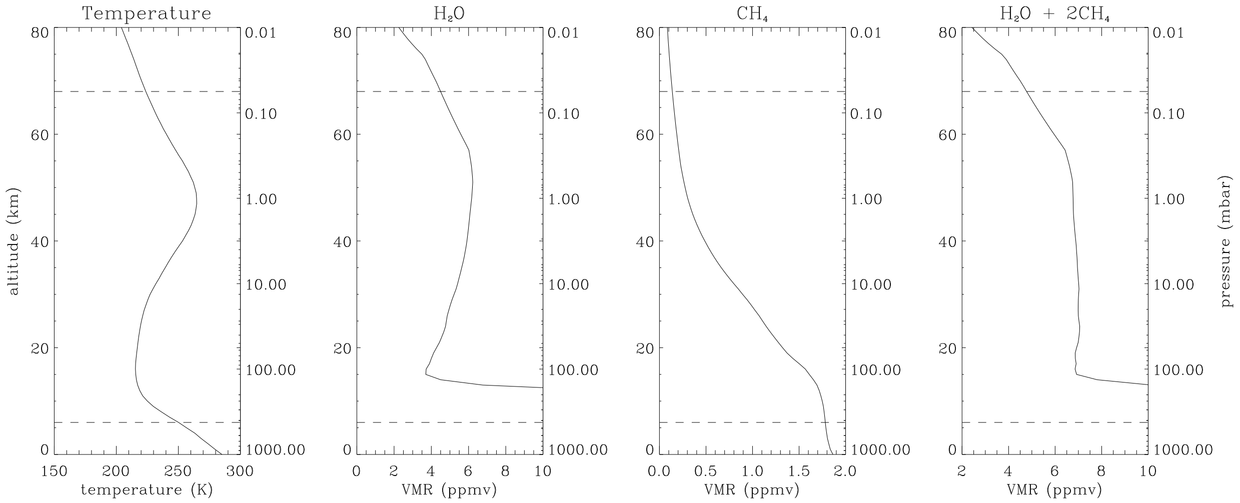

Figure 1.1: Mid–latitude day–time climatological profiles of (left to right) temperature, water vapour, methane and equivalent water (Remedios, 1999). Dotted lines at 68 and 6 km show the top and bottom of the MIPAS measurement range in altitude.

and time will be discussed in the sections which follow.

Trace constituents in the stratosphere, water vapour and methane included, tend to have relatively small variations along a latitude circle and the zonal dimension adds little information. Exceptions to this are the lowermost stratosphere and the regions of the polar vortices, particularly the Arctic vortex, which is often displaced somewhat from the pole. Variations in these regions are touched on in this Chapter, but in general, stratospheric results here are discussed in terms of zonal averages.

Although methane is well–mixed in the troposphere, the distribution of water vapour is highly variable, showing large variations in the vertical, meridional and zonal dimensions. Spatial distributions of water vapour in the upper troposphere will be touched on here, but not discussed in detail. Detailed examinations of the spatial variability of water vapour in the upper troposphere can be found in e.g. WMO (2000) and references therein.

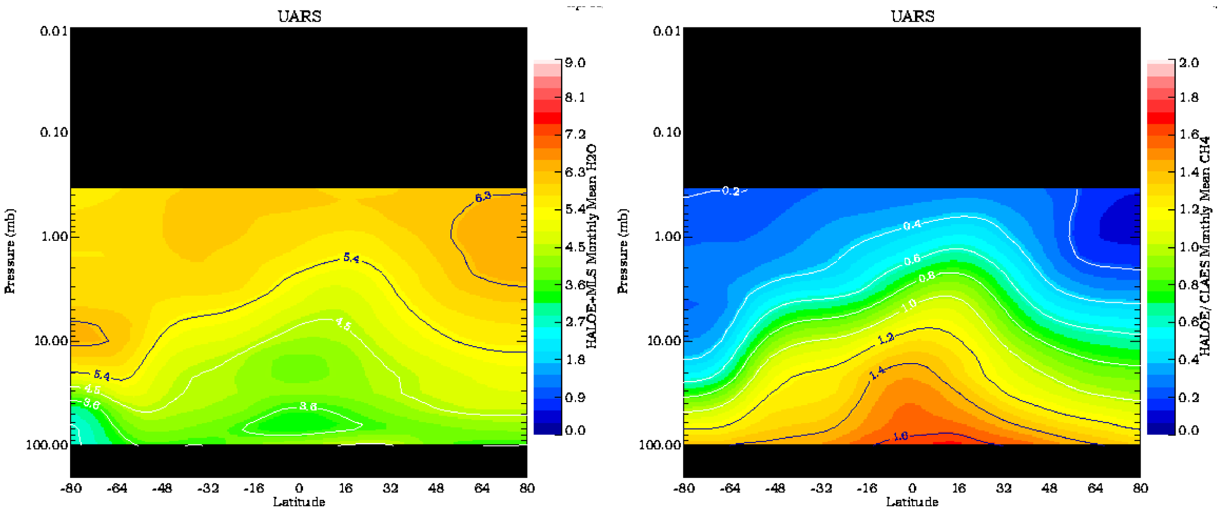

Figure 1.2: Latitude/pressure distribution of monthly mean water vapour (left) and methane (right) for August 1992 as measured by instruments on the Upper Atmosphere Research Satellite (UARS). The H_2O dataset was constructed using profiles from HALOE (see table 1.3) and MLS (see table 1.2), while the CH_4 dataset was constructed using profiles from HALOE and CLAES (see Table 1.2) (HALOE, 2005).

1.4.1 Stratosphere

Figure 1.2 shows distributions of water vapour and methane in the stratosphere, measured by instruments aboard the Upper Atmosphere Research Satellite (UARS) in August 1992.

The key features in the methane distribution are a bulge in the isopleths (lines of constant mixing ratio) in equatorial regions, due to a general ascending motion in this area, and gradual decreases in mixing ratio with altitude.

The water vapour distribution also shows a bulge in the isopleths in equatorial regions due to ascending motion, but, unlike methane, does not show a monotonic decrease in mixing ratio with altitude. The key features in the water vapour distribution are a sharp vertical gradient at the tropical tropopause and in the extratropical lower stratosphere, a minimum in the tropics at or just above the tropopause and gradual increases upward and poleward.

The key features in the distribution of methane in the stratosphere can be understood as a balance between the following processes (WMO, 2000): (1) a meridional circulation and (2) stratospheric chemistry. An understanding of the mean distribution of water vapour in the stratosphere requires consideration of the following additional processes: (3) dehydration at the tropical tropopause, (4) seasonal dehydration in the polar regions and (5) a variety of processes through which tropospheric moist air leaks into the extratropical lower stratosphere.

(1) Meridional circulation

The large–scale motions of the stratosphere, summarised in Figure 1.3, are characterised by ascending motion in the tropical stratosphere and descending motion at the poles. The mid–latitudes tend to be well mixed while the polar regions may well be isolated and dynamically stable due to the polar vortex, especially in the winter.

The tropical region is where the largest net influx of air to the stratosphere from the troposphere is believed to take place. Long–lived chemical species with mixing ratios that are nearly uniform throughout the troposphere, such as methane, are observed to have their largest stratospheric mixing ratios immediately above the tropical tropopause, matching tropospheric values. These species show upward extending plumes of relatively large mixing ratios throughout the depth of the tropical stratosphere, consistent with upward transport in this region and a degree of isolation from the extratropics (Holton et al., 1995).

Water vapour is expected to show a similar upward extending plume, but in contrast with methane, very low values of the water vapour mixing ratio extend upward from a minimum within a few kilometres of the tropopause. Rapid isentropic mixing ensures that the low water vapour values extend polewards to create a very dry layer in the lower stratosphere in general.

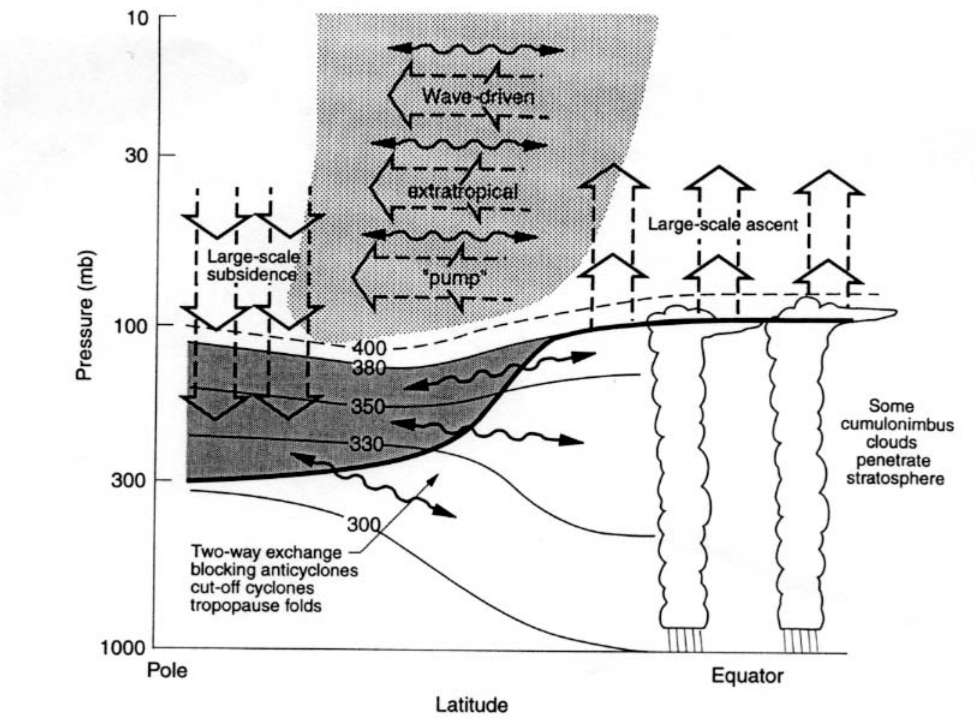

Figure 1.3: Dynamical aspects of stratosphere–troposphere exchange. The thick line represents the tropopause. Thin lines are isentropic surfaces labelled in Kelvin. The wavy double–headed arrows denote meridional transport by eddy motions and the broad arrows show transport by the global–scale circulation of the stratosphere (Holton et al., 1995)

(2) Stratospheric chemistry

Water vapour is formed in the stratosphere by the oxidation of methane, leading to the observed increase of water vapour and decrease of methane with altitude in the stratosphere. This can happen directly, by the oxidation of methane by an OH radical or indirectly by the oxidation of methane by $O(^1D)$, chlorine or other halogens (Le Texier et al., 1988) to form formaldehyde (CH_2O), which is then oxidised to form water vapour. The methane oxidation chain is summarised in Figure 1.4. The oxidation of formaldehyde may also result in an end product of molecular hydrogen rather than water vapour. The oxidation of methane results in roughly two molecules of water for every molecule of methane destroyed (Le Texier et al., 1988; Brasseur and Solomon, 1986). The exact number varies somewhat with latitude and altitude, depending on the production of H_2O/H_2 from the oxidation of formaldehyde. The sum $H_2O + 2CH_4$ (referred to as "equivalent water") is, as a consequence, expected to be nearly constant in the stratosphere except where air is significantly influenced by dehydration, like in the polar regions (see below) and where air retains the cycle of tropopause temperatures (see § 1.5.1). Water is also produced in the stratosphere, to a lesser extent, by the oxidation of molecular hydrogen, which may also disrupt the constancy of equivalent water.

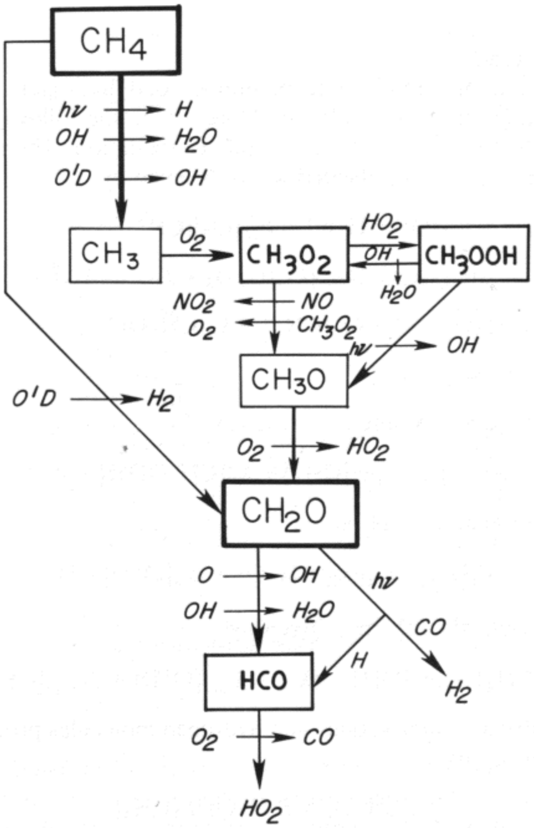

Figure 1.4: Diagram of the methane oxidation chain of photochemical reactions (Le Texier et al., 1988)

In the upper stratosphere and lower mesosphere, water vapour reacts with excited oxygen to form hydroxyl radicals and higher still, water vapour is destroyed by photolysis (Brasseur and Solomon, 1986), leading to the observed decrease in water vapour mixing ratios at these altitudes. Methane is also destroyed by photolysis above the stratopause.

(3) Dehydration at the tropical tropopause

There is widespread agreement that nearly all of the air that enters the stratosphere above the global hygropause originally travelled through the tropical tropopause (Holton et al., 1995) and that the tropopause region acts as a “cold trap”, in which air is dehydrated to very low values. Only in the tropics are tropopause temperatures low enough to dehydrate air to the mixing ratios observed in the stratosphere (Brewer, 1949). It is generally agreed that convection, along with the meridional circulation, plays a role in dehydration, but many important details are unclear.

Several theories to explain the entry mechanisms of water vapour into the stratosphere in the tropics exist (Holton et al., 1995). One suggests a slow ascending motion (Brewer, 1949). The other main theory is that a rapid dehydration takes place through over–shooting convective cells that penetrate into the stratosphere (Danielsen, 1982). It has been suggested (Newell and Gould-Stewart, 1981) that this rapid dehydration takes place at specific locations and times, like some kind of “stratospheric fountain”. The suggested location and time was over the Indonesian maritime continent during Northern hemispheric winter (the coldest location and time of the year). However, there are conceptual problems with this idea (Rosenlof, 2003). Satellite data show that air enters the stratosphere throughout the year (Mote et al., 1995). Also, there is evidence that the average motion over the Indonesian subcontinent is downward (Sherwood and Dessler, 2000). In addition, the amounts of water vapour in the mid–latitude lower stratosphere have been observed to be increasing (Oltmans et al., 2000) while the tropical tropopause and lower stratosphere have cooled (Zhou et al., 2001).

More recently, discussions of the entry of water vapour into the stratosphere in the tropics have involved the concept of a transition layer between the troposphere and the stratosphere, rather than a well–defined tropopause. This layer is referred to as the tropical tropopause layer (TTL). In this layer both rapid dehydration in specific regions and slower ascending motions could take place. The air masses mix inside the transition layer through horizontal motions (Sherwood and Dessler, 2000).

It is now generally thought that dehydration may occur with contributions from both mechanisms (Dessler, 2002; Gettelman and Forster, 2002). Recent aircraft–borne water vapour isotope measurements by Webster and Heymsfield (2003) indicate that air transported into the stratosphere through the TTL is dehydrated through a mixture of convective (fast) dehydration and dehydration by condensation accompanying gradual ascent. An understanding of the relative contributions of these two processes is necessary in order to investigate the reported change in water vapour (Rosenlof, 2001) and to predict how possible changes in convection intensity and detrainment altitude, cloud microphysics and TTL temperatures may alter the humidity of air entering the stratosphere in the future (McCarthy et al., 2003a).

There has been considerable recent interest in the use of measurements of the isotopic composition of water vapour to provide an additional constraint in determining the method of entry of air and water vapour into the stratosphere.

(4) Dehydration in polar regions

In the polar vortices, temperatures are sometimes low enough in winter for the air to reach saturation. The water vapour mixing ratio is then lowered by dehydration. In the southern polar vortex, this seasonal dehydration is strong enough to affect the annual mean there. In spring and early summer, dehydration can affect mid–latitudes below the 400 K potential temperature surface but has little influence on the rest of the stratosphere (Mote et al., 1995). Dehydration has been observed in the Arctic (e.g. Herman et al. (2003)) but occurs less frequently there due to the generally warmer temperatures.

(5) Tropospheric leakage to the extratropics

Air in the mid–latitude lower stratosphere below the altitude of the tropical tropopause has considerably higher water vapour mixing ratios than in the tropical stratosphere and so must have entered the stratosphere without passing the tropical tropopause cold trap (Brewer, 1949; Dessler et al., 1995).

It has been suggested (Hintsa et al., 1998) that air can enter the mid–latitude lower stratosphere in three ways. The first (pathway 1 in Figure 1.5) is by diabatic descent from the "overworld" (the stratosphere above the 380K isentropic surface). The second is by adiabatic transport along isentropes from the upper tropical troposphere. This process works both ways between the tropical upper troposphere and the mid–latitude lower stratosphere, where the isentropes cross the tropopause (pathway 2 in Figure 1.5, also indicated by the wavy arrows in Figure 1.3). The third way that air can enter the stratosphere in mid–latitudes is by upward transport across the mid–latitude tropopause (pathway 3 in Figure 1.5). This can occur through events such as cut–off cyclones and tropopause folds (Vaughan et al., 1994). These events may also result in downward transport of air from the stratosphere to the troposphere.

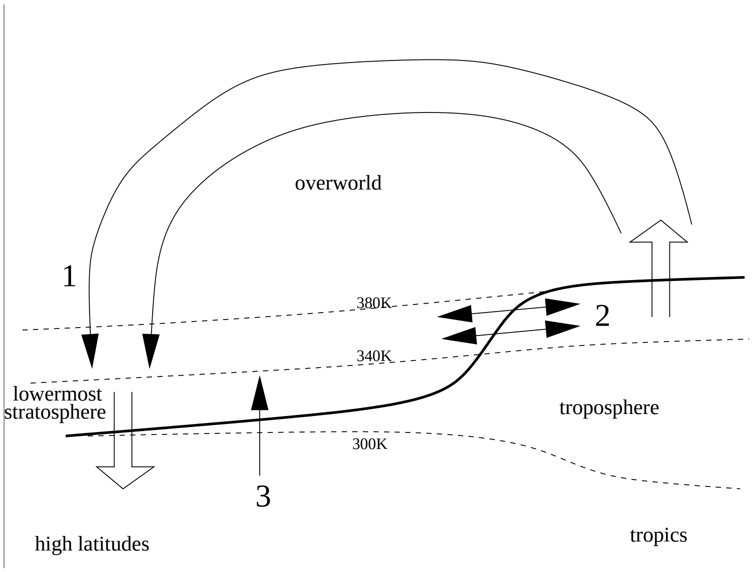

Figure 1.5: Schematic picture of the transport into (and away from) the mid–latitude lower stratosphere. The thick line denotes the tropopause, the thick arrows show stratosphere–troposphere exchange through the large–scale circulation and the labelled arrows show pathways by which air may enter the lower stratosphere (Hintsa et al., 1998).

Concluding remarks

The distribution of methane and water vapour in the stratosphere can be broadly understood as a balance of the above processes. However, a full picture requires consideration of the seasonal variations in the mechanisms that influence the distribution.

1.4.2 Upper troposphere

As previously mentioned, methane is well–mixed in the troposphere and is not expected to show any large spatial variations in the upper troposphere. Water vapour mixing ratios in the troposphere however are strongly modulated by thermodynamic constraints and mixing ratios decrease by several orders of magnitude from the surface to the tropopause. Since upper tropospheric water vapour exhibits very strong seasonal and interannual variations, it may be better to discuss the distribution in the context of later sections. However, a brief overview is provided here.

In general, upper tropospheric water vapour is higher in tropical regions than elsewhere. There are three areas in the tropics where mixing ratios are particularly high (WMO, 2000): over the maritime continent and Indonesia, over the equatorial part of South America and over central Africa. These three tropical maxima are associated with the ascending branches of three tropical monsoon systems: the African Monsoon, the Austral–Asian Monsoon and the South American Monsoon. The maxima also coincide with areas of more frequent sub–visible cirrus clouds (Wang et al., 1996)

Minima in upper tropospheric humidity are found in the sub–tropics. These minima are not symmetrical, and vary significantly with season. These can be accounted for dynamically as descending branches of a steady circulation.

1.5 Seasonal variations

In most of the stratosphere above about 20 km, the seasonal cycle is dominated by the meridional circulation discussed in § 1.4.1. It is worth noting that there is a marked hemispheric asymmetry in the zonal distributions of water vapour and methane shown in Figure 1.2. This asymmetry is due to the difference between the prevailing dynamical situation in summer and winter. The winter–time stratosphere is dominated by large–amplitude Rossby waves propagating upward from the troposphere. Intermittently these waves break, stirring air more or less isentropically across large distances of the winter stratosphere within a region that has become known as the "surf zone" (McIntyre and Palmer, 1983). This region is bounded by sharp gradients of potential vorticity (PV) and of tracers in the winter sub–tropics (the "sub–tropical barrier") and at the edge of the polar vortex (Plumb, 2002). These "barriers" can be seen in the latitudinal distributions of both water vapour and methane shown in Figure 1.2. The summer–time stratosphere is less turbulent and does not show these barriers.

Seasonal variations in water vapour and methane in specific latitude regions are described below. Seasonal variations in stratospheric methane in tropical and mid–latitude regions are generally linked with variations in dynamics. For these regions the discussion is focussed on water vapour.

1.5.1 The tropics

Seasonal variations in water vapour in the tropics are strongly linked with seasonal variations in temperature. The amount of water entering the stratosphere is largely controlled by the tropopause temperature, since that is the lowest temperature a rising air parcel will experience whilst travelling from the troposphere into the stratosphere (Mote et al., 1995). This temperature experiences a very pronounced annual cycle, leaving alternating low and high amounts of water vapour in the lowest part of the stratosphere (see Figure 1.6). An air parcel passing the tropopause and carried upward in the large scale stratospheric circulation will thus be marked with the "entry mixing ratio" in the same way as a magnetic tape is marked by the recording head (Mote et al., 1996). This recorded signal is rather isolated because of the sub–tropical barriers. It can be used to study the ascent rate, the diluting from mixing through the barriers and the effect of the quasi–biennial oscillation (QBO — see § 1.6.2) on the rising motions. However, the details of the mechanisms controlling the input of water vapour through the tropopause are somewhat unclear.

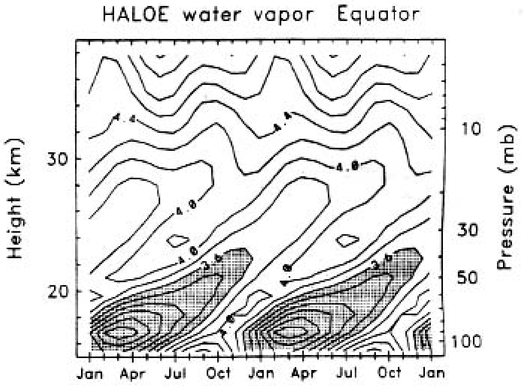

Figure 1.6: Height–time seasonal variation of water vapour mixing ratio (ppmv) at the equator derived from HALOE data. Two consecutive seasonal cycles are shown. (Figure reproduced from Randel et al. (2001).)

1.5.2 Mid–latitudes

Time series of polar water vapour from satellite measurements show evidence of downward mass flux in the middle stratosphere throughout winter in both hemispheres (WMO, 2000). CH_4 (Randel et al., 1998) and H_2O observations (WMO, 2000) suggest downward movement at a rate of around 1.5 km per month.

There is evidence for a seasonal cycle of water vapour in the mid–latitude lower stratosphere (WMO (2000) and references therein). The cycle shows a relative minimum in the vertical profile of water vapour in the lower stratosphere, centred near 15 km in winter and near 18 km in summer.

In mid–latitudes, care must be taken to separate seasonal variability from large amplitude meteorological variations. Hintsa et al. (1994) observe a seasonal cycle with higher values in autumn than in spring.

1.5.3 Polar regions

There are low values of water vapour in the Southern Hemisphere polar regions during winter–spring, associated with dehydration in the Antarctic polar vortex. HALOE data (Rosenlof et al., 1997) indicates that the dehydration influences latitudes 10°–20° outside the vortex. Mote et al. (1995) shows that the influence from polar dehydration in the Southern Hemisphere extends equatorward to 50°S after vortex break–up. Polar dehydration thus significantly affects zonal mean concentration of water vapour in the lowest regions of the stratosphere poleward of 40°–50°S.

During the polar night, there is no $O^1(D)$ or OH available. This means that there is no production of water vapour from methane oxidation. The rather rapid increase of water vapour concentration with altitude is instead due to downward transport from higher altitudes. This transport and the dehydration in the vortex will cause a maximum in the water vapour mixing ratio at about 30 km. This feature can be seen in the water vapour distribution in Figure 1.2.

Since there is no methane oxidation taking place, one might expect higher methane values in polar winter than in polar summer. However, methane values are likely to be low because of the general descending motion bringing methane–poor air from higher altitudes.

1.5.4 Seasonal variations in the upper troposphere

The distribution of water vapour in the upper troposphere is strongly influenced by temperature and dynamics. In mid–latitudes and polar regions, the dynamical situation is highly variable.

Seasonal water vapour variability in the tropical and sub–tropical upper troposphere is closely tied to the vertical circulation cells associated with the seasonal Hadley and Walker circulation. Upper tropospheric maxima in water vapour are associated with upward motion and minima with downward circulation. Water vapour seasonality is closely tied to the meridional movements of tropical convective upwelling.

A detailed discussion of seasonal variations of water vapour in the upper troposphere can be found in (WMO, 2000).

1.6 Non–seasonal variations

In addition to the seasonal variations described in the previous section, there are a number of variations in distributions of water vapour and methane at both longer and shorter time scales. Brief discussions of semi–annual and interannual variations and of transient variability are provided in this section.

1.6.1 Semi–annual oscillation

There are variations in both water vapour and methane in the stratosphere which are linked with the semi–annual oscillation (SAO) in the equatorial zonal wind. There are two peaks in the amplitude of the zonal wind; one at the stratopause (around 45–50 km) and one at the mesopause (around 80 km). The SAO in the equatorial zonal wind is accompanied by an SAO in temperature and in meridional circulation, and so the influence of the SAO extends beyond the equator and below the stratopause. In periods when there is a westerly acceleration of the winds there is induced descent near the equator and ascent in the subtropics below the level of maximum forcing. There is ascent near the equator and descent in the subtropics above this level. (The circulation is in the opposite sense for an easterly acceleration of the equatorial winds.)

The effects are sufficiently strong to produce absolute descent over the equator at times of westerly forcing. This descending motion over the equator leads to an observed “double peak” structure in the water vapour and methane (and other long–lived tracers) (Ruth et al., 1997). The maximum westerlies at the stratopause are attained around 1 month after the equinoxes, so this is the time associated with the double peak structure.

1.6.2 Interannual variation

Interannual variations in the stratosphere and upper troposphere are almost completely independent. There are interannual variations in both methane and water vapour in the stratosphere caused by the quasi–biennial oscillation (QBO), while there are significant interannual variations in water vapour in the troposphere due to the El Niño Southern Oscillation (ENSO) in the troposphere. Only at the tropical tropopause are both phenomena evident.

The QBO is a fluctuation in the mean zonal wind in the equatorial stratosphere with an average (but somewhat irregular) period of around 28 months. The fluctuation in the mean zonal wind is accompanied by temperature perturbations of a few degrees. The QBO leads to anomalies in ascent in the equatorial stratosphere and therefore affects the distribution of trace gases like water vapour and methane. The QBO signature in water vapour and methane from HALOE has been examined by Randel et al. (1998). Although the QBO is a tropical phenomenon, it also appears to affect trace constituents at mid–latitudes. It induces large changes in meridional gradients in the sub–tropics (Gray and Russell, 1999) and also acts to modulate the double–peaked semi–annual oscillation patterns in the upper stratosphere (Kennaugh et al., 1997). The effects of the QBO on the water vapour distribution are reviewed in detail in WMO (2000).

The El Niño Southern Oscillation (ENSO), an irregular variation of the tropical Pacific Ocean and overlying atmosphere with a return period of 2–7 years, is the leading pattern of global interannual variability in the troposphere. In the cool or La Niña phase of the Southern Oscillation, the warmest water and convection are located in the western Pacific. In the warm or El Niño phase, warm water and convection spread eastward, usually over a greater longitudinal range. Upper tropospheric water vapour is greatly influenced by the ENSO, and not just in the tropics. A detailed review of the effects of ENSO on upper tropospheric water vapour can be found in WMO (2000).

1.6.3 Transient variability

The focus of this thesis is on data from MIPAS, a satellite instrument. The strength of satellite observations lies in the ability to look at large spatial scales, and therefore this will also be where the focus of the thesis lies. However, it should be recognised that spatial distributions of atmospheric constituents are far from smooth. The existence of transient small–scale variations is important to recognise as it complicates efforts to validate satellite measurements against *in situ* data.

1.6.4 Long–term changes

The MIPAS dataset does not span a long enough timescale to yield useful information on long–term changes and trends, so long–term changes will not be discussed in any great detail here.

The main point to note is that water vapour in the lower stratosphere is increasing. Analysis of measurements of water vapour mixing ratios by satellite and balloon measurements has led Rosenlof (2001) to suggest that stratospheric water vapour may have increased by about 2 ppmv over the past 45 years (roughly 1 % per year). Since water vapour is an important greenhouse gas, changes in stratospheric water vapour are expected to have an impact on tropospheric warming and stratospheric cooling (Forster and Shine, 2002). Methane concentrations are also increasing. Anthropogenic emissions of methane are strongly related to food production and population growth, and might therefore be expected to rise in the future. The radiative effects of methane increases would also be expected to have an impact on long–term climate change.

Long–term changes in water vapour and methane are discussed in detail in e.g. WMO (2000) (water) and Dlugokencky et al. (2003) (methane).

1.7 Conclusions

Although a great deal is already known about distributions of water vapour and methane in the upper troposphere and stratosphere, the atmosphere is continually changing, and monitoring of these changes is important. Also, although the distributions are reasonably well understood in many respects, questions remain, in particular with regard to the global, regional and seasonal distribution of water vapour in the lower stratosphere and the entry of air and water vapour into the stratosphere from the troposphere.

MIPAS offers good global coverage, simultaneous measurements of water vapour and methane, a vertical range which (in cloud–free cases) extends down into the upper troposphere and the potential for isotopic measurements. These attributes mean that MIPAS data have the potential to make a useful contribution to the field of knowledge.

Chapter 2

MIPAS

Profiles of H_2O and CH_4 (and other trace gases) are not measured directly by MIPAS, but are obtained from MIPAS measurements via a long chain of processing. This chapter aims to provide an introduction to the principles of remote sounding from limb sounders in general and to the processing required to obtain measurements from the MIPAS instrument in particular.

2.1 Remote sounding from a limb sounding spectrometer

2.1.1 Viewing geometry

The limb viewing geometry is depicted in Figure 2.1. The atmosphere is viewed tangentially and the viewing angle is changed in order to view tangent layers at different altitudes. The emission comes mainly from the tangent layer. Limb sounding requires very precise information about the field of view and the line of sight in order to accurately determine instrument pointing. This viewing geometry offers the potential for good vertical resolution. In addition, the long atmospheric path and the well–known background (cold space) can give a high sensitivity to trace species. The long atmospheric path can, however, be a disadvantage, in that measurements are often affected by cloud at low altitudes. Another disadvantage of limb viewing is poor horizontal resolution.

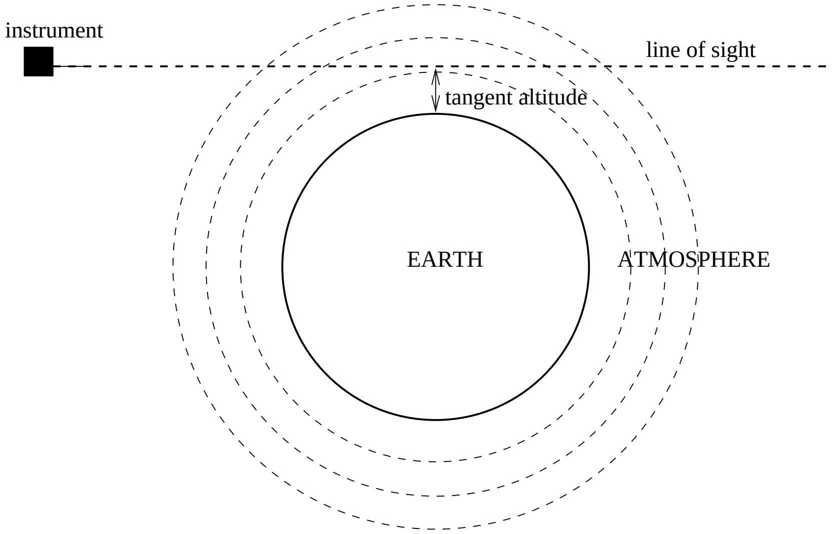

Figure 2.1: Limb viewing geometry

2.1.2 Radiative transfer

Measurements of atmospheric structure and composition from satellite instruments such as MIPAS require the use of remote sounding techniques. These techniques are based on the fact that the atmosphere emits, absorbs and scatters electromagnetic radiation and that the details of the spectrum depend on the molecules present. Almost every molecular species has its own characteristic spectral signature in the infrared and/or microwave regions. Measurements of infrared or microwave emission may therefore be used to determine atmospheric temperature and composition.

The theory of radiative transfer relates the remotely–measured electromagnetic radiation to the atmospheric state (the temperature and composition) in which we are interested. A brief outline of radiative transfer is provided here. For more in–depth coverage of the theory of radiative transfer, see e.g. Goody and Yung (1989).

The atmosphere absorbs and emits radiation in infrared and microwave wavelengths according to its temperature and to the gases and aerosols present. The radiance leaving the atmosphere is a function of the distribution of these gases and aerosols and the temperature.

The radiance reaching the instrument from a certain atmospheric path is made up of the radiance transmitted from one end of the path, and the emission along the path to the instrument. If scattering is negligible (a reasonable approximation at infrared wavelengths in the absence of cloud) and the atmosphere is in Local Thermodynamic Equilibrium (LTE), then the emitted radiation is given by the Planck function,

$$B(\nu, T) = \frac{2hc^2\nu^3}{\exp(hc\nu/k_BT) - 1}, \tag{2.1}$$

where ν is wavenumber, h is the Planck constant, c is the speed of light, k_B is the Boltzmann constant and T is temperature.

The monochromatic transmittance between a source at position x_s and an observer (the instrument) at position x_{obs} is given by

$$\tau\left(\nu, x_s, x_{obs}\right) = \exp\left(-\int_{x_s}^{x_{obs}} \Sigma_i k_i(\nu, x)\rho_i(x)dx\right). \tag{2.2}$$

The sum is over absorbers, where i is the i^{th} absorber with monochromatic absorption coefficient $k_i(\nu, x)$ and absorber number density $\rho_i(x)$.[1] The radiance L at wavenumber ν detected at x_{obs} from the source is

$$L(\nu, x_{obs}) = L(\nu, x_s)\tau(\nu, x_s, x_{obs}) + \int_{x_s}^{x_{obs}} B(\nu, T(x))\frac{\partial\tau(\nu, x, x_{obs})}{\partial x}dx, \tag{2.3}$$

---

[1] The sum of absorption coefficients over all absorbers is known as the absorption cross–section

and hence

$$L(\nu, x_{obs}) = L(\nu, x_s)\tau(\nu, x_s, x_{obs}) + \int_{x_s}^{x_{obs}} B(\nu, T(x))\tau(\nu, x, x_{obs})\Sigma_i k_i(\nu, x)\rho_i(x)dx. \tag{2.4}$$

For infrared emission measurements through the limb of the atmosphere, $L(\nu, x_s)$ is the emission of cold space, which is negligible.

2.1.3 Molecular spectroscopy

Spectral lines at infrared wavelengths arise from vibrational–rotational transitions in gas molecules. The positions, sizes and shapes of the spectral lines are determined by the type of molecule, the pressure and the temperature. Lines have line shape and line strength. The absorption coefficient k of a line centred at wavenumber ν_0 is a function of the line strength S and the line shape function g,

$$k(\nu, T, \rho) = S(T)g(\nu - \nu_0, T, \rho), \tag{2.5}$$

where ρ is the density of the absorber (molecule) in question.

Spectral lines are broadened by the Doppler effect, due to molecular motion, and by collisions with other molecules (Lorentz broadening). Doppler broadening dominates above about 40 km and is temperature dependent. Lorentz broadening dominates below about 10 km and is a function of pressure and temperature.

Collisional broadening of spectral lines of any particular molecular species can be further subdivided into two categories: self broadening, due to collisions of molecules of the same species, and foreign broadening, due to collisions of molecules of the species in question with N_2 and O_2, the most abundant molecules in the atmosphere. For most trace gases under most atmospheric conditions, the effects of self broadening can be considered negligible in comparison with the effects of foreign broadening.

2.1.4 Non local thermodynamic equilibrium

The use of Equation 2.4 to calculate the radiation reaching the instrument depends on the assumption that the atmosphere is in LTE. This means that the temperature of the Boltzmann distribution describing the populations of the vibrational levels of any given molecule is equal to the kinetic temperature and that the emission of atmospheric radiation is given by the Planck function at the local kinetic temperature. The assumption of LTE is expected to be valid at the lower altitudes where kinetic collisions are frequent. In the stratosphere and mesosphere, excitation mechanisms such as photo-chemical processes and solar pumping, combined with the lower collision relaxation rates, enable many of the vibrational levels of atmospheric constituents responsible for infrared emissions to have excitation temperatures that differ from the local kinetic temperature.

A general discussion of non–LTE radiative transfer can be found in Lopez Puertas and Taylor (2001), while a discussion of non–LTE effects in the MIPAS spectra can be found in Lopez Puertas et al. (2003). Studies of non–LTE effects in MIPAS spectra are not within the scope of this thesis. For the purposes of this thesis, it should be noted that non–LTE effects are expected to be dependent on illumination conditions, and would therefore be expected to lead to differences between day–time and night–time spectra for trace gases whose concentrations are not expected to show diurnal variations.

2.1.5 Aerosol, clouds and continuum features

There will also be contributions to the radiance measured at the satellite from emission and absorption due to things other than trace gases, namely cloud and aerosol.

Clouds occur on a variety of spatial scales and their radiative effects are governed by their physical and microphysical properties, which vary widely. In general, the presence of clouds in the line of sight leads to a strongly increased broadband continuum signal in the spectra, which may obscure the detection of gaseous emission lines. It is therefore reasonably straightforward to detect the presence of cloud in limb emission spectra, but it is notoriously difficult to then glean information about the position and properties of the cloud present. A detailed discussion of clouds in limb spectra can be found in Ewen (2005).

The presence of aerosol in the line of sight also leads to an increased broadband continuum signal in the spectra, which may also obscure the detection of gaseous emission lines. Measurements of trace gases from various instruments on the UARS satellite in the early 1990s were adversely affected by the presence of large amounts of volcanic aerosol in the lower stratosphere after the eruption of Mount Pinatubo.

Radiative transfer (Equation 2.4) in the presence of clouds or aerosol is complicated by terms due to scattering and is therefore more difficult to model than for trace gases alone.

A contribution to the continuum signal in atmospheric spectra is also made by water vapour, which, in addition to emission and absorption lines, also exhibits continuum emission and absorption across wide reaches of the infrared spectrum (Bignell, 1970).

2.1.6 Principle of remote sounding

Understanding the relationships between measured radiance, radiative transfer and molecular spectroscopy enables the measurements to be interpreted. The measurements contain information which can be extracted to form an estimate of the atmospheric state. It is possible to use inverse theory (retrieval theory — see Chapter 3) to obtain profiles of atmospheric temperature and composition from the measurements.

2.2 Fourier transform spectrometry

Fourier transform spectrometers (FTS) can provide high spectral resolution measurements in the infrared and can provide high sensitivity to trace gases. They have been used in ground–based, balloon and rocket–borne atmospheric research and are increasing in use as space–borne instruments. The design and implementation of FTS instruments for remote sensing applications is covered in detail in e.g. Beer (1992) and Persky (1995), but general concepts are introduced here.

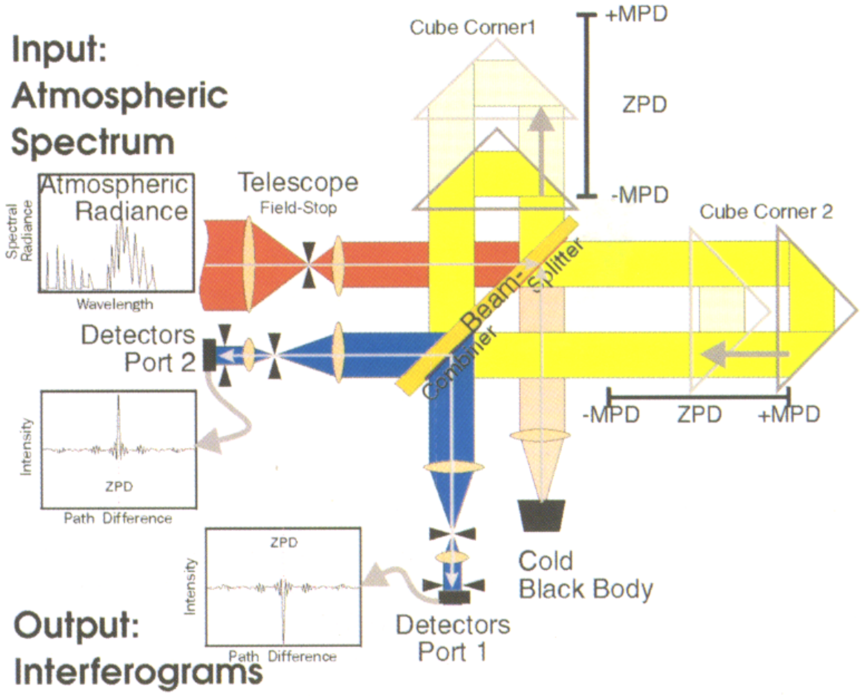

Figure 2.2: Simplified layout of the Fourier transform Interferometer (Envisat, 2001)

An example of an FTS system is the Michelson Interferometer. A schematic diagram of the Michelson Interferometer in MIPAS is shown in Figure 2.2. The interferometer functions as follows (Envisat, 2001): the input radiance is divided at the beamsplitter into two beams of similar intensity. They are directed to the moving retroreflectors (in MIPAS these are corner cubes) which return them to the beam combiner. Here the beams are superimposed and interfere, so that the resulting intensity in the output ports varies as a function of the optical path difference. At equal path length in both arms (ZPD = zero-path difference), constructive interference in one output port increases the intensity to (almost) twice the average value, while destructive interference in the other port reduces the intensity there to (almost) nothing. When the optical path difference is changed, interference causes the intensity to fluctuate between the two output ports (but the sum of the intensity in both ports stays constant). This interference-modulated signal as a function of optical path difference is an interferogram.

The interference pattern consists of a series of cosine waves, each of which corresponds to a spectral wavenumber in the input signal. The interference pattern $I(x)$ is therefore the cosine Fourier transform of the input,

$$I(x) = \int F(\nu)\cos(2\pi\nu x)\,\mathrm{d}\nu, \tag{2.6}$$

where ν is the wavenumber and x is the optical path difference in the interferogram domain. The input spectrum, $F(\nu)$, can therefore in principle be recovered from the interferogram by Fourier transform,

$$F(\nu) = \frac{1}{L}\int I(x)\cos(2\pi\nu x)\,\mathrm{d}x. \tag{2.7}$$

In practice, the integral transform is replaced by a discrete Fourier transform using a summation (Beer, 1992), and a fast Fourier transform (FFT) (e.g. Griffiths and de Haseth (1986)) is used to reduce the number of computations required.

Thus the interferograms, together with auxiliary satellite and instrument data, contain all the information required to obtain the required measured radiance spectra. The spectral resolution of an interferometer is mainly determined by the maximum path difference (MPD) achievable.

Since the path difference of the instrument is finite, so also must be the interferogram. A finite path difference of the instrument is equivalent to multiplying an infinite interferogram with a boxcar function the size of the MPD. Multiplication in the interferogram domain is equivalent to convolution of the spectrum with a sinc function (the Fourier transform of a boxcar) in the spectral domain,

$$F(\nu) = \mathcal{F}(I(x)B(x)) = F(\nu) * \mathcal{F}(B(x)), \tag{2.8}$$

with $B(x) = 1$ for $0 \leq x \leq \text{MPD}$. $\mathcal{F}(B(x))$ denotes the Fourier transform of $B(x)$. The effect of this is to smear out the fine structure in the spectrum with a sinc function. The width of the sinc function is proportional to the inverse of the MPD, and determines the spectral resolution of the instrument. The spectral sampling can be increased by "zero–filling" the interferogram, but this does not change the fundamental spectral resolution.

A sinc function (see Figure 2.3) has sidelobes and negative peaks which extend out either side of the main peak. The effect of these oscillations is to cause interference between spectral lines. They can be damped out using a numerical operation known as 'apodisation'. Apodisation reduces the oscillations, but also widens the peak, reducing the spectral resolution and introducing correlations between noise in spectral points.[2]

In an idealised instrument, the sinc function would be the instrument line shape (ILS), the maximum achievable resolution would be determined by the MPD and the actual resolution of the spectra would be purposefully reduced slightly by apodisation. In a real instrument, the ILS varies slightly from a sinc function due to the finite field of view (FOV) of the instrument. The finite FOV means that incoming rays are not parallel, hence the rays will travel paths of differing lengths within the instrument. The interferogram is not sampled by a perfect boxcar function, but instead by a function whose edges are not perfectly sharp. This leads to "self–apodisation" within the instrument, which reduces the maximum achievable resolution. The actual ILS is determined during data processing.

---

[2] With Fourier transform spectrometers, it is usually assumed that noise in the spectrum is uncorrelated between spectral points. In reality, noise is uncorrelated between points in the interferogram, but the act of transforming the interferogram will in fact introduce correlations between spectral points. However, these correlations are not considered in the MIPAS retrievals.

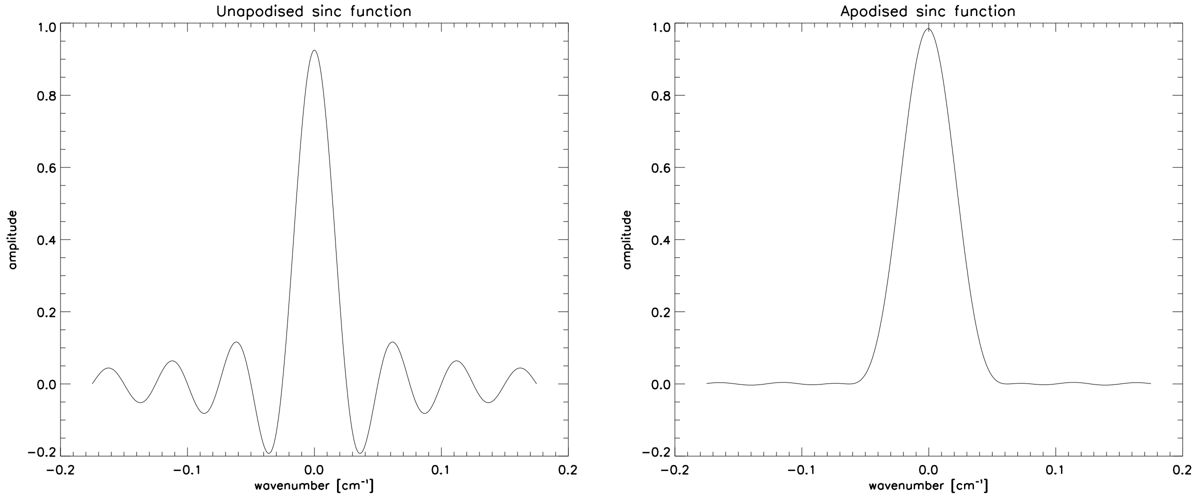

Figure 2.3: Sinc function (left) and apodised sinc function (right) with Norton–Beer strong apodisation (Norton and Beer, 1977).

Other steps involved in data processing for an FTS instrument include the checking of interferograms. Interferograms with spurious spikes, errors or instabilities during a scan should be discarded. The processing also requires a phase correction. Phase errors due to optical, electronic or sampling effects result in an asymmetric interferogram. This produces a complex spectrum (with both real and imaginary components). The phase is determined from the imaginary component and a phase correction is applied to obtain the true real spectrum. It may be necessary to apply a non–linearity correction in order to correct for a non–linear response of the detector to the signal. Radiometric calibration is required to convert the signal intensity obtained from the Fourier transform of the interferogram into physical units of spectral radiance and spectral calibration is required in order to assign the correct wavenumber values to the spectral axis. The time, position and altitude of the spectra must also be determined (geolocation).

Table 2.1: The Envisat Payload

Atmospheric Instruments	
MIPAS	Michelson Interferometer for Passive Atmospheric Sounding
GOMOS	Global Ozone Monitoring by Occultation of Stars
SCIAMACHY	SCanning Imaging Absorption spectroMeter for Atmospheric CHartographY
Surface Instruments	
AATSR	Advanced Along Track Scanning Radiometer
ASAR	Advanced Synthetic Aperture Radar
MERIS	MEdium Resolution Imaging Spectrometer
Geodetic Instruments	
RA-2	Radar Altimeter 2
MWR	MicroWave Radiometer
DORIS	Doppler Orbitography and Radiopositioning Integrated by Satellite

2.3 The MIPAS instrument

2.3.1 ENVISAT

MIPAS is one of the core experiments on the European Space Agency's ENVIronmental SATellite (Envisat), launched on 1st March 2002. Envisat is a polar-orbiting Earth observation satellite which will provide measurements of the atmosphere, ocean, land and ice over its five year mission lifetime. The Envisat mission aims to extend and improve the current European Earth observation programme, providing data required to further the understanding, modelling and prediction of environmental and climatic changes (ESA, 2000a).

Envisat carries nine instruments, listed in Table 2.1. The positions of these instruments on the satellite are shown in Figure 2.4.[3]

The satellite is in a sun-synchronous orbit. The mean altitude of the orbit is 800 km, and the satellite crosses the equator in the south to north direction (the ascending node crossing) at 10:00 am local time. This orbit provides a 35 day repeat cycle.

---

[3] For further information on these instruments, see the Envisat web pages (Envisat, 2001).

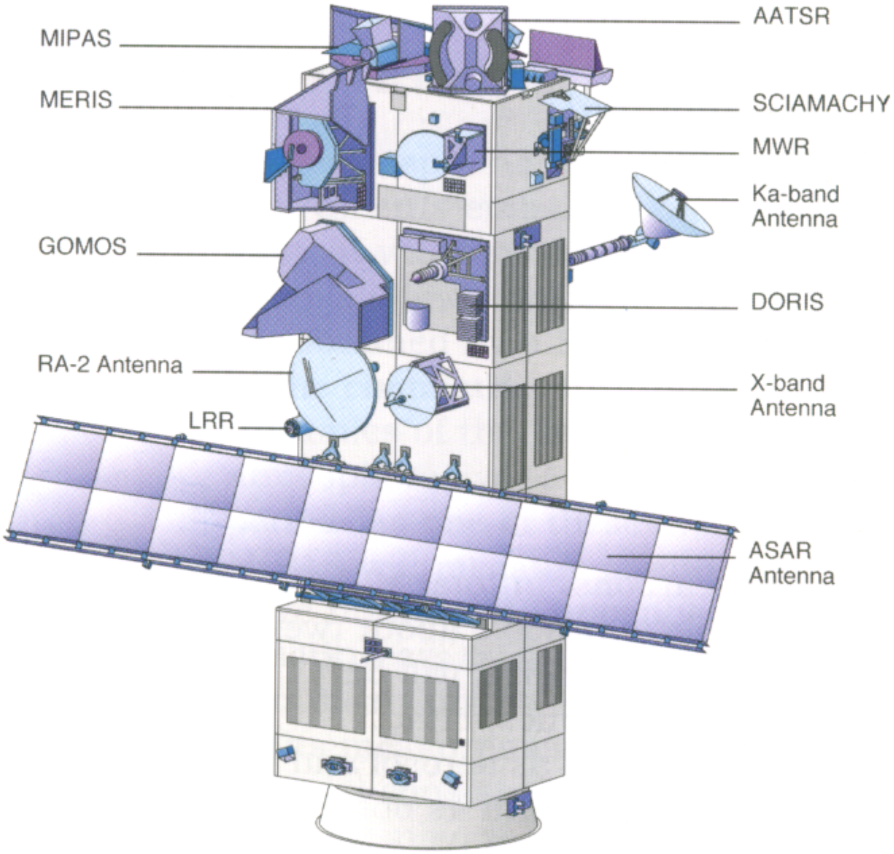

Figure 2.4: The Envisat instrument payload (ESA, 2000b)

2.3.2 MIPAS background

MIPAS measures infrared atmospheric limb emission spectra from 685–2410 cm^{-1} (wavelengths of 14.5–4.1 μm) over an altitude range 6–68 km. After suitable ground processing, these spectra allow retrieval of profiles of atmospheric pressure, temperature and the concentrations of numerous trace species. In addition, the distribution of aerosol particles, tropospheric cirrus, and stratospheric ice clouds (including polar stratospheric clouds, which are linked with ozone destruction) can also be derived from MIPAS data. The mid-infrared region can be used to observe a number of important trace gases in the atmosphere. MIPAS combines the ability to operate in this part of the spectrum with a high spectral resolution and flexibility in viewing geometry. Measurements are made on a global scale, for all seasons, both day and night.

2.3.3 MIPAS viewing geometry

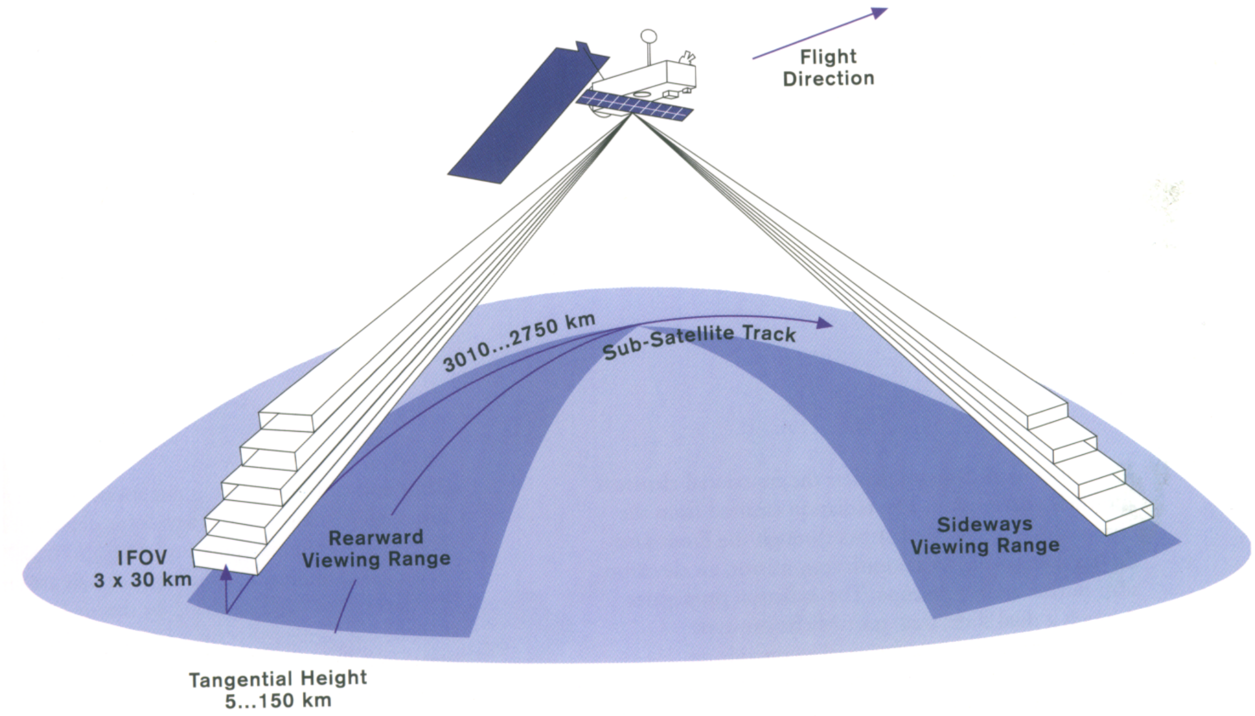

Figure 2.5: Scanning possibilities for MIPAS (ESA, 2000b)

MIPAS is designed to operate in both the day and night parts of Envisat's orbit, with an azimuth scan geometry in the anti-flight direction (looking backwards) which ensures complete global coverage. In the nominal observation mode, measurements are made in this anti-flight direction, as the observation geometry provides good coverage, including the polar regions. The field of view of the instrument at the tangent point is 3 km high (to achieve good vertical resolution) and 30 km wide (to collect sufficient radiance). The nominal observation mode measures emission spectra in 3 km steps from the upper troposphere to the upper stratosphere, and larger spacing above (6–42 km in 3 km steps, 47, 52, 60, 68 km — 17 steps in total). One complete spectrum can be recorded in approximately 4.6 seconds, so a typical scan sequence takes around 78 seconds. For this observing mode, the distance along track between two measurements at the same altitude is around 500 km. There are just over 14 orbits per day, corresponding to around 1100 complete limb scans. Since MIPAS is in a sun–synchronous orbit, the same latitude will only be sampled at two local solar times in an orbit. However, MIPAS is also capable of pointing perpendicularly to the flight track, a scanning geometry permitting diurnal changes to be detected and special events (such as volcanic eruptions) to be observed. This mode also allows East–West views to be made across the Atlantic, along the main transatlantic flight corridor, in order to determine any effects from aircraft emissions. Figure 2.5 shows the scanning possibilities for MIPAS.

2.3.4 Measurement principle

The atmospheric radiance is collected by the front–end optics (Figure 2.2), mainly steering mirrors and a telescope and directed to the Michelson interferometer. The field stop inside the telescope determines the instrument field of view. The beam then enters the interferometer, where the incoming signal is transformed into an intensity modulated signal (interferogram) depending on the optical path difference in the two interferometer arms.

For MIPAS, the MPD of the interferometer is 20 cm, which should theoretically give a resolution of 0.025 cm^{-1} (this is the grid on which the spectra are supplied). However, the actual spectral resolution is about 0.035 cm^{-1} (0.006 nm at 4.15 μm wavelength) due to self–apodisation within the instrument (§ 2.2).

The output beams are reduced in size by an afocal reducer and directed to eight cooled detectors in different wavenumber ranges by a series of optical filters. The detectors are cooled by active Stirling–cycle coolers. They operate at about 70 K, allowing a relatively high signal–to–noise ratio.

The spectral range is split up into five bands, each band being covered by one or two specific detectors, allowing some overlap in the case of detector failure. The ranges of the spectral bands are summarised in Table 2.2. A non–linearity correction (§ 2.2) is applied in the spectra from bands

A, AB and B. Figure 2.6 shows the positions of the spectral features of some of the gases that can be found in the MIPAS spectral bands.

Table 2.2: MIPAS spectral bands

Band	Spectral Range [cm^{-1}]
A	685–970
AB	1020–1170
B	1215–1500
C	1570–1750
D	1820–2410

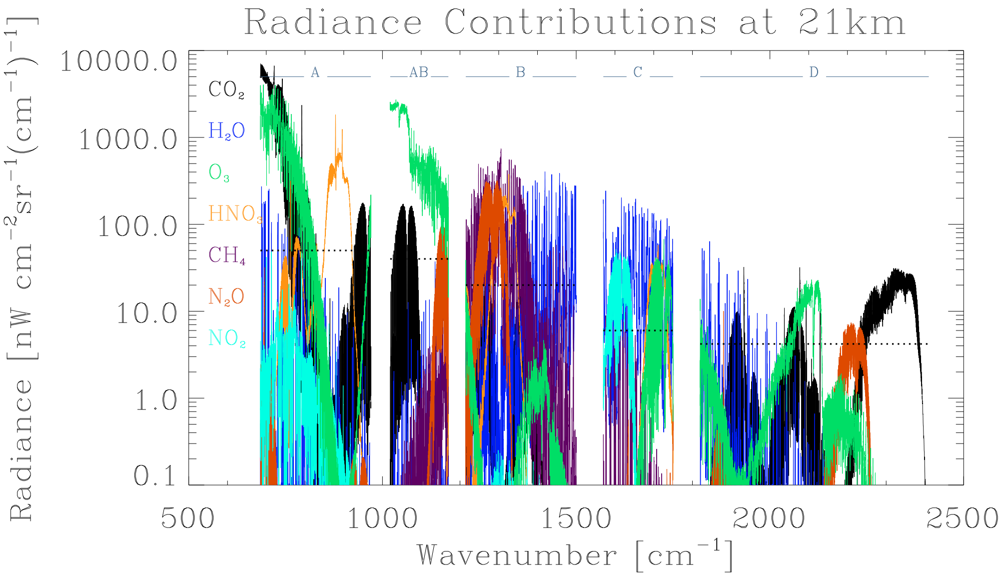

Figure 2.6: MIPAS bands and typical radiance contributions from various atmospheric species, calculated for a tangent height 21 km. Dashed lines show expected values of the noise equivalent spectral radiance (NESR) in each of the bands.

2.3.5 Calibration measurements

In order to properly calibrate the radiometric output from the instrument, it is necessary to regularly acquire measurements of well–defined targets. Measurements are made of an internal calibration blackbody and of deep space (representing a source for which the radiance is effectively zero). The deep–space measurement provides a value for the offset – the contribution to the atmospheric signal from the self–emission of the instrument, while the internal target allows the gain — the instrument responsivity — to be determined. Gain calibration also provides information about phase distortions used for the phase correction of the interferograms during ground–processing (ESA, 2000b). Offset calibration measurements are performed every four elevation scans, while the gain calibration is performed every five days.

Line of sight (LOS) calibration is required for accurate in–flight determination of the instrument pointing. LOS calibration measurements are made by observing stars moving through the field of view with short wavelength channels. The time of a star crossing can be correlated with the expected time as computed by Envisat pointing information in order to determine the pointing correction (ESA, 2000b). The LOS calibration measurements are performed once a week. The absolute pointing is known to within 1.8 km, while the relative pointing knowledge for adjacent sweeps during one scan is better than 900 m. The pressure retrieval should improve the relative pointing knowledge to better than 300m.

2.3.6 Data availability

MIPAS data are available almost continuously from the beginning of July 2002 until 26^{th} March 2004. On 26^{th} March 2004 MIPAS was switched off due to problems with the interferometer slides. The instrument has been switched on intermittently since this date to perform tests and to make measurements in a new mode of operation with reduced spectral resolution, but there has been no operational data processing since then.

The MIPAS data used for the work in this thesis all come from before March 26^{th} 2004, and include only data relating to spectra supplied on the 0.025 cm^{-1} grid. In addition, this thesis only considers data from the nominal mode and not from any of the special modes.

2.3.7 MIPAS data processing

There are a number of steps involved in retrieving atmospheric composition from the raw data received from the satellite. The data processing chain is defined in terms of the following product levels:

- Level 0: Reformatted, time-ordered satellite data, in computer-compatible format
- Level 1A: Reconstructed interferograms
- Level 1B: Radiometrically and spectrally calibrated geolocated spectra
- Level 2: Profiles of atmospheric pressure, temperature and trace species

Level 1

During Level 1 processing, a number of reconstruction, calibration and transformation steps are performed. The Level 1A processing leads to fully reconstructed interferograms and Level 1B processing transforms the interferograms into calibrated emission spectra. Corrections are performed for radiometric gain and offset, detector non–linearities, spectral shift, Doppler shift (due to spacecraft motion), spurious spikes in the interferogram and phase errors. The Level 0 to Level 1B calibration process is described in detail in Lachance (1999). As part of the Level 1 processing, the ILS, NESR (noise equivalent spectral radiance), instrument pointing and geolocation are also determined in order to be used as input to the Level 2 processor.

Level 2

This thesis will deal with Level 2 processing (retrieving profiles of atmospheric trace species from the calibrated spectra).

Until MIPAS was switched off on 26th March, altitude profiles of atmospheric pressure and temperature (pT) and volume mixing ratios (VMRs) of six high-priority species (O_3, H_2O, CH_4, N_2O, NO_2 and HNO_3) were routinely retrieved operationally by ESA in near real time (NRT Level 2 processing). These products have also been retrieved by ESA using an "off–line" (OFL) processor (see § 4.2 for further details). Oxford was involved in the development of this operational retrieval scheme, and has a continuing role as an 'Expert Support Laboratory' in order to validate and monitor the quality of the ESA Level 2 products. Chapters 4 and 5 describe the validation work carried out for this thesis. The OFL products benefit from a number of processor upgrades and are therefore expected to be of better quality than the NRT products. For this reason, the validation work shown in this thesis has been performed on the OFL products.

Separate retrieval schemes have also been developed at various European institutions, including Oxford, both to validate the operational retrieval and to extend the range of products retrieved from the MIPAS spectra (AMIL2DA, 2002a). The Oxford retrieval scheme is described in more detail in § 5.2.2. It is not as fast to run as the operational retrieval, but allows for greater accuracy and the investigation of additional interesting species. Amongst the 'non-operational' species which have signatures in the spectral range covered by MIPAS are the nitrogen species (NO, $ClONO_2$, N_2O_5), chlorine reservoirs ($ClONO_2$, HOCl), chlorine source species (CFC-11, CFC-12, CFC-22, CCl_4), chlorine radicals (ClO), dynamic tracers (CF_4, SF_6) and many others, e.g. CO, OCS, NH_3, HCN, C_2H_2, C_2H_6 (AMIL2DA, 2002b).

In addition, the high spectral resolution of the MIPAS spectra means that it is possible to distinguish between the different isotopes of many of these gases. Knowledge of global distributions of minor isotopes is presently very poor. MIPAS measurements could make a valuable contribution in this area. Work carried out on retrievals of minor isotopes from MIPAS measurements is described in Chapter 6.

Chapter 3

Retrieval Theory and Applications

3.1 Introduction

In remote sounding of the atmosphere, the measurement obtained by the instrument is often a complicated function of the parameter that is required. A retrieval scheme is required to perform an inversion of the complicated function, in order to obtain (retrieve) the required parameter from the indirect measurement. This chapter provides an introduction to retrieval terminology and to certain specific applications of retrieval theory which will be used and referred to in the later chapters.

The theory of retrieval of atmospheric parameters such as profiles of atmospheric temperature and composition is well established. In § 3.2 and § 3.3 some of the definitions and key concepts are described. The theory and definitions presented here follow Rodgers (1976, 1996, 2000).

The microwindow selection method presented in § 3.4 and the error analysis technique presented in § 3.5 are both specific applications of retrieval theory which have been used in this project.

3.2 Definitions

In order to express the problem and ways of solving it, it is first necessary to define some notation and commonly used concepts. Consider a set of n parameters to be determined (the 'state vector') $\mathbf{x}$ from a set of m measurements $\mathbf{y}$. The aim of the retrieval is to gain as much information as possible about $\mathbf{x}$ given $\mathbf{y}$. The state vector $\mathbf{x}$ is generally a profile of some atmospheric parameter, e.g. trace gas concentration, at a sufficient number of levels to give an adequate representation of the atmosphere. The measurement vector $\mathbf{y}$ in this case is a set of radiances over a range of wavenumbers and tangent altitudes. The measurements will have some error or measurement noise $\boldsymbol{\epsilon}$ associated with them.

3.2.1 The forward model

The measurement vector and the state vector are related by the forward model, $\mathbf{F}(\mathbf{x})$, which contains the physics involved (usually with some approximations). Assuming a perfect forward model,

$$\mathbf{y} = \mathbf{F}(\mathbf{x}) + \boldsymbol{\epsilon}. \tag{3.1}$$

In addition to describing how the measurements are related to the atmospheric state, the forward model incorporates knowledge of the instrument that is used to make the measurements, principally via convolutions with the instrument line shape and the field of view.

3.2.2 Weighting functions

It is most convenient to consider a linear problem. If the problem is not linear, it is generally possible to linearise about a reference state $\mathbf{x}_0$,

$$\begin{aligned} \mathbf{y} - \mathbf{F}(\mathbf{x}_0) &= \frac{\partial \mathbf{F}(\mathbf{x}_0)}{\partial \mathbf{x}} (\mathbf{x} - \mathbf{x}_0) + \boldsymbol{\epsilon} & (3.2) \\ &= \mathbf{K}(\mathbf{x} - \mathbf{x}_0) + \boldsymbol{\epsilon}, & (3.3) \end{aligned}$$

which defines the $m \times n$ weighting function matrix $\mathbf{K}$, in which each element is the partial derivative of a forward model element with respect to a state vector element, i.e. $K_{ij} = \partial F_i(\mathbf{x}_0)/\partial x_j$. $\mathbf{K}$ is also known as the Jacobian or kernel matrix.

3.2.3 Error Covariances

Measurements, estimates and retrievals are made to finite accuracy, which is represented in covariance matrices. Elements of the measurement covariance matrix $\mathbf{S}_\epsilon$ are defined by

$$S_{\epsilon ij} = E\{\epsilon_i \epsilon_j\}, \tag{3.4}$$

where $E\{\ldots\}$ is the expectation value. The diagonal elements of the matrix $\mathbf{S}_\epsilon$ are the variances of the individual elements of $\mathbf{y}$ and the off-diagonal elements represent error correlations.

3.3 Solving the retrieval problem

In general, the retrieval problem does not have a unique solution, so the best solution must be selected from a number of them. There are various methods that can be used to solve the retrieval problem, some of them better than others. Presented here are the ‘least squares fit’ method, which is used in the operational MIPAS retrievals, and ‘optimal estimation’, the method used for the Oxford retrieval.

3.3.1 Least Squares Fit (solution without *a priori* data)

It is possible to fit the profile to the measurements only, using a weighted least squares fit method (Ridolfi et al., 2000). A solution is sought which minimises the cost function

$$\chi^2 = (\mathbf{y} - \mathbf{F}(\hat{\mathbf{x}}))^T {\mathbf{S}_\epsilon}^{-1} (\mathbf{y} - \mathbf{F}(\hat{\mathbf{x}})), \tag{3.5}$$

where $\hat{\mathbf{x}}$ is an estimate of the true state vector, $\mathbf{x}$. In this case it can be shown (Rodgers, 2000) that the solution for the state vector is

$$\hat{\mathbf{x}} = \left(\mathbf{K}^T \mathbf{S}_\epsilon^{-1} \mathbf{K}\right)^{-1} \mathbf{K}^T \mathbf{S}_\epsilon^{-1} \mathbf{y}, \tag{3.6}$$

with covariance matrix

$$\hat{\mathbf{S}} = \left(\mathbf{K}^T \mathbf{S}_\epsilon^{-1} \mathbf{K}\right)^{-1}. \tag{3.7}$$

If the forward model is nearly linear, and it is indeed possible to linearise the model about some state, then this solution is fine. The errors associated with linearising in this way must be smaller than the measurement errors or the required accuracy of the solution. If the problem is non–linear (which in practice, is usually the case) then it is necessary to numerically and iteratively find a solution which fits the measurements.

The ESA operational retrievals use the Levenberg–Marquardt method (Press et al., 1987) for iteration. The iterative form of the equation used is (Ridolfi et al., 2000)

$$\hat{\mathbf{x}}_i = \hat{\mathbf{x}}_{i-1} + \left(\mathbf{K}_{i-1}^T \mathbf{S}_\epsilon^{-1} \mathbf{K}_{i-1} + \gamma \mathbf{I}\right)^{-1} \mathbf{K}^T \mathbf{S}_\epsilon^{-1} \left(\mathbf{y} - \mathbf{F}(\hat{\mathbf{x}}_{i-1})\right), \tag{3.8}$$

where $\mathbf{x}_i$ and $\hat{\mathbf{x}}_{i-1}$ are the retrieved state vector for the current and previous retrieval respectively and γ is a factor that reduces the amplitude of the parameter correction vector. The factor γ is initialised to a user–defined (less than 1) number and is increased or decreased during the retrieval iterations depending on whether the χ^2 function increases or decreases. The use of this factor should ensure that the calculated correction acts to move the solution towards, rather than away from, the minimum χ^2. Convergence criteria are needed to establish when a value close enough to the minimum of the χ^2 function has been reached. Details of the convergence criteria applied to the ESA retrievals can be found in Ceccherini et al. (2003).

In general, the least squares solution works best for problems where the algebraic form of the solution is known from sound physical reasoning and the number of unknown parameters is considerably smaller than the number of independent measurements. There should also be sufficient information in the measurements to retrieve each parameter independently. This is generally not the case for the atmospheric retrieval problem, since the information in the measurements is generally not quite at the profile resolution. This kind of retrieval is often unstable, leading to unrealistic oscillations in retrieved profiles. To reduce these instabilities, additional smoothing constraints are generally used, e.g. Tikhonov-Phillips regularisation (Tikhonov and Arsenin, 1977). A least squares fitting method is used for the MIPAS operational retrievals, but explicit regularisation is not used. The ESA near real time retrievals are, in practice, only run over a limited number of iterations, and so there is some residual bias towards the initial guess profile and associated smoothing. The ESA off–line retrievals are subject to stricter convergence criteria than the near real time (Ceccherini et al., 2003), and should be less affected by this sort of smoothing.

3.3.2 Solution with *a priori* data

Knowledge additional to the measurements themselves is often useful in retrieval problems, such as an independent measurement of the state, an estimate derived from climatology or from previous experiments, or previous measurements from the same instrument. Such "virtual measurements" $\mathbf{x}_a$ are called *a priori* information and have an associated *a priori* covariance matrix $\mathbf{S}_a$. Measurements and *a priori* information can be used together to find the best estimate of the atmospheric state.

Using *a priori* data which are independent of the measurements, $\mathbf{y}$, considered for the retrieval, a solution is sought which minimises a joint cost function

$$\chi^2 = (\mathbf{y} - \mathbf{F}(\hat{\mathbf{x}}))^T {\mathbf{S}_\epsilon}^{-1} (\mathbf{y} - \mathbf{F}(\hat{\mathbf{x}})) + (\hat{\mathbf{x}} - \mathbf{x}_a)^T {\mathbf{S}_a}^{-1} (\hat{\mathbf{x}} - \mathbf{x}_a). \tag{3.9}$$

The following expression may be derived for the most probable solution $\hat{\mathbf{x}}$:

$$\begin{aligned}\hat{\mathbf{x}} &= \mathbf{x}_a + \left(\mathbf{K}^T\mathbf{S}_\epsilon^{-1}\mathbf{K} + \mathbf{S}_a^{-1}\right)^{-1}\mathbf{K}^T\mathbf{S}_\epsilon^{-1}(\mathbf{y} - \mathbf{K}\mathbf{x}_a) & (3.10)\\ &= \mathbf{x}_a + \mathbf{G}(\mathbf{y} - \mathbf{K}\mathbf{x}_a), & (3.11)\end{aligned}$$

where $\mathbf{G}$ is the 'gain matrix'. The covariance $\hat{\mathbf{S}}$ of this solution is given by

$$\hat{\mathbf{S}} = \left(\mathbf{K}^T\mathbf{S}_\epsilon^{-1}\mathbf{K} + \mathbf{S}_a^{-1}\right)^{-1}. \tag{3.12}$$

This is called the "Optimal Estimation" retrieval, and is the method used in the Oxford MIPAS retrieval.

Again, if the problem is non–linear, which in practice it usually is, an iterative approach is required. The iteration step for the optimal estimation approach using Levenberg–Marquardt iteration is

$$\begin{aligned}\hat{\mathbf{x}}_i = \hat{\mathbf{x}}_{i-1} + &\left[\left((1+\gamma)\mathbf{S}_a^{-1} + \mathbf{K}_{i-1}^T\mathbf{S}_\epsilon^{-1}\mathbf{K}_{i-1}\right)^{-1}\right.\\ &\left.\left(\mathbf{K}_{i-1}^T\mathbf{S}_\epsilon^{-1}[\mathbf{y} - \mathbf{F}(\mathbf{x}_{i-1})] - \mathbf{S}_a^{-1}[\mathbf{x}_{i-1} - \mathbf{x}_a]\right)\right]. \qquad (3.13)\end{aligned}$$

Details of the convergence criteria used in the Oxford retrieval can be found in Dudhia (2004a).

3.3.3 Averaging kernels

The averaging kernel matrix indicates how the true profile is smoothed by the retrieval. It is defined as

$$\mathbf{A} = \frac{\partial\hat{\mathbf{x}}}{\partial\mathbf{x}}. \tag{3.14}$$

In the absence of noise, the retrieved profile is a weighted mean of the true state and the *a priori* estimate, with the averaging kernel as a weight,

$$\hat{\mathbf{x}} = \mathbf{A}\mathbf{x} + (\mathbf{I} - \mathbf{A})\mathbf{x}_a. \tag{3.15}$$

The presence of noise leads to an additional term.

$$\hat{\mathbf{x}} = \mathbf{A}\mathbf{x} + (\mathbf{I} - \mathbf{A})\mathbf{x}_a + \mathbf{G}\epsilon \tag{3.16}$$

The rows of the matrix **A** are the "smoothing functions" or averaging kernels and the width of these averaging kernels is a measure of the resolution of the retrieval. The area of the averaging kernel is approximately equal to 1 where the retrieval is accurate, and can be seen as a measure of the fraction of the retrieval that comes from the measurements as opposed to the *a priori*. An ideal observing system would have δ–function averaging kernels and no noise.

The columns of **A** show the response of the averaging kernel to a δ function perturbation of the state.

3.4 Microwindow selection

High resolution Fourier transform spectrometers such as MIPAS obtain many atmospheric spectra, each containing a large number of spectral points. In order to use the data efficiently, and to save on computational time, it is usual to select "microwindows", or smaller regions of spectrum, with which to perform the retrieval. Sets of microwindows are chosen for each of the parameters to be retrieved, containing a limited set of measurements chosen specifically to target one or more particular species. Using microwindows (a collection of adjacent spectral points) offers several advantages over using a collection of isolated measurements, e.g. in terms of forward model efficiency, noise, apodisation and fitting of continuum and offset. Figure 3.1 shows the positions of the microwindows used in the ESA operational processing in the wavenumber and tangent altitude domain. The microwindow selection process developed at Oxford (Jay, 2000; Dudhia et al., 2002a) is outlined here.

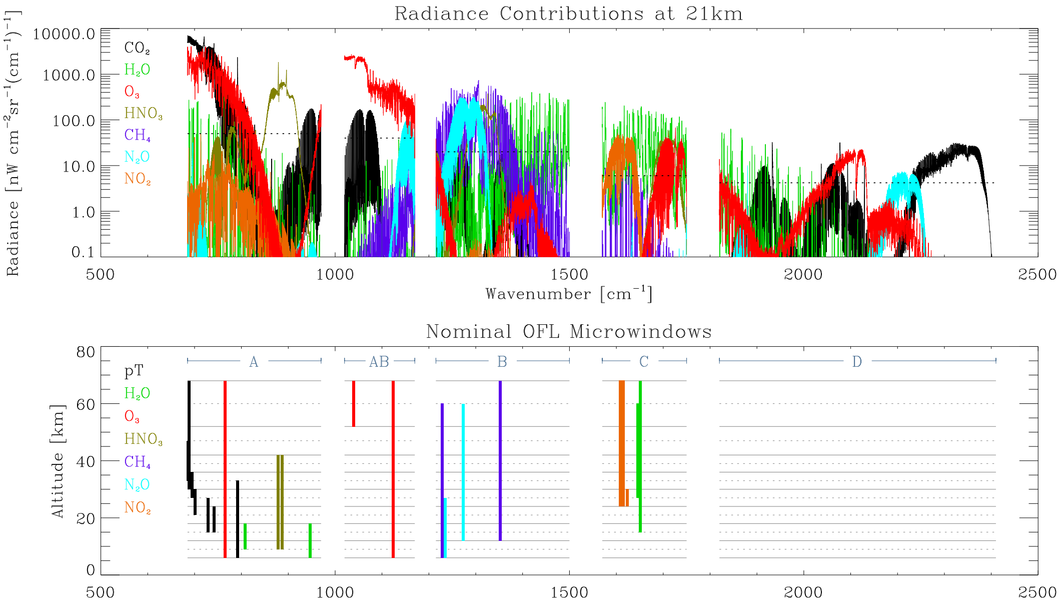

Figure 3.1: Radiance contributions from different atmospheric gases (top), and positions of the microwindows used in the ESA OFL Level 2 processing in the wavenumber and tangent altitude domain (bottom).

3.4.1 Retrieval errors

A thorough analysis of the errors involved in a retrieval of atmospheric composition is a vital part of the retrieval process. The total error resulting from a retrieval consists of a random error component (from measurement noise, which prior to apodisation is generally assumed to be uncorrelated between measurements) and a systematic error component (from incorrect assumptions or uncertainties in parameters in the forward model or from problems in the instrument calibration, correlated between measurements). It might be expected that the retrieval error would decrease as more spectral points are included in the retrieval. If only random errors were present, this would be true. However, the presence of systematic errors means that certain measurements may contribute a high systematic error component and therefore degrade the retrieval.

3.4.2 Systematic errors and error spectra

Systematic errors are those errors which arise from sources other than random noise. They are correlated between measurements or forward model calculations. It can be seen from Figure 3.1 that a region of the spectrum where there are strong lines from the species we wish to retrieve may also contain lines from other species. An obvious source of systematic error is therefore lines from other gases which have to be modelled but for which the concentration is not known. In general, systematic errors will also be correlated between one profile and the next according to various time/spatial scales. Such errors are usually difficult to characterise, but estimates are required as input to the microwindow selection process.

The following sources of error have been considered:

- Calibration errors

  uncertainty in radiometric gain calibration (±1 %)

  uncertainty in instrument line shape calibration (±2% width)

  uncertainty in spectral calibration (±0.001 cm^{-1})

- Forward model parameter errors

  climatological 1-σ variabilities of 28 species

  uncertainty in modelling gaseous (mostly H_2O) continua (±25 %)

  estimated uncertainties in HITRAN line parameters (molecule/band specific)

  effect of propagation of temperature retrieval errors (± 1 K)

  effect of propagation of pressure retrieval errors (± 2 %)

- Forward model errors

  effect of assuming local thermodynamic equilibrium (LTE) applies at all altitudes

  effect of ignoring CO_2 line-mixing effects effect of assuming horizontally homogeneous atmosphere in line-of-sight direction (± 1 K/100 km temperature gradient)

The spectral signature of each systematic error with an assumed uncertainty can be pre–computed as an 'error spectrum', and may be used to determine its contribution to the retrieval error. The error spectrum $\delta\mathbf{f}^i$ is the difference between spectra calculated with and without the systematic error i present. Standard deviations (1σ errors) can be determined for different gases from climatological variability.

3.4.3 Inclusion of systematic errors

The MIPAS retrieval considers only random noise. The covariance matrix $\hat{\mathbf{S}}$ expressed in § 3.3 represents the random retrieval error covariance only. The effect of ignoring systematic errors should therefore be accounted for when selecting microwindows, so that measurements which degrade the retrieval are excluded.

The systematic error components for the different error sources can be added to the (random) retrieval error covariance $\hat{\mathbf{S}}$ to give a total error $\hat{\mathbf{S}}^{\mathrm{tot}}$:

$$\begin{aligned} \hat{\mathbf{S}}^{\mathrm{tot}} &= \hat{\mathbf{S}}^{\mathrm{rnd}} + \sum_i \mathbf{S}^i, \qquad (3.17) \\ \mathbf{S}^i &= (\delta\mathbf{f}^i)(\delta\mathbf{f}^i)^T. \qquad (3.18) \end{aligned}$$

The best points for use in the retrieval are those which lead to the greatest reduction in the total retrieval error $\hat{\mathbf{S}}^{\mathrm{tot}}$.

3.4.4 Information content

In information theory, information content describes how the uncertainty of a value is decreased by measuring it. Shannon and Weaver (1949) use the logarithm to the base 2 of the ratio of the prior and posterior uncertainties. Shannon compares the probability density function after the measurement $\mathrm{P}(\mathbf{x}|\mathbf{y})$ to the probability density function before the measurement $\mathrm{P}(\mathbf{x})$ by means of the *entropy* S of the probability density function,

$$S(P) = -\int P(\mathbf{x}) \log_2 P(\mathbf{x}) d\mathbf{x}, \tag{3.19}$$

(the base 2 logarithm means that the entropy is expressed in 'bits' — an increase in information content of one bit indicates that the uncertainty of a value has been halved) and defines the information content H as:

$$H = S(P(\mathbf{x})) - S(P(\mathbf{x}|\mathbf{y})), \tag{3.20}$$

i.e. the change in entropy following a measurement. It can be shown (Rodgers, 2000) that, for Gaussian statistics, $S(P) = \frac{1}{2}\log_2 |\mathbf{S}|$, so the information content is

$$H = \frac{1}{2}\log_2 |\mathbf{S}_a| - \frac{1}{2}\log_2 |\hat{\mathbf{S}}|, \tag{3.21}$$

where $\hat{\mathbf{S}}$ is the solution covariance and $\mathbf{S}_a$ is the *a priori* covariance.

In simpler terms, if we start knowing some parameter x with a variance σ_a^2 (the *a priori* uncertainty, e.g. from climatology), and after a retrieval we have reduced its uncertainty to σ_x^2, the ratio σ_a^2/σ_x^2 is a scalar quantity that expresses the information obtained from the retrieval. Expressed in 'bits', this is

$$H = \frac{1}{2}\log_2 \sigma_a^2 - \frac{1}{2}\log_2 \sigma_x^2. \tag{3.22}$$

If the uncertainty is reduced from 100% to 50%, the ratio of variances is $\frac{1}{4}$ and the information content is one bit.

3.4.5 The selection process

In the early days of atmospheric spectroscopy, microwindows were defined and selected by experienced spectroscopists, by visual inspection of the spectral fit between the measurements and the forward modelled spectra. Selections were usually made without concerns over CPU cost and for specific atmospheric conditions. However, in the face of today's more automated data analysis, there is a need to define and select optimised microwindows in a quantitative, objective and reproducible manner, for global application and for near–real–time processing.

One approach is to simulate the propagation of random noise through the retrieval and select measurements which maximise the information content (Rodgers, 1996, 1998), or which best satisfy other criteria (Rabier et al., 2001). While this is reasonable if the retrieval errors are predominantly due to random measurement errors, it does not allow for systematic errors associated with unretrieved parameters, such as the uncertainties in modelling the concentrations of contaminant species.

An approach has also been tried which addresses this problem by selecting microwindows which minimise the total error (both random and systematic components) (von Clarmann and Echle, 1998; Echle et al., 2000). However, this was achieved by approximating the profile retrieval as a set of independent, single–layer retrievals. As a result, the effect of inter–level correlations in the retrieval is ignored.

The microwindow selection process developed at Oxford (Jay, 2000; Dudhia et al., 2002a) selects microwindows by simulating a full profile retrieval including the propagation of systematic error terms. Microwindows are 'grown' (see Figure 3.2) in the measurement domain, which can be thought of as having wavenumber in the x–direction, and altitude (tangent height) in the y–direction.

The microwindow selection method sequentially selects points that maximise some figure of merit for the retrieval (e.g. the information content in the Shannon sense (Dudhia et al., 2002a; Rodgers,

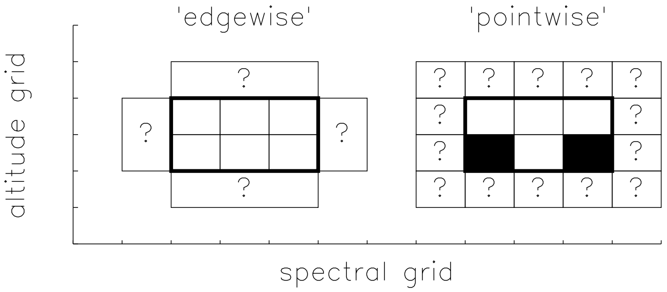

Figure 3.2: Sketch indicating two possible methods of growing microwindows. A microwindow, currently bounded by the thick line, contains 6 measurements (3 spectral points × 2 tangent altitudes). Growing 'edgewise' all points along one boundary are tested together and, if this improves the Figure of Merit, the microwindow is expanded in that direction. Growing 'pointwise' all points along the boundary are tested individually, and only those points with positive impact on the Figure of Merit are included. This can leave 'masked' points within the microwindow, as indicated by solid squares, corresponding to measurements which are excluded from the retrieval.

1996)). The figure of merit is a scalar function which expresses the reduction in retrieval error from stage $i-1$ to stage i,

$$I = \frac{1}{2}\log_2 F_{i-1} - \frac{1}{2}\log_2 F_i. \tag{3.23}$$

Using this definition, the figure of merit is expressed in 'bits'. F is some function of the retrieval error covariance.

The Shannon information content uses the determinant of the full covariance matrix, $F_i = |\hat{\mathbf{S}}_{\text{total}}|$. Alternatively, it is also possible to use a weighted sum of the systematic and random parts of the error covariance matrix, where a heavily weighted systematic part will bias towards selection of points with low systematic errors. It is also possible to incorporate a penalty for the increased computational time incurred by large microwindows.

The microwindow selection process follows these steps (Dudhia et al., 2002a):

- Survey the complete spectral range at all altitudes, computing a figure of merit for each individual point.

- Select the spectral point at the wavenumber and altitude that gives the highest figure of merit as a starting point.
- 'Grow' a microwindow around this point by adding the best points at neighbouring wavenumbers and/or altitudes.
- Stop growing when a specified maximum microwindow size is reached or the figure of merit no longer increases.
- Select the next starting point, and so on.

This method of microwindow selection was developed into a software package by Anu Dudhia under an ESA contract. This software, named MWMAKE, has been used extensively in this project (see § 6.2).

3.5 Residual and Error Correlation (REC) Analysis

The residuals for a particular retrieval, $\mathbf{r}$ are defined as the difference between the measurements, $\mathbf{y}$, and the spectrum produced by using the forward model to calculate the 'measurements' that would be produced by the retrieved atmospheric state $\hat{\mathbf{x}}$ (Eq. 3.1):

$$\mathbf{r} = \mathbf{y} - \mathbf{F}(\hat{\mathbf{x}}) + \boldsymbol{\epsilon}. \tag{3.24}$$

The retrieval aims to adjust the state vector so that the only difference $\mathbf{y} - \mathbf{F}(\hat{\mathbf{x}})$ between the forward modelled radiances and the measurements is just the random noise on the measurements. Examining the residual difference is an essential part of the validation of a retrieval, since it often shows up features which indicate some systematic error in the forward model assumptions or in the instrument calibration.

In the past, with only a few spectra, examination of the residuals was often done by eye. However, since MIPAS measures a new spectrum every 4.6 seconds, some automation is required for the purposes of monitoring the residuals. Using the pre–computed error spectra used for the microwindow selection (§ 3.4), it is reasonable to attempt to investigate statistical correlations between the shape of the residuals and the error spectra.

The REC analysis (Jay et al., 2002) is a technique developed at Oxford. It involves fitting the pre–calculated spectral error signatures to retrieval residuals, in order to assess whether any systematic error sources contribute more than expected to the residuals. The REC analysis reduces a large number of residual spectra to a short table of numbers. The principle is shown in Figure 3.3. It provides a quick numerical method of identifying potential problems in the retrieval, which can be used no matter what the retrieval method.

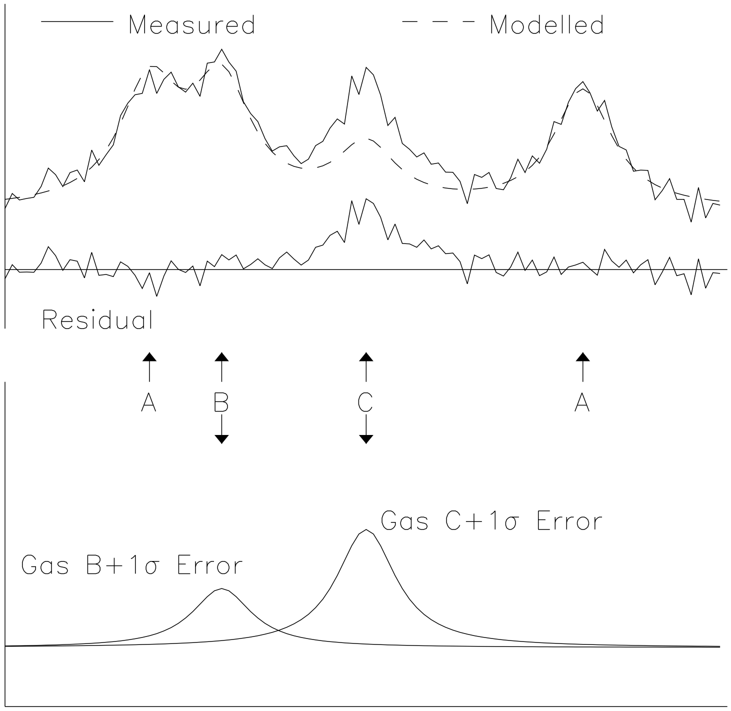

Figure 3.3: Diagram illustrating the principle of REC analysis. The retrieval of species A adjusts the concentration profile until the modelled spectrum best fits the measured spectrum, including noise (upper plot) assuming fixed, climatological concentrations of contaminant species B and C. If the concentration of species C is incorrect, it should show up as a feature in the residual (=measured - modelled) spectrum. The lower plot shows pre–computed spectra corresponding to climatological 1σ perturbations of species B and C. By attempting to correlate these with the residual spectra it should be possible to determine not only which species are modelled incorrectly, but also the magnitude and sign of the deviation.

If the residuals are a combination of the different systematic error components $\delta\mathbf{f}^i$, each multiplied by a coefficient c_i, then

$$\mathbf{r} = \sum_i \delta\mathbf{f}^i c_i + \boldsymbol{\epsilon} \equiv \mathbf{K_c c} + \boldsymbol{\epsilon}. \tag{3.25}$$

Following Eq. 3.11, the set of error coefficients $\hat{\mathbf{c}}$ can be estimated using

$$\hat{\mathbf{c}} = \mathbf{c_a} + \mathbf{G}_c(\mathbf{r} - \mathbf{K}_c\mathbf{c}_a), \tag{3.26}$$

where $\mathbf{G}_c$ is the optimal estimation gain matrix (see Equation 3.11) and $\mathbf{c}_a$ is a vector containing the *a priori* values of the coefficients for each error source.

As each error spectrum $\delta\mathbf{f}^i$ is the effect of a $+1\sigma$ perturbation, each coefficient is given an *a priori* value of 0 and an *a priori* variance of 1.

The REC analysis has been used as part of the routine monitoring of the quality of the ESA Level 2 products performed at Oxford, and has been a useful tool in the validation work carried out in the course of this project.

Chapter 4

Validation of the ESA OFL H_2O and CH_4

4.1 Introduction

This chapter describes work done on the validation of the MIPAS ESA OFL profiles of H_2O and CH_4. A description of the MIPAS ESA Level 2 processing is provided in § 4.2.

The aim here was to gain a large scale picture of the quality of the dataset. The validation work includes both internal checks (the examination of averaged residuals in § 4.4, and the examination of day/night differences in § 4.10) and comparisons with external data.

A large amount of external validation work has been carried out on the MIPAS Level 2 data, by many people at many different institutions. Comparisons of the MIPAS water vapour and methane profiles have been made with a variety of ground–based, balloon, aircraft and other satellite measurements and with meteorological analyses (e.g. Dethof et al. (2004); Fricke et al. (2004); Camy-Peret et al. (2004); Pappalardo et al. (2004); Oelhaf et al. (2004); Weber et al. (2004); Lahoz et al. (2004)).

Comparisons with meteorological analyses allow excellent coverage in space and time and have the advantage of including assimilated measurements from a wide range of other instruments. However, meteorological models are primarily geared to model the troposphere, and there are few accurate measurements assimilated into the models in the stratosphere and lower mesosphere. The stratospheric part of the analyses may not, therefore, be very reliable.

Ground–based, aircraft and balloon measurements can offer accurate profiles with which to compare the MIPAS profiles. Dedicated validation campaigns (Oelhaf et al., 2004; Camy-Peret et al., 2004) have been undertaken in order to obtain a high number of good spatial and temporal coincidences. Nevertheless, the coverage of these measurements in space and time is limited.

Measurements from other satellite instruments (see Tables 1.1, 1.2 and 1.3 for examples) are likely to be less accurate, and may contain their own systematic errors which are hard to quantify. However, measurements from other satellite instruments allow better coverage and so should be useful when assessing the quality of MIPAS data over a large range of locations and atmospheric conditions. In this chapter, the aim was to gain an overview of the quality of the entire dataset. Comparisons with other satellite measurements are therefore useful.

A number of approaches are possible when comparing measurements from different satellite instruments. One approach is a statistical comparison of pairs of measurements (or profiles) which are nearly coincident in space and time (see, for example, Weber et al. (2004); Bracher et al. (2004)). This method is only useful if a large number of coincident measurements can be obtained. Since exact coincidences are highly unlikely, this approach requires the definition of some arbitrary window in space and time over which measurements are deemed to be coincident. This window may need to be made large in order to obtain the number of coincidences necessary for a good statistical comparison. There may therefore be some uncertainty as to whether differences are due to biases between measurement techniques or to natural atmospheric variability. It is possible to get around this problem to some extent by grouping profiles/measurements by other tracers, such as potential vorticity.

Another possible approach is to use a data assimilation technique. The use of a direct inversion technique (Juckes, 2004) allows the comparison of data from multiple sources, offering the ability to represent spatial and temporal coincidences in the fields being observed and the contributions these variations make to differences between observations which are near but not coincident.

A third possible approach to the intercomparison of satellite measurements is the comparison of zonal means over daily, monthly or seasonal timescales. This is the approach that will be used in the comparisons made in this Chapter. This approach can be useful when dealing with a large amount of data and trying to gain a global overview.

MIPAS OFL H_2O and CH_4 are compared here with the IG2 climatological dataset (§ 4.5) and with data from the Halogen Occultation Experiment (HALOE — § 4.6). MIPAS H_2O is also compared with data from the Odin Sub–Millimetre Radiometer (SMR) (§ 4.8) and from the Microwave Limb Sounder (MLS) on the Aura satellite (§ 4.9).

Mention is also made of the Atmospheric Chemistry Experiment (ACE – § 4.7), since it offers simultaneous measurements of H_2O and CH_4 in a time period that overlaps with the MIPAS OFL dataset. However, due to limited time between the release of processed ACE data and the completion of this DPhil project, no direct comparisons between ACE and MIPAS have been made here. There are other satellite measurements of H_2O which overlap in time with the MIPAS OFL dataset, notably from the POAM III and SAGE II instruments (see Table 1.3) which have not been covered in this work. Comparisons of MIPAS H_2O with SAGE II and POAM III data can be found in Weber et al. (2004).

4.2 ESA MIPAS Level 2 processing

The ESA Level 2 operational code is based on the Optimised Retrieval Model (ORM), a scientific code developed in the framework of an ESA–supported study: "Development of an optimised retrieval algorithm for routine p, T and VMR retrievals from MIPAS limb emission spectra". Full details of the ESA–supported study, and a detailed description of the ORM can be found in Ridolfi et al. (2000), but a summary of the main features of the forward model and of the retrieval approach adopted are provided in this section.

4.2.1 The Optimised Forward Model

The Optimised Forward Model (OFM) is the forward model used by the ORM. Starting with an initial guess of the atmospheric state and using information on observation geometry and instrumental parameters and characteristics, the forward model computes simulated spectra, which can then be compared with the measured MIPAS Level 1B spectra. Iterative equations (see § 3.3.1) are then applied in order to determine the atmospheric parameters/state that best fit the forward–modelled simulations to the observations.

The signal measured by MIPAS is the atmospheric radiance that reaches the instrument modified by instrumental effects. The main causes of modification are the finite spectral resolution and the finite field of view (FOV) of the instrument (see § 2.2). If the instrument is pointing to the limb at tangent altitude z_t, then the radiance, L, at wavenumber ν reaching the instrument can be calculated using the radiative transfer equation (Equation 2.4).

The actual signal measured by the MIPAS instrument, $S(\nu, z_t)$, can be simulated by convolving the atmospheric limb radiance with the apodised instrument line shape (AILS) (§ 2.2) and with the MIPAS field of view (FOV) function,

$$S(\nu, z_t) = \int\int L(\nu - \nu', z_t - z_{t'}) \times \mathrm{AILS}(\nu')d\nu'\mathrm{FOV}(z_{t'})dz_{t'}. \tag{4.1}$$

A full description of the optimisations applied in the OFM and their implementation can be found in Ridolfi et al. (2000). Selected time-saving measures adopted in the OFM and their effects on the retrievals are investigated in further detail in Chapter 5.

4.2.2 General features of the retrieval approach

The main features of the approach adopted in the ESA operational retrievals are listed below:

- **Use of microwindows**: See § 3.4 and § 4.3
- **Sequential retrieval of the species**: First, temperature and tangent pressures are retrieved simultaneously (p, T retrieval). Then the VMR profiles are retrieved individually in the following order: H_2O, O_3, HNO_3, CH_4, N_2O, NO_2. The order was chosen so that the species which have the greatest spectral interference in the microwindows of the others are retrieved first. This means, for example, that any water vapour lines present in the methane microwindows should be fitted well, since the water vapour has already been retrieved. In principle it is also possible to retrieve the species jointly rather than sequentially, but this approach requires more memory and more computing time. (Dinelli et al., 2004). It should be noted that the p, T error propagation is not included explicitly in the VMR retrievals. However, the microwindows for the VMR retrievals are chosen to try to minimise the effect of p, T errors.
- **Global fit analysis**: Spectral data for a complete limb–scanning sequence are fitted simultaneously (Carlotti, 1988).
- **Least squares fit retrieval**: (See § 3.3.1.) This approach has advantages in terms of being unbiased (since there is no *a priori* constraint on values retrieved) and maximising vertical

resolution (since there is no smoothing constraint, ie no regularisation). A disadvantage is that the retrievals can be prone to instability.

In the p, T retrieval, the quantities to be fitted are the pressures at the tangent points, the temperature profile sampled at the tangent pressures, atmospheric continuum and an altitude–independent offset. In each VMR retrieval, the fitted quantities are the VMRs of the considered gas sampled at the tangent points, the atmospheric continuum and an altitude–independent offset. Continuum values are fitted for each microwindow, at each tangent altitude, but only for altitudes below 30 km. The fitted continuum should take account of any broad spectral features that are not well represented in the forward model. The offset is fitted to take account of the fact that the instrument looking at a zero–radiance scene would be unlikely to measure zero radiance. It could also be referred to as the "instrumental zero level calibration correction".

Since MIPAS is a limb sounder, there are often clouds in the tangent path for the lower tangent altitudes, and since MIPAS views the atmosphere at infra–red wavelengths, the emission from any clouds in the path may mean that the spectral lines for the target species cannot be distinguished clearly enough for a good retrieval. Since July 2003, the ESA MIPAS OFL processor has included a cloud–detection method (Spang et al., 2004). The cloud detection method relies on the ratio between the radiance from two small regions of the spectrum, 788.20–796.25 cm^{-1} and 832.30–834.40 cm^{-1}. A threshold value of 1.8 for this ratio was chosen after examination of a large number of measurements from other instruments. All ratios falling below the threshold value are flagged as cloudy. Spectra from sweeps flagged as cloudy are not included in the measurement vector for the retrieval. The threshold of 1.8 is thought to be somewhat conservative, and does not take into account the continuous gradient of cloud optical thickness, but is expected to remove most cloudy sweeps.

4.2.3 Near–real–time and off–line ESA processing

Until MIPAS was switched off on 26^{th} March 2004, ESA was producing both near–real–time (NRT) and off–line (OFL) Level 2 products. Both use the same forward model. The ESA OFL Level 2 processing differs from the NRT processing in the following ways:

- **Extended altitude range:** In the ESA operational processor, retrieval of profiles at very low altitudes can be affected by lack of information below a certain altitude, large horizontal gradients and by clouds. With the least–squares fit method used in the ESA processing, retrievals of species with low concentration at high altitudes can result in strongly oscillating profiles that may induce problems lower down in the profile. In addition, non–LTE effects (§ 2.1.3) can significantly increase systematic errors at high altitudes. Also, before the launch there were concerns about CPU time for NRT processing, and retrievals over a reduced altitude range mean less time spent in the forward model. For these reasons, it was originally decided not to exploit all the spectra of a MIPAS scan in the NRT ESA retrieval. A customised retrieval range in the limits 12–68 km was defined for each species for the purposes of NRT processing, according to the information content for each species in the MIPAS measurements. However, there can be certain advantages in using the full measurement range in the retrieval. Use of the full altitude range allows the derivation of information in the upper troposphere. Also, the profiles are affected somewhat by the assumption of the initial guess profile outside the retrieval range (see Ceccherini et al. (2003), test MIP_MV_2_25/1). Use of the full measurement range can extend the height range in which the profiles are not affected by this assumption. Tests carried out with the ORM by the team from the Istituto di Fisica Applicata "Nello Carrara" (IFAC) (Ceccherini et al. (2003), test MIP_MV_2_25/2) indicate that retrievals on the whole MIPAS measurement range offer advantages over those on a reduced measurement range. The OFL retrievals therefore use an extended altitude range. The ranges of the NRT and the OFL products are shown in Table 4.1.

- **More stringent convergence criteria:** There was some concern that the NRT retrievals were not iterating to convergence, and were therefore constrained somewhat by the initial

Table 4.1: Altitude ranges of NRT and OFL ESA L2 products

Product	Range for NRT (km)	Range for OFL (km)
pT	12–68	6–68
H_2O	12–60	6–68
O_3	12–60	6–68
HNO_3	12–42	9–42
CH_4	12–60	6–68
N_2O	12–47	6–60
NO_2	24–47	24–47

guess profile used. The OFL retrievals therefore use more stringent convergence criteria. For details of the convergence criteria applied, refer to Ceccherini et al. (2003).

- **Continuity through an orbit:** Due to time constraints in NRT processing, different parts of an orbit may be processed in different places (ESRIN or Kiruna). This affects the choice of initial guess. If the orbit is not processed as a unit, the retrieval will use climatological profiles for the initial guess atmosphere instead of retrieved quantities from the previous scan. In the OFL processing, each orbit is processed as a unit, and so the initial guess used for each scan should be closer to the truth. In theory, the choice of initial guess should not affect the end result. In practice, the extent to which the end result is affected by the initial guess may depend on the convergence criteria chosen.

- **Processor version:** Since MIPAS was launched, the Level 2 products have been subjected to monitoring and validation. There have been updates to the processor arising from feedback from these monitoring and validation activities. The OFL data have been reprocessed with an updated processor version while the NRT data have not.

Since the OFL products have benefited from updates to the processor, they are of better quality than the NRT products. Processor updates are not confined to Level 2 processing. The OFL dataset also benefits from updates to the Level 1 processing. OFL retrievals use Level 1 data with better calibration and pointing than the NRT retrievals. Also, as the MIPAS instrument is no longer fully operational, NRT products are no longer being produced continuously. For these

Table 4.2: Spectral and altitude ranges of the ESA OFL H_2O and CH_4 microwindows

Microwindow label	Spectral range	MIPAS spectral band	Altitude range
H2O_0001	1650.025–1653.025 cm^{-1}	C	15–68 km
H2O_0002	807.850–808.450 cm^{-1}	A	6–18 km
H2O_0007	1645.525–1646.200 cm^{-1}	C	27–60 km
CH4_0001	1227.175–1230.175 cm^{-1}	B	6–68 km
CH4_0012	1350.875–1353.875 cm^{-1}	B	6–60 km

reasons, the decision was made to present results of the validation of OFL products only.

4.3 The operational microwindows

The positions of the nominal microwindows used in the ESA OFL retrieval have already been shown in Figure 3.1. The spectral and altitude ranges of the microwindows for H_2O and CH_4 are listed in Table 4.2. Figures 4.1 to 4.5 show the expected radiance contributions for different gases, as well as Jacobian spectra (∂y) for a 1 % perturbation in VMR at the top, middle and bottom tangent altitudes of each of these operational microwindows. There are alternative microwindows that can be used if, for example, the data from one spectral band is corrupted in some way. However, these alternative microwindows are used only rarely and will not be considered here. (Monthly statistics on how often any non–nominal microwindows were used can be found on the Oxford MIPAS group web pages (Dudhia et al., 2004) under "Occupation matrix statistics".)

Some points worth noting about these microwindows are listed below:

- **H2O_0001**: This microwindow contains one strong H_2O line and 3 weaker ones. The jacobian spectrum shows that the strong line is saturated throughout the altitude range (Figure 4.1).
- **H2O_0002**: This is where all the low altitude information for the water vapour retrieval comes from. The information comes from one strong and one weak H_2O line. In addition to the H_2O line, the window contains significant radiance contributions from CO_2, $ClONO_2$ and

a particularly strong contribution from O_3 (Figure 4.2).

- **H20_0007**: Contains one strong H_2O line. It can be seen from the Jacobian spectrum at 27 km that this line is saturated at lower altitudes. The centre of the line is masked out at these lower altitudes (Figure 4.3).
- **CH4_0001, CH4_0012**: The methane microwindows are expected to contain significant radiance contributions from CO_2, N_2O and H_2O. H_2O is retrieved before CH_4 in the retrieval sequence, so it would be hoped that the H_2O lines would be well modelled (Figures 4.4 and 4.5).

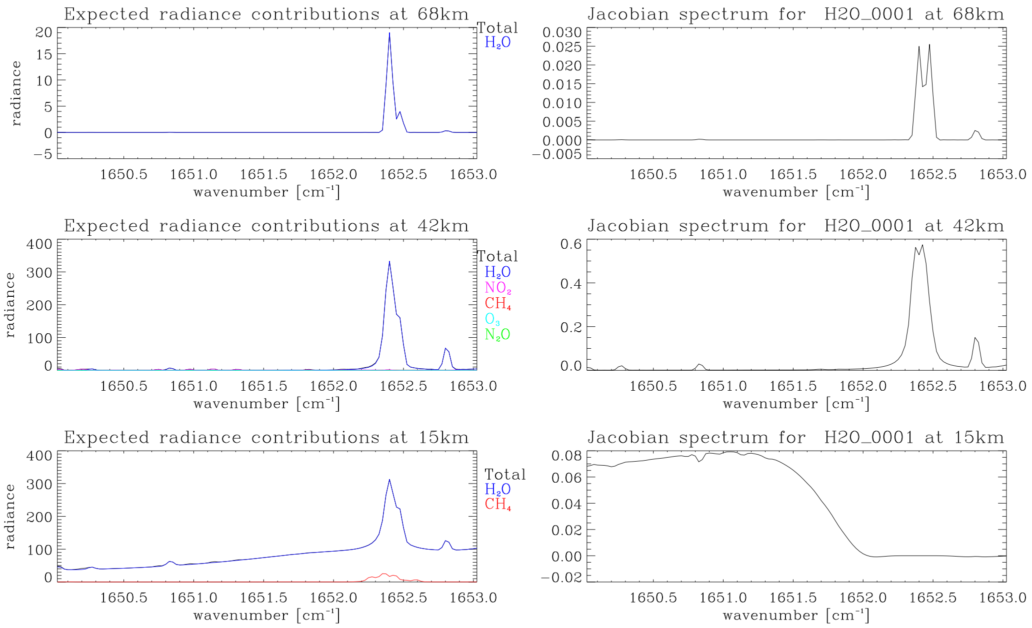

Figure 4.1: Expected radiance contributions and jacobian spectra (∂y) from different gases in the first ESA OFL water vapour microwindow (H2O_0001) at the uppermost, middle and lowermost tangent altitudes of the microwindow. Radiance units are nW cm^{-2} sr^{-1} $(cm^{-1})^{-1}$.

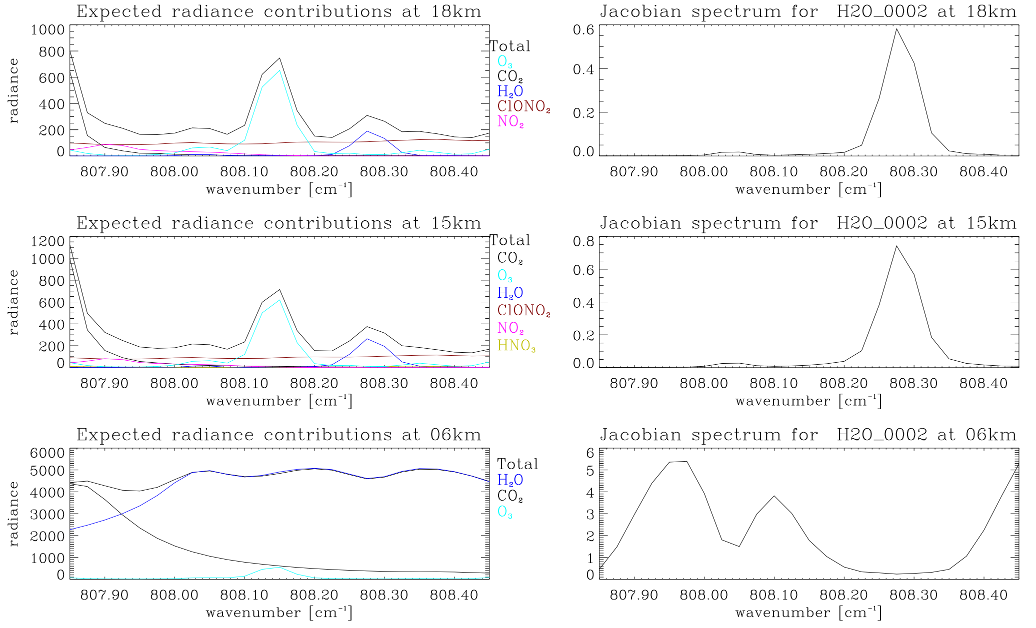

Figure 4.2: As above, but for the second ESA OFL water vapour microwindow (H2O_0002).

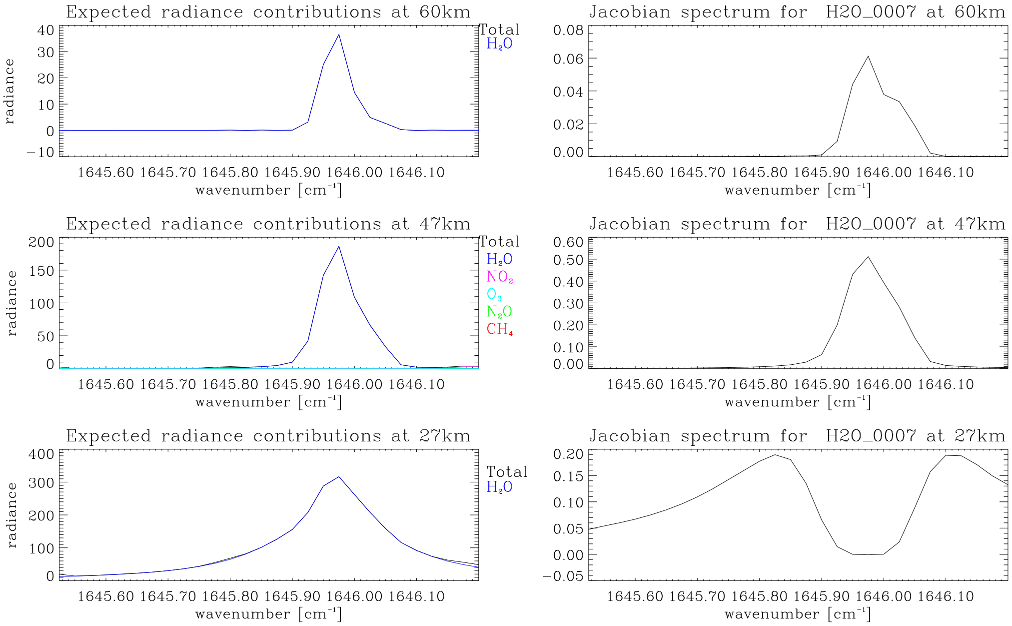

Figure 4.3: Expected radiance contributions and jacobian spectra (∂y) from different gases in the third ESA OFL water vapour microwindow (H2O_0007) at the uppermost, middle and lowermost tangent altitudes of the microwindow. Radiance units are nW cm^{-2} sr^{-1} (cm^{-1})$^{-1}$.

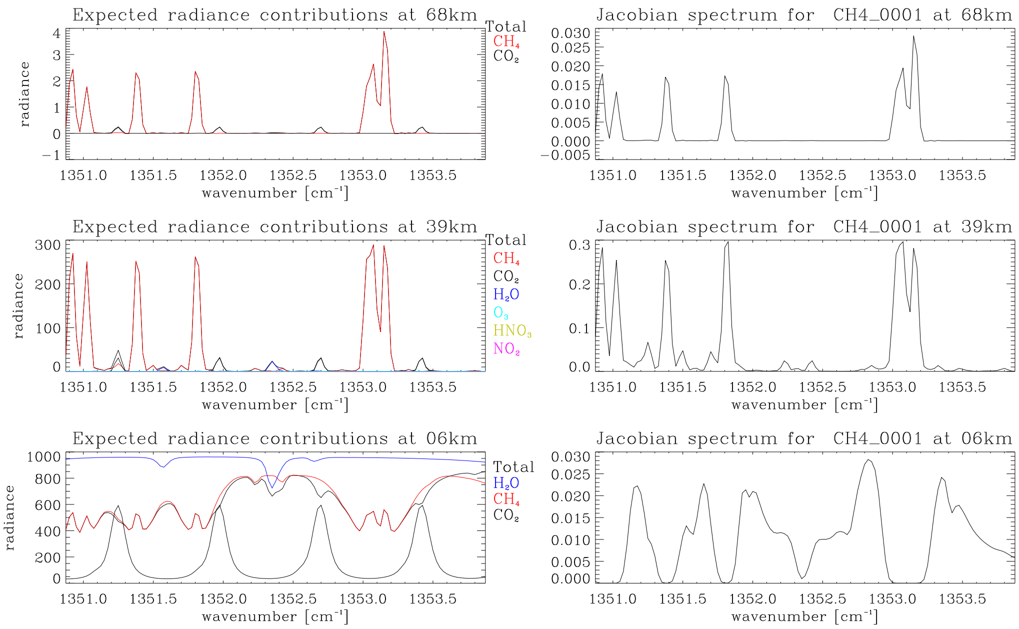

Figure 4.4: Expected radiance contributions and jacobian spectra (∂y) from different gases in the first ESA OFL methane vapour microwindow (CH4_0001) at the uppermost, middle and lowermost tangent altitudes of the microwindow. Radiance units are nW cm^{-2} sr^{-1} (cm^{-1})$^{-1}$.

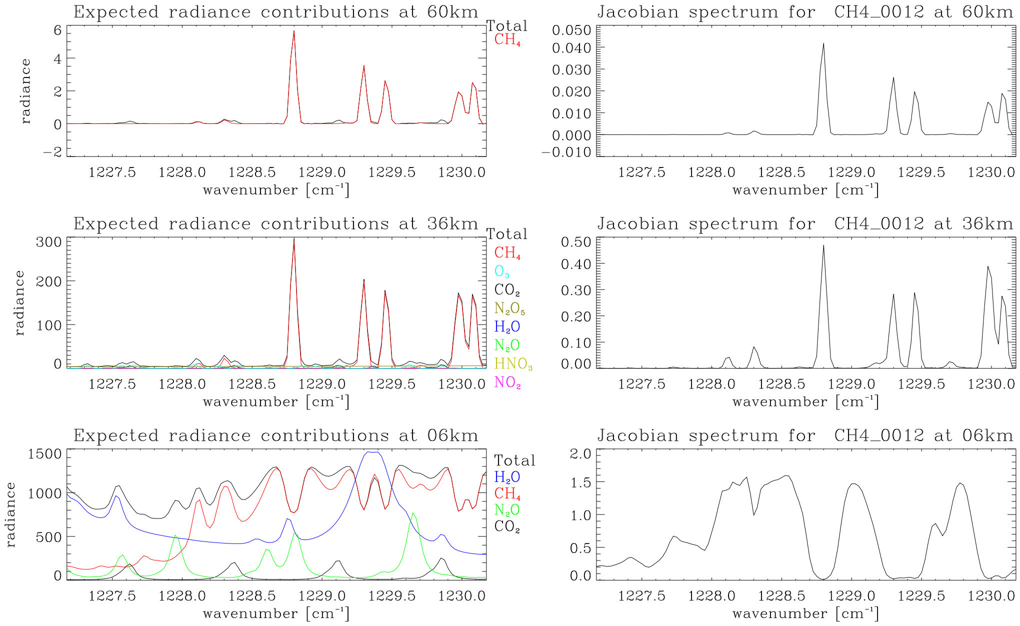

Figure 4.5: As above, but for the second ESA OFL methane vapour microwindow (CH4_0012).

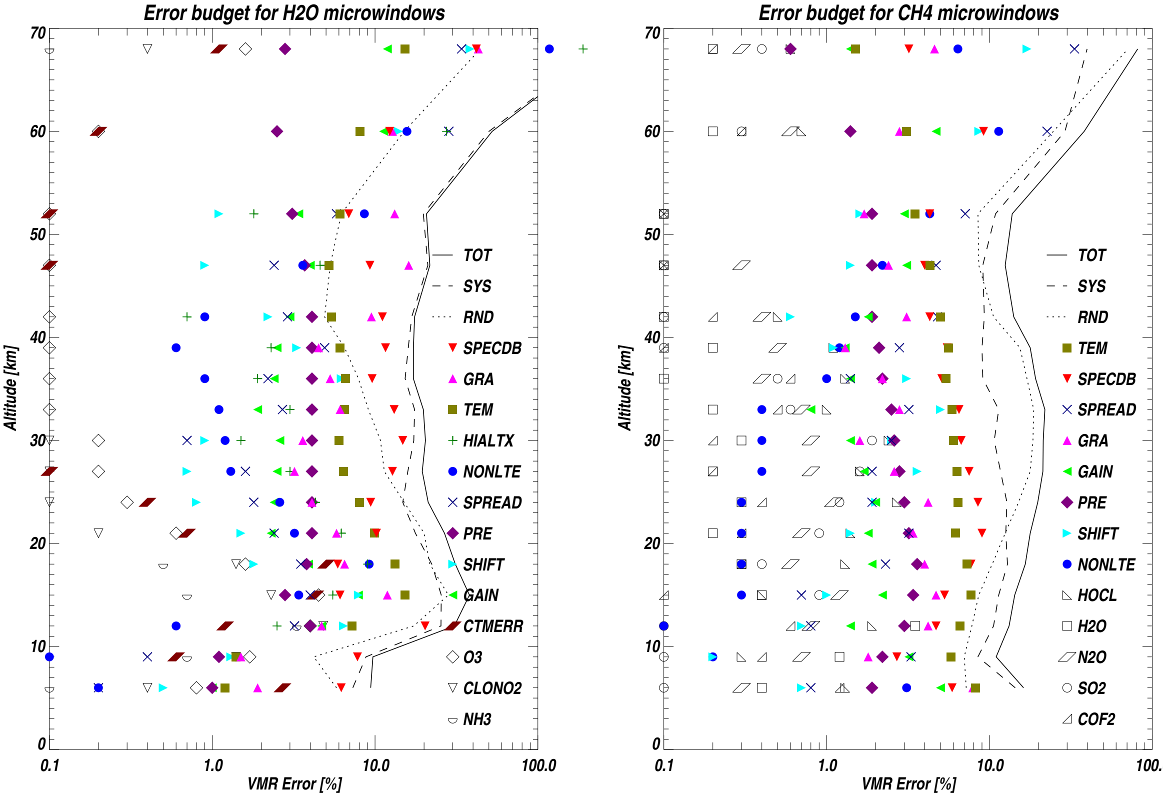

Figure 4.6: Error analysis for nominal sets of microwindows used in ESA OFL processing for H_2O (left) and CH_4 (right) (Dudhia et al., 2004). Systematic error sources have previously been described in more detail in § 3.4.2.

Figure 4.6 shows the error analysis from the MWMAKE microwindow selection software for the operational microwindows for H_2O and CH_4. The error budget for the H_2O microwindows is strongly dominated by systematic errors above 24 km while for CH_4 systematic errors dominate below 20 km and above 47 km. The most important systematic errors throughout most of the MIPAS altitude range for both H_2O and CH_4 are uncertainties in temperature (TEM) and in the spectroscopic database (SPECDB). Non–LTE effects are expected to become important in both the H_2O and the CH_4 retrievals at 52 km and above, but not below 52 km. The 2 % uncertainty in the width of the ILS (labelled in Figure 4.6 as "SPREAD") becomes comparable with the temperature error at 39 km in H_2O and at 42 km in CH_4. In the H_2O retrievals, the uncertainty in atmospheric state above the retrieval range (labelled "HIALT") is expected to be a significant source of systematic error at 47 km and above.

Although radiance contributions from contaminant species may be large (for example the O_3 line in the H2O_0002 microwindow), it can be seen from Figure 4.6 that contaminant species contribute only a small error to the overall budget. This is because other gas lines only influence the retrieval where they coincide with the Jacobians of the target species.

4.4 Averaged residuals

The residual spectra ($\mathbf{y}$-$\mathbf{f}$) associated with the OFL retrievals can provide information useful for internal validation of the Level 2 products. For an ideal retrieval, the residuals would consist only of noise. In reality, it is likely that the residuals will contain some signatures of systematic errors. These signatures of systematic errors may be of the same order of magnitude or smaller than the noise, in which case the error signatures will not be obvious by visual inspection of the residuals. The large number of residual spectra available in the ESA OFL Level 2 dataset means that it is possible to average them, effectively removing the noise and so allowing signatures of any systematic errors to be more clearly distinguished.

The residuals were divided into the following domains for the purposes of averaging:

- Time — monthly averages.
- Altitude — nominal sweep tangent height (6–68 km).
- Latitude — six latitude bands (90°S–65°S, 65S°–20°S, 20°S–0°, 0°–20°N, 20°N–65°N and 65°N–90°N)
- Wavenumber — position of the microwindow in the MIPAS spectral range

Since there are 14 orbits per day, with around 75 limb scans in any one orbit, it might be expected that there would be of the order of $(14 \times 75 \times 30)/6 = 5250$ residual spectra included in the average for each nominal tangent altitude of each microwindow for each month. Lower altitudes are likely to include fewer residual spectra in the average, since many of the lower sweeps would be cloudy, and would therefore not have been used in the retrievals.

Residuals were also divided into day–time and night–time. Since neither H_2O nor CH_4 are expected to show diurnal variations, this was expected to be a useful internal consistency check.

REC analyses (see § 3.5) have been performed on these monthly averaged residuals. The results can be viewed on the Oxford MIPAS Group web pages (Dudhia et al., 2004). Inspection of the variation of the results of the REC analyses with time shows the following:

- that there are signatures of the target gases in the target microwindows. This is somewhat surprising, given that the aim of the retrieval is to adjust the profile to make the modelled spectra fit the measurements. This may be indicative of problems with convergence.
- that there are differences between the residual fits for day–time and night–time residuals for both H_2O and CH_4
- that the fit coefficients for the target gases are worse in summer (for both day–time and night–time residuals) than in winter, for both hemispheres.

4.4.1 Water vapour microwindows

Figures 4.7 and 4.8 show averaged residual spectra as a function of altitude from January 2003 (northern hemisphere winter, southern hemisphere summer), from the first water vapour microwindow (H2O_0001) for mid–latitudes bands of both hemispheres, separated into day–time and night–time. If the retrievals were perfect, it would be expected that there would be no apparent features in the residuals. It is clear from these figures that the averaged residuals contain distinct features corresponding to the positions of the strong and the weak water vapour lines in this microwindow. The features change shape somewhat with altitude. The change in shape of the residual spectra with altitude would seem to suggest a shift in the position of the line maximum with altitude.

These figures serve to illustrate the points that showed up in the REC analyses: that there are signatures of the target gas in the target microwindows, that there are day/night variations in the residual spectra and that the fit to the residuals is worse in summer than in winter.

The magnitude of the residual signature at the position of the strong water vapour line is large at low altitudes. However, it is worth noting that the main part of the line is masked out (positions of masked points are shown in the figures with crosses) and is not actually used in the retrievals at these altitudes. There are also some features to the left of the water vapour lines in these figures which indicate that the modelled NO_2 is too high in the day–time and too low in the night–time. However there are no NO_2 lines which interfere directly with the H_2O lines, so this should not adversely affect the H_2O retrievals.

Figures 4.9 and 4.10 show averaged residual spectra from January 2003 (northern hemisphere winter, southern hemisphere summer), from the second water vapour microwindow (H2O_0002) for mid–latitude bands, separated into day–time and night–time. Again, the averaged residuals show distinct spectral features, although in this case there is not such an obvious correlation with the water vapour lines. The most obvious correlations with spectral lines are with the O_3 line in the centre of the microwindow and with the NO_2 line at the left of the microwindow. There are obvious day/night differences in the fit of the lines of NO_2 and O_3, but it is not immediately clear what effect these have on the fitting of H_2O in this microwindow.

Figures 4.11 and 4.12 show averaged residuals for the third water vapour microwindow (H2O_0007). The residual signatures for the strong water vapour line in this microwindow look broadly similar to those for the strong water vapour line in H2O_0001. The residuals show similar day/night variation and seem to exhibit some kind of altitude dependent shift. Both of these microwindows are located in the C band and are close to one another (see Figure 3.1). It could be that the similar shape of the residual spectra for these microwindows is related to a problem which is particular to this spectral region.

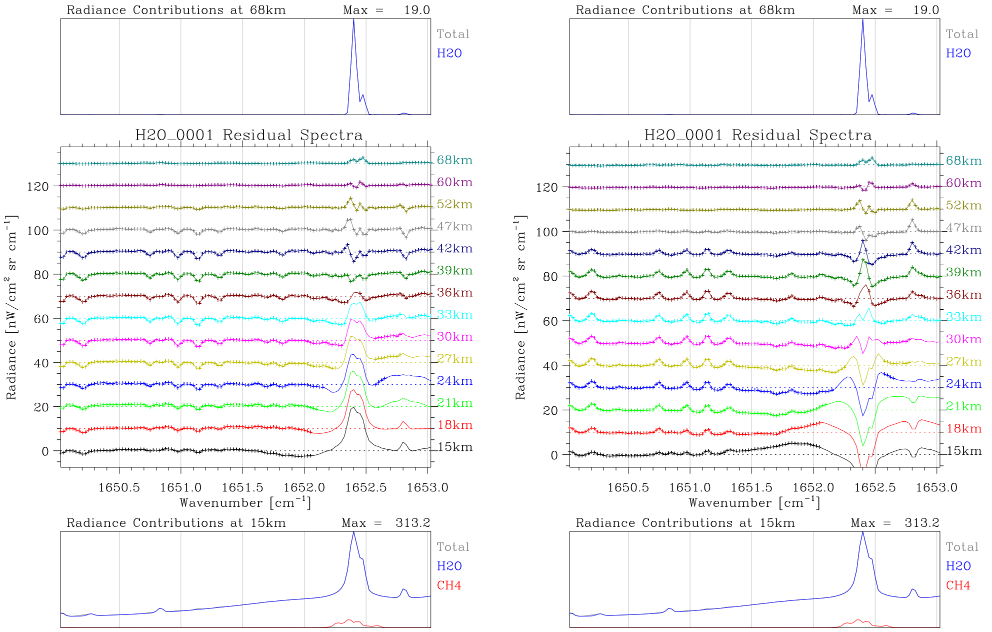

Figure 4.7: Averaged residual spectra in the latitude band 65°S–20°S for January 2003 (southern hemisphere summer) from the first OFL water vapour microwindow (H2O_0001). Radiance offsets have been added in order to distinguish residuals from different nominal altitudes. Crosses show positions of unmasked points. Top and bottom panels show simulated radiance contributions from different gases at the top and bottom altitudes of the microwindow, in order to relate positions of features in the residuals to those of spectral lines. The left–hand plot shows day–time residuals while the right–hand plot shows night–time residuals.

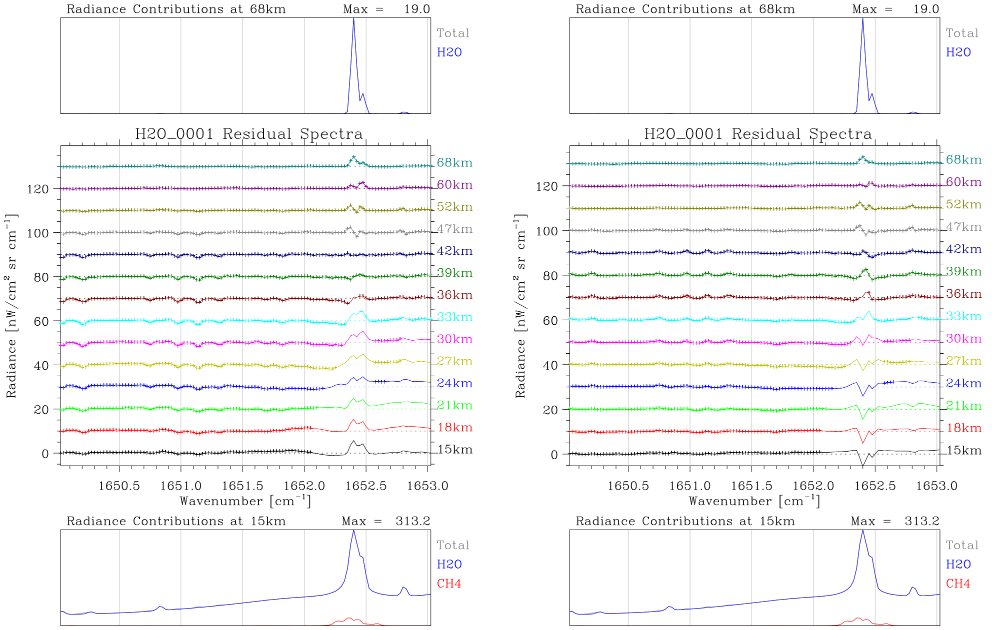

Figure 4.8: As above, but for the latitude band from 20°N–65°N for January 2003 (northern hemisphere winter).

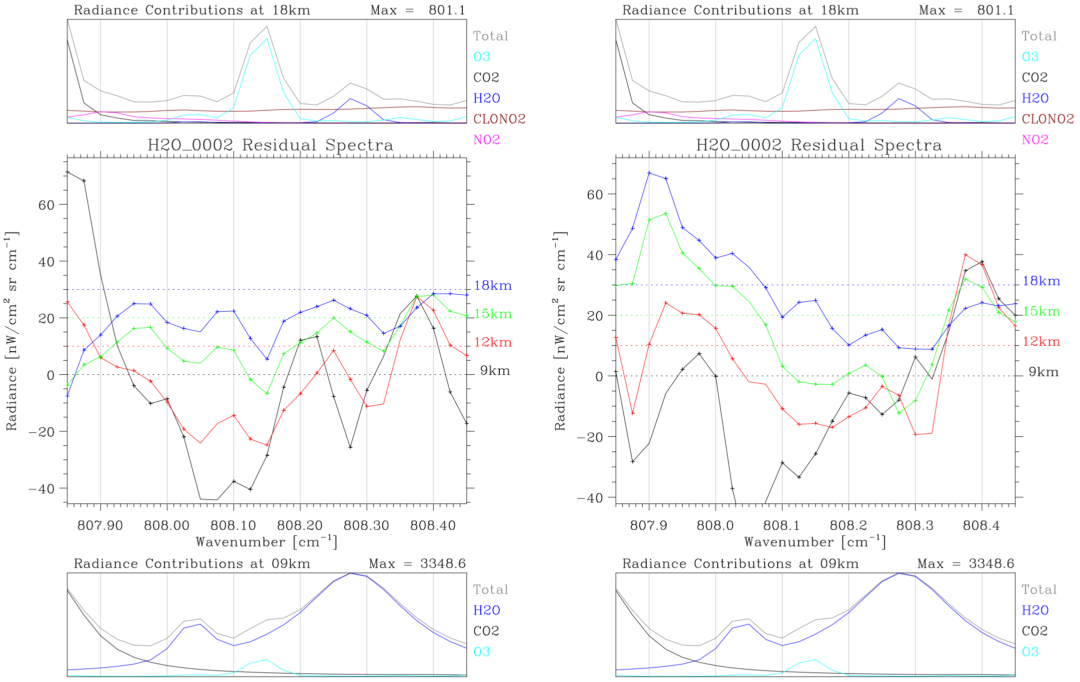

Figure 4.9: As for Figure 4.7, but for the second ESA OFL water vapour microwindow (H2O_0002).

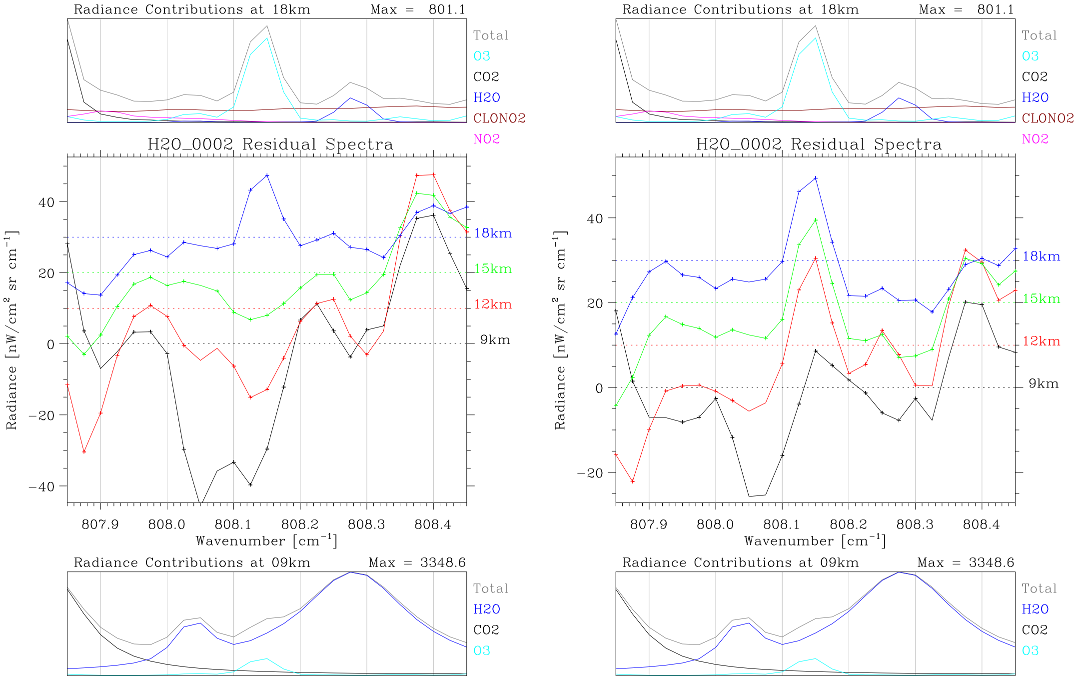

Figure 4.10: As above, but for the latitude band from 20°N–65°N for January 2003 (northern hemisphere winter).

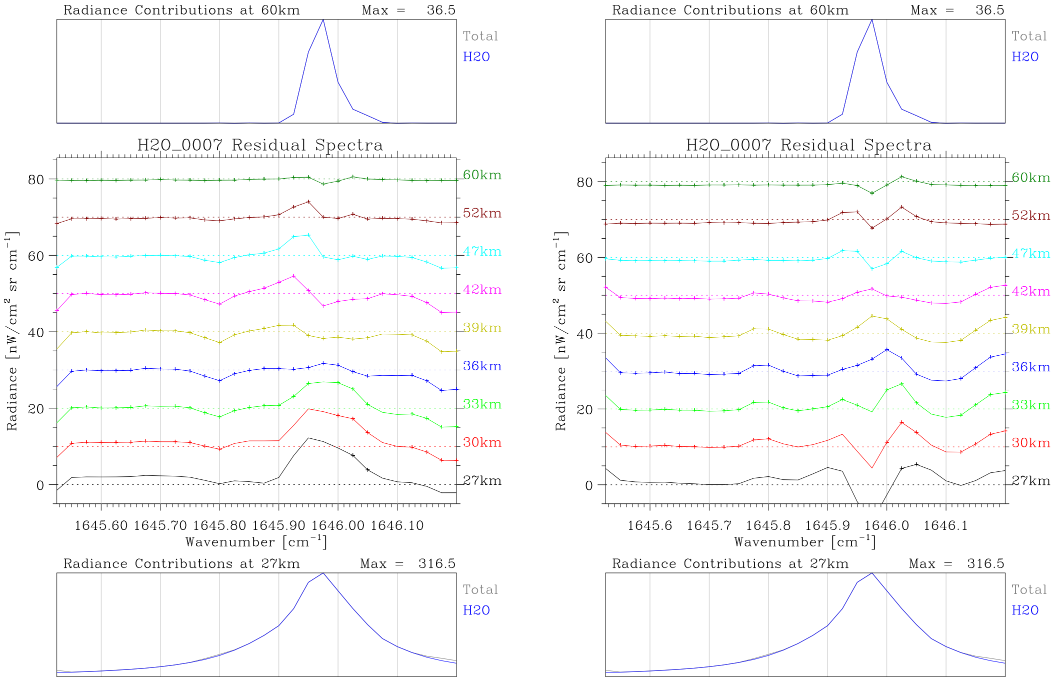

Figure 4.11: As for Figure 4.7, but for the third ESA OFL water vapour microwindow (H2O_0007).

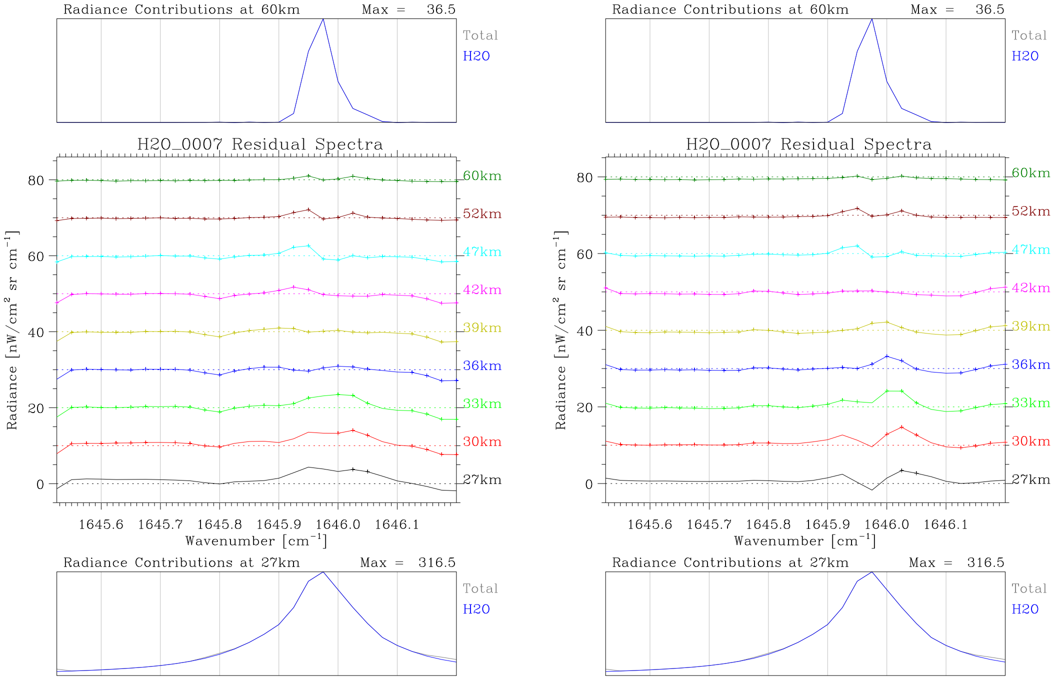

Figure 4.12: As above, but for the latitude band from 20°N–65°N for January 2003 (northern hemisphere winter).

4.4.2 Methane microwindows

Figures 4.13 and 4.14 show averaged residuals for the first methane microwindow (CH4_0012). The residual spectra at 6 and 9 km indicate that there are considerable difficulties here in fitting the modelled spectra to the measurements, but the complicated structure of the residual spectra make it difficult to separate the causes of the poor fitting by visual inspection. Residual spectra in the altitude range 12–30 km show a negative feature at around 1277.5 cm^{-1} in both the day–time and night–time residuals which corresponds to the position of an H_2O line. This could either indicate an overestimate in the H_2O in this altitude range or an error in the H_2O line strength in the HITRAN database for this particular H_2O line. In addition, residual spectra for this microwindow show positive features at around 1227.6 cm^{-1} and 1229.9 cm^{-1} which correspond to the positions of CO_2 lines. This could either indicate an error in CO_2 line strength in the spectroscopic database, an underestimate in the climatological CO_2 profile or a low bias in the retrieved pressure.

Day/night differences in the residual signatures for CH_4 itself are not obvious.

Figures 4.15 and 4.16 show averaged residuals for the second methane microwindow (CH4_0001). As in the other methane microwindow, positive features can be seen in both the day–time and night–time residual spectra which correspond to the positions of CO_2 lines. Unlike the other methane microwindow, the residuals in this microwindow show strong day/night differences.

4.4.3 Summary

Residual spectra from the ESA OFL retrievals of water vapour and methane were divided up according to month, latitude, altitude and microwindow and averaged in order to reduce the random noise component. Since the point of the retrieval is to fit the modelled spectra to the measurements, it would be expected that the target species would be fitted well in the target species microwindows. It appears that this is not the case. The residuals for both the water vapour and methane microwindows show distinct spectral features corresponding to the positions of lines of the target gas. There are also features corresponding to lines of other trace gases, but these would not be expected to have a large effect on the retrieval of the target species.

There are distinct and unexpected day/night differences in the residual spectra for all the microwindows examined. Day/night differences in the residuals are most obvious at low altitudes. In addition, the residuals for both day–time and night–time spectra appear to be worse in the summer months than in the winter for both hemispheres.

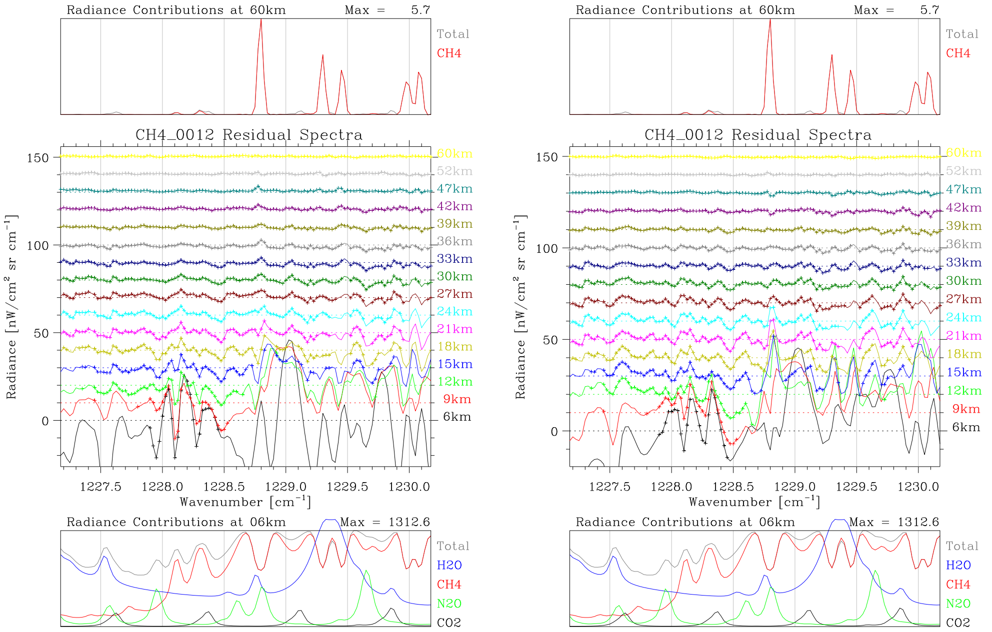

Figure 4.13: Averaged residual spectra in the latitude band 65S°–20°S for January 2003 (southern hemisphere summer) from the first ESA OFL methane microwindow (CH4_0012). Radiance offsets have been added in order to distinguish residuals from different nominal altitudes. Crosses show positions of unmasked points. Top and bottom panels show simulated radiance contributions from different gases at the top and bottom altitudes of the microwindow, in order to relate positions of features in the residuals to those of spectral lines. The left–hand plot shows day–time residuals while the right–hand plot shows night–time residuals.

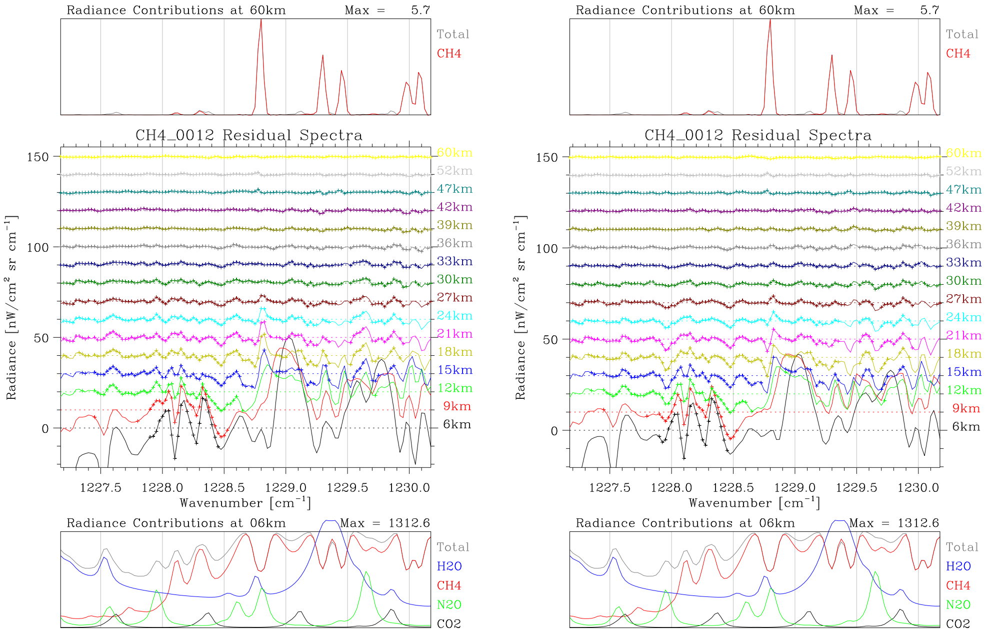

Figure 4.14: As above, but for the latitude band from 20°N–65°N for January 2003 (northern hemisphere winter).

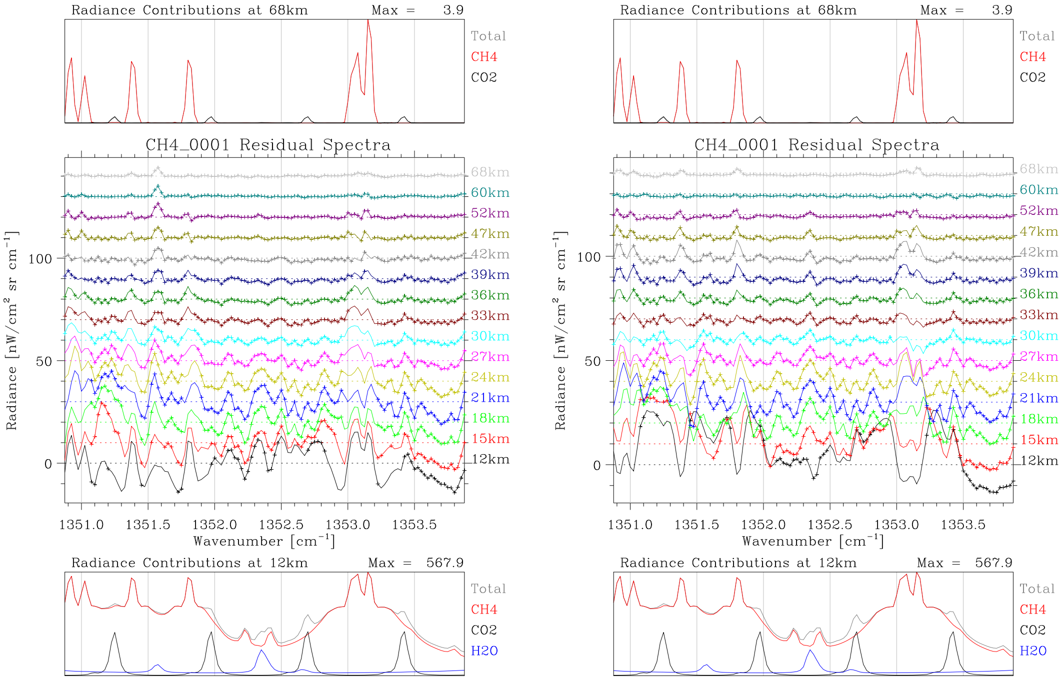

Figure 4.15: As for Figure 4.7, but for the second ESA OFL methane microwindow (CH4_0001).

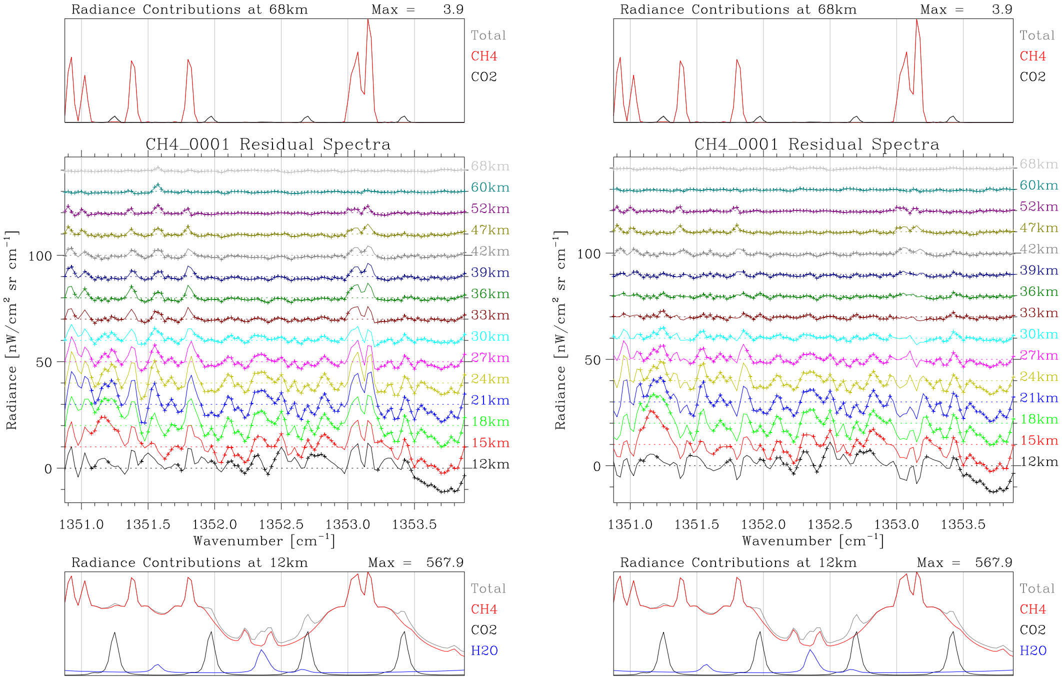

Figure 4.16: As above, but for the latitude band from 20°N–65°N for January 2003 (northern hemisphere winter).

4.5 Comparison of MIPAS monthly mean profiles with climatology

One way of obtaining a large–scale picture of the quality of the data is to examine a time–series of monthly mean profiles. Monthly mean profiles of H_2O and CH_4 were calculated for all the available months of OFL Level 2 retrieved from the 0.025 cm^{-1} resolution spectra, from July 2002 until March 2004. The profiles were split into six latitude bands for the calculation of the means, and the monthly mean profiles for each of the products plotted as time–series. The six latitude bands (90°S–65°S, 65°S–20°S, 20°S–0°, 0°–20°N, 20°N–65°N, 65°N–90°N) were chosen because these are the bands into which the initial guess data (Remedios, 1999) for the MIPAS OFL retrievals are split. Some spike detection was used in the averaging process, excluding values of CH_4 greater than 10 ppmv and H_2O greater than 1000 ppmv. The intention of looking at the time–series of the monthly means of the MIPAS H_2O and CH_4 was to give an overview of the quality of the data and to identify any persistent features or problems in the profiles.

The time series of monthly means shown in this section have been plotted using the MIPAS OFL monthly mean pressures as a vertical coordinate. Figure 4.17 shows the MIPAS retrieval levels (nominal altitudes) as a function of pressure in order to allow an approximate conversion between altitude and pressure.

In order to assess the quality of the MIPAS OFL monthly mean profiles, they are compared here with profiles from the IG2 ("initial guess 2") climatological dataset. The IG2 climatology was produced by Remedios (1999) for the purpose of providing initial guess profiles for the MIPAS retrievals. As a climatology, the IG2 dataset would be expected to give a reasonable idea of expected VMRs for water vapour and methane in different latitude bands and seasons, but would not be expected to show any extremes of variability.

The comparisons performed here are complementary to other work with the IG2 dataset performed

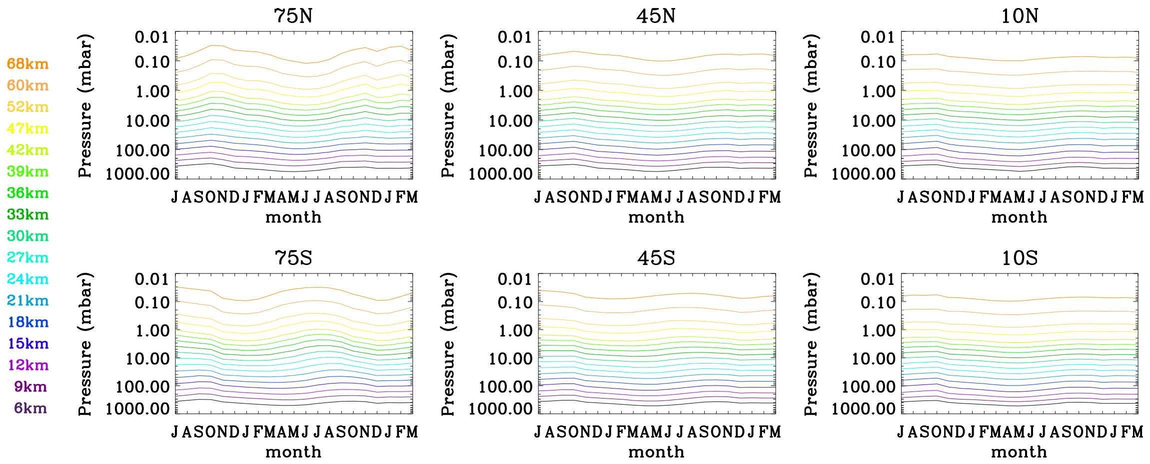

Figure 4.17: Time series of monthly mean pressures at each of the seventeen nominal altitudes for six latitude bands. This figure is intended to allow an easy approximate conversion between altitude and pressure.

at the University of Leicester (Waterfall et al., 2004).

The IG2 dataset is provided in the form of profiles of pressure, temperature and VMRs of numerous trace gases (including water vapour and methane) for six latitude bands (Table 4.3), for four seasons ("January", "April", "July" and "October"). The IG2 water vapour profiles are largely based on measurements from the early 1990s, from instruments on the Upper Atmosphere Research Satellite (UARS), namely the Microwave Limb Sounder (MLS) (Barath et al., 1993) and the Halogen Occultation Experiment (HALOE) (§ 4.6). The UARS measurements were supplemented by model data from TOMCAT (Chipperfield, 1999) in the stratosphere and from ECMWF data and a SAGE II climatology in the troposphere. The methane profiles are largely based on measurements from HALOE and from the Cryogenic Limb Array Etalon Spectrometer (CLAES — another UARS instrument) (Roche et al., 1993) and are also supplemented by model data from TOMCAT. Tropospheric methane values are set to measured surface values. The dataset is divided in terms of latitude and season only, and does not include any information on diurnal variations. Water vapour and methane are not expected to show any diurnal variations in any case.

It is important to note that in the ESA retrievals, the IG2 data are used only in the construction of the initial guess profiles for the retrievals and not as an *a priori* constraint.

For the purposes of this comparison, the IG2 profiles were interpolated in time in order to avoid large steps in the data from one month to the next.

Table 4.3: Latitude bands as used in the monthly mean analysis

Label	Latitude Range
75N	090°N–065°N
45N	065°N–020°N
10N	020°N–000°
10S	000° –020°S
45S	020°S–065°S
75S	065°S–090°S

4.5.1 Time series comparisons: H_2O

Figure 4.18 shows a time series of the monthly mean profiles of MIPAS OFL H_2O from July 2002 until March 2004, while Figure 4.19 shows the corresponding profiles from the IG2 climatology. Features that would be expected in the distribution of H_2O in different latitude and altitude regions were previously discussed in Chapter 1 but are reiterated here.

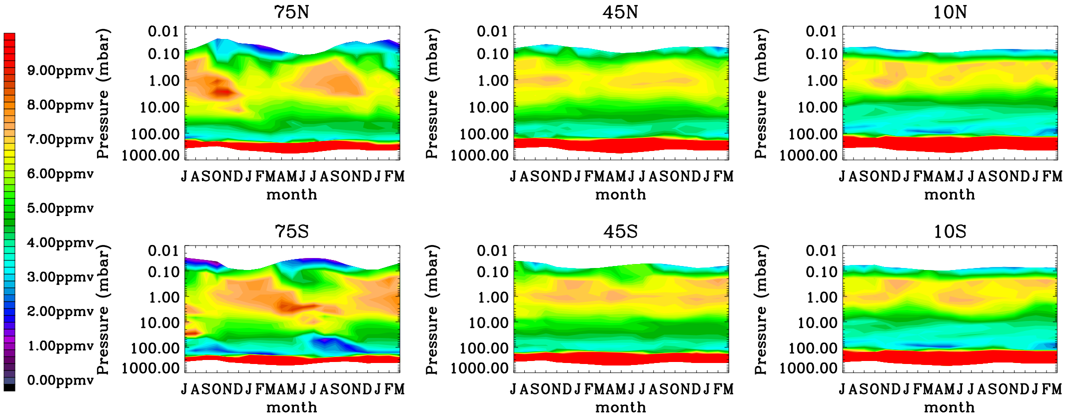

Figure 4.18: Monthly mean profiles of MIPAS ESA OFL H_2O, from July 2002 until March 2004, split into six latitude bands.

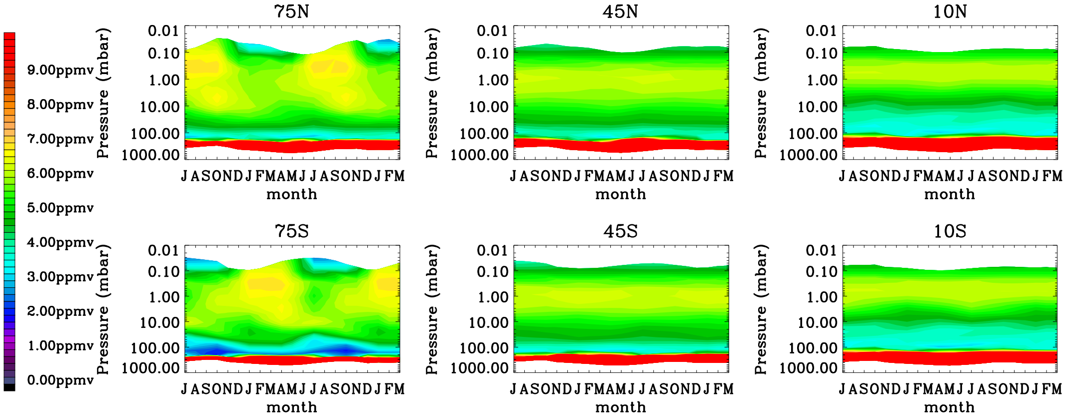

Figure 4.19: Time series of H_2O generated from the IG2 climatological dataset.

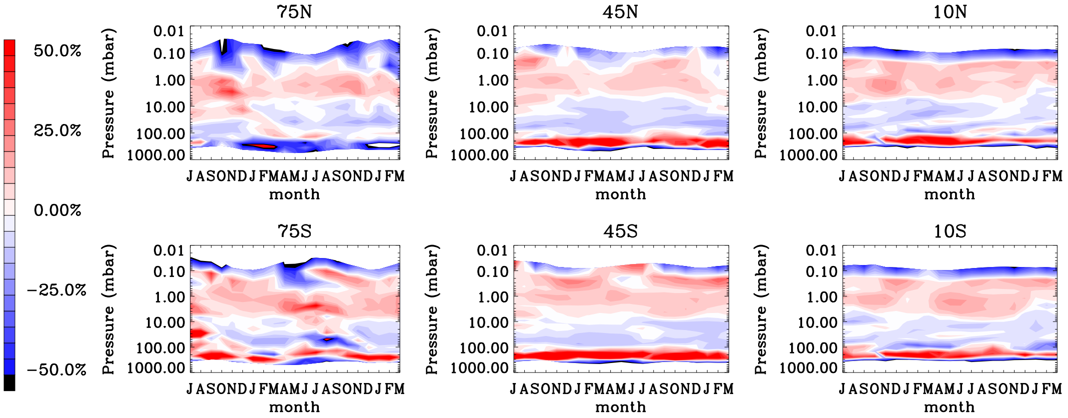

Figure 4.20: Time series of the percentage difference of the MIPAS OFL monthly mean H_2O from the IG2 climatological dataset. Difference shown is ([MIPAS-IG2]/IG2).

Monthly mean profiles for all latitude bands show the highest values in the upper troposphere, at the bottom of the MIPAS altitude measurement range. The profiles show a minimum in the lower stratosphere, with increasing H_2O values up to around 1 mbar, as would be expected due to the production of water vapour in this region by the oxidation of methane. Above about 1 mbar (around the 52 km level) water vapour values begin to decrease, as would be expected as the reaction of water vapour with excited oxygen to form hydroxyl radicals becomes an important sink.

Although Figures 4.18 and 4.19 show the same qualitative variation with height and with latitude, there are persistent biases in the MIPAS monthly mean H_2O profiles with respect to the climatology. Figure 4.20 shows a time series of the percentage differences between the two datasets.

There are large differences in H_2O below the tropopause. This is not altogether surprising, given the difficulties in measuring the absolute volume mixing ratio of H_2O, which may vary by an order of magnitude over an altitude range of a few kilometres in this region, with the 3 km vertical resolution offered by MIPAS. It is also worth noting that the MIPAS tropospheric values will be biased towards cloud–free cases. The climatology, which is based on model values in the troposphere, will not. The mid–latitude and equatorial latitude bands for both hemispheres show that the MIPAS OFL H_2O is persistently lower than climatological values at 6 km and persistently higher then climatological values at 9 km.

The vertical structure of differences between the MIPAS OFL and IG2 water vapour is largely consistent across altitudes and with time. MIPAS H_2O is generally around 5–10 % lower than climatology in the 100–10 mbar (about 12–27 km) region. At higher altitudes (30–60 km), MIPAS H_2O values are around 10–20 % higher than the climatology.

At the uppermost retrieval altitude (68 km), MIPAS values are consistently lower than climatology. Comparison of Figure 4.20 with similar plots for the NRT data (Payne et al., 2003), where the H_2O retrieval stops at 60 km rather than 68 km, indicate that the low values are a feature of the uppermost retrieval altitude rather than a feature of the retrieval at 68 km.

4.5.2 Seasonal cycles: H_2O

Extremely low values of H_2O can be seen at the tropical tropopause, particularly in February–April, coinciding with the time of year at which the tropical tropopause is coldest, as would be expected. The plots in Figure 4.18 also show evidence of ascent of this drier air in the tropics (the tropical tape recorder effect — see Chapter 1). This ascending motion can be seen more clearly in Figure 4.21. The tape recorder effect is far stronger in the MIPAS data than in the IG2, and so can also be seen in the pattern of differences in Figure 4.20.

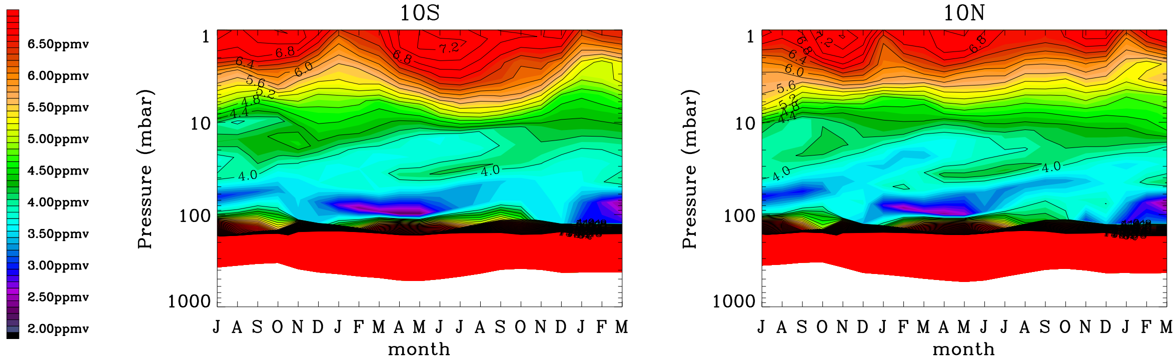

Figure 4.21: The tropical tape recorder effect in the MIPAS OFL water vapour.

Extremely low values of H_2O can also be seen in the Antarctic winter at around 30 mbar, descending with time to 100–130 mbar in the Antarctic spring. This might be expected due to dehydration events in the polar vortex. Figure 4.18 also shows evidence of air descending from the mesosphere in polar regions, with a six–monthly offset between the northern and southern polar regions.

Figure 4.18 shows particularly high H_2O values in the region of about 5 mbar in the polar regions of both hemispheres in autumn to early winter. The maximum values are at an altitude of around 33–36 km. This feature is also present in the climatology, but the seasonal cycle is stronger in the

MIPAS OFL data.

In order to examine seasonal variations more clearly, time series plots were produced of the variation from the 2003 annual mean. Annual mean profiles for 2003 were calculated from the monthly means. The annual mean was then subtracted from each of the monthly means, and the results plotted as a time series. Figures 4.22 shows time series of the percentage deviation from the 2003 annual mean for H_2O. Monthly deviations from the 2003 annual mean temperature profile are shown in Figure 4.24 in order to relate these monthly deviations in the H_2O to other seasonal changes in the atmosphere.

The water vapour shows a very pronounced seasonal cycle in the upper troposphere (below around 100 mbar) in all six latitude bands. Months where there is high water vapour in the upper troposphere compared to the annual mean correspond to months where the temperature in the upper troposphere is high compared to the annual mean. This is as would be expected.

In the tropics, the warmest temperature anomalies (and the positive water vapour anomalies) in the upper troposphere are in the Northern Hemisphere Spring (March to May). Despite the large differences between the MIPAS OFL H_2O and the climatology below the tropopause that were observed in Figure 4.20, it can be seen from Figure 4.22 that both datasets show the same pattern of seasonal variations in this altitude region. The times of warm (high water vapour) anomalies in the upper troposphere correspond to the times of cold (low water vapour) anomalies in the tropical lower stratosphere. This is in agreement with what would be expected.

It is clear from Figures 4.22 that the seasonal variations are larger than any apparent trends in the data. For a proper examination of trends, a much longer dataset would be necessary.

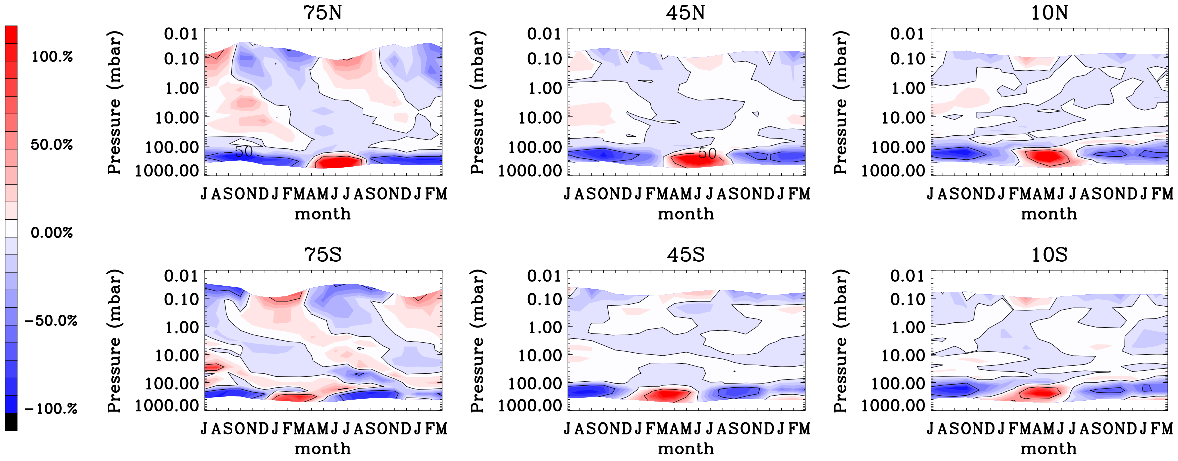

Figure 4.22: Time series of the percentage difference of the MIPAS OFL monthly mean H_2O from the 2003 annual average.

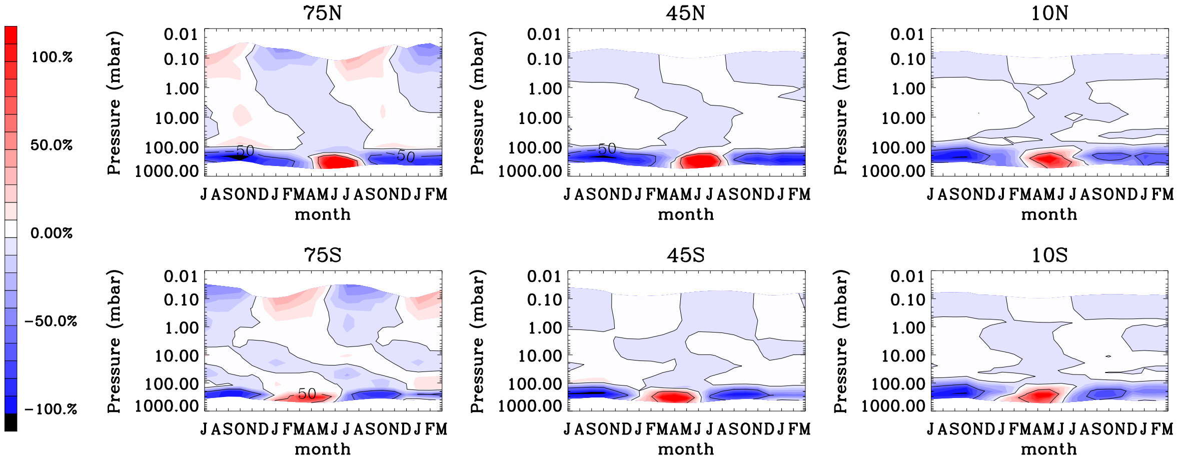

Figure 4.23: Time series of the percentage difference of IG2 climatological H_2O (interpolated in time) from an annual average.

4.5.3 Time series comparisons: CH_4

Figure 4.25 shows a time series of the monthly mean profiles of MIPAS OFL CH_4 from July 2002 until March 2004, while Figure 4.26 shows the corresponding profiles from the climatology.

In general, the highest values of CH_4 can be seen in the troposphere, with the volume mixing ratio decreasing monotonically with height, as would be expected. However, this is not the case in the

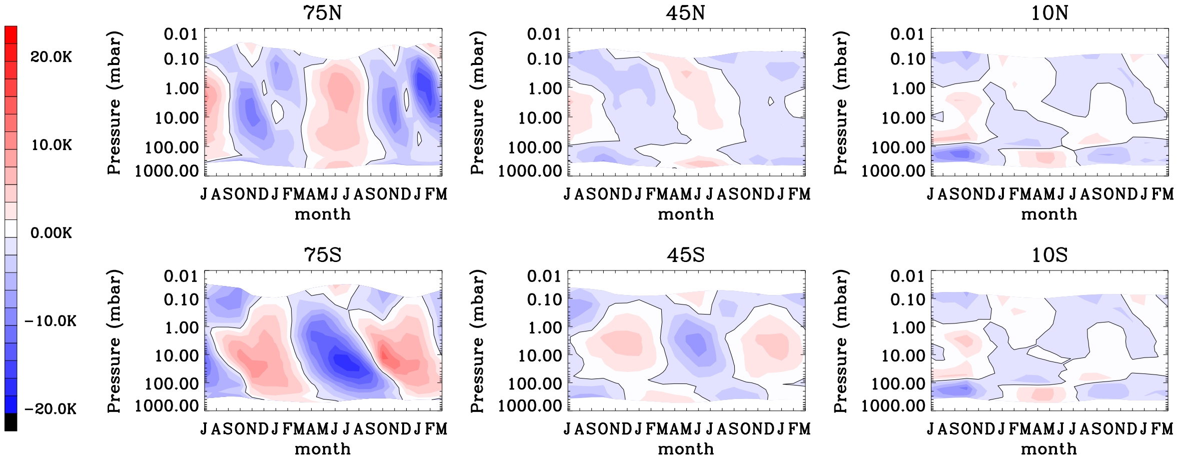

Figure 4.24: Time series of the percentage difference of the MIPAS OFL monthly mean temperature from the 2003 annual average.

MIPAS OFL tropical monthly means. The tropical profiles for both hemispheres show a persistent local minimum in the VMR at around 100 mbar, the approximate location of the tropopause in this region. Given that there are no known sources of methane in the stratosphere, there is no physical explanation for a local minimum in methane just above the tropopause. This feature would appear to indicate that there is some kind of persistent problem in the OFL retrievals.

Figure 4.27 shows percentage differences between monthly mean MIPAS OFL CH_4 profiles and the IG2 climatology. In general, the MIPAS monthly mean values are around 10–20 % higher than those from the IG2 climatology throughout the upper troposphere and stratosphere. Differences are much greater in the polar regions, but this appears to be due to seasonal variations which are much more pronounced in the MIPAS data than in the climatology (see § 4.5.4). The general high bias of MIPAS OFL CH_4 with respect to climatology could perhaps be accounted for by the fact that the climatology is largely based on data from the early 1990s. Mixing ratios of methane in the atmosphere have increased since then. Numbers compiled by Dlugokencky et al. (2003) indicate that tropospheric methane mixing ratios increased by approximately 3 % from 1990 to 2003. However, this increase is not large enough to fully account for the magnitude of the differences in Figure 4.27.

Figure 4.27 also shows evidence of the problem with the methane retrievals in the tropics mentioned previously. It would appear that the persistent local minimum is part of a persistent oscillation.

Like the water vapour, the MIPAS OFL methane profiles show a consistent low bias at the highest retrieval altitude with respect to the IG2 climatology.

Mid–latitude monthly mean MIPAS OFL CH_4 profiles show a markedly less smooth shape than the IG2 profiles. It is possible that the more complicated shape of the MIPAS profiles is due to dynamical activity in the atmosphere which is not accounted for by the climatology.

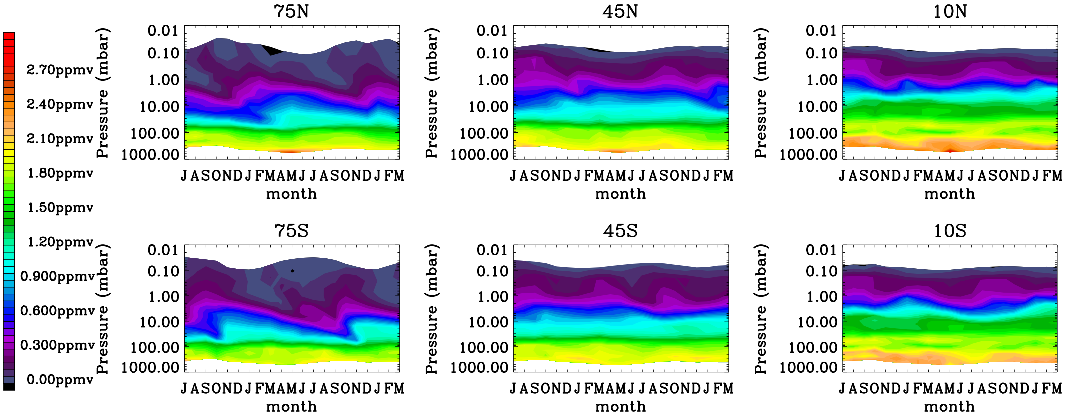

Figure 4.25: Monthly mean profiles of MIPAS ESA OFL CH_4, from July 2002 until March 2004, split into six latitude bands.

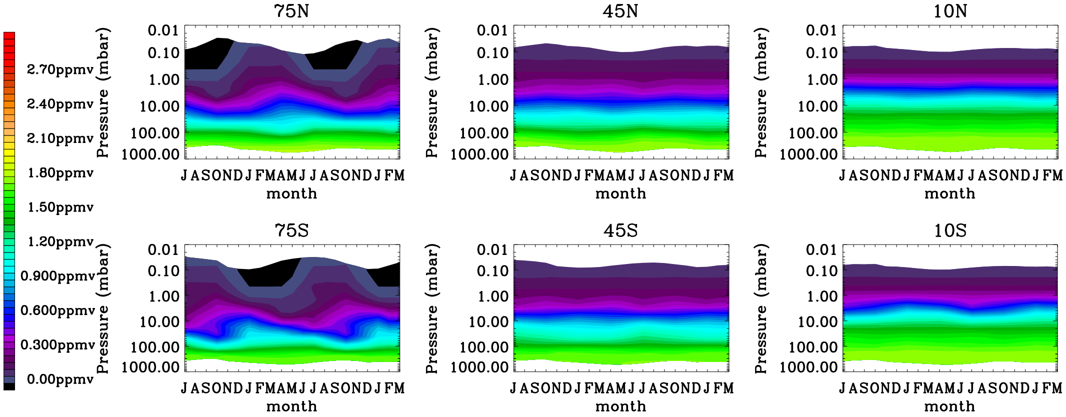

Figure 4.26: Time series of CH_4 generated from the IG2 climatological dataset.

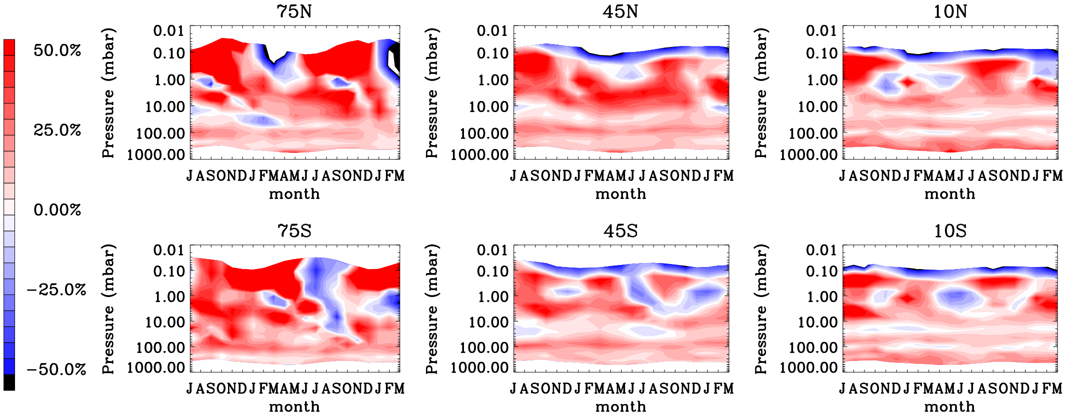

Figure 4.27: Time series of the percentage difference of the MIPAS OFL monthly mean CH_4 from the IG2 climatological dataset. Difference shown is ([MIPAS-IG2]/IG2).

4.5.4 Seasonal cycles: CH_4

Figure 4.28 shows time series of the percentage variation of the monthly mean OFL CH_4 profiles from the 2003 annual mean, while Figure 4.29 shows the equivalent time series for the IG2 climatology. Seasonal variations in the MIPAS OFL data and the climatology are qualitatively similar, but are stronger in the MIPAS OFL data, as might be expected. The MIPAS variations from the 2003 annual mean also exhibit more structure than the variations in the climatology. It is likely that this is due to a degree of dynamical variability in the real atmosphere that is not represented in the climatological trace gas profiles.

4.5.5 Equivalent water

The quantity H_2O+2CH_4 (often referred to as "equivalent water" (McCarthy et al., 2003b) is expected to be a conserved quantity in the lower stratosphere (§ 1.1) except where water is lost, for example due to ice formation and gravitational settling in the winter vortices. Conservation of equivalent water is not expected to hold in the tropics either, due to the seasonal cycle of the entry of water vapour into the stratosphere there. In mid–latitudes, the constancy of equivalent water is only expected to hold up to around 30–35 km (about 7–10 mbar). The equivalent water is expected to show a broad maximum in the mid–stratosphere and decrease at higher altitudes (Abbas et al., 1996).

The exact number of H_2O molecules produced for each CH_4 molecule destroyed varies somewhat with latitude and altitude, depending on the production of H_2O/H_2 from the oxidation of formaldehyde (§ 1.4.1). The number is expected to be around 2.0, but may lie between about 1.6 and 2.0 (Le Texier et al., 1988).

Figure 4.30 shows time series of monthly mean profiles of equivalent water from the MIPAS OFL data, while Figure 4.31 shows the corresponding profiles from the IG2 climatological dataset.

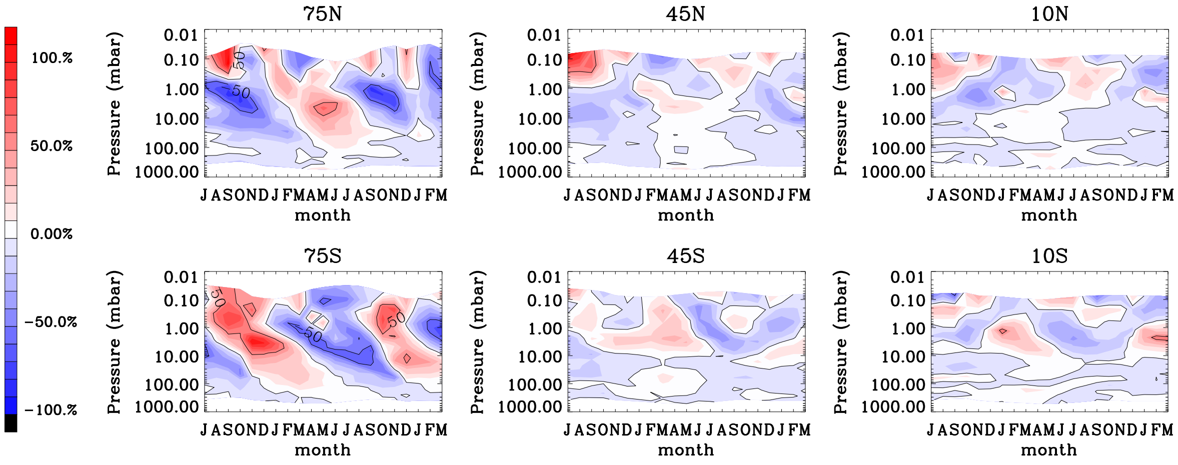

Figure 4.28: Time series of the percentage difference of the MIPAS OFL monthly mean CH_4 from the 2003 annual average.

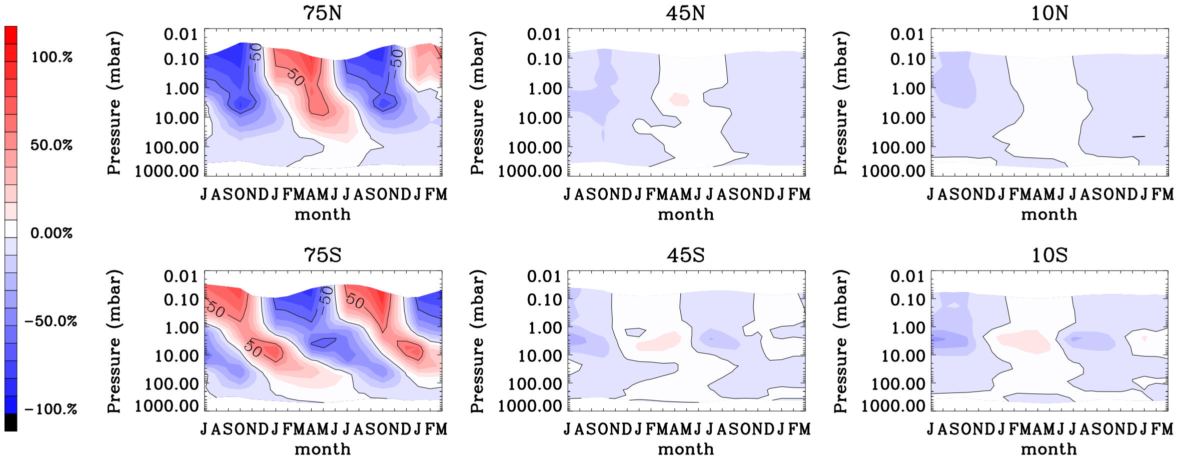

Figure 4.29: Time series of the percentage difference of IG2 climatological CH_4 (interpolated in time) from an annual average.

Figure 4.30 does show profiles of H_2O+2CH_4 which are approximately constant with altitude in the lower stratosphere at mid–latitudes, with a broad maximum in the mid–stratosphere and a decrease at higher altitudes. There are distinct seasonal variations in the equivalent water in the region of 1 mbar, the location of the broad maximum. The temporal location of the maximum in this altitude region appears to be displaced by six months between the two hemispheres, which is an encouraging sign that the retrievals are capturing some kind of real atmospheric variation.

However, the IG2 climatological equivalent water does not appear to show a broad maximum above 35 km and shows far less variation in altitude than the MIPAS OFL equivalent water.

Since total hydrogen (H_2+H_2O+$2CH_4$) is a conserved quantity, equivalent water can be used to infer the mixing ratio of H_2. This has been done before using measurements from HALOE (Harries et al., 1996b) and the space shuttle borne ATMOS instrument (Abbas et al., 1996). Some assumptions are necessary in order to infer H_2 fields from equivalent water. Firstly, it must be assumed that the mixing ratio of H_2 in the lower stratosphere is constant. The limited amount of observational evidence available (McCarthy et al., 2003a; Enhalt, 1980; Schmidt, 1974; Fabian, 1979) suggests that this is so. Previous works (Abbas et al., 1996; Harries et al., 1996b) have assumed a lower stratospheric H_2 mixing ratio of 0.5 ppmv. The second assumption necessary is that the total hydrogen is indeed conserved at all altitudes and that H_2O, CH_4 and H_2 are the only members of the hydrogen family that are present in sufficient quantities to be taken into account.

Making these assumptions, it would be possible to infer H_2 fields from the MIPAS equivalent water. The seasonal variations in the MIPAS equivalent water around 1 mbar could therefore be assumed to be indicative of seasonal changes in H_2. It is clear by looking at Figure 4.30 that the MIPAS equivalent water is not absolutely constant in the lower stratosphere. The inferred H_2 would therefore also show some variation, which negates the original assumption to some extent. (Profiles from H_2O+$2CH_4$ from the HALOE instrument (Harries et al., 1996b) show similar variation.) It is not clear whether this variation in the MIPAS equivalent water is due to errors in H_2O and CH_4, or whether it is an indication that there are variations in H_2. Since measurements of H_2 in the stratosphere are sparse, variations are difficult to determine.

A plot of the correlation between H_2O and CH_4 would be expected to show a gradient approximately equal to, or slightly less than, 2.0. Figure 4.33 shows the correlation between H_2O and CH_4 for the MIPAS OFL monthly means, while Figure 4.34 shows the equivalent plot for the IG2 climatology.

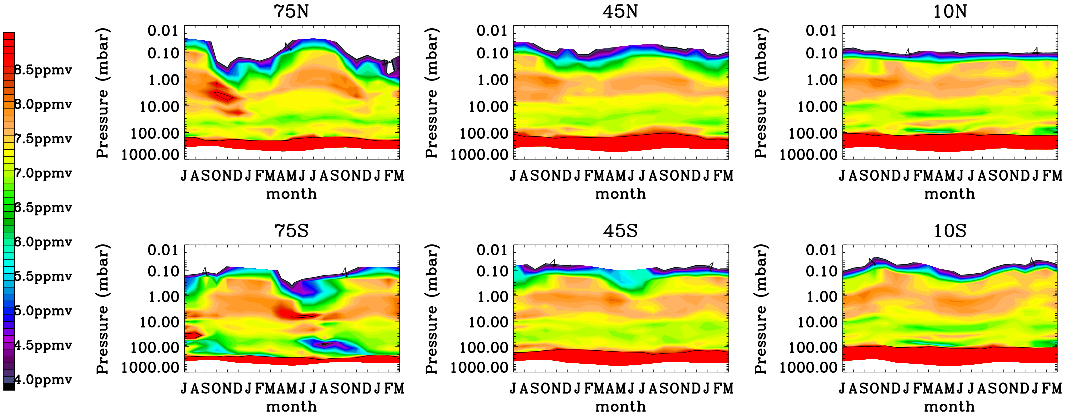

Figure 4.30: Time series of the MIPAS OFL monthly mean profiles of H_2O+2CH_4.

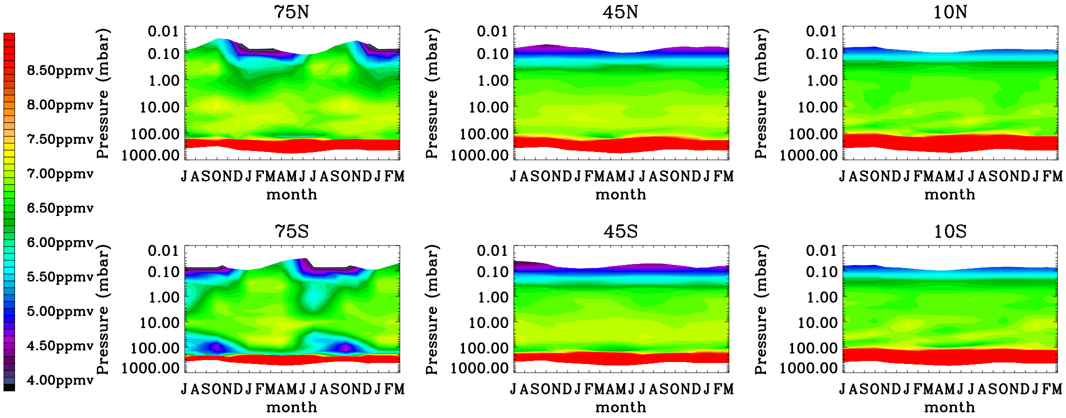

Figure 4.31: Time series of H_2O+2CH_4 (interpolated in time) calculated from the IG2 dataset.

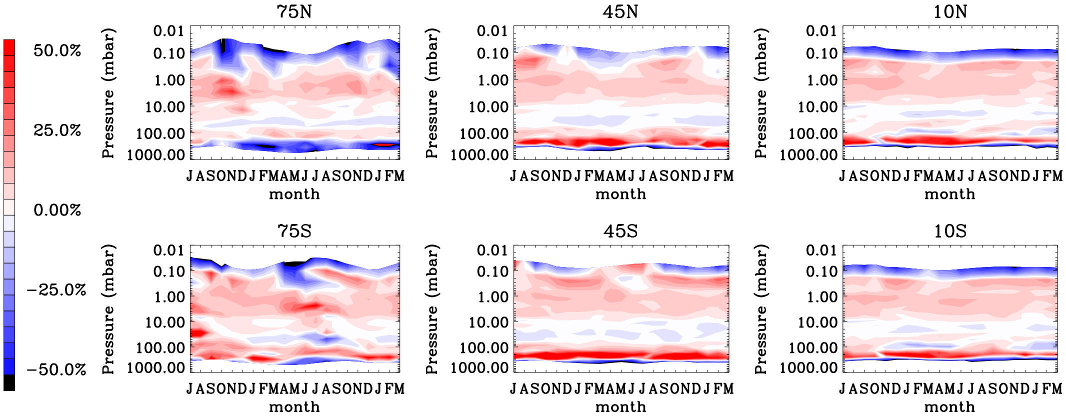

Figure 4.32: Time series of the percentage difference between H_2O+2CH_4 from MIPAS OFL data and from the IG2 dataset. Difference is $100\times[(\text{MIPAS-IG2})/\text{IG2}]$.

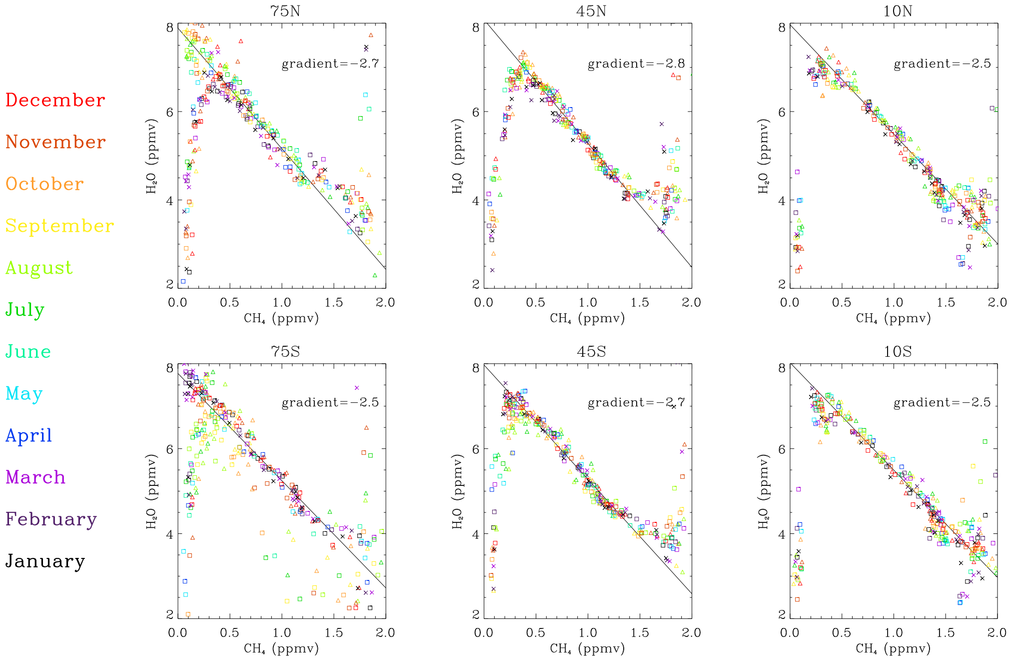

Figure 4.33: Scatter plot of MIPAS OFL monthly mean values of CH_4 against H_2O. Different colours denote different months, while different symbols denote different years. Squares are 2002, triangles are 2003 and crosses are 2004. Straight lines have been fitted to data from 18 to 39 km.

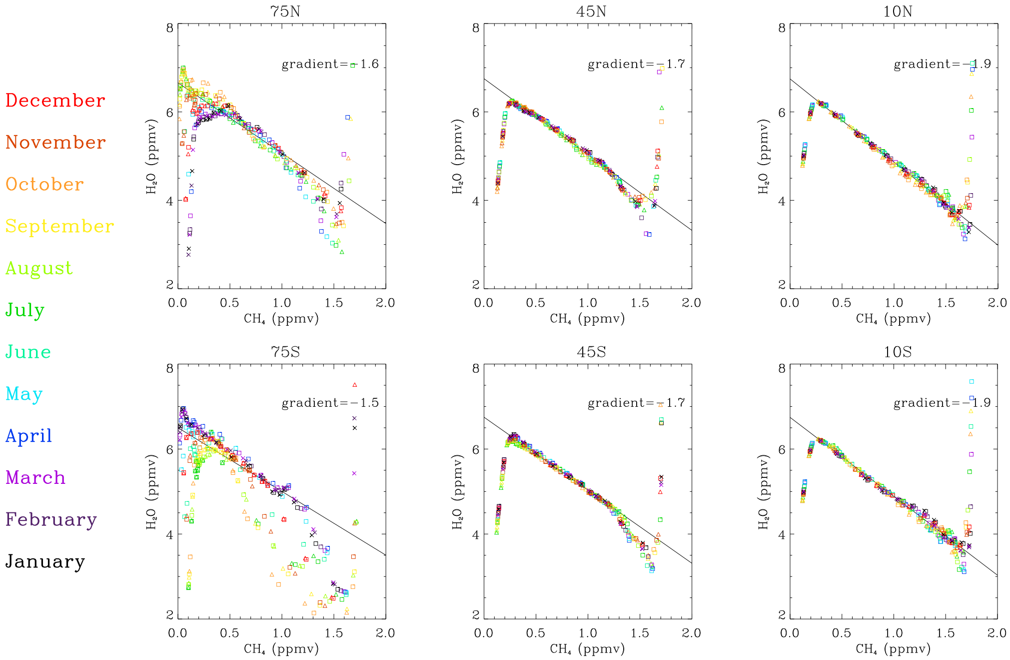

Figure 4.34: Scatter plot of IG2 values of CH_4 against H_2O. Profiles have been interpolated onto MIPAS nominal altitudes. Straight lines have been fitted to data from 18 to 39 km.

In some respects, Figures 4.33 and 4.34 show features which are similar. Both show a reasonably tight correlation between H_2O and CH_4, exhibiting a good fit to a straight line throughout the stratosphere. Low–altitude points (highest methane values) show high H_2O values, which stray from the straight line, while high–altitude points (low methane values) show decreasing H_2O values due to the destruction of water vapour at these altitudes. Similar seasonal behaviour in polar regions at high altitude can be seen in both the MIPAS data and the IG2 data.

However, the gradients of straight lines fitted to stratospheric MIPAS data in the different latitude bands are considerably steeper than the gradients of lines fitted to the IG2 data. Gradients in the IG2 correlations are less than 2.0, while gradients in the MIPAS correlations are greater than 2.0. This is consistent with a high bias in the MIPAS water vapour with respect to the climatology. There are also differences in the behaviour of the gradient at low altitudes. In mid–latitudes and polar regions, the IG2 data exhibit a steeper gradient in the lower stratosphere than in the stratosphere in general, while the MIPAS data show a shallower gradient in the lower stratosphere. This is probably related to the vertical structure of the bias pattern for water vapour.

4.5.6 Summary of comparisons with climatology

Qualitatively, MIPAS monthly mean profiles of H_2O show the same variations in latitude, altitude and time that would be expected from climatology. There are stronger seasonal variations in MIPAS OFL data than in IG2 but this is as it should be.

Quantitatively, there are marked differences between absolute values. There are large discrepancies between water vapour values below the tropopause in the MIPAS monthly means and the climatology. Water vapour shows a low bias of 5–10 % with respect to the climatology below about 10 mbar, and a high bias of around 10 % with respect to climatology between about 10 and 0.2 mbar. The MIPAS OFL water vapour also shows a distinct low bias with respect to climatology at the uppermost retrieval altitude (68 km, or around 0.1 mbar). Profiles of equivalent water (H_2O+2CH_4)

from the MIPAS monthly means show a broad maximum in the mid–stratosphere (in agreement with measurements by Abbas et al. (1996) and model results from Le Texier et al. (1988), although the maximum values from MIPAS are higher than those from Abbas et al. (1996)). Profiles of equivalent water from the IG2 climatology do not show a broad maximum in the mid–stratosphere. At a stretch, this could indicate that the climatology has something of a dry bias in this region. This issue will be explored further in following sections.

MIPAS OFL monthly mean methane values are, in general, 10–20 % higher than those in the IG2 climatology. The differences are too large to be accounted for by the increase in atmospheric methane since the compilation of the climatology in the early 1990s. Neither can the differences be accounted for by day/night differences in the MIPAS methane profiles.

There is a persistent local minimum in CH_4 in the region just above the tropical tropopause, linked with persistent oscillation in this region.

MIPAS methane profiles outwith the tropics are more complicated in shape than the IG2 profiles. It is possible that this is also indicative of a problem. However, it is also possible that this is due to dynamical effects in the atmosphere which are not taken account of in the climatology. It is hoped that further comparisons will resolve this issue.

If the stronger seasonal variations in the MIPAS data are taken into account, bias patterns are largely consistent in time and across different latitudes.

4.6 HALOE comparisons

4.6.1 Introduction to HALOE

The Halogen Occultation Experiment (HALOE) is one of 10 instruments aboard NASA's Upper Atmosphere Research Satellite (UARS), launched on 12th September 1991. Data collection began on 11th October 1991 and continues to the present (HALOE, 2005).

HALOE uses solar occultation to measure vertical profiles of ozone (O_3), hydrogen chloride (HCl), Hydrogen Fluoride (HF), methane (CH_4), water vapour (H_2O), nitric oxide (NO), nitrogen dioxide (NO_2), aerosol extinction, and temperature versus pressure with an instantaneous vertical field of view of 1.6 km.

HALOE views the atmosphere for each spacecraft sunrise and sunset event (nominally 15 per day). The latitude/longitude location of the HALOE data varies with the spacecraft–Earth–Sun position. For a given day, the locations tend to be in two distinct latitude bands and to sweep across the full longitude range. Coverage across the full range of latitudes is achieved on a time period ranging from about two to six weeks depending upon the time of year. The latitudinal coverage varies over the course of the year between 80°S and 80°N, with the maximum northerly and southerly latitudes occurring in spring and autumn in the few weeks either side of the equinoxes. Measurements cover the stratosphere and lower mesosphere.

The instrument uses Gas Filter Correlation Radiometry to make measurements of HCl, HF, CH_4 and NO, and Broadband Filter Radiometry for measurements of O_3, H_2O, NO_2 and the temperature as a function of pressure using a CO_2 channel. Aerosol extinction is also measured in each of the gas filter channels. Further information on these measurement techniques can be found in Russell et al. (1993).

HALOE has now been making measurements for a long time, and the data have been subject to extensive validation. The accuracy of HALOE H_2O is quoted to be within ±10 % over most of the altitude measurement range and within ±30 % at the boundaries (Harries et al., 1996a). Extensive comparisons of HALOE data with other stratospheric water vapour measurements were conducted for the Stratospheric Processes and their Role in Climate (SPARC) water vapour assessment study (WMO, 2000). The SPARC assessment (WMO, 2000) divides the atmosphere into three altitude regions for the purposes of intercomparisons. Below 100 mbar, satellite measurements are deemed to be unreliable. The three regions used are are 100–50 mbar, 50–10 mbar and 10–1 mbar. HALOE H_2O is known to show a dry bias in the lower stratosphere (50–100 mbar) of around 5–20 % compared to available aircraft or balloon measurements. In this assessment, HALOE also showed a dry bias of around 5–10 % in the 10–50 mbar and 1–10 mbar regions. However, HALOE displayed a slight wet bias with respect to MLS in all three regions. Validation of HALOE CH_4 by means of comparisons with correlative measurements and internal consistency tests (Park et al., 1996) indicate that for the 0.3–50 mbar region, the total error, including systematic and random components, is less than 15 % and that the precision is better than 7 %.

4.6.2 Calculation of HALOE monthly means

The HALOE data used in these comparisons are version 19 Level 3 data. Documentation on the Level 3 data can be found on the websites of HALOE (HALOE, 2005) and the BADC (BADC, 2003). In the Level 3 data, the profiles have already been interpolated onto the UARS standard pressure grid of six levels per decade, i.e. 100, 68, 46, 33, 22, 15, 10 .... etc.

The data span an approximate altitude range of 10–65 km, with vertical spacing between levels of approximately 2.5 km. The documentation indicates that the HALOE data at the bottom of the altitude range may be somewhat unreliable. For this reason, these comparisons between MIPAS and HALOE will focus on the region above the 100 mbar surface.

MIPAS provides continuous global coverage both day and night and measures approximately

$14 \times 75 = 1050$ profiles per day. In contrast, HALOE only makes measurements at sunrise and sunset and measures approximately 30 profiles per day. While MIPAS provides extensive and reasonably uniform latitudinal coverage in the course of a month, the latitudinal coverage provided by HALOE varies considerably from one month to the next. The variation in HALOE coverage is demonstrated in Figures 4.35, 4.36 and 4.37. Due to this variation in HALOE latitudinal coverage from one month to the next, six latitude bands (as used in the MIPAS comparisons with climatology in § 4.5) were not sufficient for a meaningful comparison of MIPAS with HALOE data. Narrower bands, 10 degrees in width, were used for the comparison here.

All available HALOE Level 3 data for the time period from July 2002 until March 2004 were downloaded from the HALOE website (HALOE, 2005). Monthly means were calculated from HALOE data on the UARS standard pressure grid and then interpolated onto the MIPAS monthly mean pressure levels for the purposes of comparison. There are disadvantages in this methodology, in that the HALOE profiles have twice undergone interpolation. However, the Level 3 data offered advantages in ease of use and it is assumed that the Level 3 should be sufficient to gain an overview of general biases between HALOE and MIPAS for the purposes of this large–scale comparison.

4.6.3 Comparison of HALOE and MIPAS results: H_2O

Figure 4.38 shows a time series of the differences between MIPAS and HALOE data in each of the 10 degree latitude bands. This figure further illustrates the issue of the difference in coverage between MIPAS and HALOE. All the gaps are due to there being no HALOE profiles for certain latitude bands for certain months. Figure 4.38 does, however, show patterns in the differences which persist over time.

Seasonal means were calculated in order to obtain a more complete picture of the variation of MIPAS/HALOE differences with latitude. Figures 4.39 and 4.40 show seasonal zonal mean distributions of H_2O from MIPAS and HALOE respectively, while Figure 4.41 shows the latitudinal variation of the difference. Figures 4.39 and 4.40 show spatial structures which are qualitatively similar. However, Figure 4.41 shows clear quantitative differences.

MIPAS/HALOE biases are reasonably consistent across latitudes and with varying seasons. MIPAS H_2O is generally within ±5 % of HALOE between 100 and 10 mbar. Between 10 and 0.2 mbar, MIPAS H_2O is of the order of 10 % higher than HALOE. At the uppermost MIPAS retrieval altitude, MIPAS shows a large low bias with respect to HALOE. The pattern of differences between MIPAS and HALOE H_2O is similar to the pattern of differences between MIPAS and the IG2 climatology, but the magnitude of the differences between MIPAS and HALOE is smaller.

Figure 4.42 shows differences with standard deviations for the MIPAS and HALOE seasonal means for a northern mid–latitude band. This figure is shown in order to compare the magnitude of the differences with the magnitude of standard deviations in the MIPAS and HALOE zonal means. The standard deviations in the MIPAS and HALOE seasonal means are reasonably similar throughout the stratosphere.

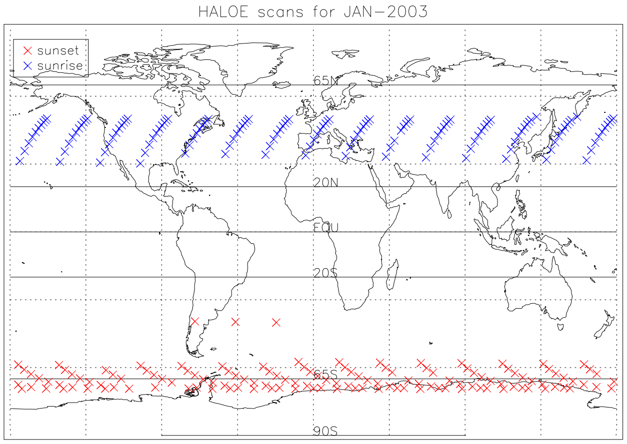

Figure 4.35: HALOE coverage for January 2003

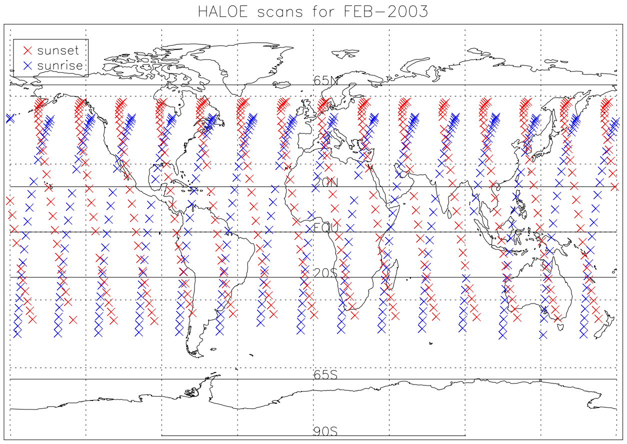

Figure 4.36: HALOE coverage for February 2003

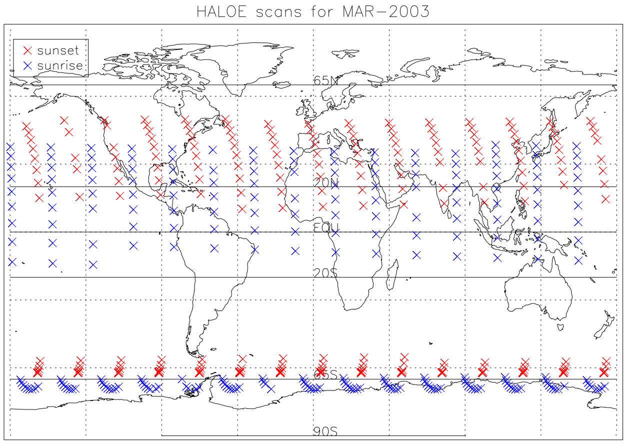

Figure 4.37: HALOE coverage for March 2003

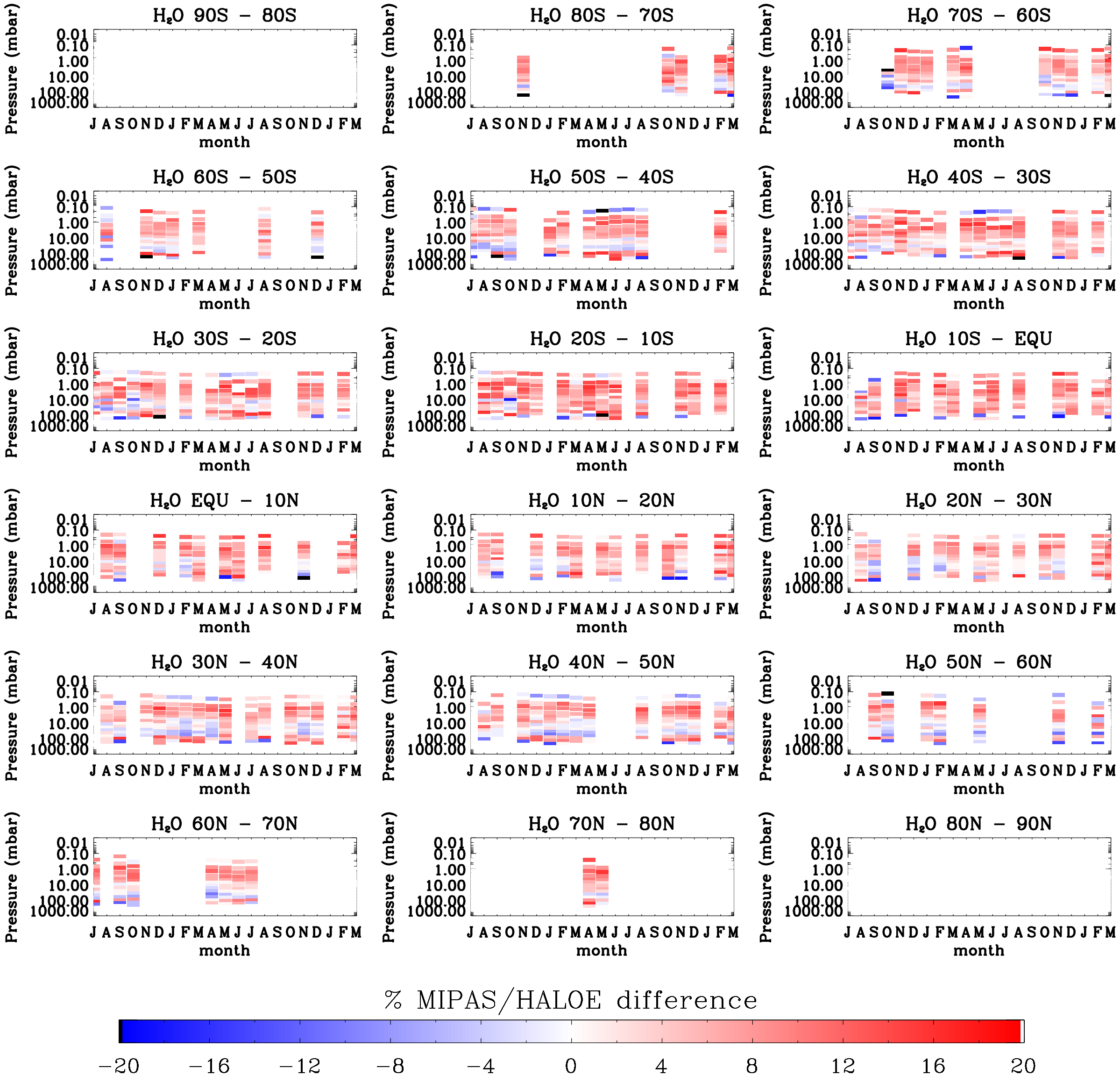

Figure 4.38: Time series of differences between MIPAS and HALOE monthly mean profiles of H_2O ([MIPAS-HALOE]/HALOE) for 10 degree latitude bands.

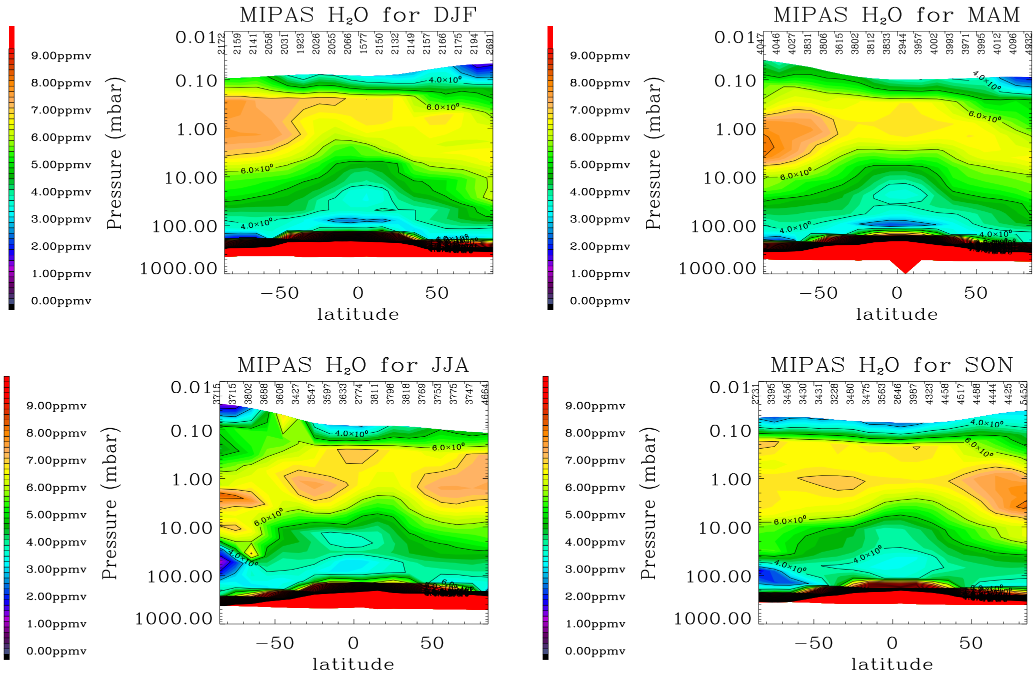

Figure 4.39: Latitudinal distribution of MIPAS H_2O for different seasons. Top left shows December–February, top right shows March–May, bottom left shows June–August and bottom right shows September–November. Numbers along the top edges show the number of MIPAS profiles in each latitude band.

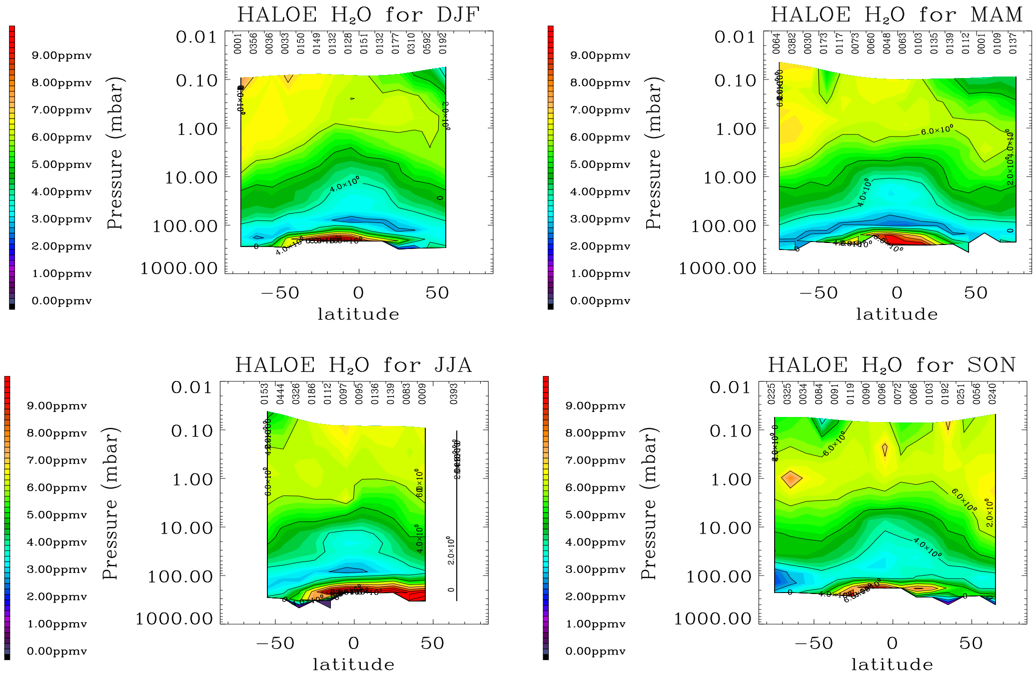

Figure 4.40: As above, but for HALOE.

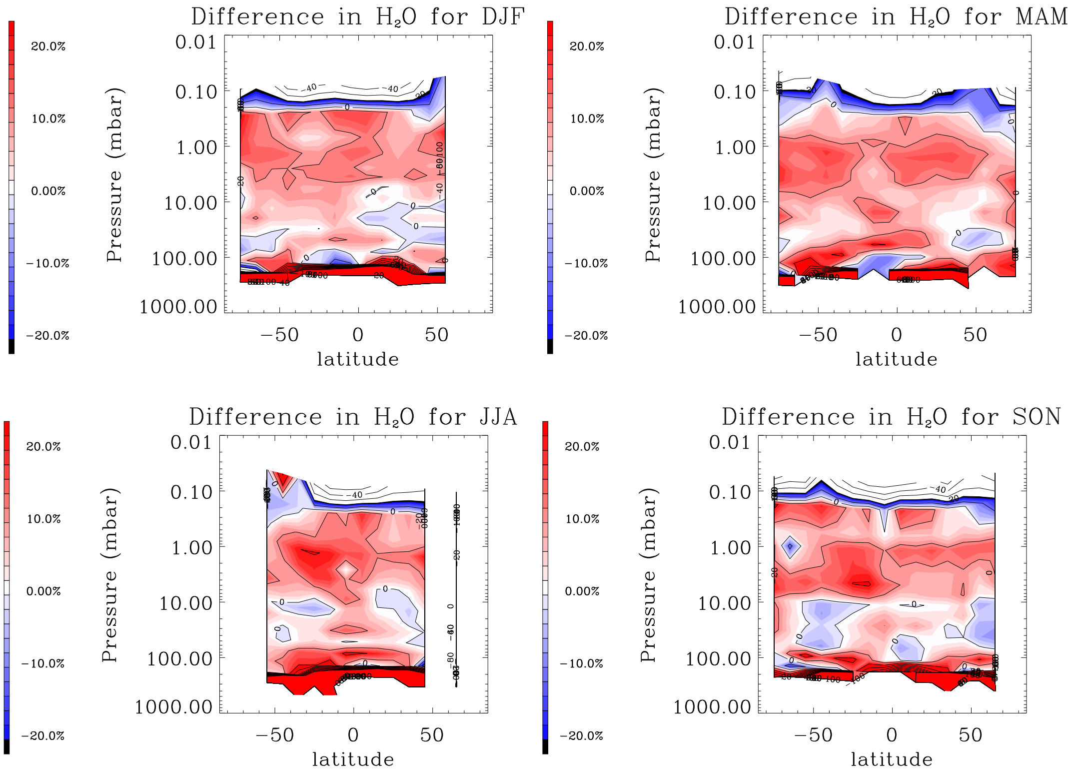

Figure 4.41: Latitudinal distribution of differences between MIPAS and HALOE H_2O ([MIPAS-HALOE]/HALOE) for different seasons. Top left plot shows difference between means for December–February, top right shows March–May, bottom left shows June–August and bottom right shows September–November. The row of numbers along the top edges of these plots show the number of MIPAS profiles in each latitude band, while the row of numbers along the bottom edges of the plots show the number of HALOE profiles in each latitude band.

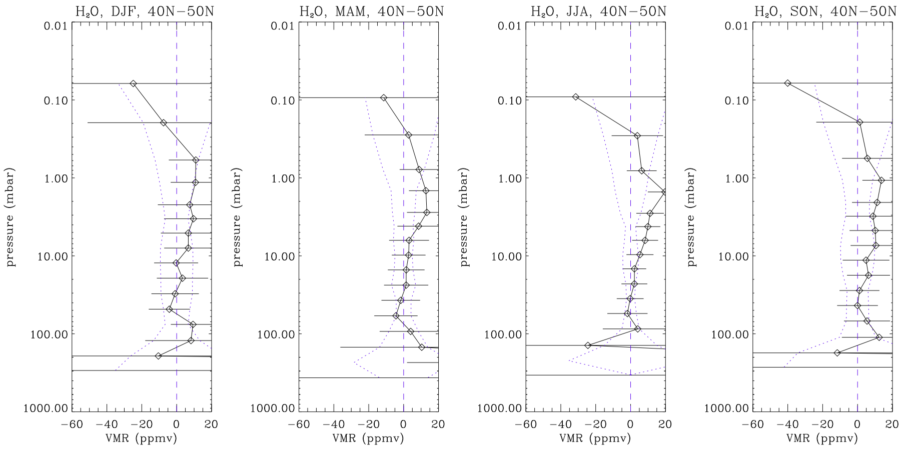

Figure 4.42: Percentage differences of MIPAS H_2O seasonal means from HALOE for the latitude band centred on 45N. Horizontal lines show standard deviation on the MIPAS seasonal means, while blue dotted lines show standard deviation on the HALOE seasonal means.

4.6.4 Comparison of HALOE and MIPAS results: CH_4

Figure 4.43 shows a time series of differences between MIPAS and HALOE monthly means of CH_4. Figures 4.44 and 4.45 show seasonal zonal mean CH_4 distributions from MIPAS and HALOE respectively, while Figure 4.46 shows the latitudinal variation of the differences between these seasonal means.

Figure 4.47 shows profiles of differences between seasonal means for a selected northern hemisphere mid–latitude band, with standard deviations on the MIPAS and HALOE means, in order to give an indication of the magnitude of the differences compared to the standard deviations.

Unlike H_2O, the MIPAS CH_4 does not show persistent biases with respect to HALOE across different latitudes and seasons. There are regions where MIPAS is low with respect to HALOE and regions where MIPAS is biased high with respect to HALOE. Broadly speaking, however, MIPAS CH_4 is higher than HALOE CH_4 over most of the MIPAS retrieval range. Like H_2O, MIPAS CH_4 shows a low bias with respect to HALOE at the uppermost MIPAS retrieval altitude. The persistent oscillation in the MIPAS CH_4 in equatorial regions (discussed in previous sections) is also evident in the MIPAS/HALOE differences.

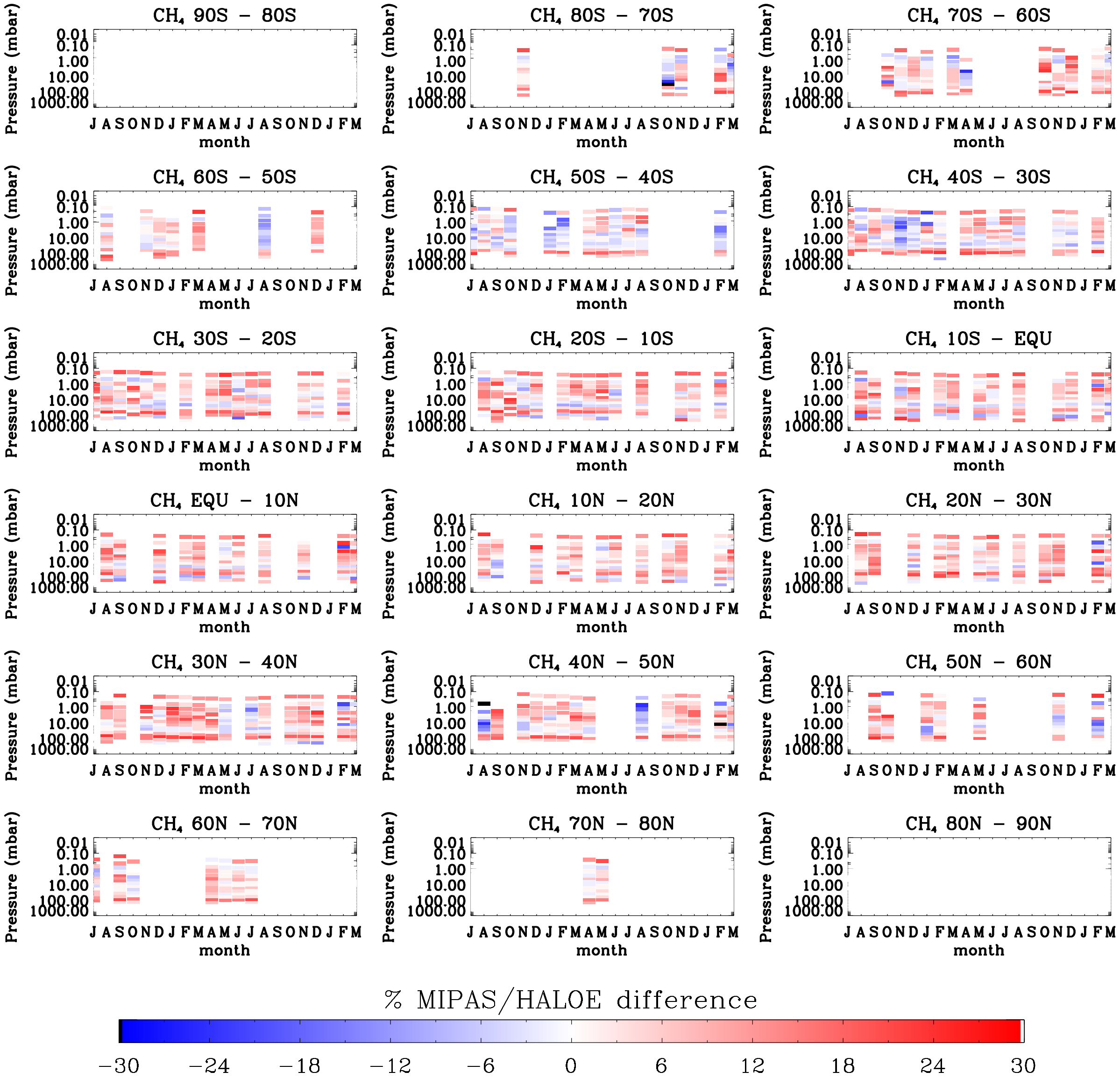

Figure 4.43: Time series of differences between MIPAS and HALOE monthly mean profiles of CH_4 ([MIPAS-HALOE]/HALOE) for 10 degree latitude bands.

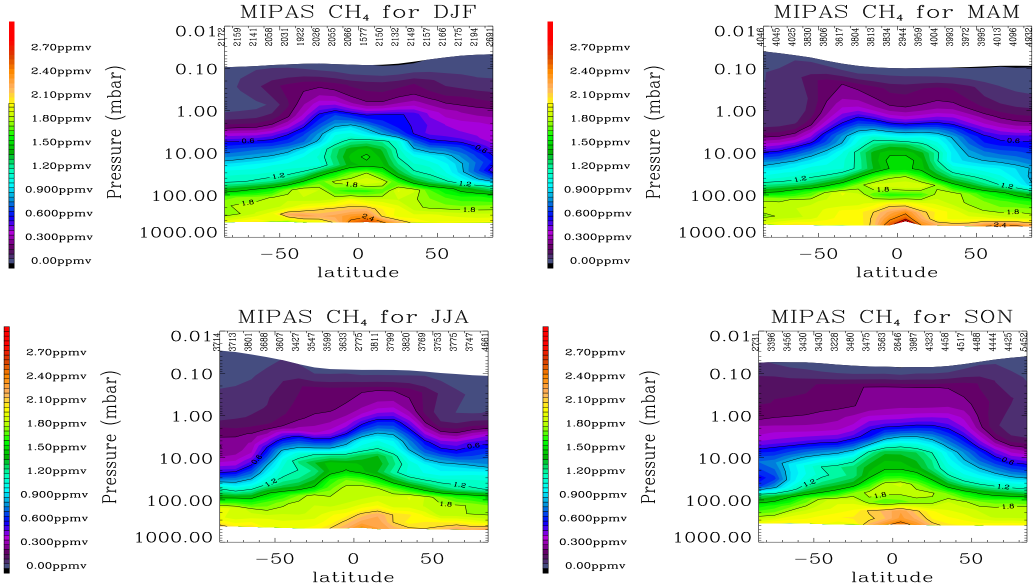

Figure 4.44: Latitudinal distribution of MIPAS CH_4 for different seasons. Top left shows December–February, top right shows March–May, bottom left shows June–August and bottom right shows September–November. Numbers along the top edges show the number of profiles in each latitude band.

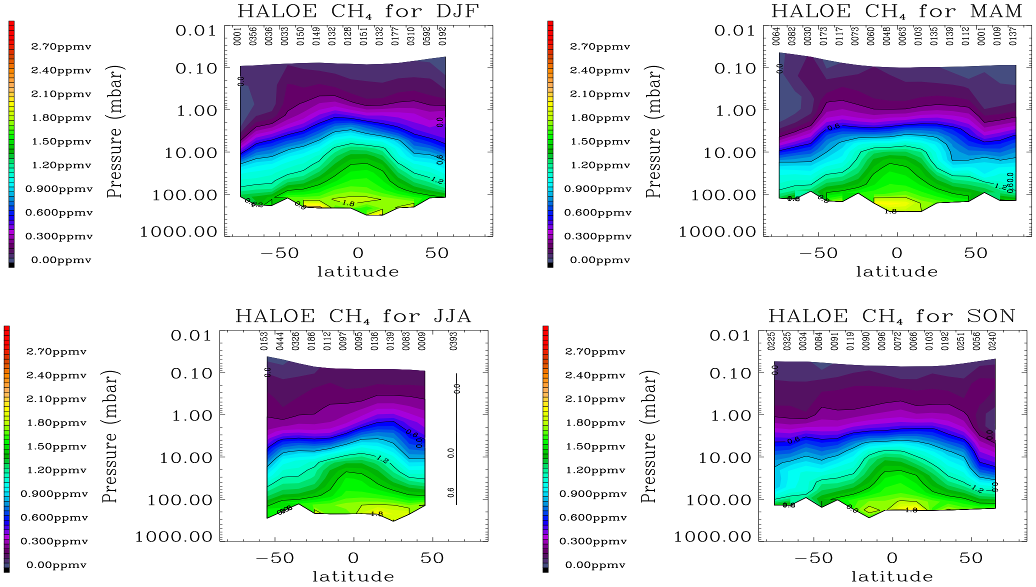

Figure 4.45: As above but for HALOE.

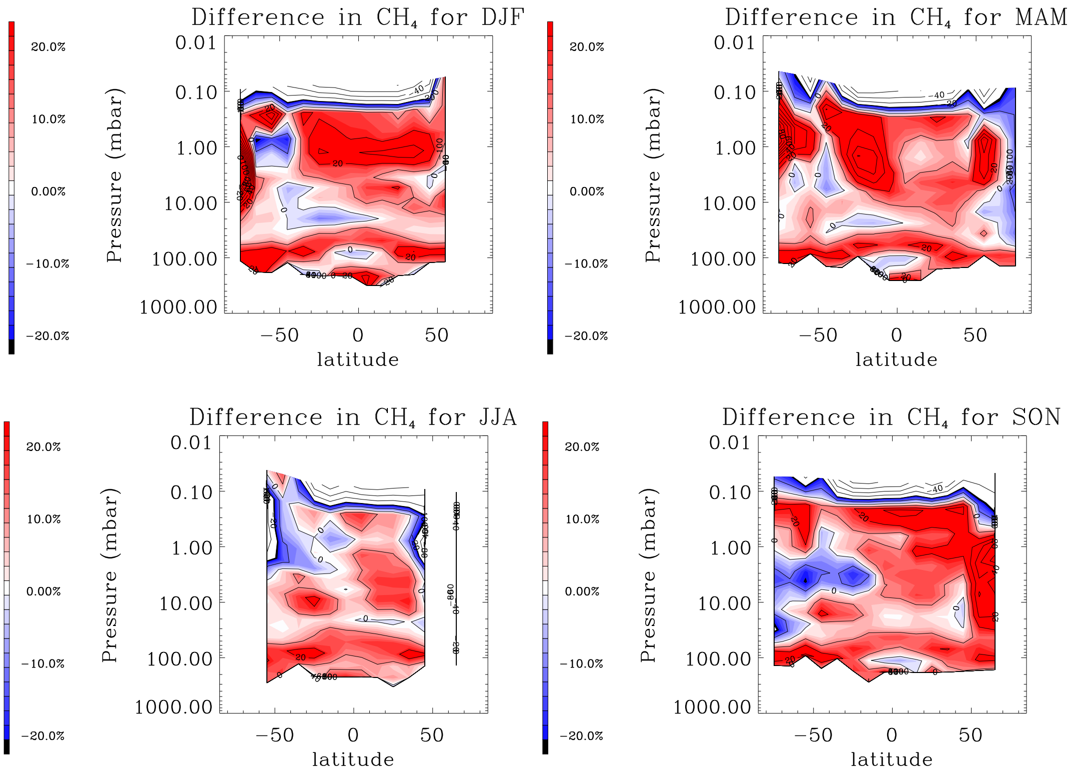

Figure 4.46: Latitudinal distribution of differences between MIPAS and HALOE CH$_4$ ([MIPAS-HALOE]/HALOE) for different seasons. Top left plot shows difference between means for December–February, top right shows March–May, bottom left shows June–August and bottom right shows September–November. The row of numbers along the top edges of these plots show the number of MIPAS profiles in each latitude band, while the row of numbers along the bottom edges of the plots show the number of HALOE profiles in each latitude band.

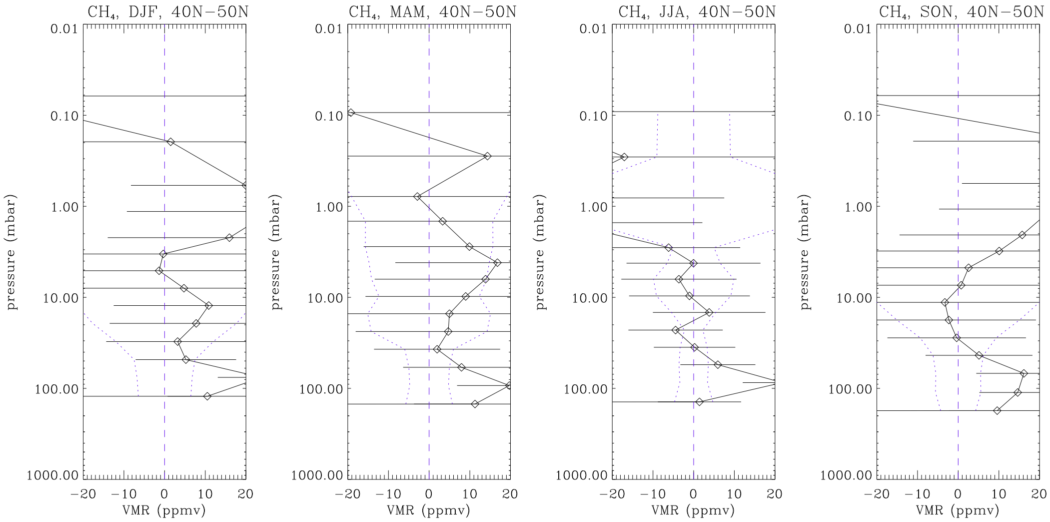

Figure 4.47: Percentage differences of MIPAS CH_4 seasonal means from HALOE for the latitude band centred on 45N. Horizontal lines show standard deviation on the MIPAS seasonal means, while blue dotted lines show standard deviation on the HALOE seasonal means.

4.6.5 Equivalent water

Figures 4.48 and 4.49 show seasonal zonal means of equivalent water vapour from MIPAS and HALOE data respectively, while Figure 4.50 shows seasonal zonal mean profiles of equivalent water from MIPAS and HALOE from a northern mid–latitude band. HALOE profiles of equivalent water do not appear to show the broad maximum in the mid–stratosphere observed in ATMOS data (Abbas et al., 1996) and expected from models (Le Texier et al., 1988). It is clear that the MIPAS equivalent water shows larger variation from a constant value than the HALOE equivalent water does.

4.6.6 Summary: HALOE comparisons

In general, MIPAS OFL H_2O agrees well with HALOE between 100 and 10 mbar, where differences are less than 5 %. Between 10 and 0.2 mbar, MIPAS OFL H_2O values are around 10 % higher than HALOE values. This is consistent with the dry bias in HALOE H_2O reported in WMO (2000). At the uppermost MIPAS retrieval level, MIPAS H_2O values are consistently considerably lower than HALOE values.

In general, MIPAS OFL CH_4 shows a high bias with respect to HALOE of around 10 % throughout the MIPAS retrieval range. However, the bias pattern varies somewhat with latitude and with time. The reason for this is not known.

Profiles of equivalent water (H_2O+2CH_4) from HALOE do not appear to show the broad maximum in the mid–stratosphere shown by MIPAS data, ATMOS data (Abbas et al., 1996) and predicted by models (Le Texier et al., 1988).

HALOE/MIPAS comparisons have also been performed by Bracher et al. (2004), using colocations. The locations of the profiles in this study were strongly biased towards northern latitudes. Comparisons between MIPAS and HALOE have also been performed by Juckes (2004), using a data

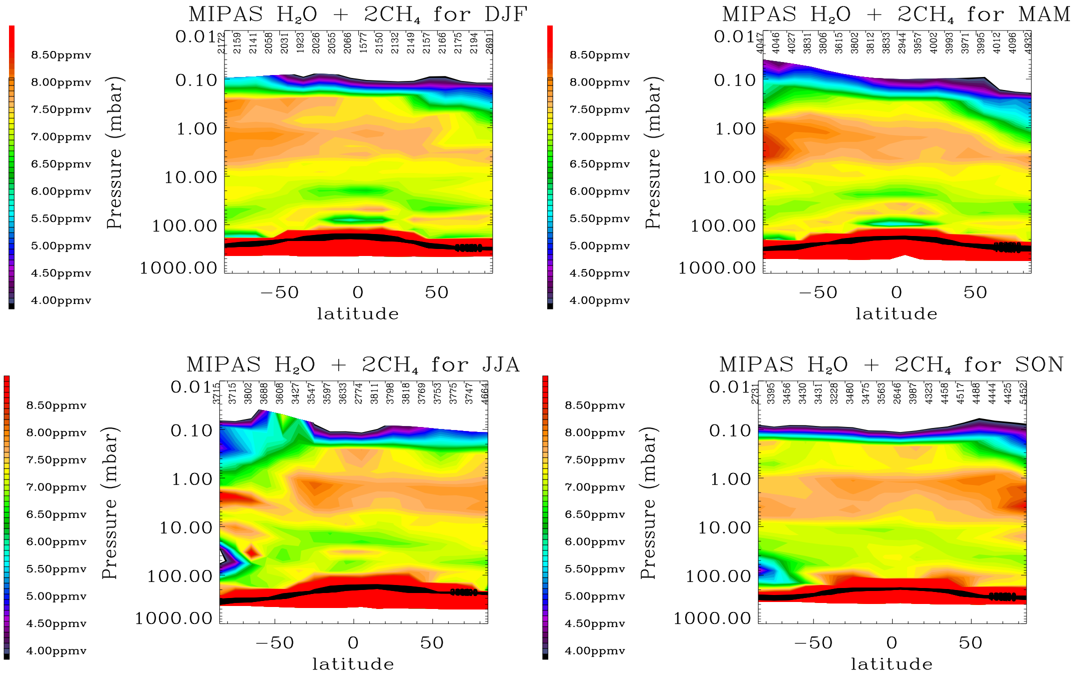

Figure 4.48: Latitudinal distribution of MIPAS H_2O + $2CH_4$ for different seasons. Top left plot shows December–February, top right shows March–May, bottom left shows June–August and bottom right shows September–November.

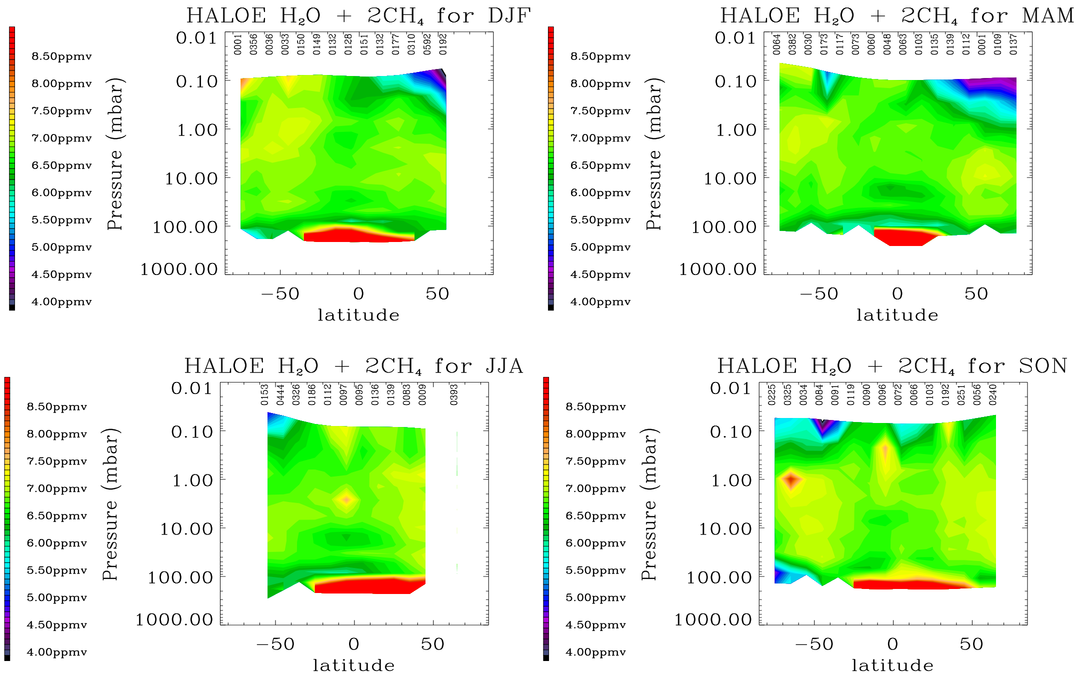

Figure 4.49: As above but for HALOE.

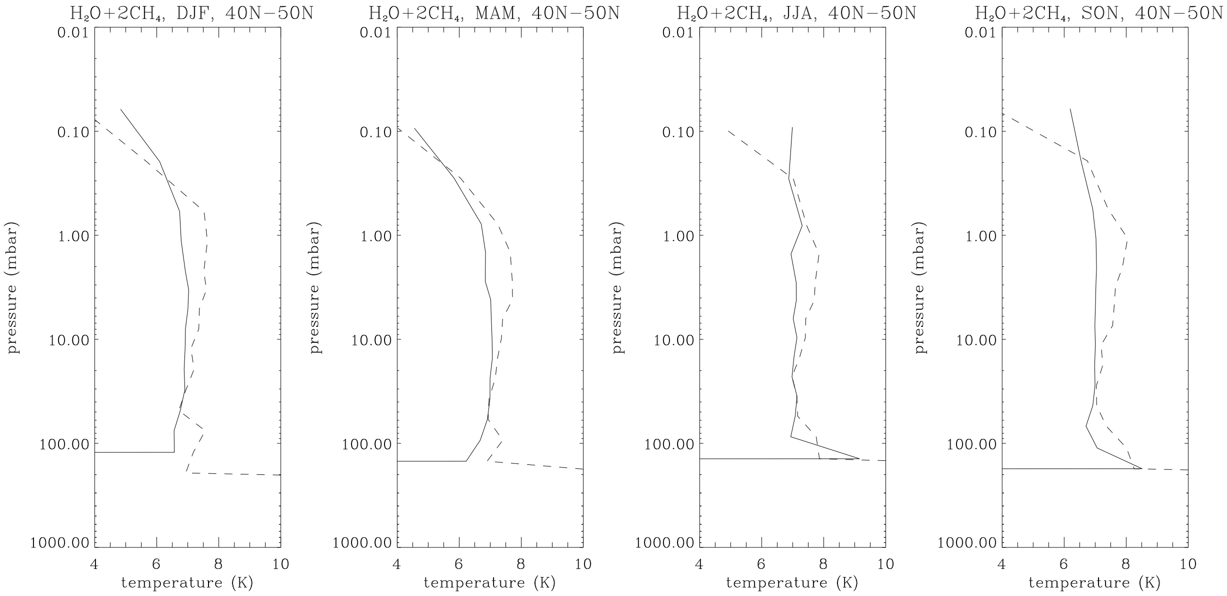

Figure 4.50: Profiles of H_2O+2CH_4 from MIPAS (dotted lines) and HALOE (solid lines) for the latitude band centred on 45N.

assimilation technique (and covering all latitudes). The magnitudes of biases in MIPAS H_2O and CH_4 compared to HALOE reported in both studies are similar to those reported here.

4.7 ACE comparisons

The Atmospheric Chemistry Experiment (ACE, also called SCISAT–1) was launched in August 2003. Vertical profiles of 18 gases (including both water vapour and methane) and temperature are now available in the version 1.0 data release. Since the release of data from ACE is relatively recent, there has not been time to perform comparisons with MIPAS in the same way as the comparisons with HALOE and with the Odin–SMR. However, it was considered important to include some reference to the ACE data here, since it is the only satellite instrument other than HALOE that can provide at least some simultaneous measurements of water vapour and methane in a time period which overlaps with the MIPAS high spectral resolution measurements.

ACE, like HALOE, is a solar occultation instrument. It tracks the sun during sunrise and sunset from a 74°, 650 km near circular orbit, producing a coverage pattern similar in most respects to HALOE (Bernath et al., 2005). The primary instrument on ACE is a Fourier Transform Spectrometer (FTS), covering 750 to 4400 cm^{-1} with 0.2 cm^{-1} resolution. The instrument has a 1.25 mrad circular FOV which corresponds to around 4 km at the tangent point. The spectrum acquisition time of 2 seconds translates to a tangent point altitude spacing of 3–5 km.

The ACE retrieval method is described in Boone et al. (2005). The earliest retrievals are from January 2004, although many of the early spectra were plagued by ice build–up on the detectors, reducing sensitivity. ACE therefore does not provide a long overlap with the MIPAS high spectral resolution dataset. In addition, because of problems with the version 1.0 retrieval software, only sunset events have been processed. No direct MIPAS/ACE comparisons have yet been made here. Instead, results of an ACE/HALOE comparison are quoted from McHugh et al. (2005). Figures 4.51 and 4.52 show the relevant plots from this paper.

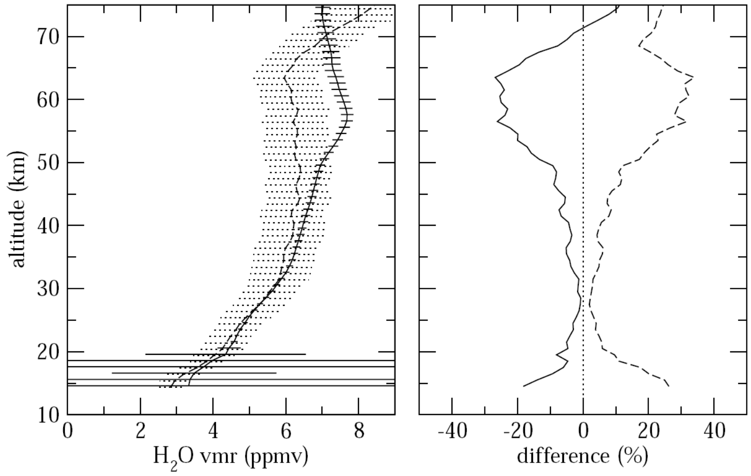

Figure 4.51: Left panel shows mean ACE (solid) and HALOE (dashed) H_2O retrievals from McHugh et al. (2005). Horizontal bars indicate the average single–profile uncertainty. Right panel shows the mean difference (solid) and the RMS difference (dashed). Relative differences are 100 %×(HALOE-ACE)/HALOE.

ACE CH_4 shows a bias relative to HALOE of similar magnitude to the bias shown by MIPAS CH_4

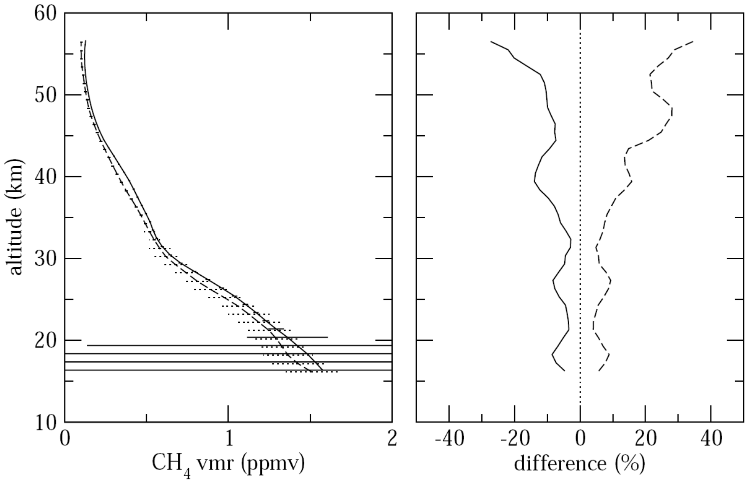

Figure 4.52: Left panel shows mean ACE (solid) and HALOE (dashed) CH_4 retrievals from McHugh et al. (2005). Horizontal bars indicate the average single–profile uncertainty. Right panel shows the mean difference (solid) and the RMS difference (dashed). Relative differences are 100 %×(HALOE-ACE)/HALOE.

relative to HALOE, while ACE H_2O, like MIPAS, shows a high bias with respect to HALOE which is small at 30 km and increases from thereon upwards. MIPAS/HALOE differences differ strongly from ACE/HALOE differences above 52 km.

4.8 The Odin Sub–Millimetre Radiometer

4.8.1 Introduction to Odin

The Sub–Millimetre Radiometer (SMR) is currently flying on board the Odin satellite. Odin is a Swedish–led mission in co–operation with Canada, Finland and France, using sub–millimetre spectroscopy for astronomical and atmospheric studies (Murtagh et al., 2002). Odin was launched in February 2001.

As Odin has a joint astronomy and atmospheric mission, the observation time is shared between astronomy and aeronomy modes. The observation time has been equally divided between the disciplines. The atmosphere is observed every third day with an additional day in each third cycle.

The Odin satellite flies in a quasi–polar orbit, at an altitude of 625 km, and takes 96 minutes to complete an orbit. The 96–minute orbit time results in around 15 orbits per day. Limb–sounding in aeronomy mode produces around 60 limb scans per orbit. Odin–SMR measurements are made in the plane of the orbit, covering the latitude range 82°S to 82°N.

On regular observation days, the SMR is operated in the so–called basic stratospheric mode with target gases O_3, ClO, HNO_3 and NO_2. On additional days, the SMR is retuned to make various measurements of water vapour and its isotopes (see § 6.7), odd nitrogen and odd hydrogen species and CO. Odin water vapour is only observed about one day per month.

Although the Odin–SMR only measures water vapour about one day per month, it provides good global coverage (similar to that provided by MIPAS) in the course of a day. For this reason, the MIPAS/Odin–SMR comparisons in this section have been made using zonal means over the course of a day rather than with monthly means.

Level 2 processing schemes have been developed in parallel in Sweden (Stockholm and Chalmers Universities) and in France (Bordeaux). The original idea was that the Swedish code would be the "operational" code (although unlike MIPAS, near–real–time processing is not currently possible) and the French code would be the "scientific" code. The Odin retrieval results presented here were produced using the Bordeaux CTSO-v223 algorithm. It should be pointed out that these results are preliminary, and yet to be validated extensively.

4.8.2 Comparison of Odin and MIPAS results

The first Odin–SMR water vapour measurements were made on $28^{th}/29^{th}$ July 2002. Since then, Odin has been making water vapour measurements approximately one day per month. However, processing is still in progress. Most of the days which have been processed are in 2002, and many of them unfortunately happen to coincide with days where MIPAS coverage is not available or not very extensive. The coverage of the MIPAS data improves significantly into 2003 and beyond.

On the timescale of this thesis project, it has not been possible to compare MIPAS and Odin data in terms of a time series, or even with data from all four seasons of the year. The comparison presented here consists of four days worth of data. An example of where processed Odin–SMR data is available and MIPAS coverage is good is 22^{nd} and 23^{rd} November 2002. The Odin team agreed to prioritise the processing of these days in 2003, in order that the consistency of a MIPAS/Odin–SMR comparison could be verified for the same days the following year.

Odin–SMR retrieves water vapour over an altitude range of approximately 20–70 km, giving a common MIPAS/Odin–SMR altitude range of 20–68 km. The retrieval levels in the Bordeaux CTSO-v223 algorithm are given by the tangent altitudes of the limb scan, with a spacing between levels of around 3 km. The vertical resolution of the Odin–SMR water vapour measurements is also around 3 km (Urban et al., 2004).

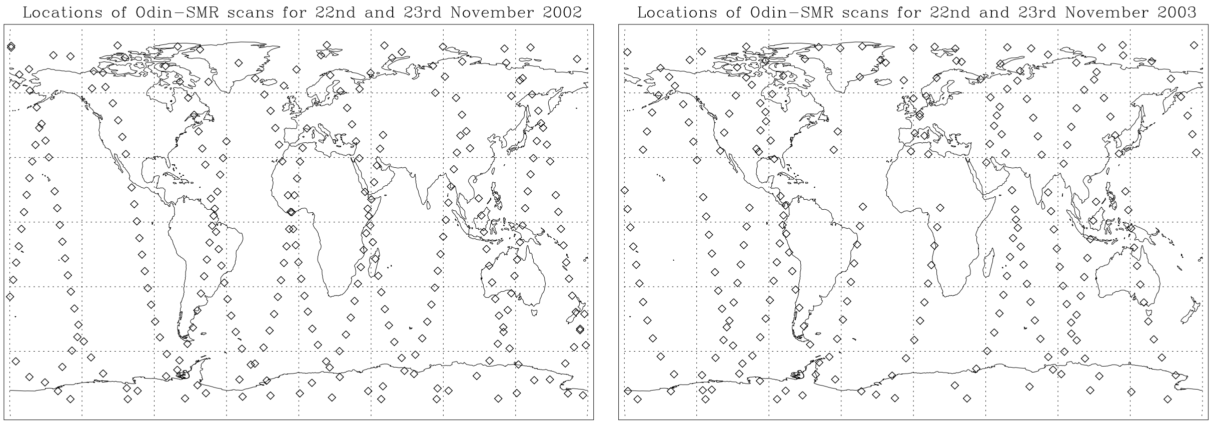

Figure 4.53: Odin–SMR coverage for $22^{nd}/23^{rd}$ November 2002 (left) and 2003 (right).

Figures 4.53 and 4.54 show the locations of the limb scans which have been processed for $22^{nd}/23^{rd}$ November 2002 and 2003 for the Odin–SMR and MIPAS respectively. It would appear from these maps that there are a number of Odin orbits which have not yet been successfully processed for

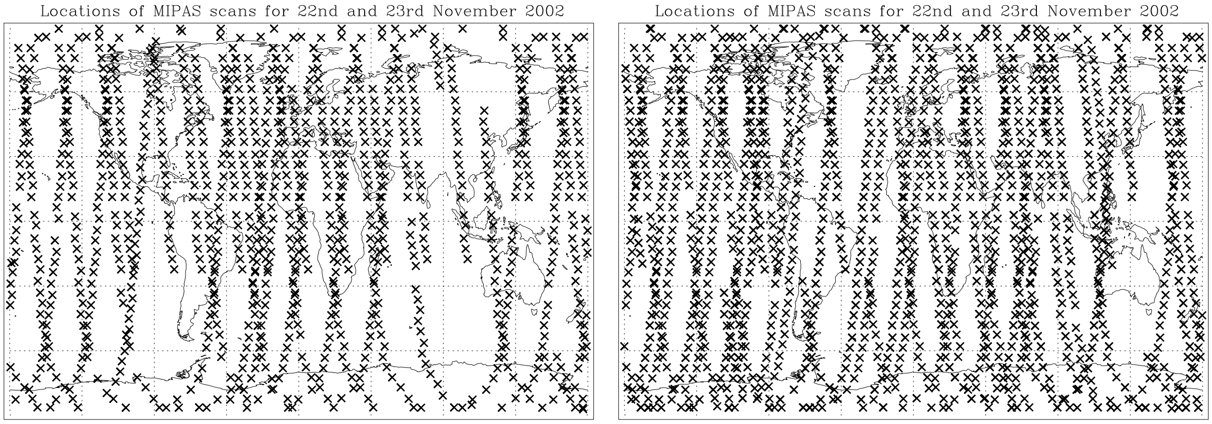

Figure 4.54: MIPAS coverage for $22^{nd}/23^{rd}$ November 2002 (left) and 2003 (right).

these days.

Figures 4.55 and 4.56 show zonal mean H_2O fields from MIPAS and the Odin–SMR for the $22^{nd}/23^{rd}$ November 2002 and 2003, while Figure 4.57 shows the difference between them. Figure 4.58 shows zonal mean profiles for MIPAS and Odin from 22^{nd} and 23^{rd} November 2003 from six of the eighteen 10 degree latitude bands. In addition to the mean profiles, this figure shows the standard deviations on the means, as well as the mean random error on the MIPAS and Odin retrievals. Any difference between the standard deviation and the mean random error represents atmospheric variability within the latitude band.

Qualitatively, the MIPAS and Odin H_2O fields show many of the same features. In general, both sets of data show the variation with altitude that would be expected, and show a degree of consistency from one year to the next.

There are, however, some discrepancies between the water vapour fields from the two instruments. MIPAS OFL data show very large H_2O values at around 5 mbar (about 36 km) in the northern polar region for this day. This feature was also present in the monthly means for both poles in Figure 4.18 and was commented on in § 4.5.2. This feature is not present in the Odin retrievals.

In addition, MIPAS data show a secondary minimum in the northern hemisphere tropics at an altitude of around 10 mbar. This is consistent with the tropical tape recorder effect, but the Odin data show no evidence of a secondary minimum in this location.

MIPAS is generally lower than Odin for the uppermost retrieval altitude of MIPAS. This problem has already been highlighted in the previous comparisons in § 4.5 and § 4.6 and can be attributed to a problem with the MIPAS H_2O.

MIPAS OFL H_2O values are higher than Odin values over the rest of the common altitude range. The magnitude of the MIPAS high bias is around 5 % in the lower stratosphere, reaching a maximum of 25–30 % at around 2 mbar. Although the high bias varies with altitude, the pattern is consistent across all latitude bands and is broadly the same for the 2002 and 2003 days.

Discrepancies in certain features of the zonal mean fields can perhaps be accounted for by the difference in coverage of the two instruments, but the general high bias of MIPAS H_2O with respect to Odin cannot.

4.8.3 Summary: Odin comparisons

In general, MIPAS and Odin appear to capture the same vertical and latitudinal variations in H_2O for the $22^{nd}/23^{rd}$ November 2002 and 2003. However, MIPAS shows a high bias with respect to Odin. The magnitude of the high bias is around 5 % in the lower stratosphere, increasing to around 25 % in the region of 2 mbar. MIPAS shows a low bias with respect to the Odin–SMR at the highest MIPAS retrieval altitude, which is consistent with the low bias of MIPAS previously observed with respect to HALOE and to the IG2 climatology at this altitude. The magnitude of the high bias of MIPAS H_2O with respect to Odin H_2O varies with altitude, but the pattern is consistent across latitude bands and does not change from one year to the next. (MIPAS/HALOE comparisons also showed a bias pattern which was largely constant in time and across latitudes.)

4.9 MLS comparisons

The Microwave Limb Sounder (MLS) (Waters et al., 1999) aboard NASA's Earth Observing System (EOS) Aura spacecraft was launched July 15, 2004. The instrument scans the Earth's limb in the forward direction of flight, viewing microwave emissions at the 118, 190, 240 and 640 GHz, and 2.5 THz spectral regions from the stratosphere into the upper troposphere. These measurements are used to derive vertical profiles of O_3, H_2O, BrO, ClO, HCl, HOCl, OH, HO2, HCN, CO, HNO_3, N_2O, and SO_2 mixing ratios, as well as relative humidity with respect to ice, cloud water/ice content, geopotential height and temperature. The vertical resolution of these data is about 3 km, and the spatial coverage is near-global (-82° to +82° latitude), with each profile spaced 1.5° (about 165 km) along the orbit track (roughly 15 orbits per day).

Although the launch of EOS Aura is relatively recent, the data processing for MLS benefits from experience gained from the previous MLS instrument on UARS.

There is no overlap between EOS MLS data and MIPAS 0.025 cm^{-1} resolution data. However, comparisons between MLS data and MIPAS data from January 2005 appear to show extremely good agreement (*Claire Waymark, private communication*). Since the biases in MIPAS OFL H_2O shown in previous sections appear to be largely consistent over time, it was thought that perhaps comparisons of MIPAS data from January 2003/2004 with MLS data from January 2005 might provide some perspective on the accuracy of the MIPAS H_2O.

Figure 4.59 shows MIPAS monthly mean profiles from January 2003/2004 alongside MLS zonal means from 28^{th} January 2005 as well as differences between them. It would seem that the agreement between MIPAS and MLS is better than the agreement between MIPAS and HALOE or Odin.

4.10 Day/night differences

Neither water vapour or methane are expected to show significant diurnal variations in the stratosphere. Consistent differences between day and night would therefore either reveal something new about the atmosphere, or more likely indicate some kind of systematic error. In order to determine whether there were consistent day/night differences in the MIPAS OFL retrievals, profiles were separated into day–time and night–time on the basis of solar zenith angle and monthly means calculated for each case.

4.10.1 Differences

Figures 4.60 and 4.61 show percentage differences between day–time and night–time monthly mean profiles from July 2002 until March 2004 for water vapour and methane respectively for the six different latitude bands. It is clear from these figures that there are persistent day/night differences.

Possible causes for day/night differences in the MIPAS OFL H_2O and CH_4 are listed below:

- A difference in latitudinal coverage between day and night.
- A systematic difference in instrument pointing between day and night. There is no obvious reason why this should be the case.
- A systematic error in the temperature retrieval, which then propagates through to the water vapour and methane retrievals. If some systematic temperature error were to result in a high bias in the temperature retrieval in the day–time, one might expect a low bias in the water vapour/methane retrievals in the day–time.
- Non–LTE effects in the water vapour/methane lines.
- Contamination of the spectral signature of the target species from a diurnally varying species, such as NO_2 or N_2O_5.

- Real diurnal variation in the atmosphere. Diurnal variation is expected in temperature, but not in water vapour or methane.

The possible causes listed above are discussed further in the sections which follow.

It was thought that the correlations between the day/night differences in H_2O with those in CH_4 might help to shed some light on possible causes. A quick visual inspection of Figures 4.60 and 4.61 would appear to indicate that certain features in particular months and at particular altitudes show correlations while others do not. Figure 4.62 shows scatter plots of the day/night differences in water vapour and methane. There are no clear correlations in the differences at high latitudes, but mid–latitudes and equatorial regions show some grouping of points from different altitudes.

4.10.2 Ascending/descending nodes

In equatorial regions, the distinction between day–time and night–time profiles is also a distinction between ascending and descending nodes of the orbit. Envisat is in a sun–synchronous orbit and always crosses the equator at 10.00 am local time in the southward (descending) direction. Equatorial day–time profiles therefore always correspond to the descending node of the satellite. The same should also apply to mid–latitude regions, but the distinction is not so clear in polar regions.

Figures 4.63 and 4.64 show differences between monthly means for ascending and descending nodes. It can be seen that these figures are effectively the same as the day/night differences in Figures 4.60 and 4.61, apart from in polar regions, where there are slight differences.

MIPAS scans through tangent altitudes starting at the uppermost altitude. This means that for limb scans where the satellite is in the ascending node, the high altitude tangent points are slightly further south than the low altitude tangent points. For limb scans in the descending node, high altitude tangent points are slightly further north than low altitude tangent points. This is illustrated in Figure 4.65. Given that there are expected to be some meridional gradients in VMRs of H_2O and

CH_4, the difference in the latitudes of the tangent points of ascending and descending nodes might be expected to result in day/night (or ascending/descending) differences in the monthly means.

In order to quantify the magnitude of the effect of the differences in latitudes of tangent points, profiles of latitude differences were calculated for six pairs of scans from orbit 06712. The mid–points of the scans in each pair were at approximately the same latitude and the six latitudes were chosen to correspond to the centres of the six latitude bands used in these comparisons. Monthly mean profiles in the six latitude bands were used to calculate representative gradients of mixing ratio with latitude ($\mathrm{d(VMR)/d}\theta$). Gradients were then multiplied by the profiles of latitude differences in order to find the expected differences between ascending and descending monthly means due to meridional gradients. The results are shown in Figures 4.66 and 4.67. There are differences of the order of a few percent, but it can be seen that the effect is not large enough to account for the differences seen in Figures 4.63 and 4.64.

4.10.3 Day/night comparisons with IG2 climatology

Figure 4.68 shows percentage differences of MIPAS day–time and night–time H_2O monthly means from the IG2 climatology (§ 4.5) for selected months in 2003. It can be seen that day/night differences are not large enough to account for the observed bias pattern in MIPAS H_2O with respect to the IG2 H_2O. The bias pattern is similar between day and night.

Figure 4.69 shows similar plots for CH_4. Again, the day/night differences are not large enough to account for differences from the IG2 climatology.

4.10.4 Systematic difference in pointing

A systematic day/night difference in the instrument pointing is one possible reason for day/night differences in the water vapour and methane retrievals. Figure 4.70 shows the difference between the mean tangent altitudes for day–time and night–time quoted in the Level 1B files (before they are "corrected" using the retrieved pressure and the hydrostatic approximation in the Level 2 processing) plotted on the day+night monthly mean pressure values. The Level 1B altitudes indicate where MIPAS is supposed to be pointing. Figure 4.70 shows positive day/night altitude differences at lower altitudes and negative day/night differences at higher altitudes, indicating that the tangent points should be more widely spaced in the night–time than in the day–time.

In the stratosphere, methane decreases with altitude while water vapour increases with altitude. A systematic day/night difference in pointing would therefore be expected to lead to an anticorrelation between day/night differences in H_2O and CH_4. This did not appear to be the case in Figure 4.62.

4.10.5 Day/night pressure differences

The day/night difference in the satellite pointing would be expected to translate into a similar day/night difference in retrieved pressures. It would be expected from Figure 4.70 that the retrieved day–time pressures would be lower than night–time values at low altitudes and higher than night–time values at high altitudes. Figure 4.71 shows percentage differences in pressure between the day–time and night–time monthly means. In equatorial regions, the day/night pressure differences are largely what would be expected from the day/night pointing differences in Figure 4.70. However in mid–latitudes and polar regions, the situation appears more complicated. The day/night differences in pressure show a strong variation in time which is not present in the Level 1B altitudes. The time variation appears to be roughly sinusoidal, with a period of one year. The fact that the variation has a period of one year would appear to indicate that it arises from some actual instrument pointing variation rather than from some problem with the pressure retrieval.

Using the night–time pressure and VMR profiles as a reference, differences in the water vapour and methane that would arise from differences in the instrument pointing indicated by the day/night pressure differences in Figure 4.71 could be calculated. Figures 4.72 and 4.73 show the results. Below about 1 mbar, the differences in these figures appear to be strongly correlated with the differences in Figures 4.60 and 4.61 but with a magnitude of only around half the size of the actual day/night differences.

4.10.6 Day/night temperature differences

Figure 4.74 shows the difference between the day–time and night–time MIPAS monthly mean temperature profiles.

There are expected to be some real diurnal variations in temperature in the stratosphere, associated with atmospheric tides. Atmospheric tides are global–scale inertia gravity waves forced by solar heating. These tides are forced by the variation of solar heating of water vapour in the troposphere and ozone in the stratosphere. They have a diurnal and a semi–diurnal component (Wood and Andrews, 1997). The tides are associated with day/night differences in temperature and wind fields. Over the equator, MIPAS day and night profiles are always separated by 12 hours in terms of local time, so in equatorial regions it would be expected that MIPAS temperatures would show some signal associated with the diurnal component of atmospheric tides. Diurnal tides in equatorial regions are expected to have some vertical wavelength associated with them. Simple models (*David Andrews, private communication*) indicate upward propagation of waves with a vertical wavelength of around 28 km. The amplitude of the diurnal temperature variations in the stratosphere is expected to be of the order of a few Kelvin (with a larger amplitude in the mesosphere). This clear upward propagation is only expected to be seen in equatorial regions. The MIPAS day/night temperature differences in Figure 4.74 appear to show evidence of a vertical wave with the expected wavelength and amplitude.

In mid–latitudes and polar regions, MIPAS day and night profiles are no longer separated by 12 hours. It might be expected that MIPAS day/night temperature differences in these regions would also be affected by the semi–diurnal component of the tides. Without considerable further analysis of the data and reference to models, it is difficult to say anything more useful about the effects of atmospheric tides on day/night differences in the MIPAS data. MIPAS data could potentially be extremely useful in a studies of atmospheric tides. However, these studies are outside the scope of this thesis.

Since the day/night temperature differences in equatorial regions show the magnitudes and spatial structure that would be expected, it is thought unlikely that the day/night differences in water vapour and methane are caused by a systematic day/night temperature error.
However, for the sake of argument, let it be said that there may be some systematic error in temperature which varies in magnitude between day and night, perhaps caused by non–LTE effects in the pT retrieval, or perhaps by something else. If the day/night differences in Figures 4.60 and 4.61 were caused by a systematic temperature error, then it would be expected that these two figures would show a correlation with each other and an anti-correlation with Figure 4.74. A quick visual inspection of these figures would appear to indicate that certain features in particular months and at particular altitudes appear to show correlations, while others do not.

In order to further clarify any correlations between day/night differences in water vapour and methane and any anti–correlations with temperature, Figures 4.75, 4.76 and 4.77 show the latitudinal variation of day/night differences in water vapour, methane and temperature respectively (this time calculated from monthly means using 10 degree latitude bands) for June 2003 and December 2003.

The most obvious feature in Figures 4.60 and 4.61 is in southern hemisphere mid–latitudes. There are particularly large positive day/night differences in the water vapour and methane in April–July 2003 in the region of 2 mbar, with large negative differences in the adjacent few months at this altitude, and large negative day/night differences in both of the November–February periods spanned by the dataset at around 100 mbar. This pattern would appear to be anti–correlated with the day/night temperature differences.

Northern hemisphere mid–latitudes also show a large positive difference in the water vapour and methane in April–July 2003 around 2 mbar with large negative differences in the few months on either side. Figures 4.75 and 4.76 also appear to show that this feature is anti–correlated with the day/night temperature difference in this region in Figure 4.77.

An attempt was made to determine the effect that a day/night temperature difference due to systematic error would have on the water vapour and methane retrievals. For the sake of argument, say that the day/night temperature differences in the monthly means are purely due to systematic error. This day/night temperature difference can be translated to a change in radiance, given by the Planck function (Equation 2.1). Since the Planck function is a function of wavenumber as well as temperature, it is necessary to choose some representative wavenumber at which to evaluate the day/night radiance change caused by the day/night temperature difference. If the assumption is made that the percentage change in radiance translates approximately linearly to a percentage change in VMR in the water vapour and methane retrievals, then it is possible to evaluate the systematic day/night differences in water vapour and methane which would arise from the systematic day/night temperature differences. Figures 4.78 and 4.79 show these percentage differences for water vapour and methane respectively. (It turns out that there is no discernible difference between these figures.)

It would appear that the day/night differences in water vapour and methane are too large to be explained by the difference in radiances due to day/night temperature differences alone.

4.10.7 Non–LTE in H_2O and CH_4

Since non–LTE effects are expected to be dependent on illumination conditions (§ 2.1.4, and since they are not included in the forward model for the ESA OFL retrievals (Ridolfi et al., 2000), they are an obvious candidate for a cause of day/night differences in the water vapour and methane retrievals.

Pre–launch studies (Lopez-Puertas et al, 1996) were performed in order to evaluate non–LTE effects in the MIPAS retrievals and non–LTE effects in the MIPAS spectra were taken into account in the selection of the microwindows (see § 4.3, Figure 4.6). Non–LTE effects are expected to be a significant source of systematic error at 52 km and above in the microwindows that were selected for the operational retrievals. It might therefore be expected that there would be significant day/night differences in the MIPAS H_2O and CH_4 retrievals at higher altitudes.

A retrieval code which includes non–LTE effects in its forward model has been developed by the group at the Institute for Astrophysics of Andalucia (IAA). This group have also been working on MIPAS measurements from a special upper atmosphere mode, with the specific aim of studying non–LTE effects in the MIPAS spectra. Significant day/night differences have been found in the upper atmosphere mode radiances. The radiance differences are greater than 10 % above 55 km, reaching 20–40 % at 70 km and above (Funke et al., 2005). These differences are attributed to non–LTE effects in the day–time producing Vibrational Temperatures which are larger than at night.

Day/night differences at the uppermost retrieval level (68 km) in both H_2O and CH_4 are large. In general, day–time values are lower than night–time values. These differences are 68 km are assumed to be related to non–LTE. Since the day–time radiances at this altitude are greater than night–time radiances, it might be expected that the day–time retrieved VMR values would be higher than the night–time values, but this is not the case.

It is clear from Figures 4.60 and 4.61 that there are day/night differences in the ESA OFL H_2O and CH_4 at altitudes well below where non–LTE effects are expected to be significant. Due to the retrieval method, it is possible that the effects of systematic errors from non–LTE at higher levels in the retrieval range could propagate downward to affect the retrieved profile at lower levels.

4.10.8 Contamination from a diurnally varying species

Examination of the spectral signatures of other gases in the operational water vapour and methane microwindows does not yield a possible candidate contaminant gas. Although there are NO_2 signatures present in the operational water vapour microwindows, they are not in positions which would directly interfere with water vapour lines.

4.10.9 Real diurnal variation

The possibility could exist that there are real diurnal variations in H_2O and CH_4. A real diurnal variation in these gases would be expected to be caused by either chemistry or dynamics.

It is conceivable that there might be some difference in chemistry between day and night. For example, reaction rates are dependent on temperature, and there are differences in the temperature between day and night (related to atmospheric tides). Another possible reason could be the availability of OH. Water vapour is produced by the oxidation of methane and the main methane oxidation reaction requires OH. There is more OH available in the day–time than in the night–time. If the OH were to drop to sufficiently low levels in the night–time, perhaps one might expect there to be slightly less methane and more water vapour in day–time than in night–time. This is thought to happen in the long polar night, but would not be expected to happen in the course of a "normal" night. Scatter plots of the day/night differences in water vapour and methane have already been shown in Figure 4.62. If the day/night differences in VMR were attributable to day/night differences in chemistry, it might be expected that the differences in water vapour would be anti–correlated with the day/night differences in methane. This does not appear to be the case.

Atmospheric tides result in dynamical differences between day and night in the stratosphere as well as temperature differences. A simplistic way of examining whether day/night differences in the VMRs of trace gases could be caused by day/night differences in the dynamical situation is to look at tracer correlations. Correlations between H_2O and CH_4 day/night differences would not be expected to be simple in terms of dynamical tracing. However, it is possible to use other MIPAS products to investigate this issue. N_2O, like CH_4, is expected to decrease monotonically with height and these two gases are expected to show a straightforward correlation in the stratosphere. If the day/night differences in VMR were due to a day/night difference in the dynamics, it would be expected that the pattern of day/night differences in N_2O and CH_4 would be correlated. Figure 4.80 shows scatter plots of CH_4 and N_2O day/night differences. This figure could be taken to provide evidence for a difference in the prevailing dynamical situation between day and night. (However, this figure would also be consistent with a systematic day/night difference in the pointing — see § 4.10.4.)

4.10.10 Summary of day/night differences

Neither water vapour nor methane are expected to show diurnal variations in the stratosphere. However, day/night differences are evident in both of these gases in the MIPAS OFL monthly means. The major points covered in the course of this section are summarised below:

- There is a large and persistent day/night difference in both water vapour and methane at the uppermost retrieval altitude (68 km). Day–time values are smaller than night–time values at this altitude. It is assumed that this problem is related to non–LTE effects in some way, and is suspected to also be related to the way that the atmosphere above the uppermost retrieval level is represented in the forward model.

- Day/night differences are also present at altitudes where non–LTE was not expected to be a significant source of systematic error. These differences are at least partially accounted for by actual day/night differences in the instrument pointing.

In the course of the work done here, it has not been possible to identify a single cause for the observed day/night differences. It is entirely possible that the observed day/night differences are due to a combination of the possible causes discussed in this section.

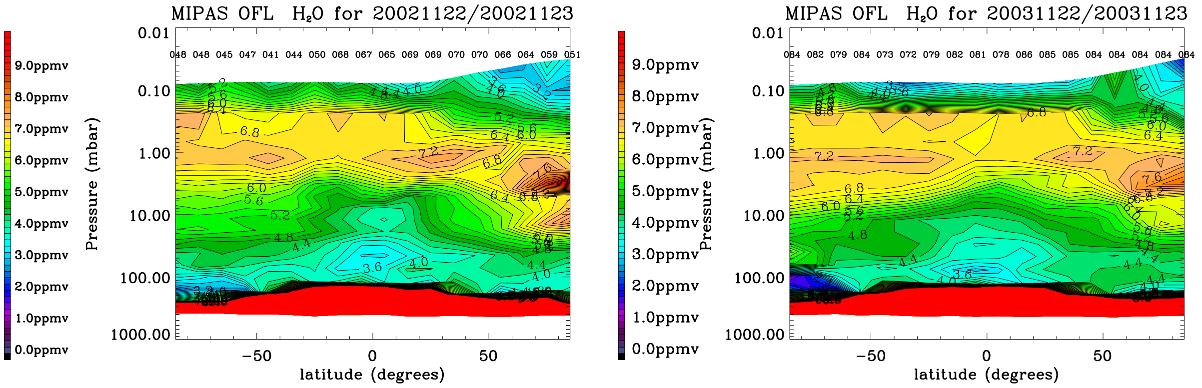

Figure 4.55: Zonal mean H_2O from MIPAS OFL data for 22^{nd} and 23^{rd} November 2002 (left) and 2003 (right).

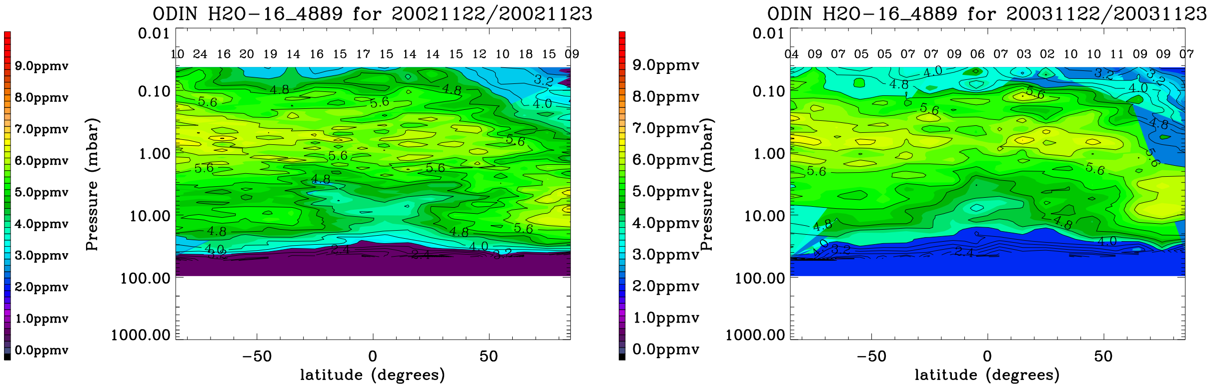

Figure 4.56: Zonal mean H_2O from Odin–SMR CTSO-v223 data for 22^{nd} and 23^{rd} November 2002 (left) and 2003 (right).

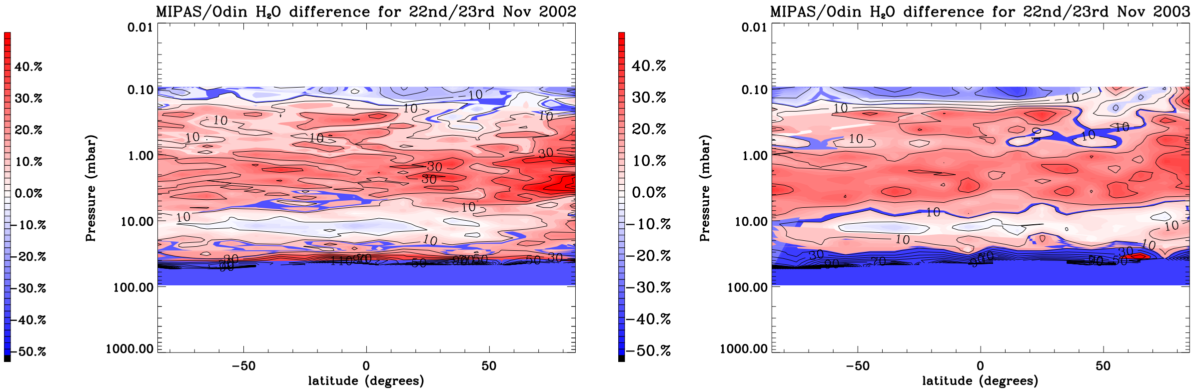

Figure 4.57: Percentage difference between zonal mean MIPAS OFL and Odin–SMR H_2O ([MIPAS-Odin]/Odin) for 22^{nd} and 23^{rd} November 2002 (left) and 2003 (right).

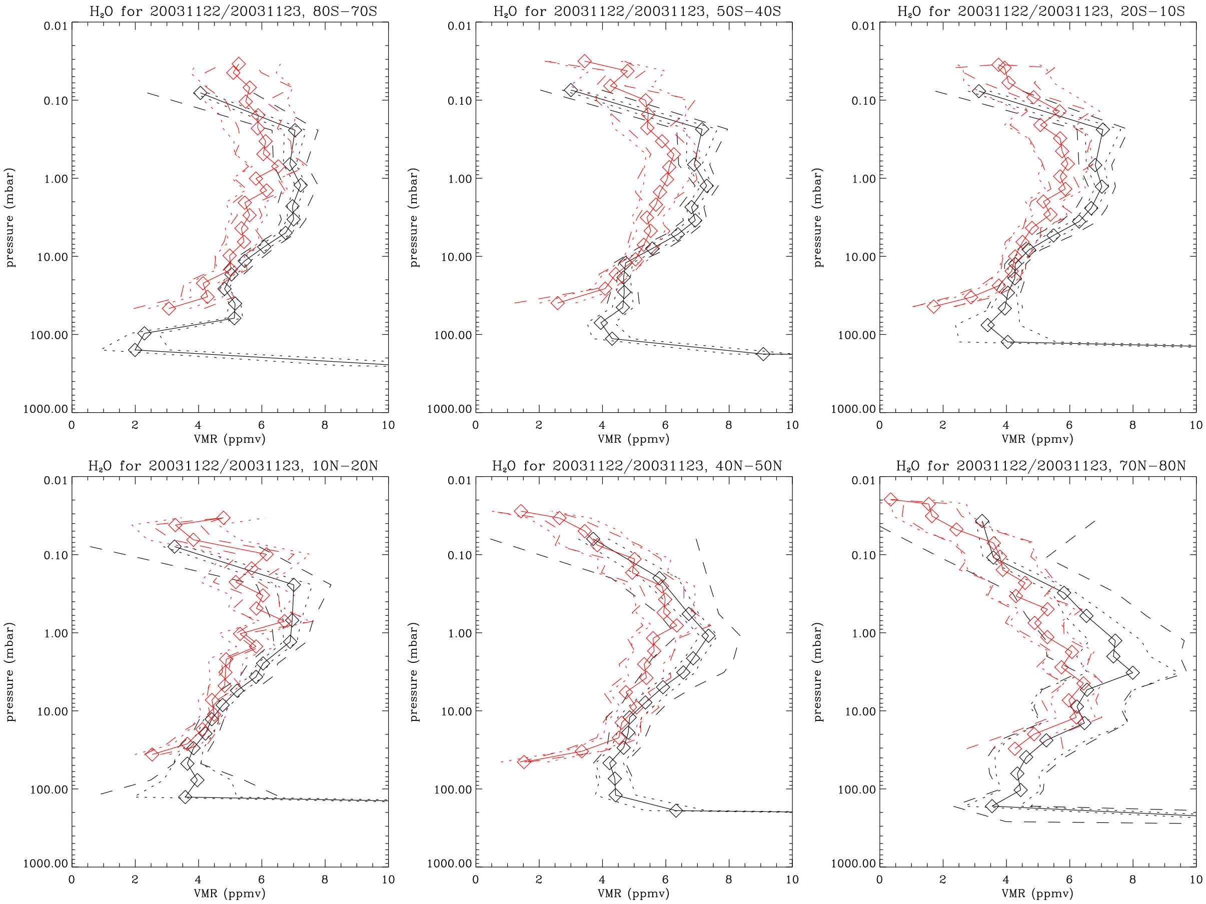

Figure 4.58: Zonal mean H_2O profiles from MIPAS (black) and the Odin–SMR (red) for six selected latitude bands. Dotted lines show the mean measurement error due to noise on the retrievals, while dashed lines show the standard deviations on the zonal means.

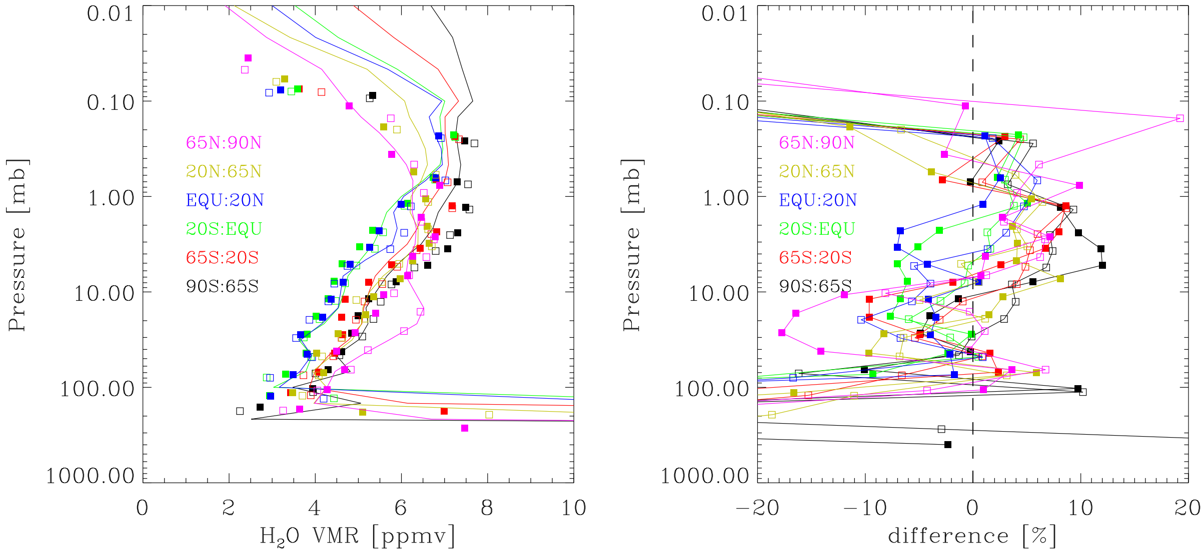

Figure 4.59: Left: MLS v1.51 data averaged for 28th Jan 2005 (lines) compared with MIPAS OFL data for January 2003 (open squares) and January 2004 (solid squares). Right: percentage difference (([MIPAS-MLS]/MLS)×100).

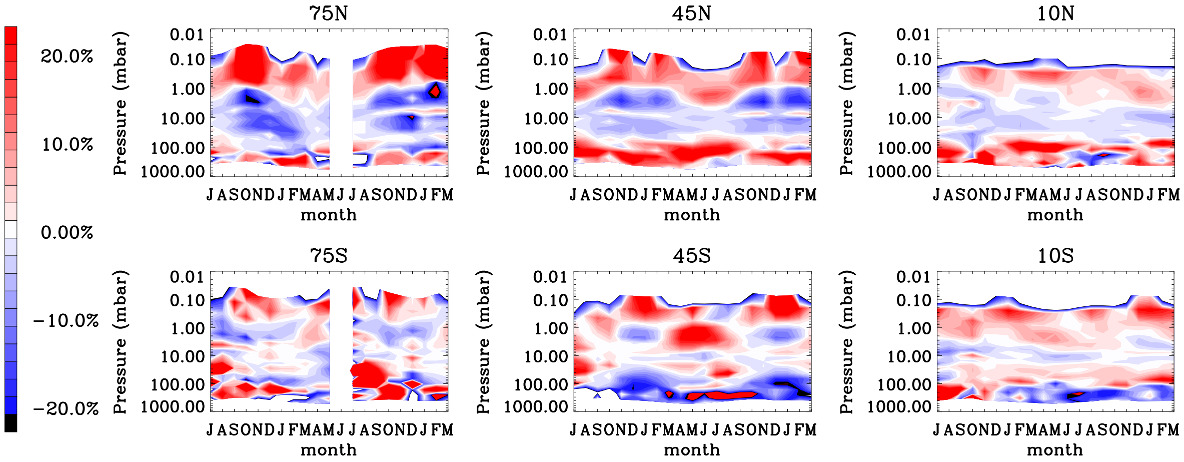

Figure 4.60: Differences between day–time and night–time ([day - night]/night) MIPAS monthly mean profiles for H_2O.

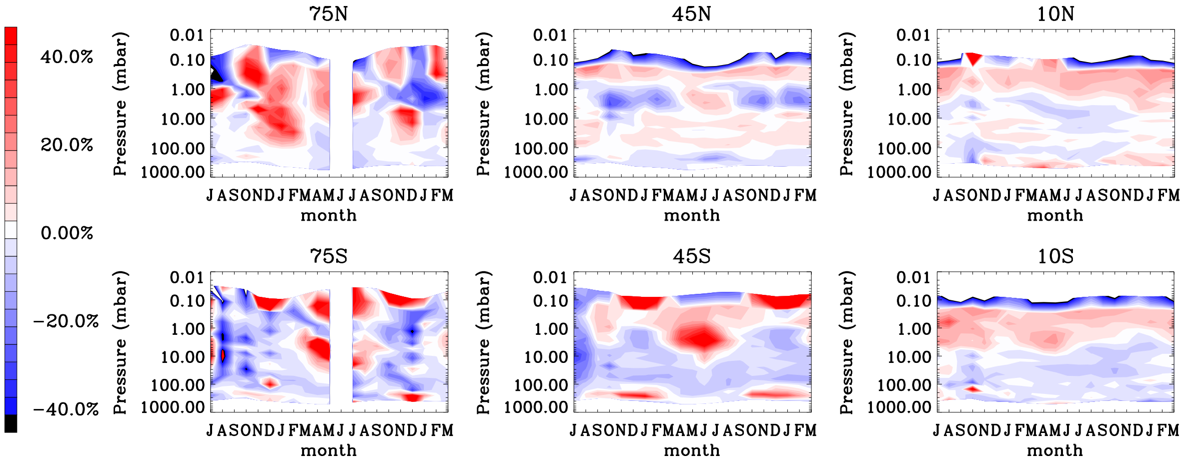

Figure 4.61: Differences between day–time and night–time ([day - night]/night) MIPAS monthly mean profiles for CH_4.

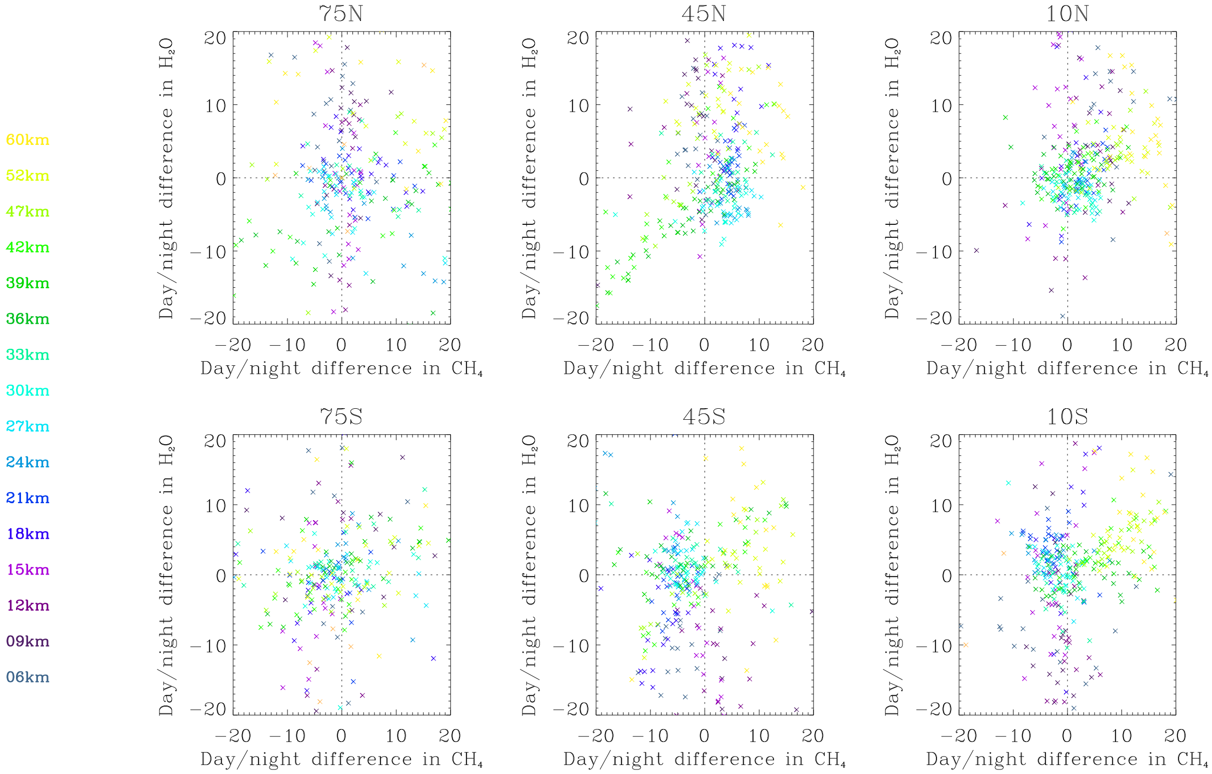

Figure 4.62: Percentage day/night differences for H_2O against those for CH_4. Different colours denote monthly means from different nominal altitudes.

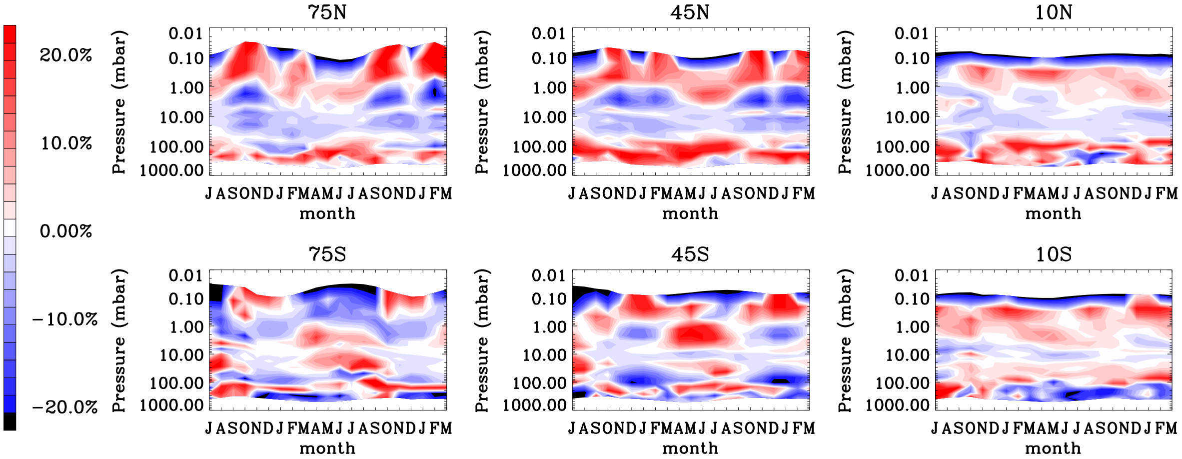

Figure 4.63: Percentage differences in H_2O between monthly means for ascending and descending nodes ([ascending-descending]/ascending).

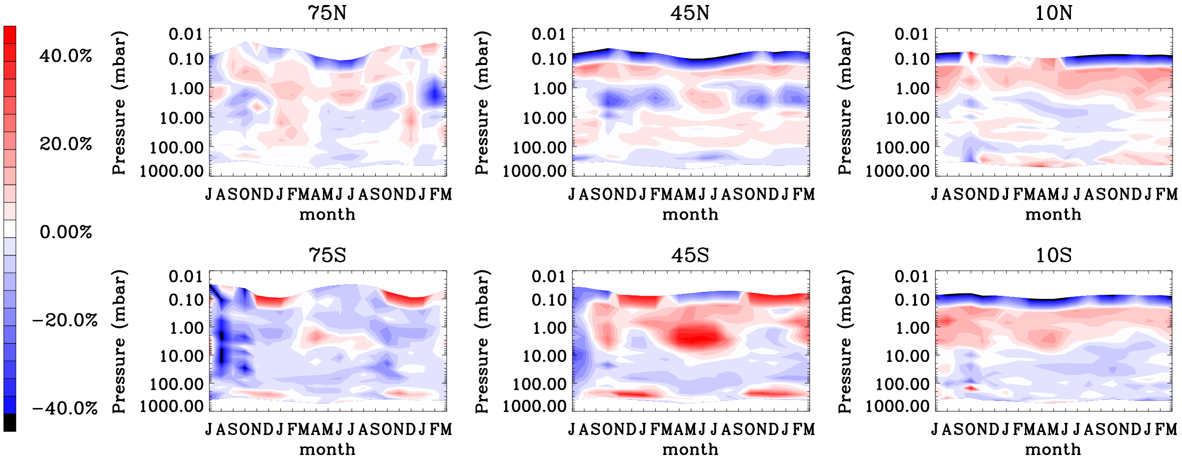

Figure 4.64: Percentage differences in CH_4 between monthly means for ascending and descending nodes ([ascending-descending]/ascending).

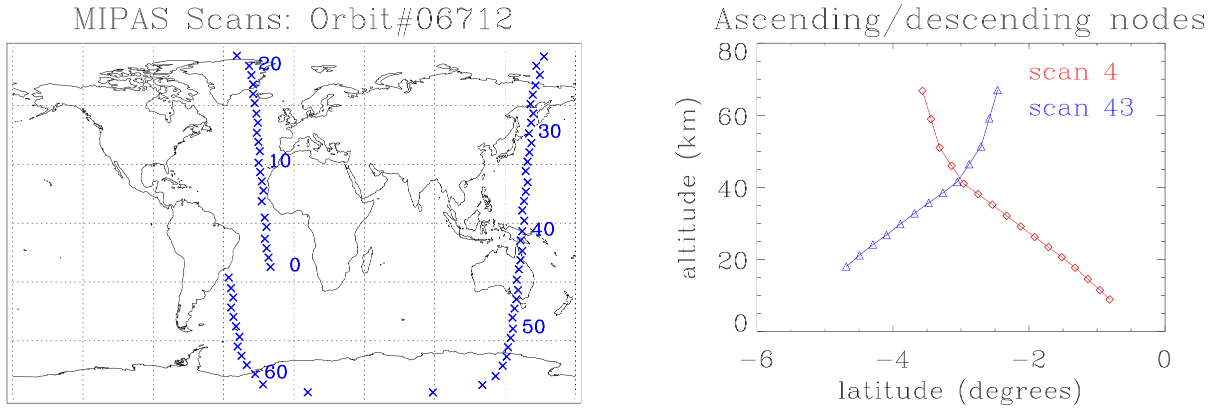

Figure 4.65: Left: Positions of mid–points of limb scans for orbit 06712. Right: Latitudes of tangent points for scan 4 (ascending) and scan 43 (descending).

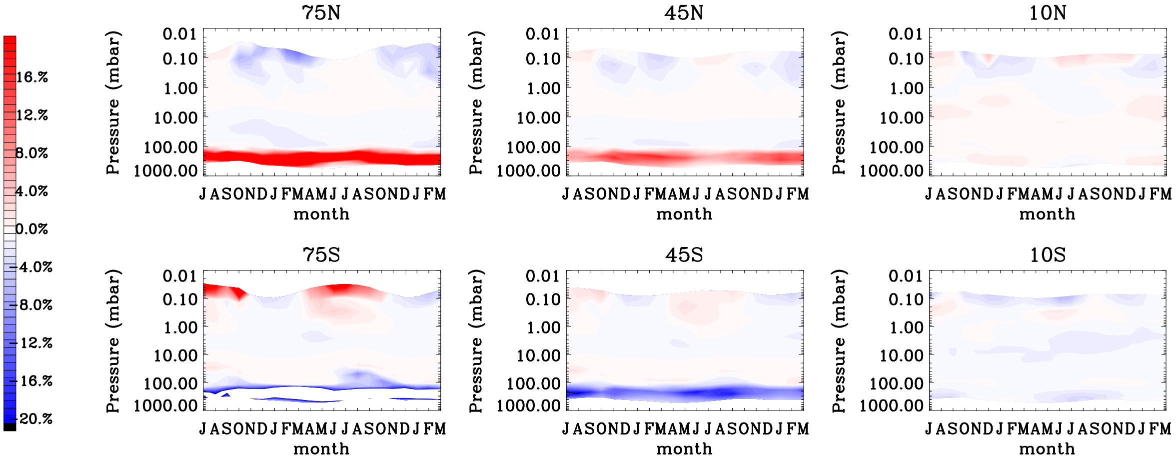

Figure 4.66: Percentage differences in H_2O induced by meridional gradients and the latitude differences between ascending and descending nodes.

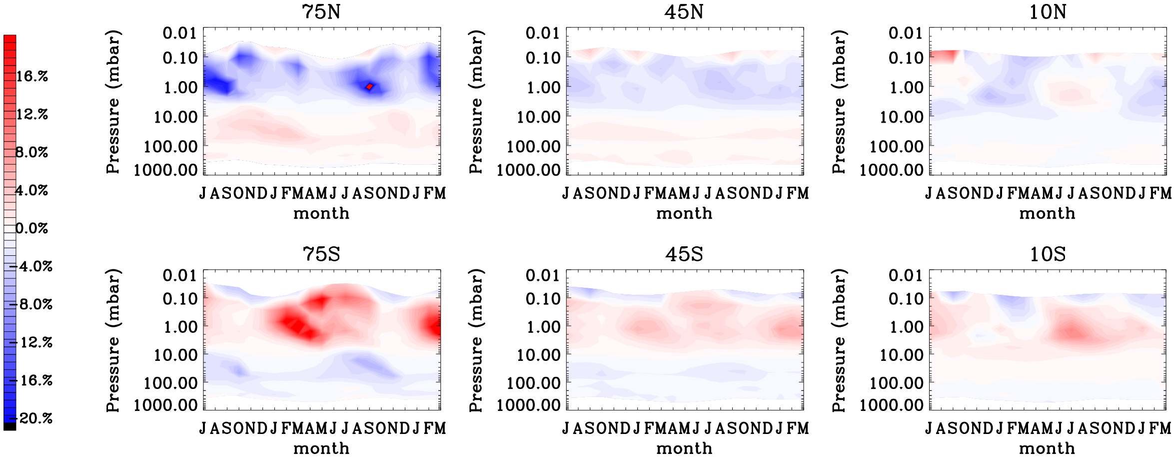

Figure 4.67: As above, but for CH_4.

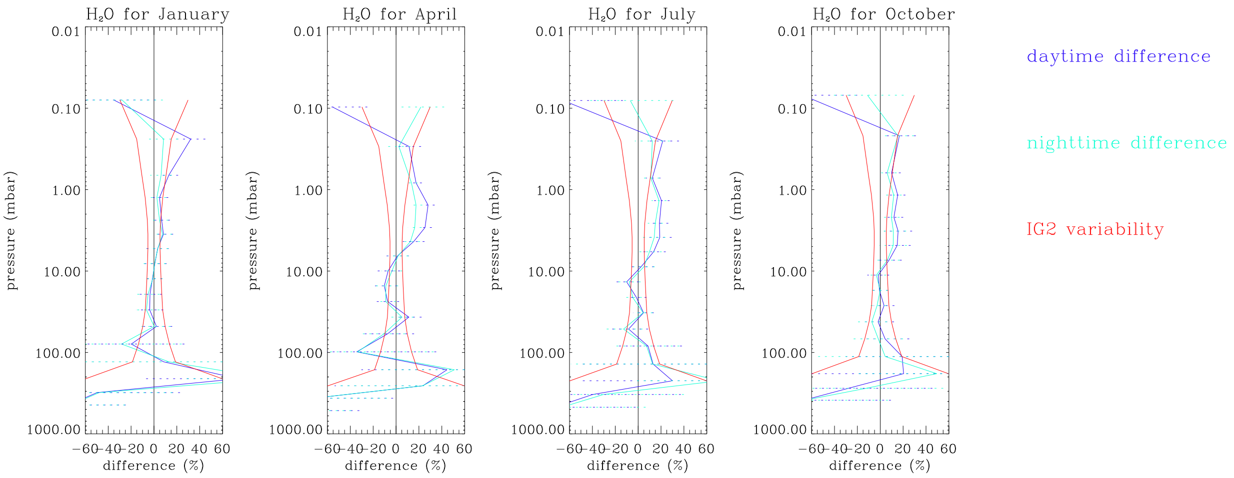

Figure 4.68: Percentage differences of MIPAS day–time and night–time H_2O monthly means from climatology, showing standard deviations in the means and expected climatological variability, for the latitude band centred on 10°S.

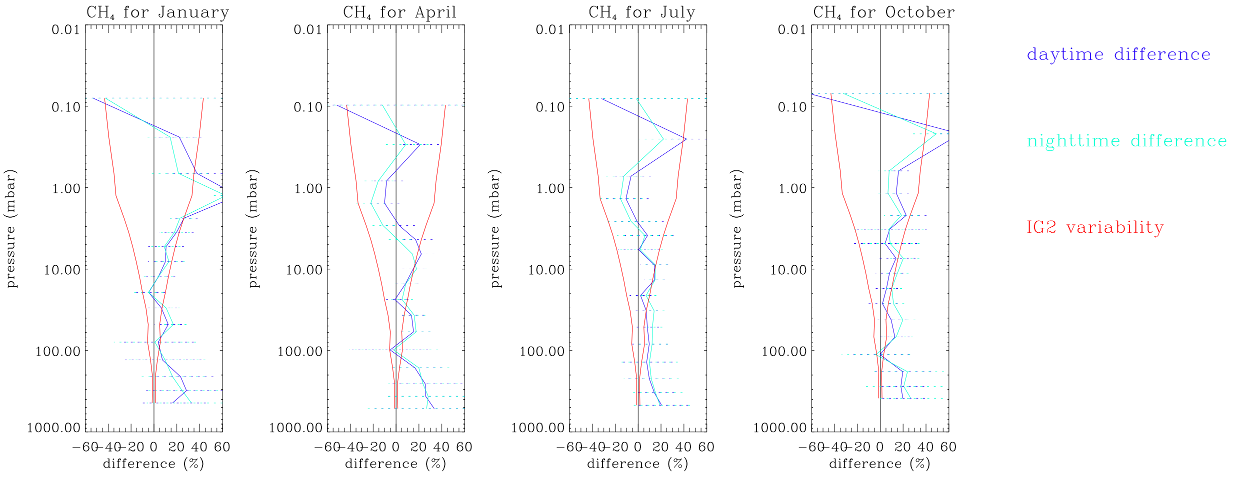

Figure 4.69: Percentage differences of MIPAS day–time and night–time CH_4 monthly means from climatology, showing standard deviations in the means and expected climatological variability, for the latitude band centred on 10°S.

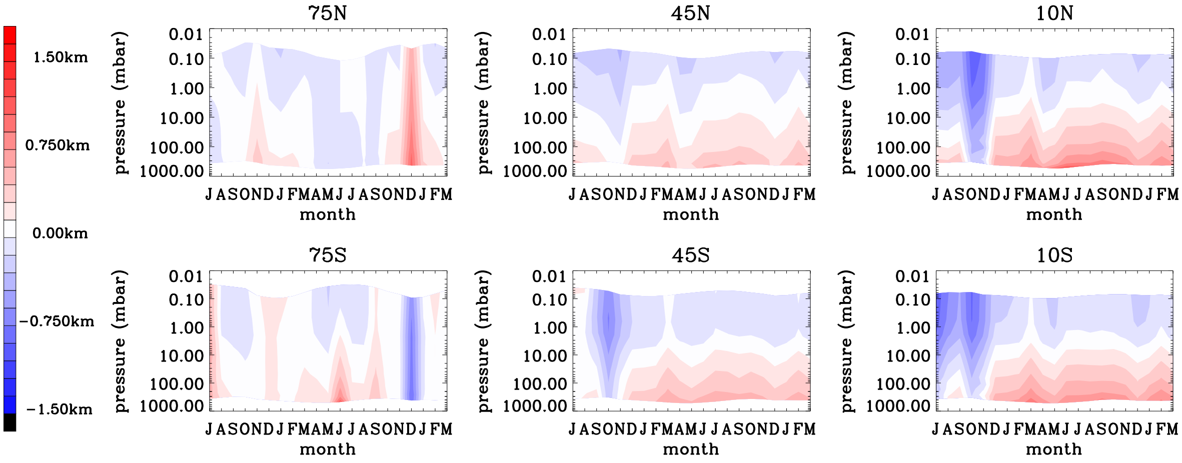

Figure 4.70: Day/night difference in monthly mean Level 1B altitudes.

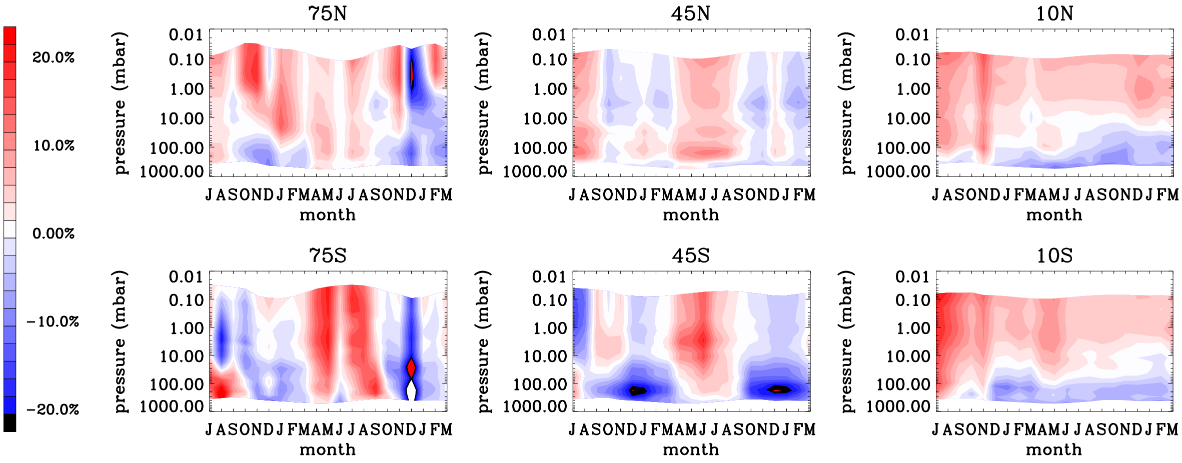

Figure 4.71: Percentage day/night difference ([day - night]/night) in pressure.

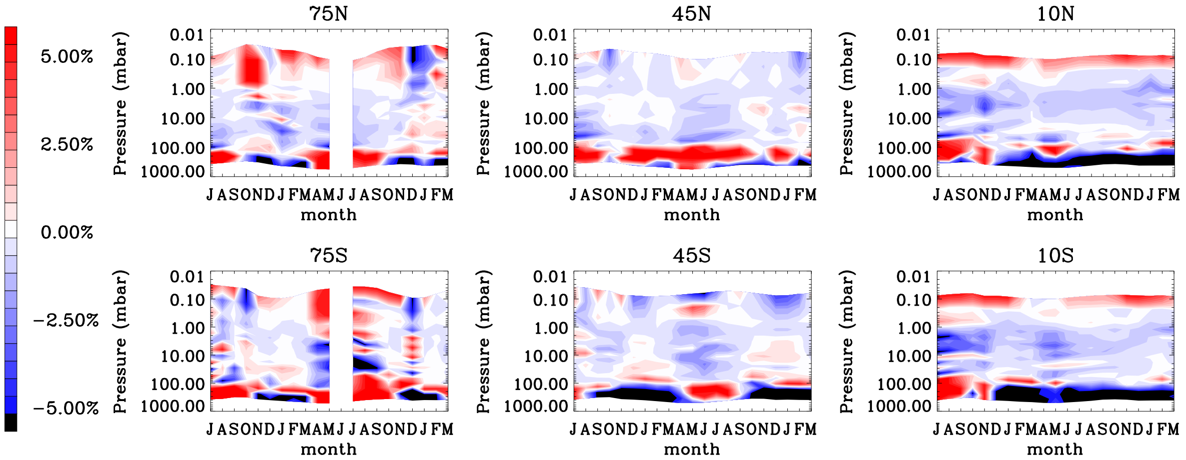

Figure 4.72: Day/night differences in H_2O which would be induced by the day/night pressure differences shown in Figure 4.71.

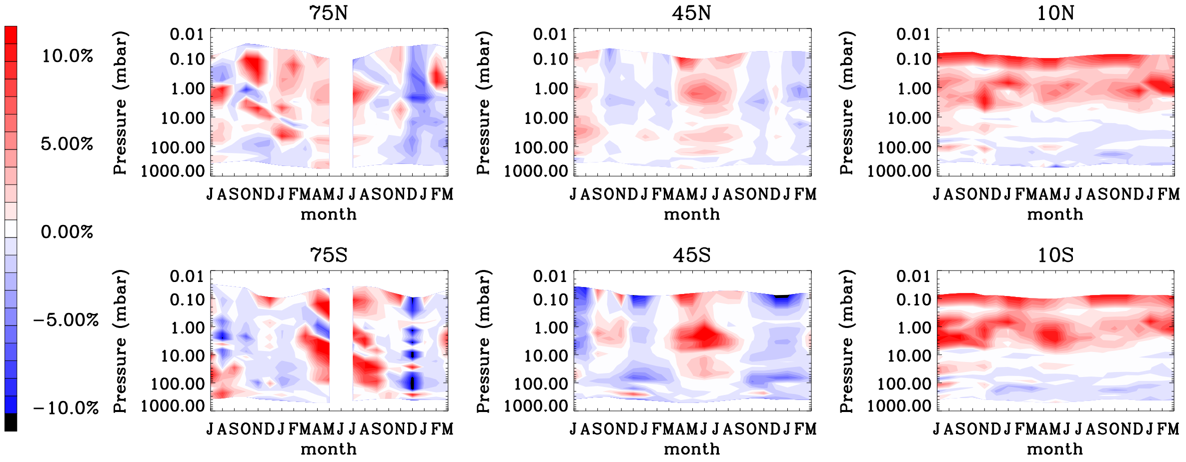

Figure 4.73: Day/night differences in CH_4 which would be induced by the day/night pressure differences shown in Figure 4.71.

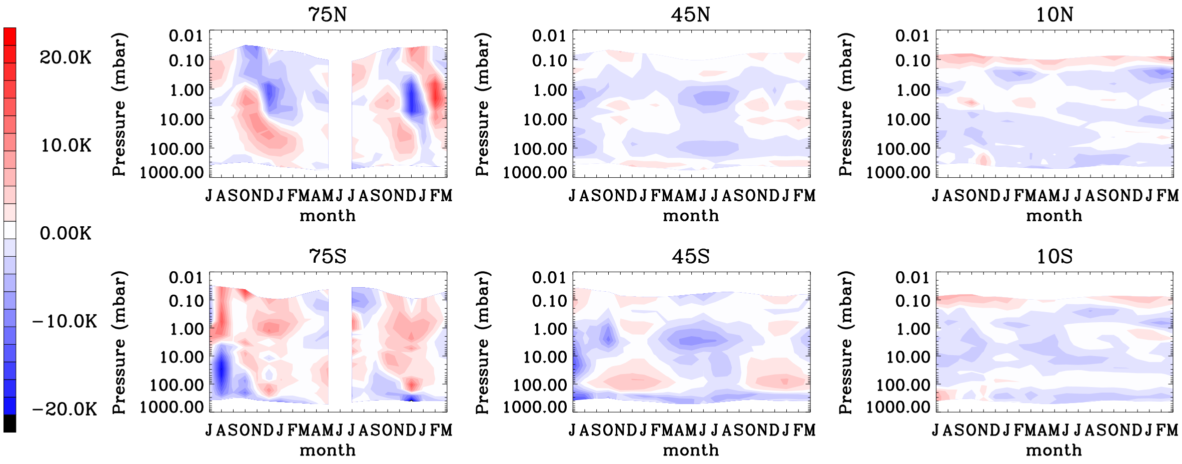

Figure 4.74: Differences between day–time and night–time (day - night) MIPAS monthly mean profiles for temperature.

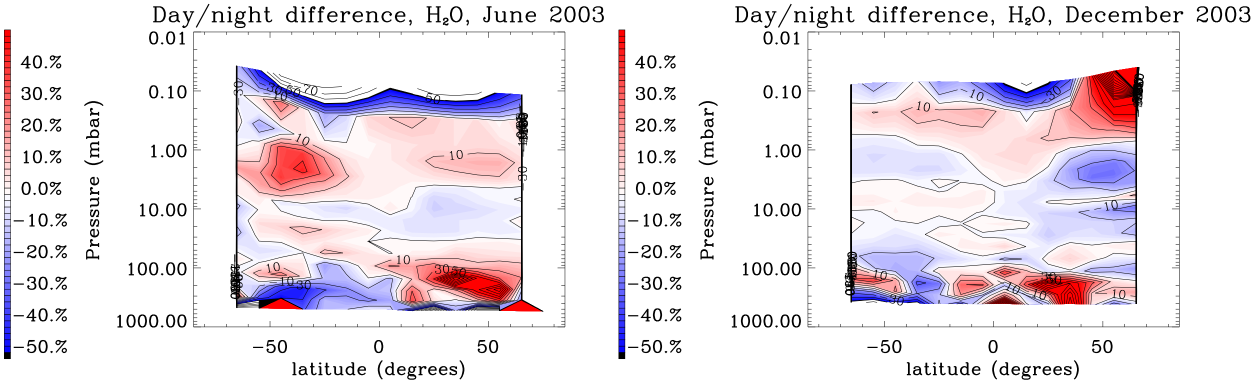

Figure 4.75: Latitudinal percentage day/night difference ([day - night]/night) in H_2O for June 2003 (left) and December 2003 (right).

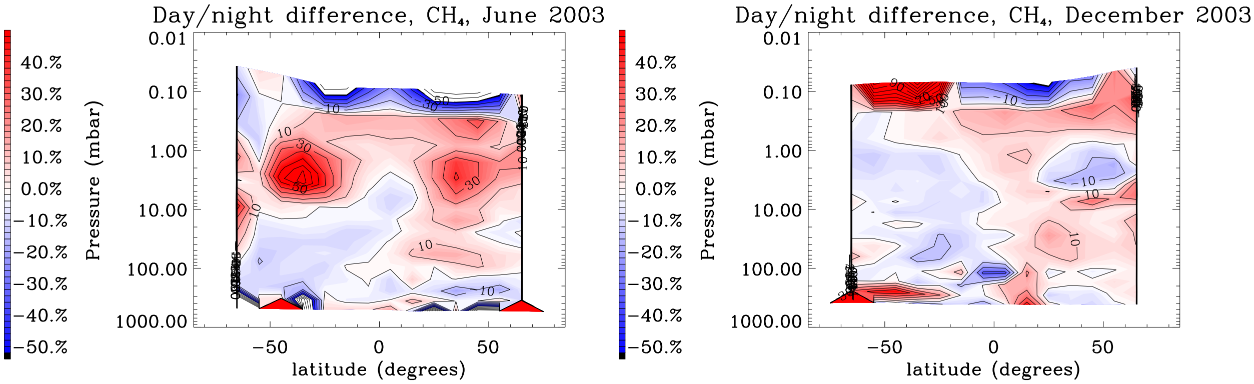

Figure 4.76: Latitudinal percentage day/night difference ([day - night]/night) in CH_4 for June 2003 (left) and December 2003 (right).

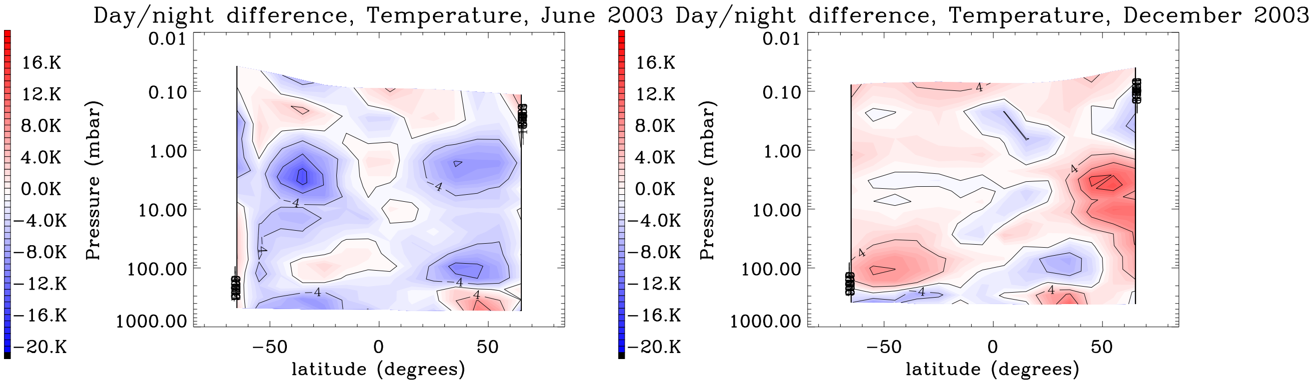

Figure 4.77: Latitudinal day/night difference ([day - night]) in temperature for June 2003 (left) and December 2003 (right).

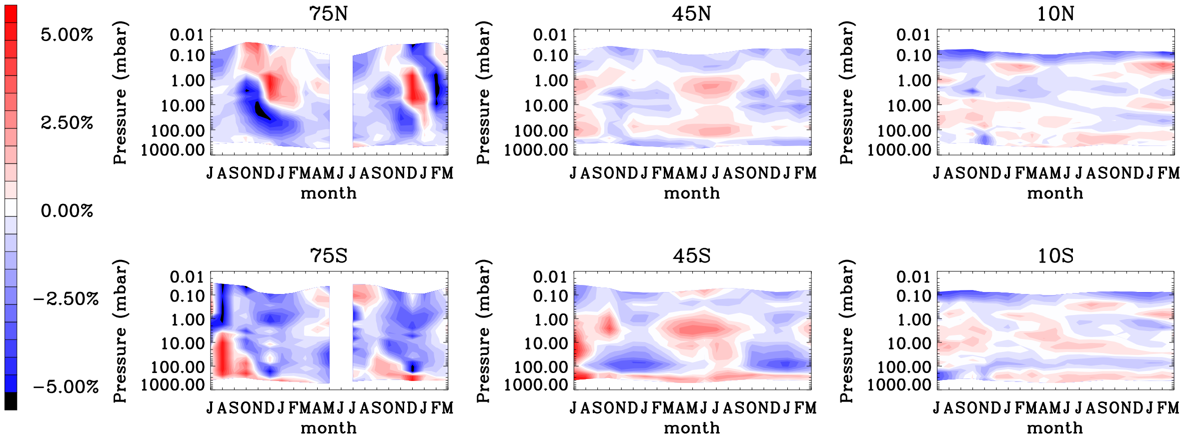

Figure 4.78: Percentage day/night difference ([day - night]/night) in radiance that would be induced by the day/night temperature difference in Figure 4.74 at a wavelength representative of the operational H_2O microwindows.

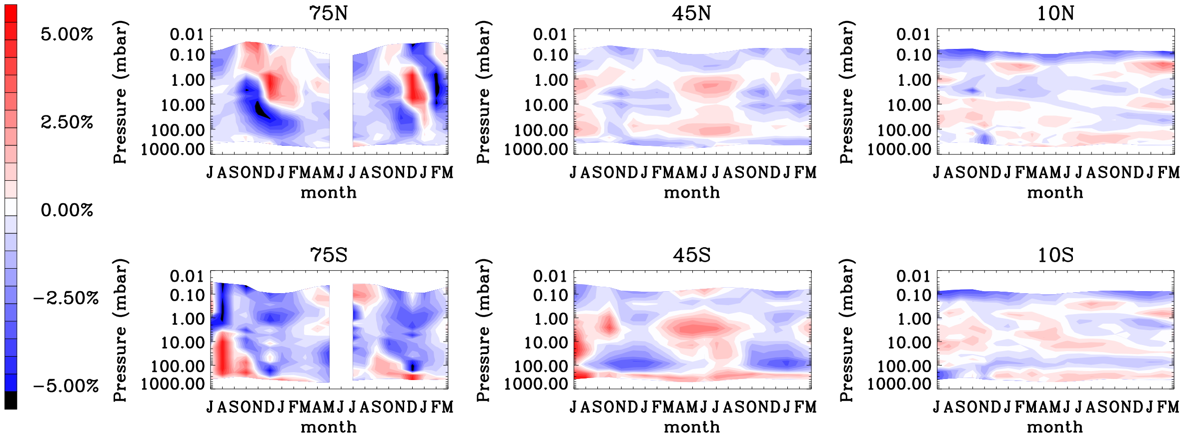

Figure 4.79: Percentage day/night difference ([day - night]/night) in radiance that would be induced by the day/night temperature difference in Figure 4.74 at a wavelength representative of the operational CH_4 microwindows.

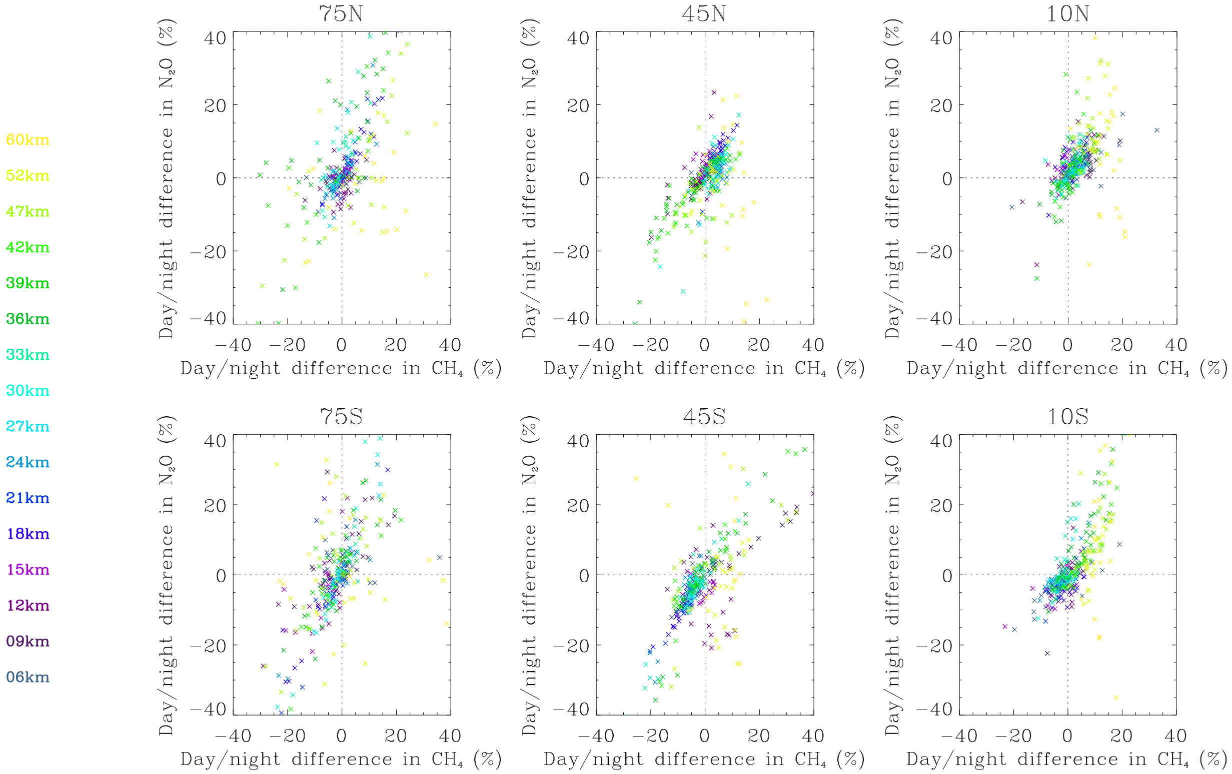

Figure 4.80: Percentage day/night differences for N_2O against those for CH_4. Different colours denote monthly means from different nominal altitudes. These two quantities would appear to be correlated.

4.11 Summary and Conclusions

4.11.1 H_2O

Work in this chapter has focused on water vapour in the stratosphere and lower mesosphere, which can generally be usefully discussed in terms of zonal means. Upper tropospheric water vapour from MIPAS has not been discussed in depth. Due to the high variability of tropospheric water vapour, zonal means are not as useful in this region. Also, comparisons with external data made in this chapter have been with the IG2 climatology, which by the nature of the dataset does not capture the variability of upper tropospheric water vapour, with data from HALOE, where upper tropospheric water vapour values are known to be somewhat unreliable (HALOE, 2005) and with data from the Odin–SMR, whose measurement range for water vapour does not extend down to the upper troposphere. Comparisons with MLS involve data separated by at least a year. Examination of spatial distributions of water vapour in the upper troposphere on, say, selected pressure levels could be a useful validation exercise, but has not been covered here.

Averaged residuals for the operational H_2O microwindows show distinct spectral features at the positions of the water vapour lines. The residual signatures show diurnal and seasonal variations.

Diurnal variations in stratospheric water vapour are not expected, but the MIPAS monthly means of H_2O show significant day/night differences. These day/night differences are thought to be due to a combination of a real day/night difference in the instrument pointing and non–LTE effects. There is some day/night pointing difference indicated in the MIPAS Level 1B altitudes, but there appear to be additional real day/night pointing differences which show up as extra day/night differences in the pressure retrievals.

Zonal mean comparisons of MIPAS H_2O were performed with the IG2 climatology dataset and with data from other satellite instruments: HALOE, the Odin–SMR and EOS MLS. An attempt to summarise the results of these comparisons is made in Figure 4.81, which shows differences between global mean profiles for each of the instruments, using IG2 profiles as a reference.

Each set of zonal mean comparisons showed a bias pattern in MIPAS with respect to the other instruments which was largely consistent with time and across latitudes.

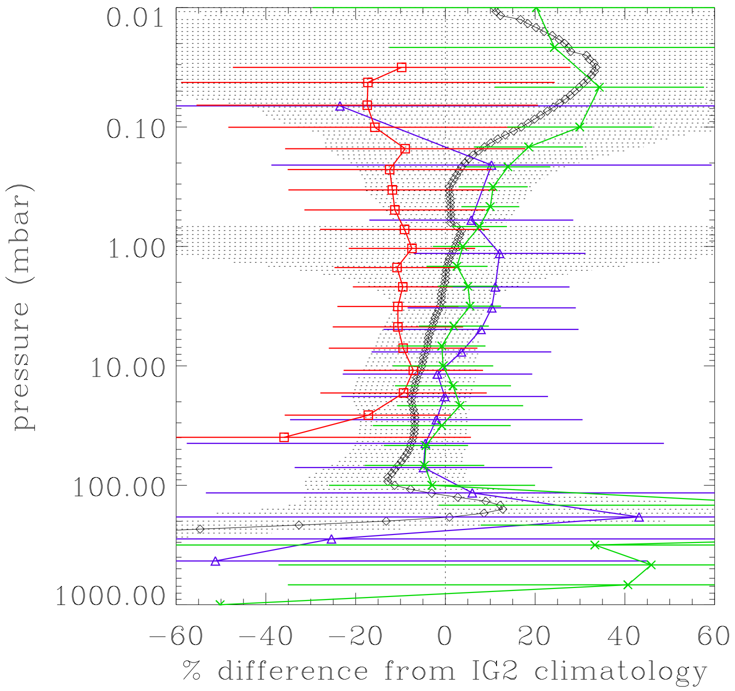

Figure 4.81: Biases of global mean H_2O calculated from MIPAS OFL Level 2 (blue), HALOE Level 3 (black), Odin–SMR Level 2 (red) and MLS Level 2 data (green) with respect to the IG2 climatology. Horizontal lines show standard deviations on the global mean for each of the instruments.

Despite the spectral features in the residuals, the observed biases and the unexplained day/night differences, qualitatively, monthly mean profiles of MIPAS OFL H_2O show the variations with altitude, latitude and time that would be expected. This is in itself an indication that the dataset is of reasonable quality.

4.11.2 CH_4

In general, monthly mean profiles of MIPAS OFL CH_4 also show the qualitative variations with altitude, latitude and time which would be expected. As with the H_2O, there are significant day/night differences in MIPAS OFL CH_4, which are thought to be caused by a combination of non–LTE effects and real day/night differences in the instrument pointing. There are also spectral features in averaged residual spectra for the CH_4 microwindows, which could indicate problems with convergence.

Zonal mean profiles of MIPAS OFL CH_4 were compared with the IG2 climatology and with data from the HALOE instrument. Global mean differences of MIPAS and HALOE CH_4 from the IG2 profiles are show in Figure 4.82. In general, MIPAS CH_4 is higher than both the IG2 and HALOE.

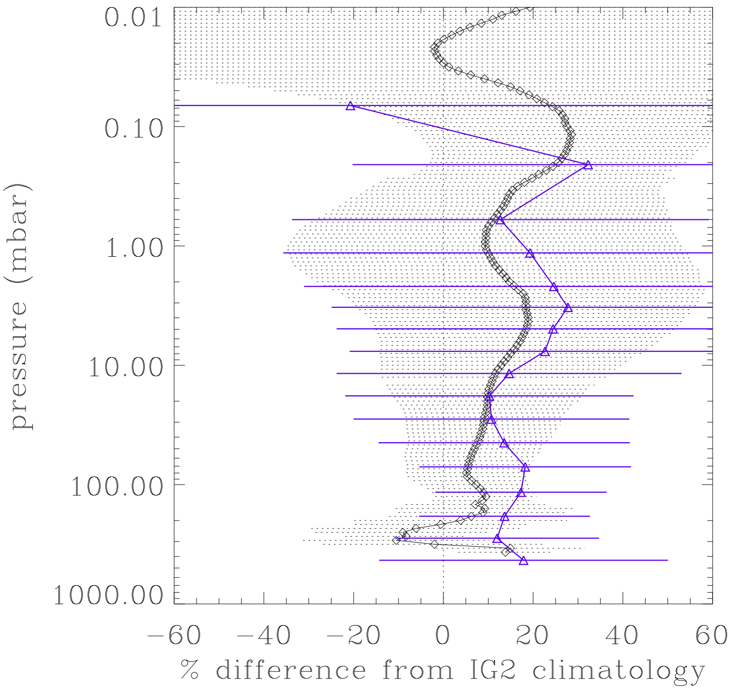

Figure 4.82: Biases of global mean CH_4 calculated from MIPAS OFL Level 2 (blue) and HALOE Level 3 (black) data with respect to the IG2 climatology. Horizontal lines show standard deviations on the global mean for each of the instruments.

4.11.3 General

It may be useful to put the comparisons performed into this chapter into the context of other comparisons with ground–based, aircraft and balloon measurements, and with other satellite measurements which have not been covered here.

In the presentations of the Second Workshop on the Atmospheric Chemistry Validation of Envisat (ACVE–2), held in May 2004, the conclusions on the quality of MIPAS water vapour and methane were as follows:

- MIPAS OFL H_2O shows a slight low bias in the lowermost stratosphere (the stratosphere below 15 km) when compared with balloon, aircraft and ground–based instruments (Pappalardo et al., 2004; Oelhaf et al., 2004).
- MIPAS OFL H_2O generally shows good agreement when compared to other satellite instruments (HALOE, POAM III, SAGE II) and to balloon and aircraft instruments in the 100–10 mbar range (15–30 km) (Oelhaf et al., 2004; Weber et al., 2004).
- Above 10 mbar, MIPAS OFL H_2O shows a positive bias of up to 20 % when compared with other satellite instruments (Weber et al., 2004)
- MIPAS OFL CH_4 is generally higher than correlative measurements

The results of the comparisons performed for this chapter would appear to support these conclusions.

In addition to any biases, and to any individual profile oscillations (§ A), the comparisons performed in this chapter also indicate that there is a persistent oscillation in the monthly means of methane in the region of the tropical tropopause.

Possible reasons for observed biases and persistent oscillations will be discussed and investigated in Chapter 5.

Chapter 5

Investigation of problems

5.1 Introduction

A number of persistent problems in the MIPAS ESA OFL H_2O and CH_4 were identified in Chapter 4. The main issues were a high bias in the H_2O above 30 km, a general high bias in the CH_4, a large negative bias in both the H_2O and CH_4 at 68 km, a persistent oscillation in CH_4 in the region of the tropical tropopause and day/night differences in the retrieved quantities which can be partially, but not entirely, accounted for by a day/night difference in pointing. Biases in the ESA OFL H_2O with respect to other data sources were largely consistent with latitude and with time, whereas biases in CH_4 were more variable. The aim in this Chapter is to use a separate retrieval code developed at Oxford (MORSE) to investigate possible causes of these problems. The Oxford forward model and retrieval processor are described in § 5.2.

Possible causes of persistent problems can be broadly divided into those which can be investigated using retrievals from simulated data and those which must be investigated using real data.

In the former category, some are assumptions in the forward model which relate primarily to the spectral domain, while others relate primarily to the vertical domain. The “spectral” forward model assumptions investigated in this Chapter with the use of simulated data are the use of look–up tables and irregular grids rather than line–by–line calculations (§ 5.3.1), the neglection of non–LTE effects in the forward model (§ 5.3.2) and first and second derivative errors ("shift" and "spread" in the instrument line shape (ILS) — § 5.3.3). Any problems caused by these assumptions might be expected to manifest themselves in a similar way at all latitudes. Assumptions which involve the vertical domain might be expected to show more variation with latitude, since they might be expected to be more dependent on atmospheric structure. For example, there are sharper changes of temperature and water vapour with height in the region of the tropopause in the tropics than in mid–latitudes (see Figure 5.1). The "vertical" forward model assumptions investigated here are the representation of the instrument field of view (FOV) (§ 5.3.5), the assumption that the atmosphere can be accurately represented on the MIPAS altitude measurement grid (§ 5.3.6), the method of interpolation of VMR between altitude grid points in the forward model (§ 5.3.7) and the neglection of the effects of refraction on the FOV (§ 5.3.8). Another possible cause of problems investigated using simulated data is the sensitivity of the retrieval to the initial guess atmosphere above the uppermost retrieval altitude (§ 5.3.4).

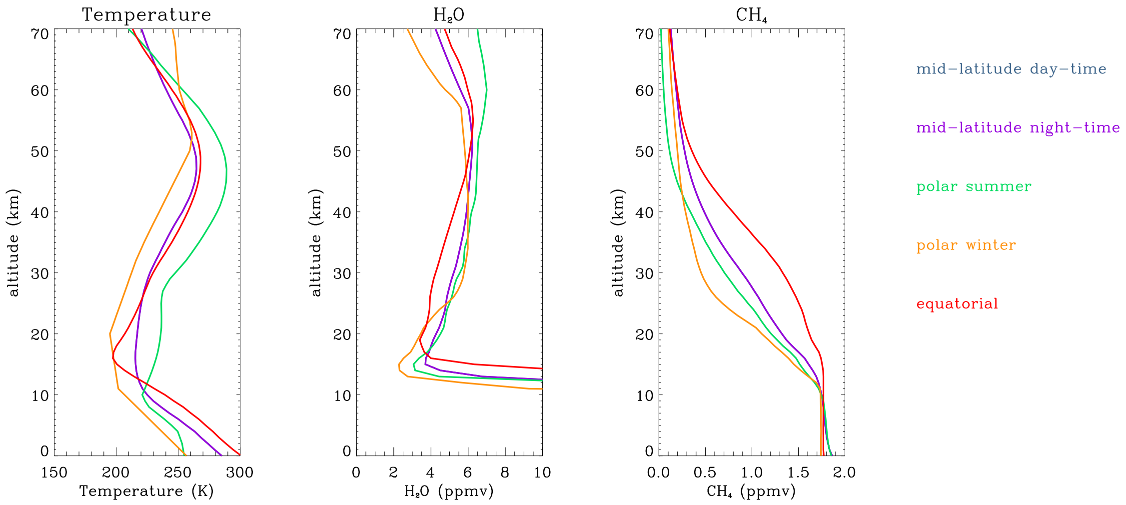

Figure 5.1: Reference atmospheres for different atmospheric conditions (Remedios, 1999)

Real data are affected by a number of sources of systematic errors. The use of simulated data offers the advantage of knowing the "true" atmospheric state and instrumental parameters, allowing the isolation of the effects of individual error sources. However, the use of simulated data requires a clear idea of the problem under investigation. This Chapter also includes the investigation of some more speculative possible causes of problems which required the use of real data. Attempts were made at using different microwindows (§ 5.4.2) and at extending the range of the continuum retrieval (§ 5.4.1).

A chapter on the use of the Oxford retrieval processor to investigate possible causes of problems in the ESA OFL processor ought to include some discussion on the differences between them. This is provided in § 5.5.

5.2 MIPAS Level 2 processing at Oxford

5.2.1 The Reference Forward Model

The Reference Forward Model (RFM) is a line-by-line radiative transfer model, which has been developed at Oxford, originally under an ESA contract, to provide reference spectral calculations for the MIPAS instrument. The model is a derivative of GENLN2 (Edwards, 1992), a general line-by-line atmospheric radiance and transmittance model developed at the University of Oxford and the US National Center for Atmospheric Research, Boulder, Colorado. Unlike the MIPAS operational forward model (OFM), the RFM is intended to perform calculations with the emphasis on accuracy rather than computation speed. The RFM also is used to generate irregular grids (GRDs) and look–up tables (LUTs) (see § 5.3.1) for use in the operational retrieval. It performs the radiative transfer calculation with user–specified instrumental parameters, measurement geometry, atmospheric model and spectroscopic data. Details and instructions for use of the RFM are in the RFM Software User's Manual (Dudhia, 2004b).

The retrievals described in this thesis make use of an updated version of the HITRAN (HITRAN, 2004) spectroscopic database. Additional measurements have been carried out specifically to improve parts of the database for MIPAS retrievals. These measurements are described in Flaud et al. (2003).

5.2.2 MORSE

The **M**IPAS **O**rbital **R**etrieval Using **S**equential **E**stimation (MORSE) is a retrieval code developed at the University of Oxford which uses the RFM as its forward model. MORSE was developed with the following aims:

- To provide a code which can either replicate or improve upon the ESA processing, in order to validate the ESA Level 2 products.
- To provide a retrieval code with which users can perform their own retrievals from the MIPAS spectra, in order to obtain products other than the ESA "high–priority" species. (For example, MORSE has been used for the retrievals of minor isotopes described in Chapter 6.)

MORSE uses a sequential estimation (see § 3.3) approach to the the retrieval problem (Rodgers, 2000). MORSE provides the option to change the auxiliary data files used, such as the microwindow lists and the FOV and ILS representations. It is also possible to change the auxiliary files in the ORM (§ 4.2). However, unlike the ORM, MORSE can provide some additional validation/verification of retrieval results by the use of a different retrieval method. In addition, unlike the least–squares fit approach used in the ESA retrievals, the use of a sequential estimation technique (§ 3.3.2) provides the opportunity to improve the robustness and stability of the retrieval by introducing some form of regularisation, here in the form of an *a priori* covariance matrix. This can be particularly useful in improving stability when trying to retrieve species with low signal to noise, such as minor isotopes (see Chapter 6). MORSE also offers the option of including an estimation of non–LTE effects (§ 2.1.3) in the retrieval. This option is utilised in § 5.3.2. In addition, MORSE can also be used to perform joint retrievals of two or more species.

It was mentioned in § 4.2.3 that the retrieved profiles are affected somewhat by the assumption of the initial guess profile outside the retrieval range. At the end of each iteration, the ESA retrieval scales the initial guess atmosphere above the top retrieval level by the ratio of the retrieved value at the top retrieval level to the value of the initial guess profile at that level, effectively treating the whole atmosphere above the top retrieval level as a single layer. MORSE can either be set to treat the atmosphere from the uppermost retrieval level upwards as one layer and scale this whole layer, or the thickness of the layer to be scaled can be defined by the user.

5.3 Forward model assumptions

Certain choices have been made in the approach to the retrieval of profiles from the Level 1B spectra which have the potential to affect the quality of the retrievals. These choices are described in detail in Ridolfi et al. (2000) and in Ceccherini et al. (2003). In this Section, some of the assumptions and approximations involved in the ESA operational retrievals are discussed and their consequences investigated.

In order to investigate the effects of selected forward model assumptions on the retrievals, a series of tests have been performed. Simulated spectra were generated using the RFM for each test case. The spectra were generated using reference atmospheres supplied by John Remedios (Remedios, 1999). Since the "true" atmospheric state and instrumental parameters are known, it should be possible to retrieve the truth exactly by using the truth as input to the forward model. The impact of different forward model assumptions on the retrieval can therefore be investigated separately by changing one assumption at a time.

"Spectral" assumptions have been investigated for a mid–latitude case only, while "vertical" assumptions have been investigated for both mid–latitude and equatorial cases.[1]

Retrievals were performed on the simulated "measurements" using MORSE. For the tests in this

---

[1] "Spectral" assumptions might also vary with latitude, depending on the effect of varying temperatures and gas concentrations on the signal to noise. However, this effect has not been investigated here.

Section, MORSE was run with 1000 % *a priori* standard deviation (100 K for temperature) and zero off–diagonal elements in the *a priori* covariance matrix in order to better emulate the ESA least squares fit retrieval. In each of the test retrievals, the initial guess profile was set to be equal to the truth. No noise was added to the simulated spectra, but the nominal NESR values were used in the construction of the measurement covariance matrix ($\mathbf{S}_\epsilon$) in the retrievals. The VMR retrievals were performed using both the true pT (in order that any difference in the retrieved profile from the truth could be attributed to the forward model assumption under investigation) and using the retrieved pT (in order to see the effects of the propagation of the pT error into the VMR retrievals).

5.3.1 Look up tables and irregular grids

The computation of cross–sections (see Equation 2.4) is a time–consuming part of the forward model calculations. There are a large number of spectral lines to be considered, a high spectral resolution is required, and there are a large number of pressure and temperature combinations for which the cross–sections must be computed. The cross–sections can either be computed line by line (LBL) with a pre–selected spectroscopic database, or read from pre–computed look–up tables (LUTs). For the purposes of the ESA operational processing, the OFM uses LUTs in order to cut down on the computing time spent on forward model calculations.

Another reason why the forward model calculations for MIPAS are time consuming is the need for a fine spectral resolution for the forward modelled spectra. Limb radiance spectra contain spectral features varying from sharp, isolated, Doppler–broadened lines at high altitudes to wide, overlapping Lorentz–broadened lines at low altitudes. To resolve the sharp features at high altitudes, a fine grid of the order of 0.0005 cm^{-1} is required. The choice of a fine spectral resolution means a large number of spectral points, implying a large number of calculations to be performed in the forward model. However, even if a fine grid is needed, not all of the points of this grid are equally important for the reconstruction of the spectral distribution. The full radiative transfer calculation need only be performed for a subset of fine grid points and the remaining spectrum can be recovered by interpolation. The subset of fine grid points (the irregular grid, or GRD) can be pre–calculated in order to save time in the forward model. The subset of suitable grid points will depend on the microwindow boundaries and on the instrument line shape (ILS — see § 2.2).

In the original study (Ridolfi et al., 2000), it was found that RFM line–by–line radiance calculations and RFM calculations using LUTs/GRDs agreed to within NESR/10. (Figure 2.6 shows the required NESR levels that were specified for MIPAS.) It was expected that this agreement was good enough that the use of LUTs and GRDs would not cause any significant differences in the retrieved profiles. In order to check this, line–by–line spectra were calculated using the RFM, and retrievals of pT, H_2O and CH_4 were performed with MORSE, using all the same settings that were used in the simulations (exactly the same ILS, FOV, geometry, atmospheric grid representation and method of interpolation between atmospheric levels) but using LUTs/GRDs rather than full line–by–line calculations. Results are shown in Figure 5.2.

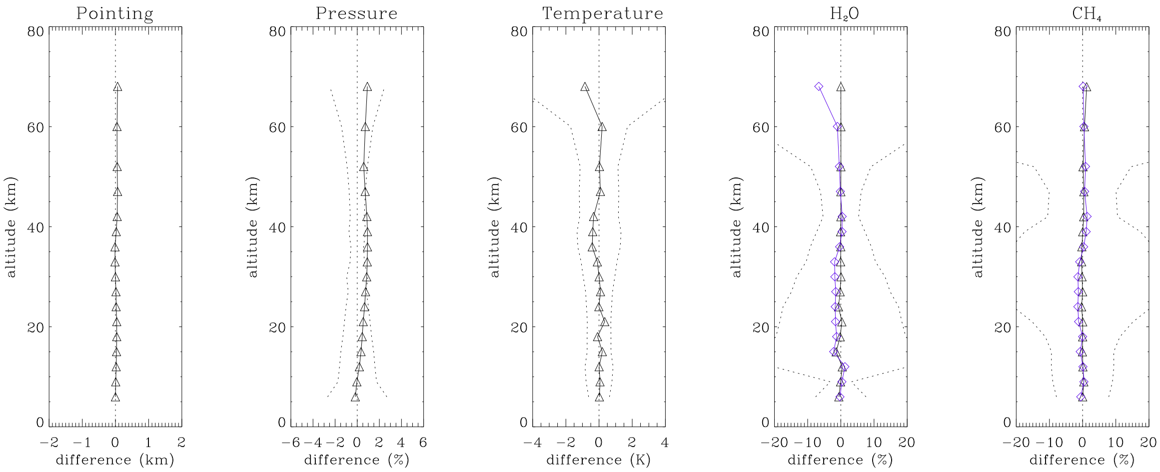

Figure 5.2: Difference between the retrieved and true profiles for altitude, pressure, temperature, H_2O and CH_4 for retrievals performed using LUTs and GRDs from simulated spectra generated using a mid–latitude day–time reference atmosphere. Temperature difference is (retrieved-truth), VMR differences are 100 %×([retrieved-truth]/truth). Dotted lines show the random error on the retrieval. For the VMR retrievals, black triangles show profiles obtained using the true pT and blue squares show profiles obtained using the retrieved pT.

It can be seen that the use of LUTs/GRDs leads to only very small differences in the retrieved profiles from the truth. It should be safe to say that the use of LUTs and GRDs rather than LBL calculations is not a cause of any of the observed problems in the ESA OFL retrievals.

5.3.2 Non–LTE

All the forward modelling involved in the ESA operational retrievals assumes that the atmosphere is in local thermodynamic equilibrium (LTE) (see § 2.1.3). This means that the temperature of the Boltzmann distribution describing the populations of the vibrational levels of any given molecule is equal to the kinetic temperature and that the source function in Equation 2.4 is equal to the Planck function at the local kinetic temperature. The assumption of LTE is expected to be valid at the lower altitudes where kinetic collisions are frequent. In the stratosphere and mesosphere, excitation mechanisms such as photochemical processes and solar pumping, combined with the lower collision relaxation rates, enable many of the vibrational levels of atmospheric constituents responsible for infrared emissions to have excitation temperatures that differ from the local kinetic temperature. Emission spectra (as opposed to absorption spectra) are particularly prone to non–LTE effects. Radiative transfer models which attempt to model non-LTE effects do exist, but the modelling of non–LTE effects was considered too complicated and uncertain to be included in the forward modelling for the ESA retrievals. An attempt to model non–LTE effects would also increase the computing time involved in the retrieval. In order to avoid using regions of the spectrum where non–LTE effects are large, non–LTE was included as a systematic error source in the selection of the operational microwindows. The microwindows that were selected should, in principle, therefore only include spectral regions where the emission is in thermodynamic equilibrium. However, for some gases, including water vapour and methane, it is very difficult to find useful lines at high altitude which are not affected by non–LTE. From the error analysis performed in the microwindow selection (see Figure 4.6), it is expected that non–LTE effects would be significant in the water vapour and methane microwindows only at the 52, 60 and 68 km tangent altitudes.

Non–LTE effects can be simulated using the RFM by supplying the model with vibrational temperature profiles. Simulated MIPAS spectra were calculated using the RFM with the inclusion of vibrational temperature profiles (Lopez Puertas et al., 2003) generated for the AMIL2DA project blind test retrievals (von Clarmann et al., 2003). Vibrational temperatures for AMIL2DA were supplied for both day–time and night–time mid–latitude conditions. Non–LTE effects are present in both day–time and night–time, but are expected to be dependent on illumination conditions and to be larger in the day–time. MORSE retrievals were performed from both day–time and night–time mid–latitude simulated spectra, assuming LTE in the forward model.

The results of the retrievals from "day–time non–LTE" RFM spectra are shown in Figure 5.3. Day–time non–LTE appears to cause a large positive bias in the temperature retrieval at 68 km and a large negative bias in the H_2O retrieval at 68 km. There is also a positive bias of up to around 5 % in the H_2O retrieval between 30 and 60 km and a positive bias of up to 12 % in the CH_4 retrieval between 30 and 68 km. If the vibrational temperatures used in the simulation are representative of the real atmosphere, then it appears that non–LTE could affect the retrievals below the range suggested by the error analysis shown in Figure 4.6.

The results of the retrievals from "night–time non–LTE" RFM spectra are shown in Figure 5.4. The night–time non–LTE in the simulated spectra does appear to have an effect on the retrievals at the highest altitudes, but the effect, as expected, is certainly not as large as for day–time non–LTE.

Although these tests have only been performed here for mid–latitude conditions, it is conceivable that non–LTE effects could vary significantly with latitude. It is possible that non–LTE effects in CH_4 could account for some of the observed variability in the bias of MIPAS CH_4 with respect to other data sources.

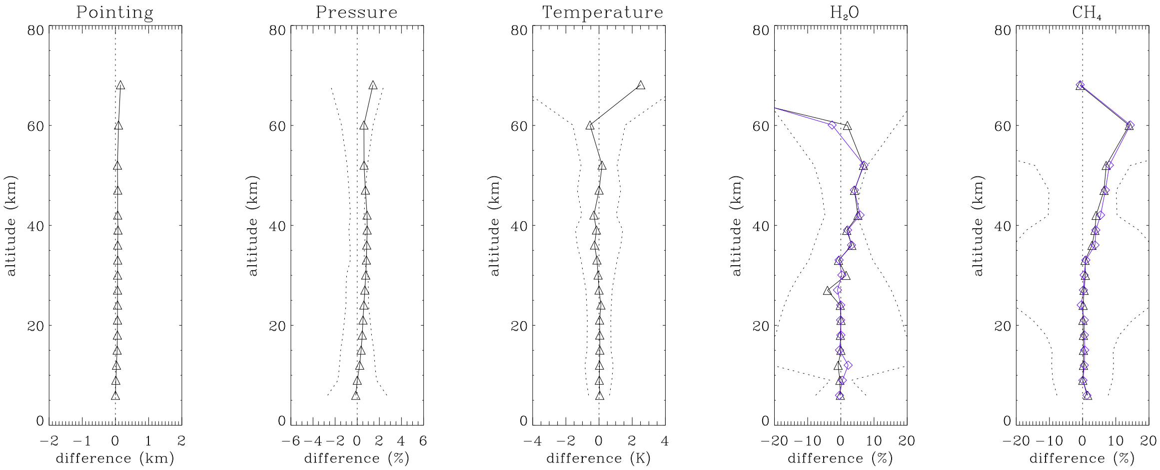

Figure 5.3: Difference between the retrieved and true profiles for retrievals performed from simulated spectra generated using vibrational temperature profiles representative of mid–latitude day–time conditions. Refer to Figure 5.2 for meanings of symbols.

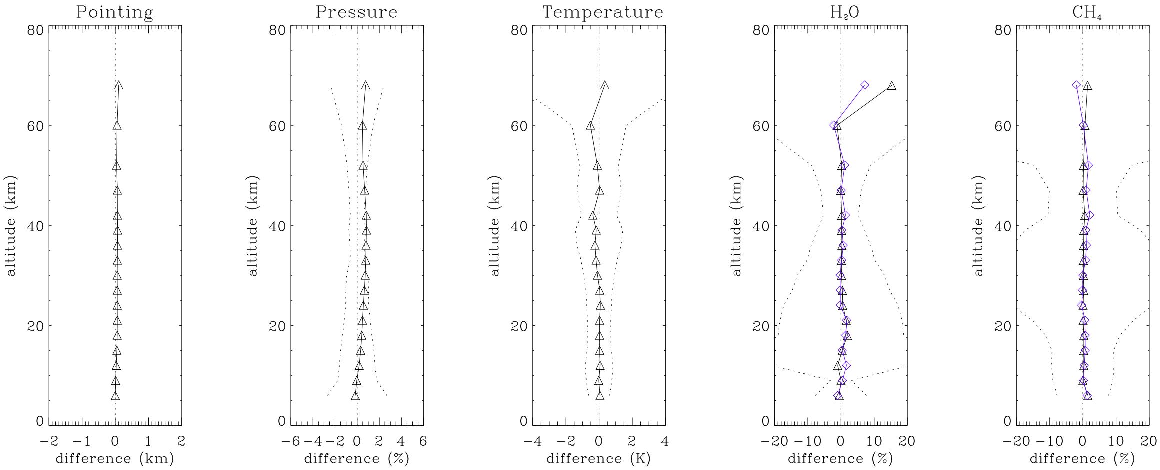

Figure 5.4: Difference between the retrieved and true profiles for retrievals performed from simulated spectra generated using vibrational temperature profiles representative of mid–latitude night–time conditions. Refer to Figure 5.2 for meanings of symbols.

5.3.3 The instrument line shape

For an idealised Fourier transform spectrometer (FTS) the instrument line shape (ILS) would be an apodised sinc function (see § 2.2). In reality, various instrumental effects result in an ILS which is likely to vary with wavenumber (and possibly with altitude) and may show some asymmetry. The shape of the ILS used in the forward model for the retrieval will have a bearing on the ability of the retrieval to fit the modelled spectra to the measurements and so has the potential to affect the retrieval results.

The residuals from the ESA OFL water vapour microwindows shown in § 4.4 contain features in the region of the water vapour lines, but these features are not the same shape as the lines. REC analysis (§ 3.5) of NRT residuals (Dudhia, 2003) indicated a possible problem with the modelling of the line shape in band C, and visual inspection of averaged OFL residuals provides additional confirmation.

In the ESA Level 2 pre–processing, the ILS is constructed using parameters supplied in the Level 1B files. These parameters should allow the construction of an ILS which takes instrumental effects into account (Lachance, 1999; ESA, 2000b). It was found in REC analyses (§ 3.5) of residual spectra from ESA NRT retrievals that there was a wavelength and altitude–dependent shift in the MIPAS spectra (Dudhia, 2003). The shift varies approximately linearly with wavenumber, ranging from approximately -0.001 cm^{-1} in the A–band microwindows to around $+0.002$ cm^{-1} in the C–band microwindows. The altitude–dependence results in a shift that is of the order of 0.001 cm^{-1} more negative at 68 km than at 6 km. Since a processor upgrade in November 2003, a correction has been applied to the ILS in the ESA Level 2 pre–processing to account for the wavelength–dependence. Effectively this acts as a correction to the spectral calibration. Due to the processor upgrade, a wavelength dependent shift is not present in the ESA OFL residuals. (The shift is still present in the Level 1B spectra, however, and so should be taken into account when performing one's own retrievals from the spectra.) No action was ever taken to account for the small altitude–dependent shift, which remains in the ESA OFL residuals.

At the time of the processor change, tests using the ORM (Ceccherini et al., 2003) on real data indicated that the correction for the wavelength–dependent shift made an improvement in the residuals and in the corresponding χ^2 values, but did not significantly affect the retrieved profiles. Real data, however, is subject to other systematic errors. In order to determine whether a wavelength–dependent shift would affect the retrievals in the absence of other error sources, simulated measurement spectra were generated using the RFM with a band–dependent shift included in the modelled ILS. Retrievals were then performed from these spectra using a forward–modelled ILS with no shift. The results are shown in Figure 5.5. The spectral shift appears to make it difficult for the retrieval to fit the temperature above 30 km. H_2O and CH_4 are also directly affected at high altitude.

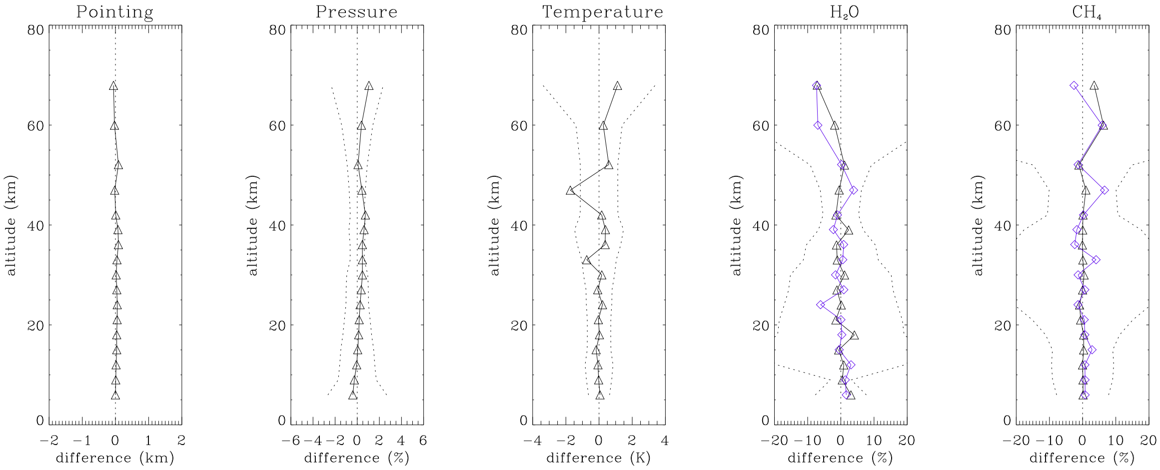

Figure 5.5: Difference between the retrieved and true profiles for retrievals performed from simulated spectra generated using an ILS with a band–dependent spectral shift applied, using a forward–modelled ILS without the band–dependent shift. Refer to Figure 5.2 for meanings of symbols.

In an attempt to determine the sensitivity of the retrieved profiles to an altitude–dependent shift in the spectra, simulated measurements were generated which included an altitude–dependent spectral shift. REC analyses (Dudhia et al., 2004) show a tendency towards a positive shift at low altitudes and a negative shift at high altitudes. With this in mind, the following spectral shifts were applied to the ILS used to generate the simulated spectra: $+0.001$ cm^{-1} between 6 and 15 km, $+0.0005$ cm^{-1} between 18 and 30 km, -0.0005 cm^{-1} between 33 and 47 km and -0.001 cm^{-1} between 52 and 68 km. Retrievals were then performed from these simulated spectra using a forward–modelled ILS with no shift applied. The results are shown in Figure 5.6. The altitude–dependent shift appears to cause some oscillations in the temperature retrieval above 30 km and causes some small oscillations in the H_2O and CH_4 retrievals. It would seem unlikely that the altitude–dependent shift is responsible for any of the persistent problems observed in the ESA OFL retrievals.

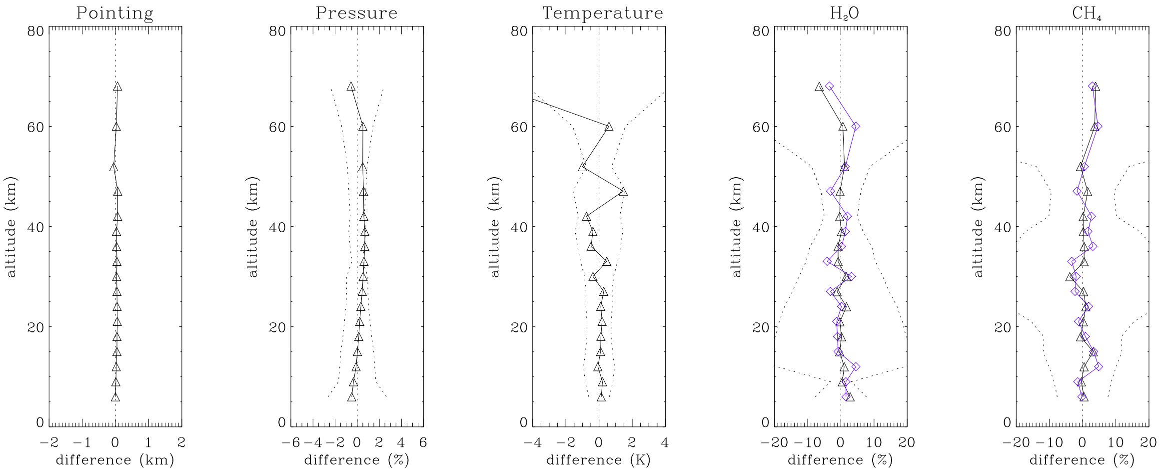

Figure 5.6: Difference between the retrieved and true profiles for retrievals performed from simulated spectra generated using an ILS with a altitude–dependent spectral shift applied, using a forward–modelled ILS without the altitude–dependent shift. Refer to Figure 5.2 for meanings of symbols.

The width of the ILS might also be expected to affect the ability of the retrieval to fit modelled spectra to the measurements. In an attempt to investigate the effect of the ILS width on the retrievals, "measurement" spectra were generated using the RFM using the idealised ILS shown in Figure 2.3. Retrievals from these simulated spectra were then performed using a narrowed and a broadened version of this idealised ILS, with the width changed by 2 % over the full spectral range in each case. The differences in the retrieved profiles from the truth in each of these cases are shown in Figures 5.7 and 5.8. A difference in the width of the modelled ILS from the width of the true ILS appears to have a strong effect on the temperature retrieval, particularly at high altitude. There are also direct effects on the H_2O and CH_4 retrievals. A problem with the ILS width does appear to be a possible candidate for biases in the H_2O and CH_4.

It should be noted that the same change in width here has been applied at all wavenumbers. It is conceivable that an error in ILS width would not be constant across all wavenumbers, in which case it would be quite possible for this problem to have a different effect on, say, H_2O and CH_4,

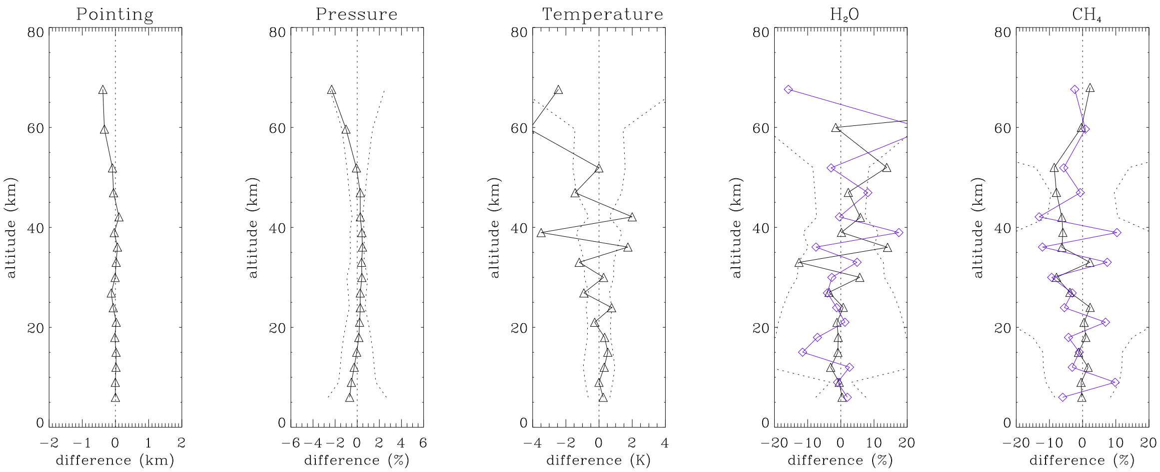

Figure 5.7: Difference between the retrieved and true profiles for retrievals performed from simulated spectra generated using the idealised ILS shown in Figure 2.3 using a modelled ILS which is 2 % narrower than the truth. Refer to Figure 5.2 for meanings of symbols.

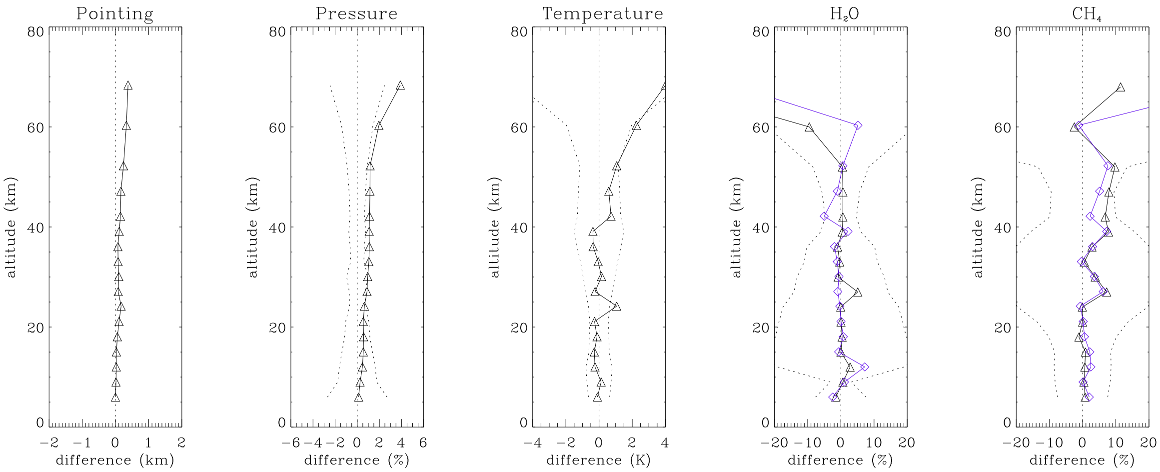

Figure 5.8: Difference between the retrieved and true profiles for retrievals performed from simulated spectra generated using the idealised ILS shown in Figure 2.3 using a modelled ILS which is 2 % broader than the truth. Refer to Figure 5.2 for meanings of symbols.

which use different spectral regions for the retrievals.

5.3.4 Initial guess atmosphere above the top retrieval level

It was mentioned in § 4.2.3 that the retrieved profiles are affected somewhat by the assumption of the initial guess profile outside the retrieval range. It was thought possible that the observed bias in the ESA OFL H_2O might be related to a poor representation of the atmospheric state above the uppermost retrieval level. The two variables thought most likely to have an effect on the H_2O bias were temperature and H_2O. The amount of CH_4 present above the uppermost retrieval level is small and was thought unlikely to be the cause of any biases in the ESA OFL retrievals.

In order to test whether or not the retrievals were sensitive to the atmospheric state above the uppermost retrieval level, MORSE was run using different initial guess profiles. In the "true" atmosphere used to generate the simulated measurements, profiles above the uppermost retrieval level were set to the the mid–latitude reference atmosphere values. Retrievals were performed with initial guess temperature profiles above the uppermost retrieval level increased by mid–latitude day–time 1σ estimates of variability suppled by John Remedios (Remedios, 1999). The results are shown in Figure 5.9. Another set of retrievals were performed where initial guess temperature profiles above 68 km were kept at IG2 values, but the H_2O profiles above the uppermost retrieval altitude were increased by mid–latitude day–time 1σ estimates of variability. The results are shown in Figure 5.10.

The effects of perturbations to the atmosphere above the uppermost retrieval level are, unsurprisingly, most apparent at high altitude. Although these tests are somewhat crude, they do show that the retrieval is sensitive to the initial guess profile above the uppermost retrieval level and so highlight this issue as a potentially useful area for further investigation.

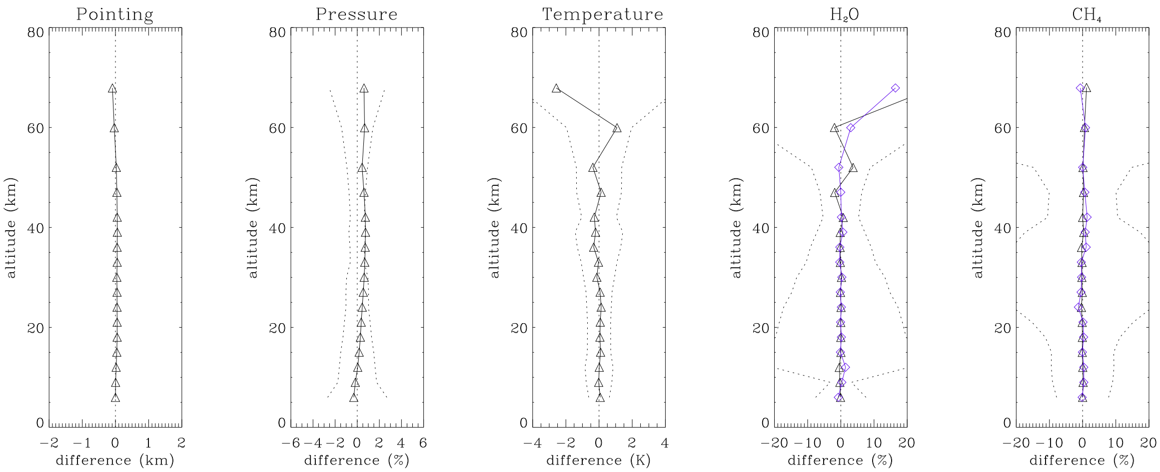

Figure 5.9: Difference between the retrieved and true profiles for retrievals performed from simulated spectra generated using a mid–latitude reference atmosphere using a perturbed temperature profile above the uppermost retrieval level. Refer to Figure 5.2 for meanings of symbols.

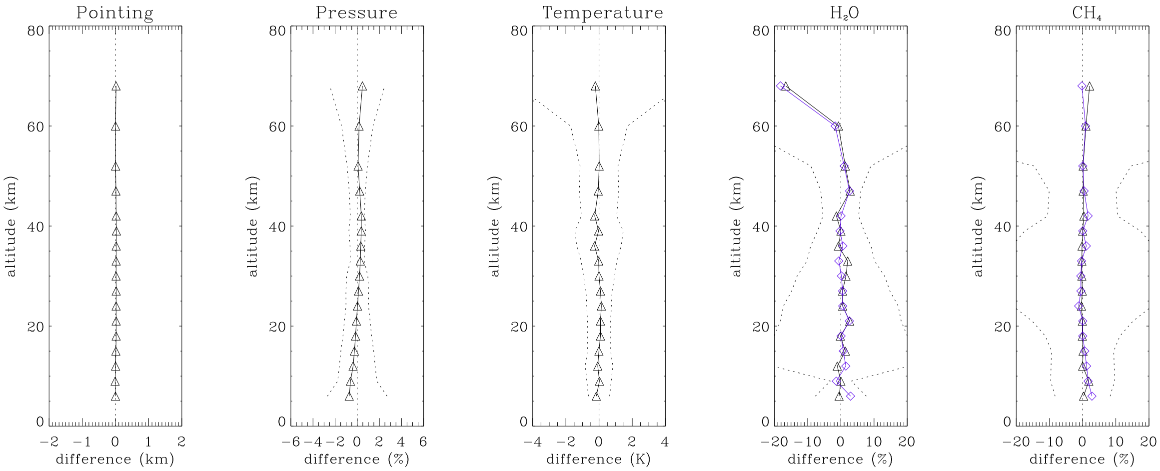

Figure 5.10: Difference between the retrieved and true profiles for retrievals performed from simulated spectra generated using a mid–latitude reference atmosphere using a perturbed H_2O profile above the uppermost retrieval level. Refer to Figure 5.2 for meanings of symbols.

5.3.5 FOV representation

The MIPAS FOV is conventionally defined as being a trapezium. The shape is determined by the viewing aperture rather than the detectors and so should be well–defined. Pre–flight measurements using a hot point source were used to verify that the FOV "seen" by all the different detectors coincided. It should be noted that for infrared instruments such as MIPAS, the minimum size of the FOV is set by the requirement to collect enough photons rather than to avoid diffraction effects, which can be significant at longer wavelengths (eg for microwave instruments).

The choice of representation of the FOV function might also be expected to affect the ability of the retrieval to fit the modelled spectra to the measurements. The convolution of the atmospheric radiance with the AILS and the FOV (see Equation 4.1) is expressed in terms of continuous integrals, but in the forward model these continuous integrals must be represented as a discrete summation over suitably small intervals of wavenumber and tangent height. In order to perform the summation, forward–model calculations are performed for a number of "pencil beam" lines of sight that span the vertical range of the FOV for each tangent altitude z_t. The number of forward model calculations required is determined by the number of points on which the FOV is represented in the forward model.

The radiance reaching the instrument from different altitudes within the span of the MIPAS FOV may vary significantly, more so the lower down in the atmosphere that MIPAS is pointing. This variation may be approximately linear with height at the higher measurement altitudes, but is likely to be non–linear at lower altitudes. A finer representation of the FOV in the forward model is advantageous from the point of view that it will lead to more realistic simulated spectra. However, a coarser representation offers the advantage of less time spent in the forward model calculations. The choice of representation of the FOV might be expected to have a greater effect on the retrievals at lower altitudes.

In the OFM, the FOV of the instrument is represented in the vertical by 4 points which form a trapezium of base 4.02 km and top edge of 2.56km. For the purposes of the convolution in Equation 4.1, the radiance is interpolated quadratically between points and the FOV is interpolated linearly between points. The RFM interpolates linearly both for the radiance and for the FOV. In the case of the FOV, this should be a reasonable approximation. In the case of the radiance variation, this is probably not such a good approximation, particularly at low altitudes.

Figure 5.11 shows a 5 point FOV function and a 12 point trapezoidal FOV function. The 5 point FOV was designed to give the same radiance as the 12 point trapezium when convolved with a quadratically varying radiance. The reasoning behind a 5 point FOV was to sample the FOV at 1.5 km in order to maximise the duplication of pencil beam calculations when sampling at 3 km between tangent altitudes. In the 1.5 km representation, the zero and the maximum values are fixed, leaving the ±1.5 km values as the adjustable parameter to get the agreement with the trapezium.

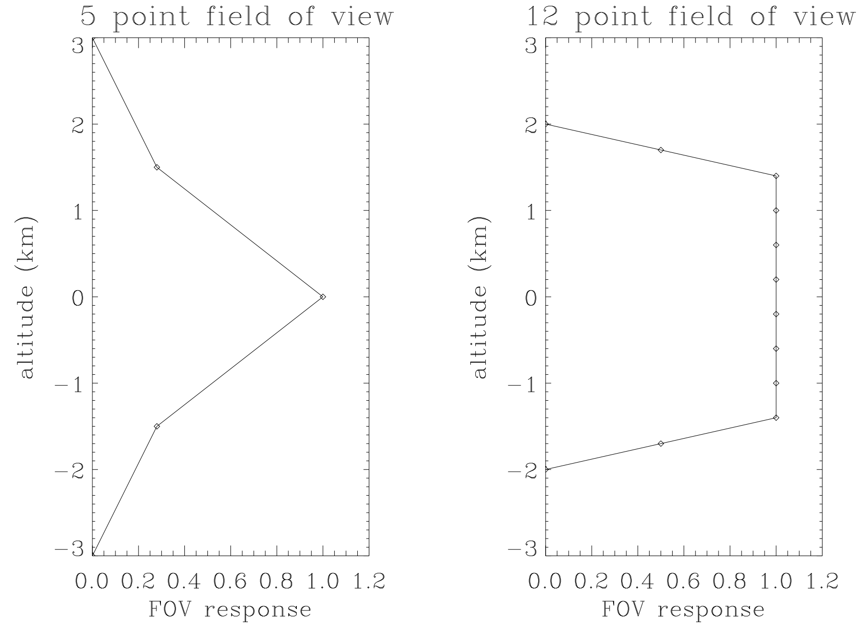

Figure 5.11: Two different possible representations of the field of view (FOV) in the vertical.

In order to determine whether the representation of the FOV has a significant effect on the retrieval, RFM spectra were generated using the 12 point trapezoidal FOV. MORSE retrievals were performed from these spectra using the 5 point FOV. Strictly speaking, this is not a test of the FOV approximation in the OFM, since the OFM handles the FOV convolution differently to the RFM. However, this test should give some indication of whether or not the retrievals are sensitive to the FOV representation used.

This is an assumption relating to the vertical domain in the forward model. As such, its effect on the retrieval might be expected to vary with the vertical structure of the atmosphere. In view of this, this test was performed using both mid–latitude and equatorial reference atmospheres. Figure 5.12 shows results from the mid–latitude case, while Figure 5.13 shows results from the equatorial case.

The effects of the FOV representation on the retrievals are certainly more marked for the equatorial case. Equatorial retrievals of H_2O and CH_4 show a marked oscillation in the region of the tropopause. It is also interesting to note that the choice of FOV representation has a markedly different effect on the pressure retrieval for the equatorial case than for the mid–latitude case.

5.3.6 Assumption of a 3 km vertical grid

Another assumption implicit in the forward modelling for the ESA operational retrievals is that the atmosphere can be represented on a grid corresponding to the MIPAS nominal tangent altitudes (ie a 3 km grid between 6 and 42 km, and wider spacing above this). In the OFM, changes in temperature and VMR are assumed to change linearly between these grid points (see also § 5.3.7).

This is particularly likely to present problems where there are sharp changes in temperature or volume mixing ratio profiles, for example, in temperature at the tropopause and at the stratopause (where the changes are not particularly sharp but the spacing of MIPAS tangent points is wide) or in water vapour around and below the tropopause.

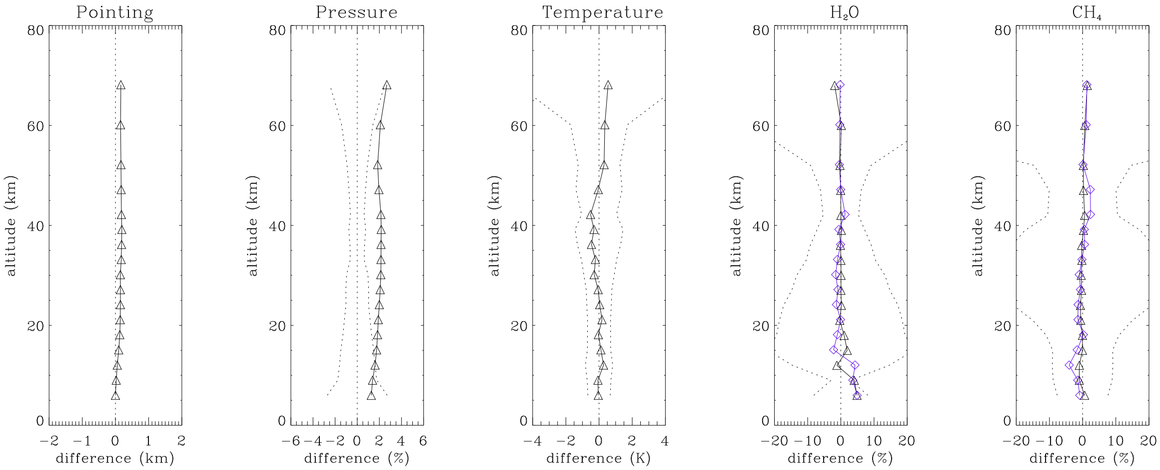

Figure 5.12: Difference between the retrieved and true profiles for retrievals performed using a 5 point FOV representation from simulated spectra generated with a 12 point FOV representation and a mid–latitude day–time atmosphere. Refer to Figure 5.2 for meanings of symbols.

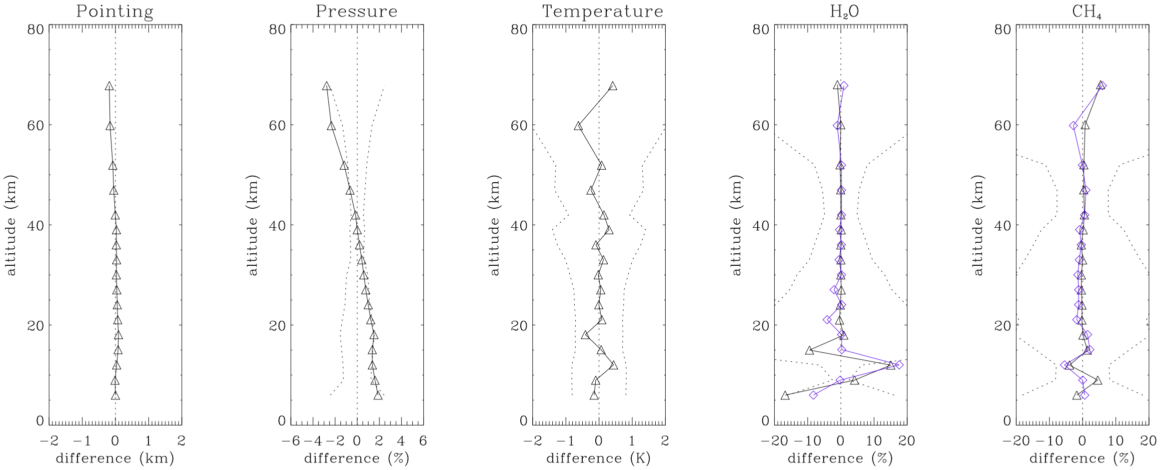

Figure 5.13: As above, but for an equatorial reference atmosphere.

Spectra were simulated using the RFM with a 1 km atmospheric grid. Retrievals were then performed on these simulated "measurements" with MORSE, using a grid corresponding to the nominal MIPAS tangent altitudes. Since this is a "vertical" assumption, tests were performed using spectra simulated from both mid–latitude and equatorial reference atmospheres. The results for the mid–latitude case are shown in Figure 5.14 while the results for the equatorial case are shown in Figure 5.15.

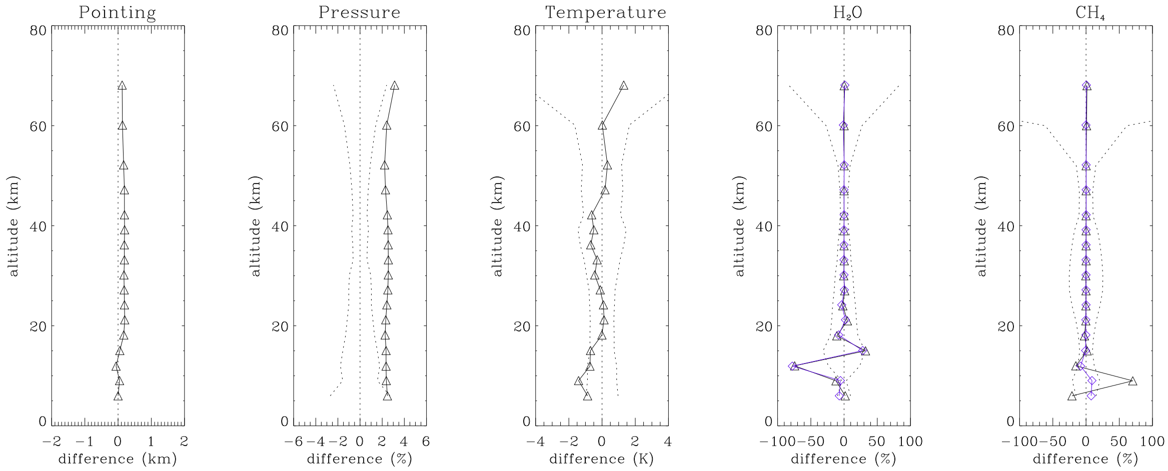

Figure 5.14: Difference between the retrieved and true profiles for retrievals performed from simulated spectra generated using a 1 km atmospheric grid and a mid–latitude reference atmosphere. Temperature difference is (retrieved-truth), VMR differences are 100 %×([retrieved-truth]/truth). Dotted lines show the random error on the retrieval. For the VMR retrievals, black triangles show profiles obtained using the true pT and blue squares show profiles obtained using the retrieved pT.

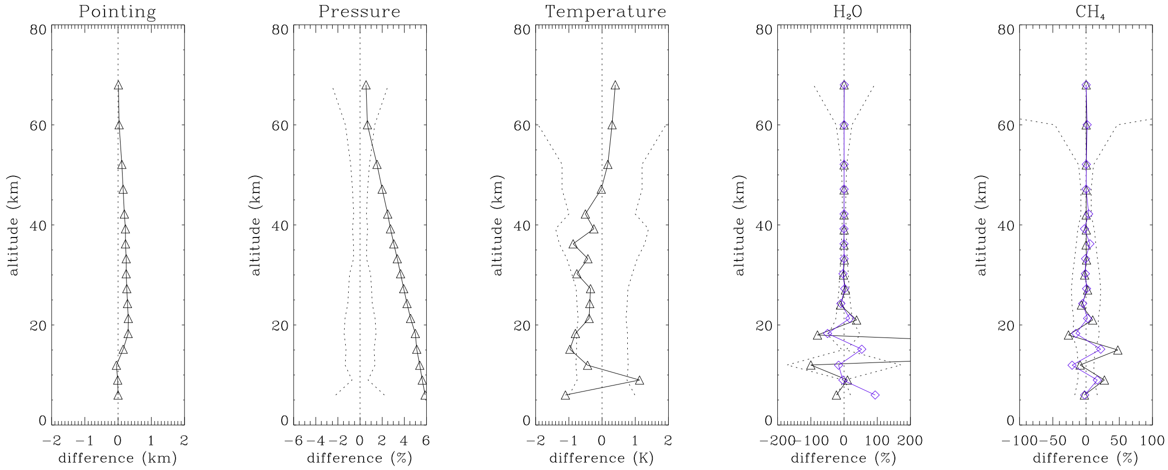

Figure 5.15: As above, but for an equatorial reference atmosphere.

The assumption of a 3 km grid can be seen to cause problems in the retrievals at low altitudes. It is clear that the effects are more marked for the equatorial case. As in the tests relating to the FOV representation, there is a markedly different effect on the retrieved pressure between the mid–latitude and equatorial cases. The issue of the vertical grid is a clear possible candidate for the causes of the persistent oscillations in the equatorial OFL CH_4 profiles.

Although the CH_4 does not change sharply with altitude in the tropics, the fact that the temperature changes sharply will mean that the radiances change sharply, affecting the ability of the retrieval to accurately model the radiances.

It should be noted here that the effect of assuming that the atmosphere can be represented on a 3 km vertical grid in the region of the tropopause will depend somewhat on the altitude of the tropopause. If the altitude of the tropopause corresponds to a MIPAS tangent altitude (say, 12 or 15 km), then it might be expected that the assumption would be less detrimental to the retrieval than if the tropopause were at, say 11 km. The altitude of the tropopause in the reference atmospheres used here can be seen in Figure 5.1.

It is also worth noting that in this case the VMR retrievals which use the retrieved pT are closer to the truth than those which use the true pT, implying that the pT retrieval compensates for the effect.

5.3.7 Assumption of linear variation of VMR

Within the OFM, the atmosphere is represented on a grid corresponding to the MIPAS nominal tangent altitudes (c.f. § 5.3.6). Trace gas profiles are interpolated in the OFM using the assumption that VMR varies linearly with altitude. Where profiles are relatively smooth and slowly varying, this is a reasonable assumption. However, where there are large variations in the VMR with altitude (for example in H_2O at low altitudes) this assumption might be expected to cause problems.

The RFM can be set to use linear interpolation of VMR between altitudes, but also provides the option of using logarithmic interpolation. Simulated measurement spectra were generated using the assumption of linear interpolation of VMR and temperature. Retrievals were then performed using logarithmic interpolation. There is an assumption here that the effect is reasonably linear, and that the differences from the truth in a "logarithmic" retrieval from "linear" measurement spectra should be of the same magnitude but of opposite sign to the differences from the truth resulting from a "linear" retrieval from "logarithmic" measurement spectra.

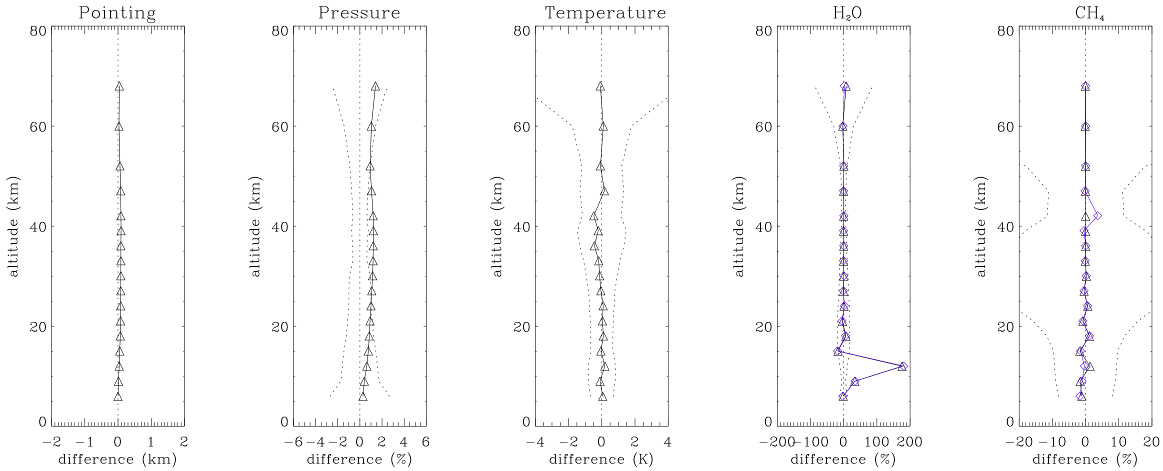

Figure 5.16: Difference between the retrieved and true profiles for retrievals (using logarithmic interpolation between levels) performed from simulated spectra generated using linear interpolation between retrieval levels and a mid–latitude reference atmosphere. Temperature difference is (retrieved-truth), VMR differences are 100 %×([truth-retrieved]/truth). Dotted lines show the random error on the retrieval. For the VMR retrievals, black triangles show profiles obtained using the true pT and blue squares show profiles obtained using the retrieved pT.

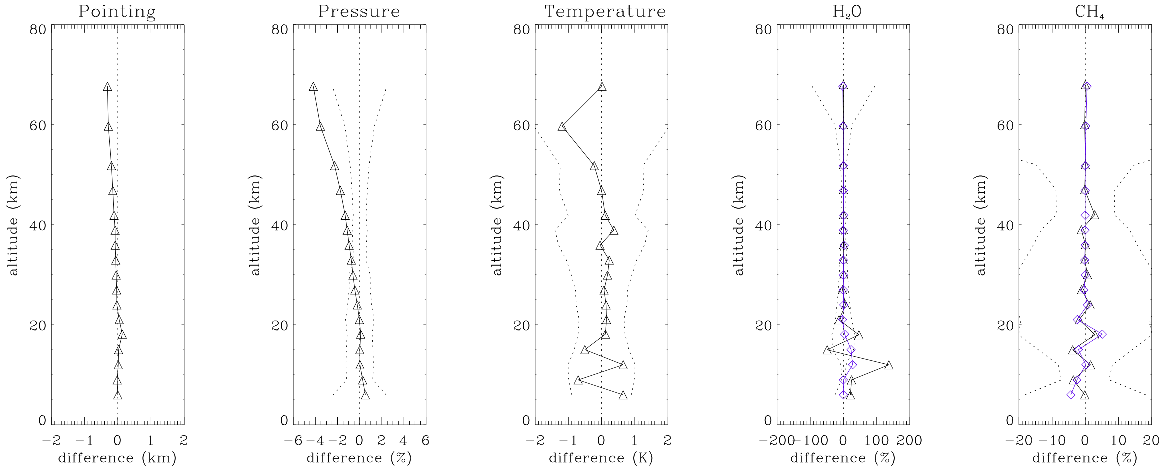

Figure 5.17: As above, but for an equatorial reference atmosphere.

Results are shown in Figures 5.16 and 5.17. These tests appear to show that the assumption of linear interpolation between levels could cause problems in the retrievals if the variation of atmospheric profiles with altitude really is logarithmic, particularly in the region of the tropical tropopause. However, these tests do not show whether "linear" or "logarithmic" variation is a better assumption for retrievals from real data.

5.3.8 Distortion of the FOV due to refraction

In the OFM, the shape of the FOV is assumed to be constant as a function of the scan angle. In reality, the projection of the FOV at the tangent point will be distorted by the effects of refraction in the atmosphere, particularly at low altitudes. Including this distortion in the forward model takes extra computing time, since the pencil beams no longer coincide for adjacent tangent paths. The RFM can model this distortion of the FOV, or can be set not to by the use of a flag.

Figure 5.18 shows the distortion of the FOV due to refraction.

Simulated measurement spectra were generated without the inclusion of the effects of refraction on the FOV. Retrievals were then performed with the forward model set to include the effects of refraction on the FOV. Again, there is an assumption here that the effect is reasonably linear, and that the differences from the truth in a "refraction" retrieval from "no refraction" measurement spectra should be of the same magnitude but of opposite sign to the differences from the truth resulting from a "no refraction" retrieval from "refraction" measurement spectra.

The results for the mid–latitude case are shown in Figure 5.19 while the results for the equatorial case are shown in Figure 5.20. Again, there are marked differences in the effect on the pressure retrieval between mid–latitude and equatorial cases. And again, there are marked effects on the H_2O and CH_4 retrievals in the region of the tropopause which are more pronounced in the equatorial case.

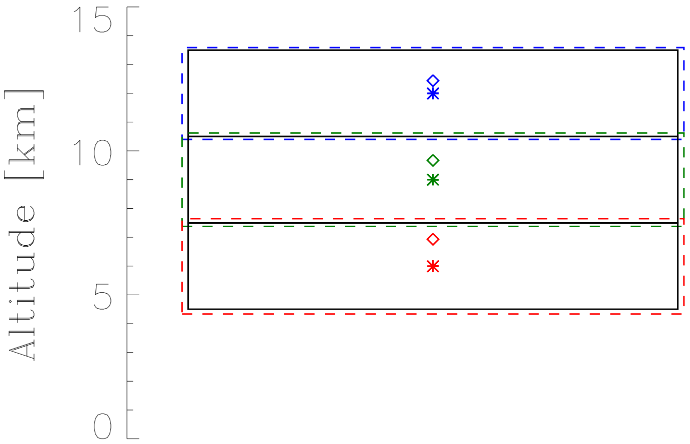

Figure 5.18: A representation of the effect of refraction on the instrument FOV at the tangent point. Diamonds are geometric tangent heights, + signs are refracted tangent heights. Black boxes represent an assumed projection of a 3km-high FOV according to the ESA retrieval. Dashed lines represent the actual broadening of the FOV due to refraction effects (+/- 150m for the 6km tangent height) and the × signs represent the centre of gravity of the distorted FOV. The distortion is fairly linear over the FOV height so that the × are almost superimposed on the + signs. The main impact on the retrievals therefore comes just from the broadening rather than any shift in the effective tangent point. (Plot supplied by Anu Dudhia.)

5.4 Retrieval assumptions

The tests performed in § 5.3 were on single profiles, using simulated data, and could all, in principle, have been performed before the launch of the MIPAS instrument. Other possible causes of problems which could not be investigated using simulated data are covered in this Section.

5.4.1 Altitude range of the continuum retrieval

It was noted in § 4.2.2 that the ESA retrievals include a fitting of atmospheric continuum in each microwindow. The continuum is fitted in order to take account of any broad spectral features which are not well represented in the forward model. Possible causes of these sorts of broad spectral features include atmospheric aerosol and thin cloud. Continuum values are fitted for each

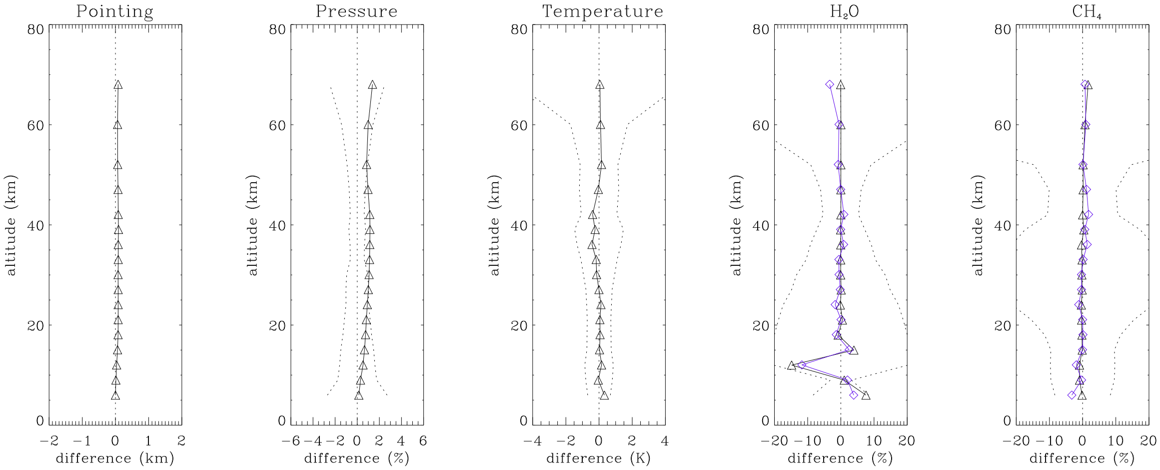

Figure 5.19: Difference between the retrieved and true profiles for retrievals (with the effects of refraction on the FOV included) performed from simulated spectra generated without the inclusion of the effects of refraction on the FOV and a mid–latitude reference atmosphere. Temperature difference is (retrieved-truth), VMR differences are 100 %×([truth-retrieved]/truth). Dotted lines show the random error on the retrieval. For the VMR retrievals, black triangles show profiles obtained using the true pT and blue squares show profiles obtained using the retrieved pT.

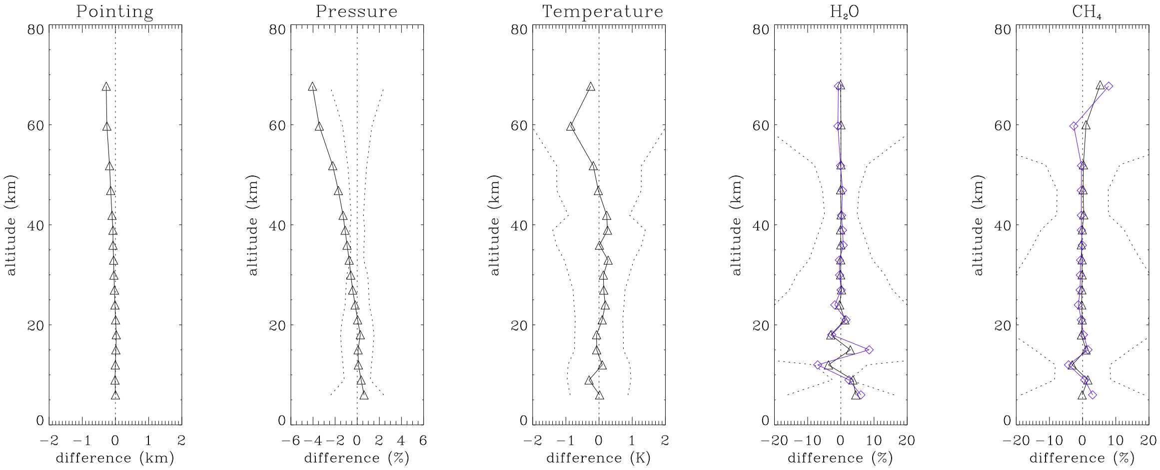

Figure 5.20: As above, but for an equatorial reference atmosphere.

microwindow at each tangent altitude, but only for altitudes up to 30 km. It has been noted that the MIPAS OFL H_2O shows a high bias above 30 km. In an attempt to determine whether this could be related to the choice of upper altitude for the continuum retrieval, MORSE retrievals were run for a sample orbit with continuum retrievals all the way up to 68 km and the results compared with a run where the continuum retrieval stopped at 30 km. The results are shown in Figure 5.21.

The average of the differences over the orbit is generally small, but the standard deviation of the differences is comparable to, and in some cases greater than, the average random error, particularly for the CH_4 retrievals. The retrieval of continuum up to 68 km results in a slight reduction in χ^2 values. It also results in slightly lower H_2O values between 30 and 60 km, but the difference is not large enough to account for the observed bias in H_2O.

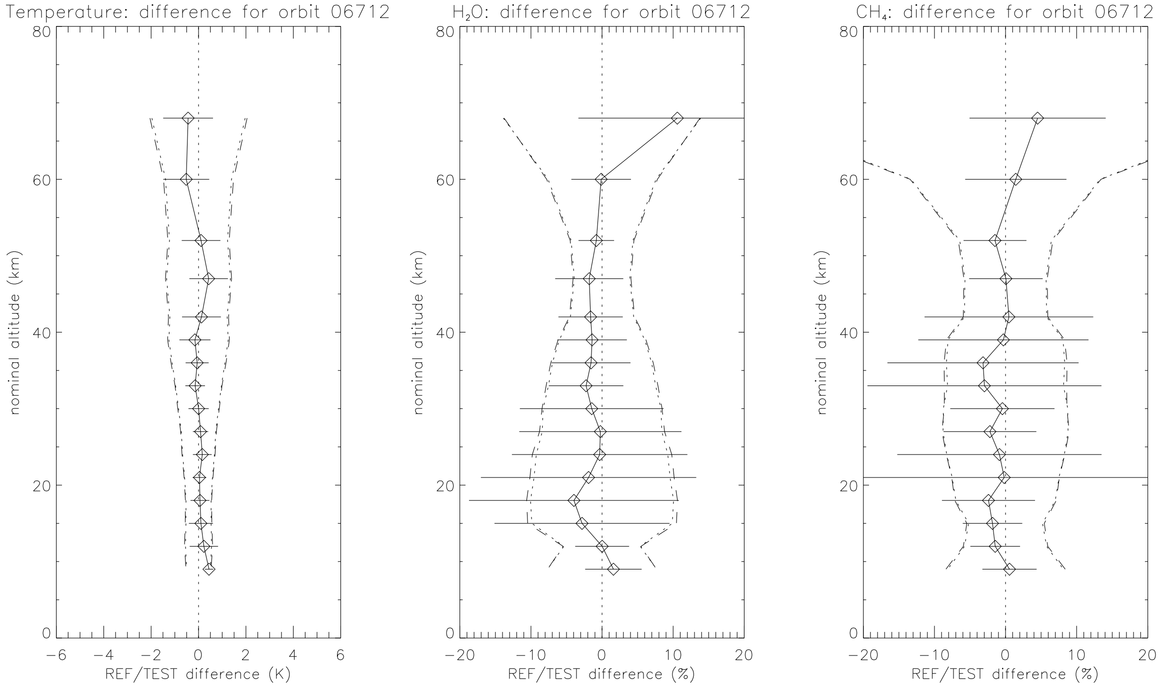

Figure 5.21: Comparison between two sets of MORSE retrievals for orbit 06712. One set includes a continuum retrieval up to 30 km (as is done in the ESA OFL retrievals — reference case) while the other includes a continuum retrieval all the way up to 68 km (test case). Plots show the mean of the differences around the orbit. Temperature difference is (test-reference), VMR differences are 100 %×([test-reference]/reference). Dotted lines represent the average random error on the reference case, dashed lines represent the random error on the test case and horizontal lines represent the standard deviations on the mean difference profile.

5.4.2 Avoiding C-band microwindows

It has been postulated (in discussions at MIPAS Quality Working Group meetings) that the observed high bias in the MIPAS OFL water vapour may be due to some problem with the modelling

Table 5.1: Spectral and altitude ranges of the non–band–C H_2O microwindows

Microwindow label	Spectral range	MIPAS spectral band	Altitude range
H2O_0002	807.850–808.450 cm^{-1}	A	9–18 km
H2O_0021	1454.525–1457.525 cm^{-1}	B	15–68 km
H2O_0023	1472.025–1473.475 cm^{-1}	B	15–36 km

of the line shape in the C band, which is where all the information for the H_2O retrieval comes from. In order to test this theory, retrievals were performed using microwindows outside the C band.

It has been mentioned previously that the operational microwindows detailed in Table 4.2 are used most, but not all, of the time in the operational processing. Alternative microwindows are supplied to the processor for use in cases where certain spectral bands are corrupted. The wider set of microwindows includes a subset of H_2O microwindows which can be used when the C band is unavailable. The spectral and vertical positions of these non–C–band microwindows are shown in Table 5.1. Note that the set includes the same A–band low altitude H_2O microwindow (H2O_0002) as the nominal set.

Results are shown in Figure 5.22. The use of non–band C microwindows does not appear to result in lower H_2O values above 30 km.

5.5 ESA/MORSE differences for a sample orbit

Since MORSE has been used in this Chapter to investigate possible causes of problems in the ESA retrievals, differences between the ESA OFL retrievals and the MORSE retrievals as used in this Section should be discussed. The ESA and MORSE retrievals in this Section used the same Level 1B spectra, the same microwindows, the same approach to cloud–clearing and the same approach to the continuum retrieval. Differences in the approach are listed below:

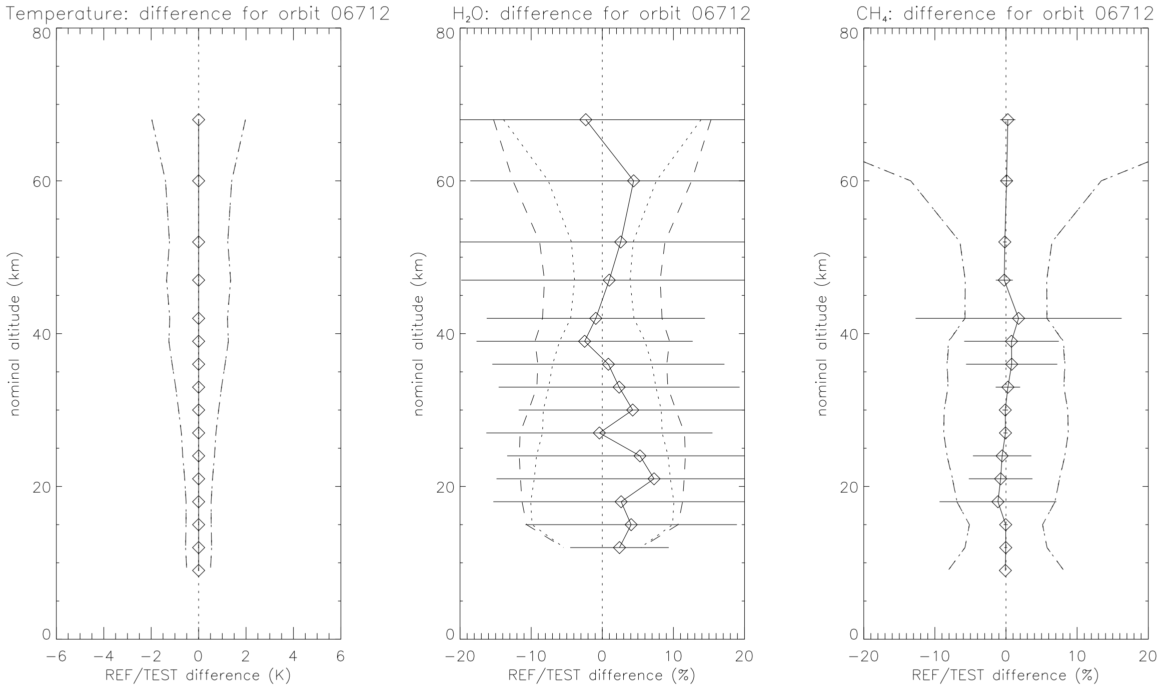

Figure 5.22: Comparison between two sets of MORSE H_2O retrievals for orbit 06712. One set (reference case) uses the operational microwindows. The other (test case) uses a set of microwindows which avoid the C band. Plot shows the mean of the differences around the orbit. VMR differences are 100 %×([test-reference]/reference). Dotted lines represent the average random error on the reference case, dashed lines represent the average random error on the test case and horizontal lines represent the standard deviations on the mean difference profile.

- **Retrieval method**: Least squares fit with no *a priori* constraints (ESA) as opposed to sequential estimation with *a priori* constraints (MORSE). For the tests on simulated data performed in § 5.3, MORSE was run using very loose constraints and zero correlation length in the *a priori* covariance matrix in order to better emulate the ESA retrieval. However, when MORSE is run in this way for retrievals from real data, the lack of constraints leads to strong oscillations in the retrieved profiles. For this reason, in this Section, MORSE has been run using 100 % *a priori* standard deviation (10 K for temperature). The *a priori* covariance matrix for the retrievals in this Section has been constructed using matrix elements given by (Rodgers, 2000):

$$\mathbf{S}_{ij} = \sigma_a^2 \exp\left(-|i-j|\frac{\partial z}{h}\right) \tag{5.1}$$

where σ is the *a priori* standard deviation, ∂z is the level spacing (e.g. 3 km) and h is the "correlation length", the length scale at which the interlevel correlation is $1/e$. The correlation length was chosen to be 50 km.

- **FOV convolution**: The OFM uses a slightly different representation of the FOV and handles the convolution slightly differently than the RFM (§ 5.3.5).
- **Initial guess**: Initial guess profiles for the ESA OFL retrievals are constructed from a combination of the IG2 climatology, ECMWF analyses and the retrieved profiles from the previous limb scan. Initial guess profiles used here for the MORSE retrievals are taken directly from the IG2 climatology.
- **The treatment of the initial guess atmosphere above the uppermost retrieval level**: In the ESA OFL retrievals, the atmosphere above the uppermost retrieval level is treated as one layer. When the target parameter at the top retrieval level is adjusted by the retrieval, so is the whole initial guess atmosphere above it. MORSE can be made to do this, but in the retrievals in this Section, MORSE was run with an extra retrieval level at 76 km, and an adjustable layer above this extending up to 90 km. Above that, the initial guess atmosphere is left unchanged by retrieval iterations.
- **Instrument line shape**: The instrument line shape used in the ESA OFL retrievals is constructed from parameters supplied in the Level 1B data using software supplied by ABB Bomem (Lachance, 1999). The MORSE retrievals shown here use band–dependent lineshapes with a wavelength–dependent shift correction applied, but are not constructed from the parameters in the Level 1B files.
- **Occupation matrices**: As the ESA retrieval is a least–squares fit, if certain sweeps or spectral regions are cloudy or corrupt, the state vector must be changed in order to exclude these problem regions from the retrieval. The ESA OFL retrieval uses "occupation matrices", pre–defined sets of microwindows and sweeps. Sometimes this means adding extra microwindows. MORSE does not switch to alternative sets of microwindows in the case of problems,

but simply does not use information from problematic altitudes or spectral regions in the retrieval.

MORSE retrievals were run using the configuration described above for orbit 06712 (which occurred on 12^{th} June 2003) and the results compared with the ESA OFL Level 2 data for the same orbit. Atmospheric parameters retrieved by the ESA OFL processor that come before each target in the ESA OFL retrieval sequence are taken from the ESA OFL Level 2 data for the scan in question (for example, the MORSE CH_4 retrievals shown here use the ESA OFL retrieved pT, H_2O, O_3 and HNO_3 profiles as input to the retrieval for each scan). Atmospheric parameters retrieved by the ESA OFL processor that come after the target species in the ESA OFL retrieval sequence are taken from the ESA OFL Level 2 data for the previous scan (the MORSE CH_4 retrievals shown here use the ESA OFL retrieved N_2O and NO_2 from the previous scan). This is done in order to minimise any differences that might arise from differences in the pT retrieval or in contaminant gas profiles.

ESA/MORSE differences for orbit 06712 are summarised in Figure 5.23. The average difference in temperature profiles is within ±1 K over most of the retrieval range, while the average difference in the VMRs of H_2O and CH_4 is generally within ±5 %. The average differences between the ESA OFL and MORSE temperature, H_2O and CH_4 are generally smaller than the average random error on the profiles. There are exceptions to this at the top and the bottom of the profiles. It might be expected that the results would show some differences, particularly at the uppermost retrieval altitude, given the differences in retrieval approach listed.

Orbit 06712 does not contain any limb scans that are flagged as cloud–free down to 6 km. This is not unusual. On the scale of an orbit, it is unlikely that there would be more than one or two anyway. The cloud flagging scheme is known to flag even clear spectra at 6 km as cloudy. It was not really designed for use below 12 km.

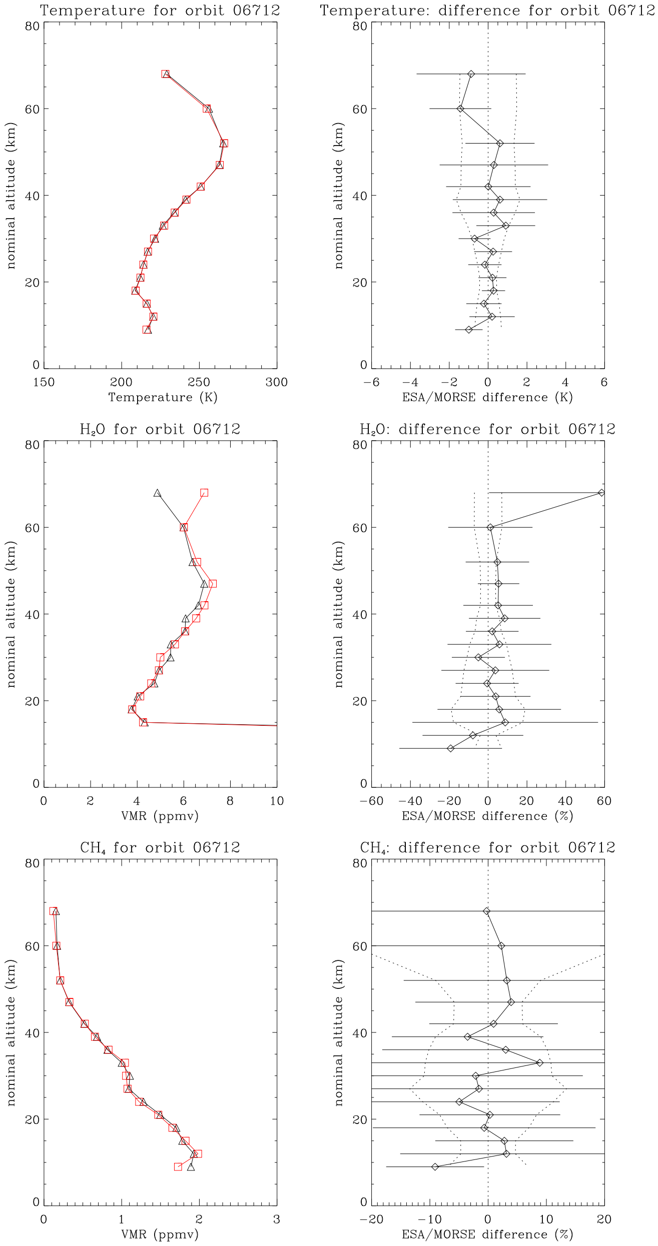

Figure 5.23: Comparison between the ESA OFL and MORSE retrieved profiles for temperature, H_2O and CH_4 for orbit 06712. Left–hand column: ESA (black) and MORSE (red) average profiles for the orbit. Right–hand column: mean of the differences around the orbit. Temperature difference is (MORSE-ESA), VMR differences are 100 %×([MORSE-ESA]/ESA). Dotted lines represent the average random error on the ESA retrieval. Since the ESA and MORSE retrievals are performed from the same Level 1B spectra, using the same microwindows, the random error is the same on both. Horizontal lines represent the standard deviation of the differences.

Figure 5.24 shows scatter plots of H_2O and CH_4 for the ESA OFL and MORSE retrievals from orbit 06712. The straight line shown in these plots is a fit to the points between 21 and 47 km (stratospheric points). A gradient of 2.0, or slightly less, would be expected. It has already been established in § 4.5 that the ESA OFL retrievals exhibit a gradient slightly greater than 2.0, which is indicative of the high bias in the water vapour retrievals above 30 km. The ESA data for this orbit give a gradient of 2.10±0.1, while the MORSE data give a gradient of 2.35±0.1. The error values quoted for the gradient are one sigma variations. It could certainly be argued that this difference is significant, but the reason for the difference is not known.

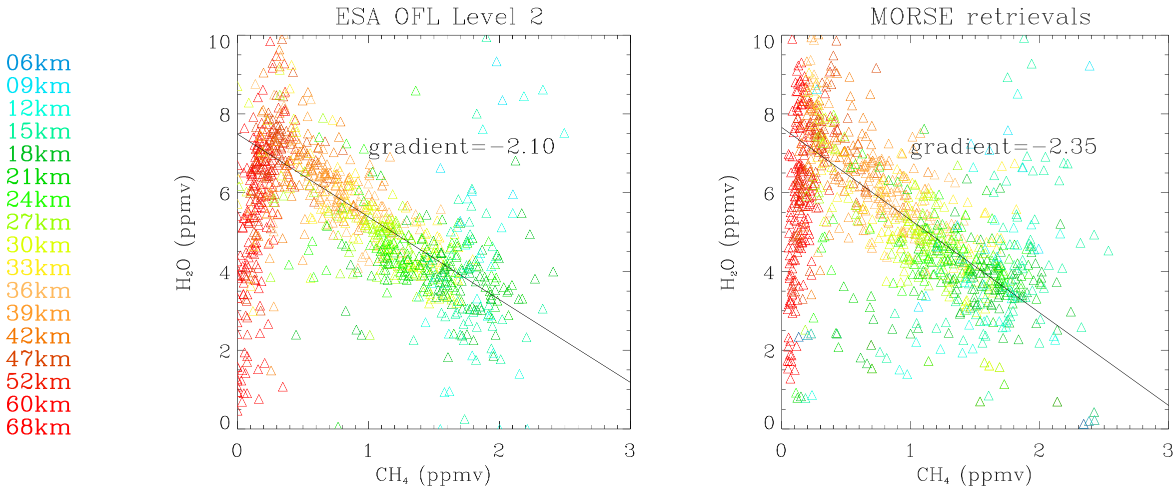

Figure 5.24: Correlations between H_2O and CH_4 for ESA OFL and MORSE retrievals for orbit 06712.

5.6 Summary

The effects of various assumptions have been examined here in isolation. In reality, it is likely that the observed problems in the data are due to a mixture of causes.

It could be argued that these sensitivity tests should really be performed with the ORM, as it uses the same retrieval method as the operational processor. However, tests with MORSE ought to give a reasonable idea of which issues merit further investigation.

It has been established in this Chapter that day/night differences in the retrievals could be caused by non–LTE effects. The observed low bias in the day–time ESA OFL H_2O and CH_4 at 68 km can most probably be attributed to non–LTE effects. It has also been observed that the effects of non–LTE on day–time retrievals extend down to around 30 km, which is further down than would be expected from the microwindow error analysis shown in Figure 4.6. It is therefore possible that the day/night differences observed in Chapter 4 could be at least partially attributed to non–LTE effects. It is also conceivable that variation in non–LTE effects in CH_4 with latitude could account for some of the variation in the CH_4 bias with respect to other data sources in latitude and time, although further work would be required to show conclusively that this is the case.

It has already been established in Chapter 4 that day/night differences in H_2O are not large enough to entirely account for the observed bias in H_2O above 30 km. Another possible candidate cause of a high bias in H_2O above 30 km is a modelled ILS which is too narrow. A modelled ILS which is too narrow would be consistent with the residual signatures in the H_2O microwindows shown in Chapter 4. Extending the continuum retrieval up to 68 rather than 30 km also appears to result in a very small reduction in the retrieved H_2O above 30 km, but residual signatures in the H_2O microwindows do not indicate a problem with the continuum.

It has already been suggested that the perceived bias in the OFL CH_4 may be partially attributed to non–LTE effects. The ILS width may also have an effect on the CH_4 bias, although this is not an effect that would be expected to result in latitudinal variations in the bias.

Biases are likely to arise through systematic errors which the retrieval can try to compensate for by changing the profile of the target species. If the retrieval is unable to better match the modelled spectra to the measurements by adjusting the profile of target species, then oscillations tend to develop. The most obvious cause of oscillations is noise. Oscillations in the retrieved profiles arising from random noise in the spectra should be random in phase, and should therefore be removed when large numbers of profiles are averaged. However, certain systematic errors may also result in oscillations which are not random in phase. An example of this is the observed differences in Level 1B radiances between forward and reverse sweeps of the MIPAS interferometer (see Appendix A), which cause oscillations in the Level 2 profiles which are distinctly anti–correlated between adjacent limb scans.

The investigations in this Chapter have identified a number of possible candidate causes for the persistent oscillations in CH_4 in the region of the tropical tropopause observed in the MIPAS data. Possible causes identified are the FOV representation, the assumption that the atmosphere can be accurately represented on the retrieval grid and the assumption that the VMR varies linearly with altitude.

All these issues also affect the H_2O retrieval. Oscillations in the H_2O retrievals in the region of the tropical tropopause from real data are more complicated than those in the CH_4 retrievals, since some oscillations are expected in the tropical H_2O due to the tropical tape recorder effect. Oscillations in the tropical OFL H_2O profiles do exist, but seem to behave in a realistic way, whereas oscillations in the tropical CH_4 profiles ought not to exist.

Cloud detection and the downward vertical extent of the retrieval were also considered as possible causes of the oscillations in the tropics, since cloud is more prevalent in the tropics than in other regions. Tropical ESA OFL CH_4 profiles were examined in conjunction with cloud indices supplied by the University of Leicester. The persistent oscillation did not appear to be dependent on how far the retrieval extended downwards or on the threshold value applied to the cloud–detection ratio.

Many of the tests performed for this Chapter also resulted in unexpected effects on the pressure retrieval which were different for mid–latitude and equatorial cases. These have not really been discussed here, but could be an interesting topic for further investigation.

Chapter 6

Retrievals of isotopic composition

6.1 Introduction

Both water vapour and methane provide the potential of additional information through measurements of their isotopic composition. Measurements of the isotopic composition of atmospheric gases are a valuable way of deriving information on the origin of these gases and can also be useful for studying physical, chemical, biological and atmospheric processes including exchange of air with the surface (oceans and biosphere), meteorology, dynamics, transport and stratospheric–tropospheric exchange.

The high spectral resolution of MIPAS makes it possible to distinguish between lines of major and minor isotopomers of water vapour and methane. Provided that the signal is large enough in relation to the noise, it ought to be possible to retrieve profiles of the isotopic composition of these gases. This Chapter describes work that has been carried out on retrievals of the isotopomers $H_2^{18}O$, $H_2^{17}O$, HDO and CH_3D.

Descriptions of the processes that result in the isotopic compositions of these gases in the atmosphere being different from their isotopic compositions at the surface (fractionation processes) are discussed in § 6.1.1. The expected distributions of the isotopes as determined by previous mea-

Table 6.1: Isotopic abundances used in the HITRAN database HITRAN (2004)

Molecule	Abundance
$H_2^{16}O$	0.997317
$H_2^{18}O$	0.00199983
$H_2^{17}O$	0.000372
HDO	0.00031609
$^{12}CH_4$	0.98827
$^{12}CH_3D$	0.00061575

surements are discussed in § 6.1.2 and 6.1.3. § 6.2 describes the work done on the selection of microwindows for isotopic retrievals with the MORSE retrieval code. § 6.3 describes the approach adopted for retrievals from real data and § 6.4 describes the error analysis for this approach. The results of these retrievals are shown in § 6.5 and 6.6. Results from HDO and $H_2^{18}O$ retrievals are compared with those from the Odin–SMR instrument in § 6.7.

6.1.1 Mechanisms for isotope fractionation

A heavier isotopomer of a particular molecule is formed if one or more neutrons are added to the nucleus of one of its constituent atoms . The charge of the atom remains unchanged, but the properties of the molecule do change. Strictly speaking, the term "isotope" refers to atoms and the term "isotopomer" to molecules, but from here onwards, for the sake of simplicity, different isotopomers of water vapour and methane will be referred to as isotopes.

Table 6.1 (de Bievre et al., 1984) summarises the relative amounts of the isotopes of water vapour and methane at the Earth's surface. These surface abundances for H_2O and CH_4 are based on the isotopic abundances of their constituent elements in samples that represent internationally recognised standards (de Bievre et al., 1984). The standard used for hydrogen and oxygen is Standard Mean Ocean Water (SMOW), a concept originally introduced by Craig (1961).

However, the isotopic ratio of light elements in various important molecular species in the Earth's

Table 6.2: Reference ratios for isotopes to be measured

Molecule	Ratio of interest	Reference ratio
$H_2^{18}O$	$^{18}O/^{16}O$	2×10^{-3}
$H_2^{17}O$	$^{17}O/^{16}O$	3×10^{-4}
HDO	D/H	1.55×10^{-4}
$^{12}CH_3D$	D/H	1.55×10^{-4}

atmosphere, including water vapour and methane, is different from that of the elements at the Earth's surface. The processes which lead to this difference in isotopic ratios, or in other words, to the fractionation of the isotopes, for water vapour and methane are the vapour pressure isotope effect and the fact that different isotopes participate in chemical reactions with different rates.

Isotopic compositions are usually expressed using "delta" notation, in which the isotopic ratios (for example deuterium to hydrogen) of the sample of interest and a reference sample are related by

$$\delta\mathrm{D} = \left(\frac{(\mathrm{D/H})_{\mathrm{sample}} - (\mathrm{D/H})_{\mathrm{reference}}}{(\mathrm{D/H})_{\mathrm{reference}}} \right) \times 1000 \tag{6.1}$$

The unit is parts per thousand (ppt), or per mil (‰) and the reference ratio is taken from the accepted standard for that particular species (in this case SMOW). The $(\mathrm{D/H})_{\mathrm{sample}}$ is the isotopic ratio of the measured water vapour and is calculated as

$$(\mathrm{D/H})_{\mathrm{sample}} = \frac{\mathrm{VMR}\,(\mathrm{HDO})}{2 \times \mathrm{VMR}\,(\mathrm{H_2O})} \tag{6.2}$$

where VMR(HDO) and VMR(H_2O) are the measured mixing ratios. The factor of 2 is required because the reference ratios are defined for single atoms, while the water vapour molecule contains two hydrogen atoms. A factor of 4 would similarly be required in the expression for the D/H ratio in methane. Table 6.2 shows the reference ratios for the isotopes that were retrieved for this project.

The dominant mechanism affecting the isotopic composition of water vapour in a given air parcel in the troposphere is the vapour pressure isotope effect (Kaye, 1987). The heavier isotopes have a lower vapour pressure than the lighter ones. When water vapour evaporates from the surface, the main isotope (which is the lightest one) will evaporate with a higher rate than the heavier isotopes. The opposite applies when water vapour condenses in the atmosphere. The heavier isotopes condense with a higher rate and will therefore rain out more efficiently. The result will be a depletion of the heavier water vapour isotopes in the Earth's atmosphere compared to the water reservoirs at the surface (mainly the oceans). Isotopic substitution of light atoms leads to a much larger vapour pressure isotope effect than substitution of heavy atoms. The depletions of heavy isotopes relative to the surface abundances are therefore expected to be more pronounced in, say, HDO than in $H_2^{18}O$. In the stratosphere, water vapour is produced by the oxidation of methane (and to a lesser extent by the oxidation of molecular hydrogen). The isotopic composition of water vapour in the stratosphere is therefore dependent on the composition of upper tropospheric water vapour and on the isotopic ratios in the methane, molecular hydrogen, molecular oxygen and ozone from which the new water vapour is ultimately formed.

Another reason that isotopic ratios in the atmosphere differ from those at the surface is that different isotopes participate in reactions at slightly different rates. The effects are particularly marked for hydrogen and deuterium. Activation energies are smaller for molecular reactants containing H rather than D, and quantum mechanical tunnelling is greater for hydrogen (Wayne, 1996). Thus reactions involving breaking of H– bonds are faster than those involving the D–substituted analogues. Since methane is not involved in phase changes in the atmosphere, this difference in the reaction rates of different isotopes is the dominant effect in determining the fractionation of methane isotopes in the atmosphere.

Methane enters the atmosphere from biological sources and venting of natural gas. The isotopic composition of CH_4 in the atmosphere may be altered from the composition of the methane sources near/at the surface by methane–oxidising bacteria, which may oxidise $^{12}CH_4$ preferentially over

CH_3D (Coleman et al., 1981), leaving tropospheric methane less depleted in deuterium than the source methane.

In the stratosphere, large kinetic isotope effects in reactions with Cl and OH preferentially oxidise the lighter isotopes, leaving the remaining methane (and molecular hydrogen) enriched in deuterium relative to their tropospheric values (Rice et al., 2003; McCarthy et al., 2003b)

6.1.2 Distribution of methane isotopes in the atmosphere

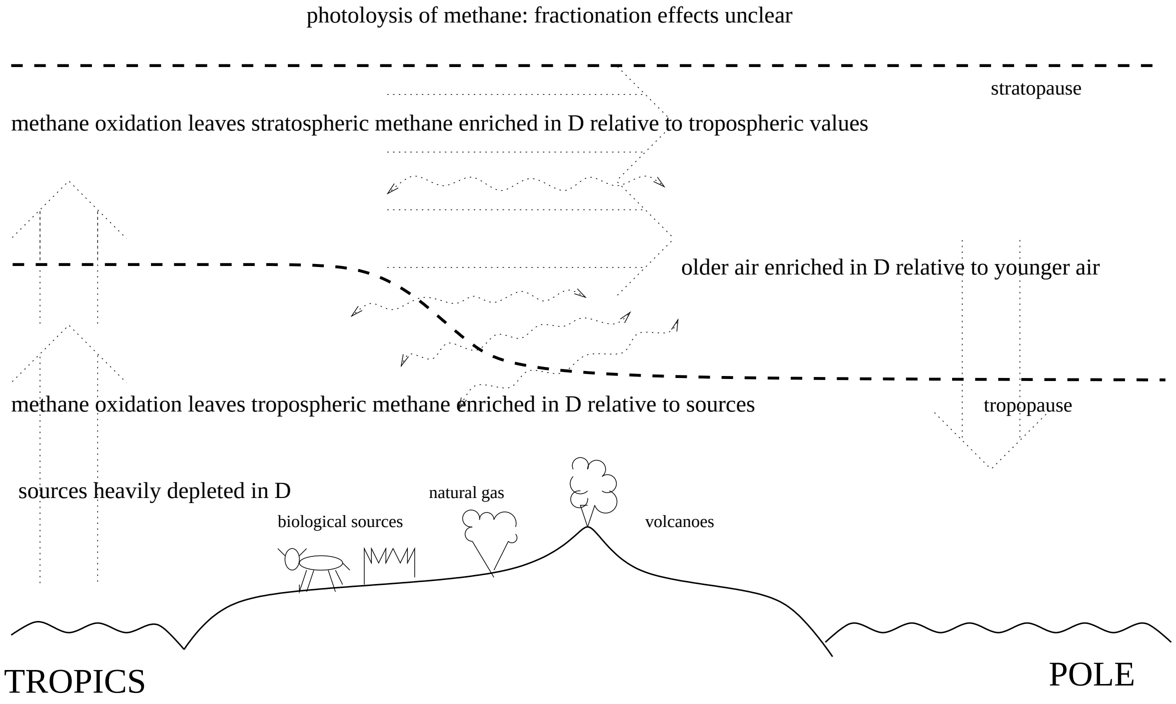

Figure 6.1: Schematic picture of the processes involved in isotope fractionation for methane

Processes affecting the deuterium content of methane are summarised in Figure 6.1. Expected values of δD are outlined in the following.

Measurements (Kaye (1987) and references therein) suggest that δD values for CH_4 in the troposphere are highly variable. Natural gases from oils have been shown to be highly depleted in D, with δD values for CH_4 ranging from -165 ‰ to -219 ‰ (Schiegl and Vogel, 1970). Values as small as -350 ‰ have been found in sewage sludge (Schoell, 1980). Even more highly D–depleted CH_4 may be found in volcanic CH_4; δD values of -487 ‰ have been found in Japan (Kiyosu, 1983). However, once in the atmosphere, methane is oxidised by OH. Since reactions involving the breaking of H–bonds are faster than those involving the D–substituted analogues, δD values in the troposphere are generally less depleted than the extremes quoted here. Quay et al. (1999) calculated mean tropospheric values of δD in CH_3D of -86±3 ‰ between 1989 and 1995 with a 10 ‰ depletion in the northern versus the southern hemisphere.

Previous experimental measurements for the D/H isotopic ratio of stratospheric methane are sparse, and so it is difficult to get a picture of the global distribution. Rice et al. (2001) report values of δD for methane ranging from -90 ‰ near the tropical tropopause to +26 ‰ in the polar vortex. These values were obtained from a number of different aircraft campaigns. Rinsland et al. (1991) measured CH_3D profiles around 27°N and 49°S from the ATMOS instrument on board the Spacelab 3 shuttle mission, and found values ranging from +141 ‰ and -133 ‰ between 18 and 28 km. The uncertainty in the ATMOS measurements is much greater than in any of the aircraft measurements.

McCarthy et al. (2003a), using high–accuracy *in situ* aircraft measurements at altitudes between 8 and 22 km, report a linear correlation between mixing ratios of CH_4 and CH_3D. Since CH_3D is destroyed more slowly than CH_4, it is expected to have a slightly longer lifetime Irion et al. (1996), using ATMOS data, calculated that the lifetime of CH_3D should be 1.2 times that of CH_4. Values of δD–CH_3D are therefore expected to be more enriched in older air.

6.1.3 Distribution of water vapour isotopes in the atmosphere

Figures 6.2 summarises the processes leading to the isotopic fractionation of water vapour.

The isotopic composition of water vapour in the troposphere is governed by phase changes. Since

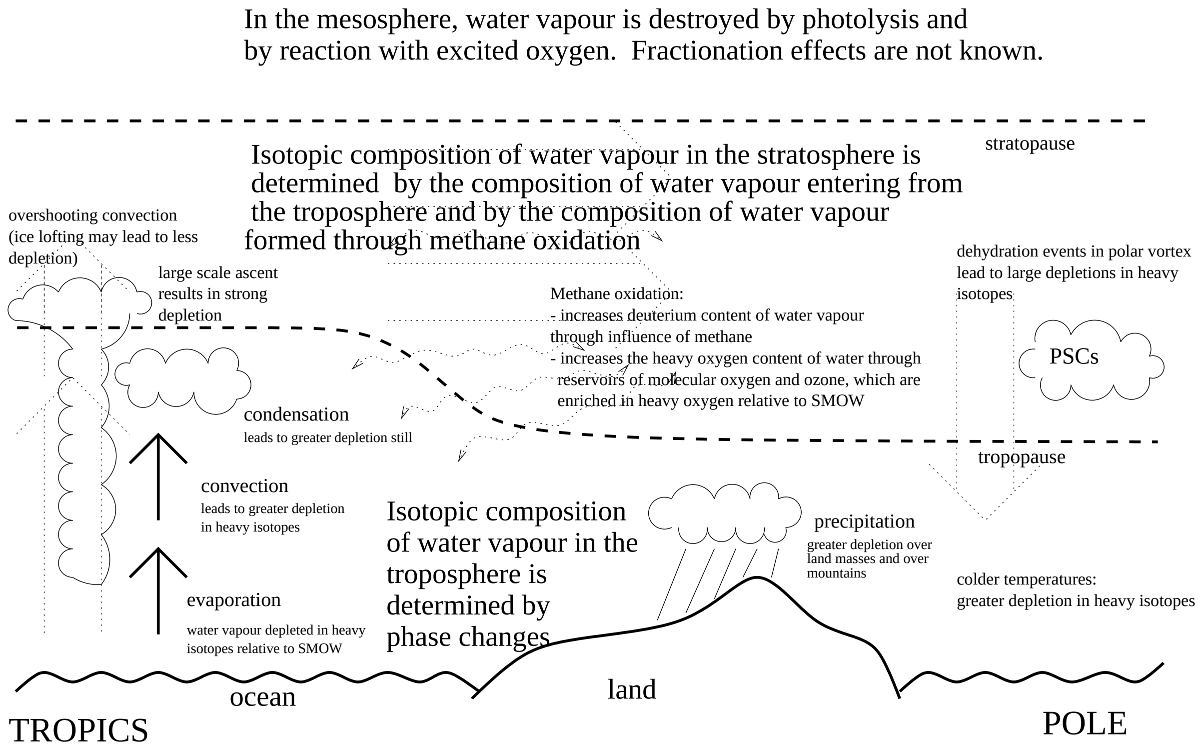

Figure 6.2: Schematic picture of the processes involved in isotope fractionation for water vapour

the main source of water vapour in the troposphere is the oceans, the isotopic composition of water vapour entering the lower troposphere from the oceans is determined by the fractionation that occurs during evaporation from the sea surface.

In general, the mean isotopic profile of tropospheric water vapour is characterised by a steep decrease of the heavy isotope content with altitude. This exponential decrease, first suggested by Eriksson (1965), was confirmed by Rozanski and Sonntag (1982). There is, however, a large variability in the isotopic ratio of any given air parcel depending on its trajectory, the phase changes it has experienced and its temperature history. Dansgaard (1964) described this by defining four isotope effects that control the mean isotopic water vapour content of tropospheric air. The first is the temperature effect. Water vapour at higher latitudes is expected to be more depleted in heavy isotopes due to the cooling of air masses on their way to higher latitudes, which leads to a successive deposition of heavier isotopes through precipitation. The second is the continental effect. The rainout of the heavier isotopes is more pronounced when the air is transported inland since there is no further supply of “isotope–rich” water vapour from the oceans. The third effect is the altitude effect. Rainout caused by orographic features, such as forced convection over mountains, causes a change in the water vapour isotopic composition. The fourth effect is the amount effect. This is the dominating effect in tropical and sub–tropical regions where there is strong convection in large convective cells. The stronger the convection the greater the loss of heavier isotopes.

These effects have been confirmed by studying the isotopic ratio in precipitation (Araguas-Araguas et al., 1998) and in tropospheric general circulation models with isotopes added to the condensation schemes. Modelling of the isotopic ratio in the troposphere and in the precipitation over glaciers has been used for some time in studies of paleoclimate (e.g. Jouzel et al. (1987); Hoffman et al. (1998)). It may sometimes be hard to distinguish between these effects. For example, the altitude effect and the temperature effect may cause a fractionation in the same area.

The two most important effects for the exchange between the troposphere and the stratosphere are the amount effect and the temperature effect. The amount effect causes large depletion in the upper tropical troposphere, where a large input of air to the stratosphere is expected. At higher latitudes, the convection is weaker, but the temperature effect will cause large isotope depletion in the upper troposphere.

Despite large variability in the isotopic composition of water vapour in the troposphere, certain relationships are expected to hold. Tropospheric measurements (Taylor, 1972) have shown that there is a linear relationship between δ^{18}O and δD:

$$\delta\mathrm{D} = (8.43 \pm 0.31)\,\delta^{18}\mathrm{O} + (16 \pm 7) \tag{6.3}$$

The relationship between δ^{17}O and δ^{18}O is determined by “mass–dependent fractionation”. Most kinetic and equilibrium isotope effects alter $^{17}\mathrm{O}/^{16}\mathrm{O}$ ratios by approximately half the degree to which the $^{18}\mathrm{O}/^{16}\mathrm{O}$ ratios change. The exact coefficient depends on molecular weight. In the case of water vapour, the molecular weight of $H_2^{16}O$ is 18, $H_2^{17}O$ is 19, $H_2^{18}O$ is 20 and the fractionated ratios expressed as per mil deviations $\delta^{18}O$ and $\delta^{17}O$ are related as follows (Thiemens, 1999):

$$\delta^{17}O/\delta^{18}O = \left(\frac{1}{18} - \frac{1}{19}\right) / \left(\frac{1}{18} - \frac{1}{20}\right) \tag{6.4}$$

or $\delta^{17}O/\delta^{18}O = 0.526$. This relationship may be modified slightly by mass–independent fractionation (Thiemens, 1999), associated with ozone photolysis and $O(^1D)$, but in the troposphere this effect is expected to be very small. The effect is expected to be larger in the stratosphere (Boering et al., 2004).

Values of δD in the lower troposphere are expected to be around −100 ‰ to −200 ‰, decreasing rapidly with altitude. In theoretical calculations using one–dimensional models where water vapour is dehydrated only by large–scale slow diabatic ascent of air (Dessler and Sherwood, 2003; Johnson et al., 2001a) the depletion of HDO in the upper troposphere is expected to be around −800 ‰ to −900 ‰. Such low values have not been found in measurements in the upper troposphere. The measurements show values in the range of -400 ‰ to −600 ‰ (Enhalt, 1974; Kaye, 1990; Smith, 1992). Moyer et al. (1996), using ATMOS measurements, estimated a value of $\delta D–H_2O$ of −670±80 ‰ at the tropopause, while Johnson et al. (2001b) inferred a value of −679±20 ‰. Smith (1992) suggested that a reason for these low depletions could be “ice lofting”, i.e. lifting of HDO–rich air parcels from lower levels in a convective cloud. The extreme depletion in the models is caused by partitioning between the vapour and the ice phases, coupled with the assumption that ice particles settle out of the air mass completely. Simulations of dehydration which include rapid vertical ascent of air by convection, in which ice particles do not completely separate from the air mass, have resulted in values for $\delta D–H_2O$ ranging from -650 to -680 ‰ (Dessler and Sherwood, 2003; Johnson et al., 2001a), which are in better agreement with the measurements.

Expected values of $\delta^{18}O$ and $\delta^{17}O$ in the upper troposphere/lower stratosphere can be inferred from the relationships in Equations 6.3 and 6.4.

The values quoted above represent some kind of average behaviour. Small–scale microphysical models (*Jamison Smith, University of Colorado, private communication*) and *in situ* aircraft measurements in subtropical convective conditions (Webster and Heymsfield, 2003) indicate that there is a large amount of variability in the isotopic composition of water vapour in the upper troposphere on small spatial scales.

The isotopic composition of water vapour in the stratosphere is mainly controlled by two factors: the composition of the water vapour entering the stratosphere from the troposphere and the composition of the water vapour produced inside the stratosphere by oxidation of methane. (The D/H ratio in water vapour is also determined to a lesser extent by the D/H ratio in molecular hydrogen, since HD can be oxidised to form HDO.) The "entry ratio" in air from the troposphere will reflect the isotopic composition of the upper troposphere while the methane–produced water vapour will reflect the isotopic composition of methane, molecular oxygen and ozone.

The "entry ratio" for δD, δ^{18}O and δ^{17}O in the lower stratosphere is expected to be the same as the values quoted for the upper troposphere. For δD this means a very large depletion with values of around -400 ‰ to -700 ‰ compared to SMOW. The δ^{18}O and δ^{17}O are also expected to be depleted compared to SMOW, but not as much as δD. From the empirical linear relationship between δD and δ^{18}O mentioned previously, δ^{18}O values are expected to be around -60 ‰ to -100 ‰ in the upper troposphere and the lowest layers of the stratosphere. Mass–dependent fractionation is expected to result in δ^{17}O values showing approximately half the depletion of δ^{18}O.

The deuterium content of the water vapour produced in the stratosphere is mainly determined by the D content of methane. Measurements indicate (e.g. Rinsland et al. (1991); Irion et al. (1996); McCarthy et al. (2003a)) that methane has a small depletion in deuterium of about δD = -50 ‰ to -100 ‰ in the lower stratosphere with a slight increase of this ratio with altitude. The water vapour produced in the stratosphere is expected to reflect this ratio, so we might expect an increase of D/H ratio in water with altitude.

Water vapour is also produced in the stratosphere, to a lesser extent, by the oxidation of H_2, which has been found to be highly enriched in deuterium relative to SMOW (Rice et al., 2003; Rahn et al., 2003).

The production of $H_2^{18}O$ and $H_2^{17}O$ is difficult to quantify since there are more steps of the oxidation chain containing oxygen compounds. The largest oxygen reservoir is O_2, which is slightly enhanced in ^{18}O with $\delta^{18}O = +25$ ‰ (Kaye, 1990). The other large reservoir that could affect the heavy oxygen content of stratospheric water vapour is ozone, which is also enriched in heavy oxygen relative to SMOW (Mauersberger et al., 2001).

Above the stratosphere, the isotopic composition of water vapour and methane is not well known. (The Odin SMR (see § 4.8 and § 6.7), followed by MIPAS, have now made the first measurements of $H_2^{18}O$ in the lower mesosphere.) The main loss mechanisms for H_2O are photolysis and reaction with $O(^1D)$, where the latter is expected to have a very small isotopic fractionation rate. The fractionation effect of the photolysis is not clear, but it is believed to be small (Kaye, 1987).

6.1.4 The deuterium budget

Since "total hydrogen" in the stratosphere is conserved (§ 1.1), total deuterium should also be conserved. Essentially all deuterium (denoted D_{total}) in the lower and middle stratosphere resides in the three reservoir species HDO, CH_3D and HD. Multiply deuterated species (e.g. CH_2D_2) are assumed to be negligible. The total deuterium can therefore be expressed as the sum of all significant deuterated species in the stratosphere:

$$D_{\text{total}} = \text{HDO} + \text{CH}_3\text{D} + \text{HD} \tag{6.5}$$

From analysis of ATMOS data performed by Irion et al. (1996), it appeared that HDO + CH_3D

was approximately constant with height between about 18 and 30 km. Irion et al. (1996) concluded from these data that fractionation effects in molecular hydrogen were not important below 30 km. However, accurate measurements of CH_3D and HD (McCarthy et al., 2003b; Rice et al., 2003; Rahn et al., 2003) and laboratory studies (Röckmann et al., 2003) have since shown that there is in fact a significant fractionation in molecular hydrogen. Stratospheric H_2 is enriched by a large isotopic fractionation factor in the oxidation pathway from CH_4 to H_2 as well as the enrichment of its source CH_4 in older stratospheric air (Rahn et al., 2003). Measured values for δD–H_2 range from 130 ‰ at the tropical tropopause to 440 ‰ in polar air. Measurements from the NASA ER–2 aircraft have shown an increase of +5 ‰ in δD–H_2 for each 1 % of CH_3D oxidised (Rice et al., 2003).

6.1.5 Summary

The focus of this Chapter is the retrieval of $H_2^{18}O$, $H_2^{17}O$, HDO and CH_3D from the MIPAS satellite instrument. Measurements of the isotopic composition of water vapour and methane within the MIPAS measurement altitude range could potentially be used in studies of various atmospheric processes. Measurements of the isotopic composition of water vapour in the tropical upper troposphere and lower stratosphere could provide an additional observational constraint, beyond water vapour mixing ratios alone, for determining the relative importance of rapid vertical ascent and large–scale slow ascent in the entrance of air into the stratosphere. Global–scale measurements could potentially also be used to study stratosphere–troposphere exchange in regions outside the tropics. Isotopic water vapour measurements could also be useful in studies of dehydration in the polar vortex. Measurements of HDO in conjunction with CH_3D measurements could potentially be used in studies of the deuterium budget and of methane oxidation in the stratosphere. Simultaneous measurements of $\delta^{18}O$–$H_2^{18}O$ and $\delta^{17}O$–$H_2^{17}O$, could, if accurate enough, be used to shed new light on mass–independent fractionation in the stratosphere, and as a constraint on stratospheric chemistry. Mass–independent fractionation has been used in other species as a measure of stratospheric/tropospheric exchange.

Isotopic measurements of water vapour (for example Pollock et al. (1980); Rinsland et al. (1984); Abbas et al. (1987); Guo et al. (1989); Dinelli et al. (1991); Johnson et al. (2001b); Webster and Heymsfield (2003)) and methane (for example Rice et al. (2001, 2003)) in the upper troposphere and stratosphere have been made previously from a range of aircraft and balloon instruments, using both *in situ* and remote sounding techniques. Simultaneous measurements of $H_2^{18}O$, $H_2^{17}O$, HDO and CH_3D have also been made from the space shuttle borne ATMOS instrument (Rinsland et al., 1991). Measurements of HDO and $H_2^{18}O$ have also been made by the Sub–Millimetre Radiometer (SMR) on the Odin satellite (see § 4.8) in the stratosphere and lower mesosphere.

The MIPAS Level 1B dataset offers advantages over aircraft and balloon measurements in that it provides continuous global coverage, day and night, for a period of 21 months. For cloud–free conditions, MIPAS can see below the tropopause, so could be useful for studies of stratospheric/tropospheric exchange. In addition, MIPAS can provide simultaneous measurement of the minor isotopes in question. This could be potentially useful in terms of validation and internal consistency checks as well as for scientific issues.

On the down side, satellite retrievals are unlikely to be able to offer such high accuracy as measurements from aircraft and balloons. There are also issues of resolution. Adjacent MIPAS limb scans are separated by approximately 500 km, while the best vertical resolution obtainable is 3 km. From the point of view of measurements of water vapour isotopes in the tropics, this means that MIPAS is unable to resolve the tropical tropopause layer, or the scales on which convection occurs. In addition, retrievals cannot be performed for cloudy conditions. Many of the interesting processes in terms of isotope fractionation occur in the tropics, which are often cloudy.

Although it will not be possible to use MIPAS isotopic measurements to study small–scale processes, it is hoped that the measurements can offer an insight into the global–scale distribution and variability of minor isotopes of water vapour and methane.

6.2 Microwindow selection

6.2.1 Approach

Microwindows were selected for HDO, $H_2^{18}O$, $H_2^{17}O$ and CH_3D using the MWMAKE software described in § 3.4.5. In order to select the best possible microwindows, realistic minor isotope profiles would be provided as input to MWMAKE for a range of atmospheric conditions (equatorial, mid–latitude night–time, mid–latitude day–time, polar winter and polar summer, say) and optimum microwindows for each set of conditions would be selected. In practice, global variations of the VMRs of minor isotopes are not well known. Also, although the use of different microwindow sets for different atmospheric conditions may be desirable, it makes large–scale processing more difficult. The approach adopted here was to select microwindows based on mid–latitude day–time conditions, using the MIPAS IG2 reference atmospheres (Remedios, 1999). Since the global distribution of minor isotopes of water vapour and methane was not well known anyway, VMR profiles of minor isotopes in the microwindow selection were assumed to be the main isotope profiles scaled by the HITRAN surface abundances shown in Table 6.1. By definition, this is an assumption of zero δ–values.

The selection of microwindows performed here was based on the retrieval of a single species. Another possible approach would be to base the selection on a joint retrieval with the main isotope or with other minor isotopes.

The MWMAKE software requires the user to define certain termination criteria, chosen with computation time in mind. The selection was set to terminate when any one of three criteria were met:

- The total number of spectral points exceeds 10000
- The number of microwindows reaches 10
- The increment in the figure of merit (in this case the information content — § 3.4.5) falls below 1.0

6.2.2 Results of the selection

Figure 6.3 shows the locations of the microwindows selected for HDO, $H_2^{18}O$, $H_2^{17}O$ and CH_3D in the spectral and altitude domain, along with simulated radiance contributions for each of these molecules (based on scaled mid–latitude day–time profiles of the main isotopes).

The selections for HDO, $H_2^{17}O$ and CH_3D were all terminated due to reaching the maximum number of spectral points allowed (10000), while the selection for $H_2^{18}O$ was terminated due to reaching the point where the increase in the figure of merit became smaller than the designated threshold value.

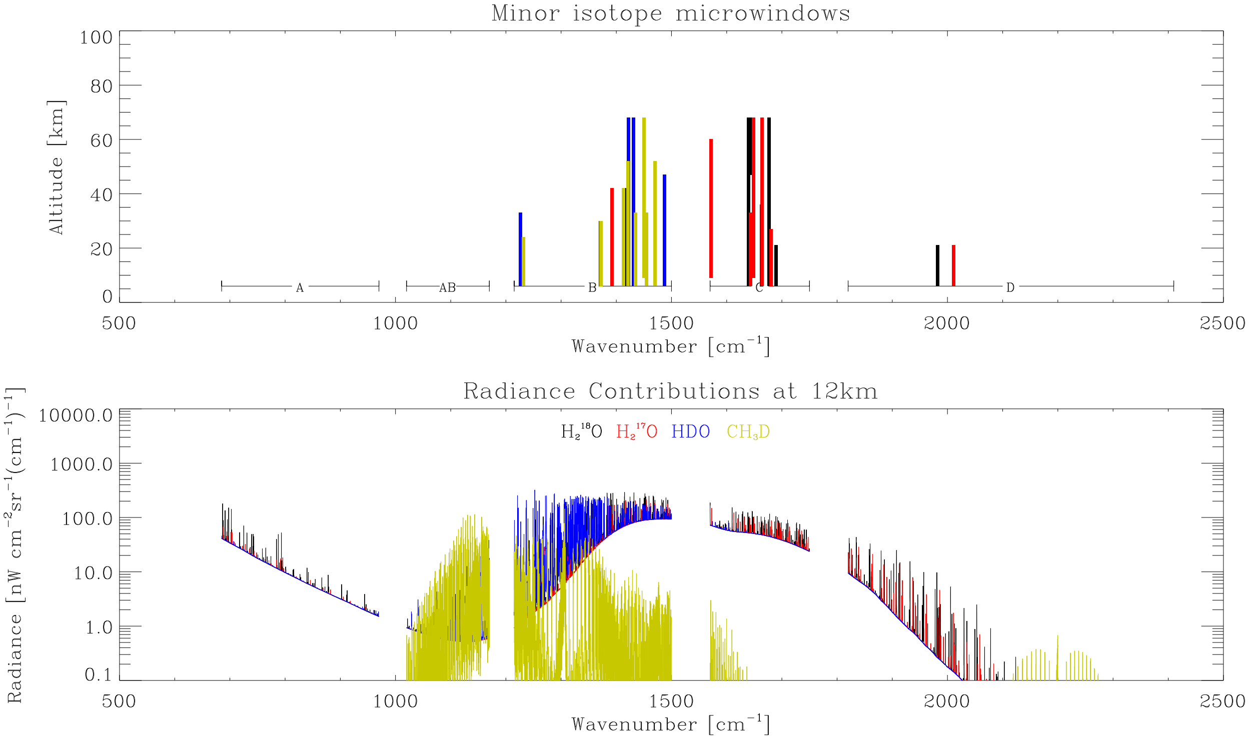

Figure 6.3: Locations of microwindows selected for the retrieval of $H_2^{18}O$, $H_2^{17}O$, HDO and CH_3D, with radiance contributions at 12 km calculated using the RFM. Radiances (and selection of microwindows) are based on minor isotope VMR profiles calculated by scaling the profiles of the major isotopes by the surface abundances in Table 6.1.

Table 6.3: Spectral and altitude ranges of the microwindows selected for minor isotope retrievals

Isotope	Microwindow label	Spectral range	MIPAS band	Altitude range
$H_2^{18}O$	2H2O0009	1675.500–1678.500 cm^{-1}	C	6–68 km
	2H2O0010	1980.275–1983.275 cm^{-1}	D	6–21 km
	2H2O0011	1638.425–1641.425 cm^{-1}	C	6–68 km
	2H2O0012	1413.875–1416.875 cm^{-1}	B	6–42 km
	2H2O0013	1661.425–1664.400 cm^{-1}	C	6–36 km
	2H2O0014	1644.700–1647.700 cm^{-1}	C	47–68 km
	2H2O0015	1687.700–1690.700 cm^{-1}	C	6–21 km
$H_2^{17}O$	3H2O0008	1647.050–1650.050 cm^{-1}	C	9–68 km
	3H2O0009	1570.475–1573.450 cm^{-1}	C	9–60 km
	3H2O0010	2009.550–2012.275 cm^{-1}	D	6–21 km
	3H2O0011	1391.075–1394.075 cm^{-1}	B	6–42 km
	3H2O0012	1662.950–1665.950 cm^{-1}	C	6–68 km
	3H2O0013	1641.600–1644.600 cm^{-1}	C	6–33 km
	3H2O0014	1679.050–1681.475 cm^{-1}	C	6–27 km
HDO	4H2O0008	1420.325–1423.325 cm^{-1}	B	6–68 km
	4H2O0009	1225.600–1228.000 cm^{-1}	B	6–33 km
	4H2O0010	1468.925–1471.925 cm^{-1}	B	6–52 km
	4H2O0011	1486.275–1489.275 cm^{-1}	B	6–47 km
	4H2O0012	1433.425–1436.425 cm^{-1}	B	6–33 km
	4H2O0013	1370.225–1373.225 cm^{-1}	B	6–30 km
	4H2O0014	1429.275–1432.275 cm^{-1}	B	6–68 km
CH_3D	3CH40008	1230.350–1233.275 cm^{-1}	B	6–24 km
	3CH40009	1420.025–1423.025 cm^{-1}	B	6–52 km
	3CH40010	1370.450–1373.450 cm^{-1}	B	6–30 km
	3CH40011	1469.000–1472.000 cm^{-1}	B	6–52 km
	3CH40012	1433.600–1436.600 cm^{-1}	B	6–33 km
	3CH40013	1411.175–1414.175 cm^{-1}	B	6–42 km
	3CH40014	1453.275–1456.275 cm^{-1}	B	6–33 km
	3CH40015	1449.025–1452.025 cm^{-1}	B	9–68 km

6.3 Retrieval approach

Retrievals of $H_2^{18}O$, $H_2^{17}O$, HDO and CH_3D were performed from MIPAS Level 1B spectra using MORSE. The retrieval approach adopted for the minor isotope retrievals performed for this Chapter is detailed below:

- Look–up tables and irregular grids (see § 5.3.1) were created for the microwindows detailed in Table 6.3 using software developed at Oxford by Dudhia et al. (2002b).
- Retrievals were performed in the following sequence: Joint retrieval of p, T and H_2O, then CH_4, $H_2^{18}O$, $H_2^{17}O$, HDO, and CH_3D (in series).
- The joint pT/H_2O retrieval and the CH_4 retrieval were performed using the microwindows used for the ESA OFL retrievals (see Figure 3.1)
- The initial guess profiles used for the p, T, H_2O and CH_4 retrievals were taken from the IG2 climatology. The *a priori* profiles for these retrievals were the same as the initial guess.
- The *a priori* covariance matrices for the p, T, H_2O and CH_4 retrievals were constructed using a 10 K uncertainty in temperature, a 50 % uncertainty in pressure and a 100 % uncertainty in VMR. Off–diagonal elements were calculated using a correlation length of 50 km.
- The minor isotope retrievals were performed as joint retrievals for the main and minor isotope in question, using the microwindows shown in Table 6.3 and Figure 6.3.
- In the joint major/minor isotope retrievals, the *a priori* covariance for the main isotope continues from the covariance from the previous main isotope retrieval but the minor isotope uncertainties were initialised to 300 %.
- The *a priori* profiles for the minor isotopes of water vapour were constructed for each limb scan by multiplying the water vapour profile obtained from the joint $p, T/H_2O$ retrieval for the scan by a constant ratio, based on tropical profiles from model output from an isotopic version of the NCAR Community Atmosphere Model (CAM3 — NCAR (2005)) supplied by David Noone at the University of Colorado. The ratio used in the construction of the *a priori*

was kept constant with latitude and with season. This results in δ–values which vary with altitude, but remain constant in latitude and in time. The *a priori* δ–values resulting from the ratios from the model output are shown in Figure 6.4.

- The *a priori* profiles for CH_3D were constructed using a ratio based on the linear relationship between CH_3D and CH_4 shown in the *in situ* aircraft measurements of McCarthy et al. (2003a).
- The initial guess profiles used for all minor isotopes were also the same as the *a priori* profiles.
- The choice was made not to transfer any information between retrievals from different limb scans. The retrievals in this Chapter are somewhat preliminary, and it was thought that the interpretation of the results would be less complicated without the possibility of propagation of problems through different scans or orbits.

It has been noted in previous Chapters that there are various problems associated with water vapour retrievals in the region of the troposphere and below. There are problems related to the inability of MIPAS to capture sharp minima in temperature profiles, as well as the sharp minimum in water vapour itself (the hygropause) and the large gradients in water vapour below the tropopause. It would be expected that there would be some cancellation of systematic error terms when taking the ratios of minor to major isotopes. It was therefore hoped that perhaps taking ratios would counteract some of these problems, and that the isotopic δ–values might be more reliable and less susceptible to systematic errors than the absolute value of the VMRs of water vapour.

6.4 Error Analysis

The results of the retrievals are profiles of VMR. However, in the literature, isotopic ratios are generally expressed as δ–values (§ 6.1.1). The δ value is expressed in terms of the ratio of the minor to major isotope as follows:

$$\delta = \left(\frac{R_{\text{sample}}}{nR_0} - 1\right) \times 1000 \tag{6.6}$$

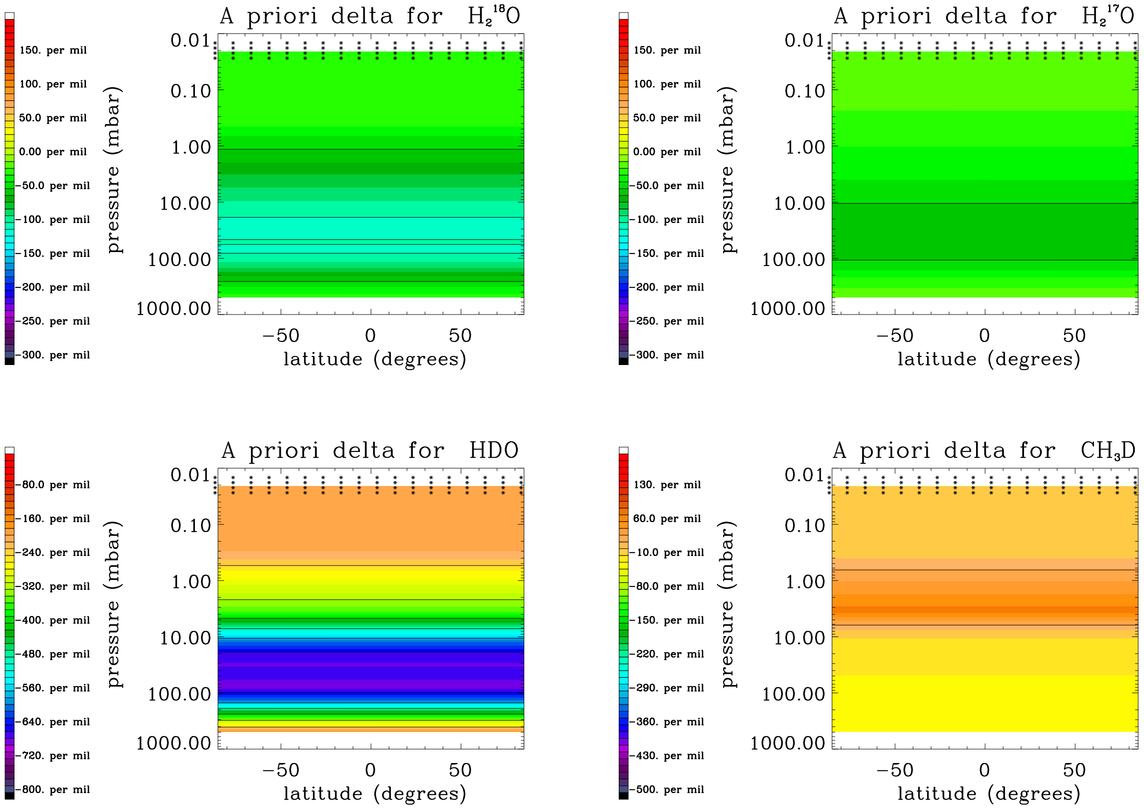

Figure 6.4: *A priori* δ–values for $H_2^{18}O$ (top right), $H_2^{17}O$ (top left), HDO (bottom left) and CH_3D (bottom right).

where R_{sample} is the ratio of the VMR of the minor isotope to that of the major isotope, R_0 is the reference ratio and n is the factor needed to relate the reference ratio for the element to the molecule in question (see § 6.1.1). If we have some error, ϵ_r on R_{sample}, it will in turn lead to some error ϵ_δ on the δ–value.

$$\delta + \epsilon_\delta = \left(\frac{R_{sample} + \epsilon_r}{nR_0} - 1 \right) \times 1000 \tag{6.7}$$

Subtracting equation 6.6 from 6.7 gives

$$\epsilon_\delta = \left(\frac{\epsilon_r}{nR_0} \right) \times 1000 \tag{6.8}$$

The ratio of mixing ratios, R_{sample}, is a function of two variables, x and y, where x is the VMR of the minor isotope and y is the VMR of the major isotope. As explained in § 3.4, the total error resulting from a retrieval consists of a random error component and a systematic error component. For random errors, we assume no correlation between errors on the mixing ratios of the minor and the major isotope. For systematic error sources, we consider each error source separately. For any particular source of systematic error, we assume that the errors in the mixing ratios of the minor and major isotopes are completely correlated.

The error covariance of the ratio, R_{sample}, can then be expressed as follows: (see Appendix B for further details)

$$\mathbf{S}_r = \mathbf{S}_x^{\mathrm{rnd}} + \mathbf{S}_y^{\mathrm{rnd}} + \sum_k \mathbf{S}_{x-y}^k \tag{6.9}$$

$\mathbf{S}_x^{\mathrm{rnd}}$ and $\mathbf{S}_y^{\mathrm{rnd}}$ describe the random error on x and y respectively, and $\mathbf{S}_{x-y}^k$ the covariance of the difference of the systematic error k in x and y. If the major systematic error terms in both x and y are approximately equal, then the total error benefits from their cancellation.

Estimates of the systematic errors on the minor isotope retrievals were obtained as output from the MWMAKE software in the course of the selection of microwindows described in § 6.2. Estimates of the systematic errors on the major isotopes in the minor isotope microwindows were then obtained by secondary runs of the MWMAKE software, and the estimates combined according to Equation 6.9.

Figure 6.5 shows the estimated error contributions for the ratios of minor to major isotopes. It was hoped that taking the ratio would virtually eliminate systematic errors such as temperature and pressure, which might be expected to affect all lines within a microwindow in the same way. However, it appears that the major and minor isotopes are affected differently by the systematic errors, and the systematic errors are not cancelled as much as might have been hoped.

Figure 6.6 shows how the estimated errors in the isotopic ratio shown in Figure 6.5 translate to errors in the δ–values. The random error component can be reduced by averaging profiles, but the total systematic error estimate could be taken as a limit on the accuracy on the δ–values that can be obtained using these microwindows and this approach to the retrievals. However, this would be a rather pessimistic estimate of the limit since systematic error contributions due to temperature, pressure and contaminant gases might be expected to become decorrelated over the timescale of a few days, and might therefore also be reduced by averaging.

The averaging kernels (§ 3.3.3) are a useful indicator of retrieval quality. Figure 6.7 shows representative single profile averaging kernels from a mid–latitude day–time profile from an orbit from November 2003. The width of the averaging kernels is a measure of vertical resolution, while the sum of each row of the matrix (shown by a black line in Figure 6.7) gives an indication of how sensitive the retrieval is to the true profile. From these averaging kernels, one might expect useful retrievals of $H_2^{18}O$ and $H_2^{17}O$ from 6 to 60 km, of HDO from 6 to around 30 km, and of CH_3D from 6 to 21 km. The averaging kernels do vary from scan to scan, so the useful retrieval altitude range will also vary somewhat.

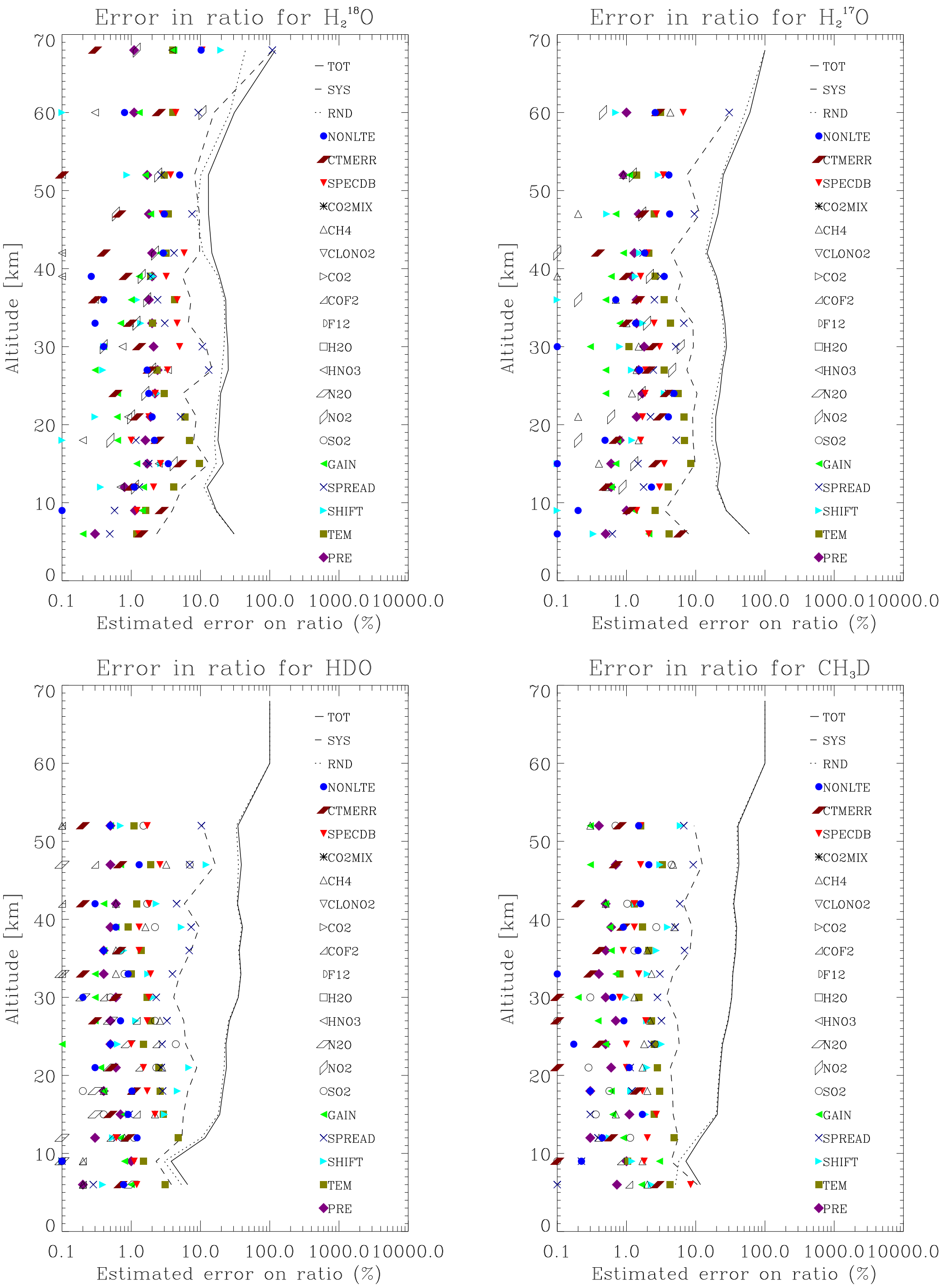

Figure 6.5: Estimated error budgets for ratios of minor to major isotopes from single profile retrievals from the microwindows selected for $H_2^{18}O$ (top right), $H_2^{17}O$ (top left), HDO (bottom left) and CH_3D (bottom right). It is clear that in all cases, the error budget is dominated by the random error component.

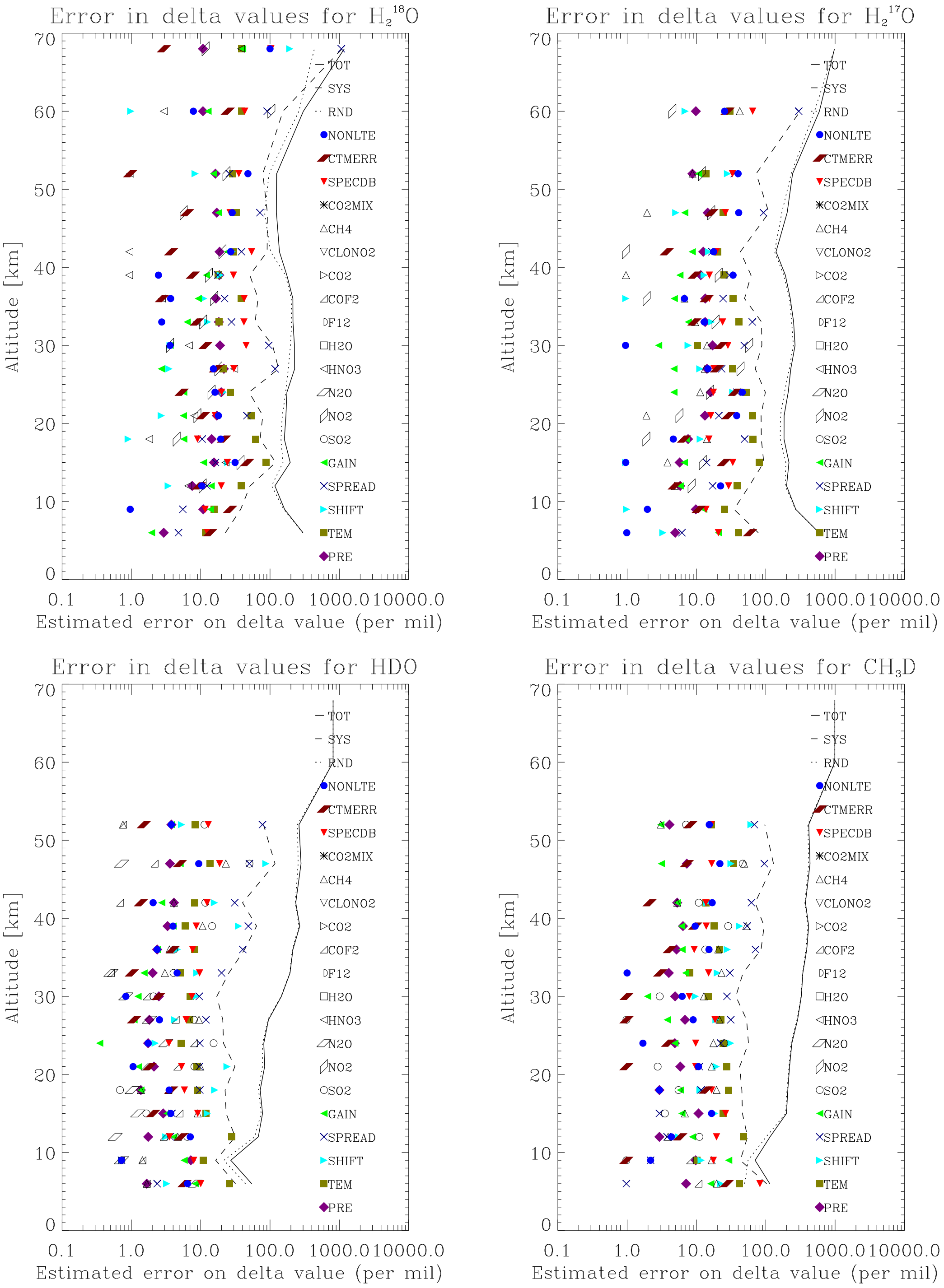

Figure 6.6: Estimated error contributions to the relevant δ–values for $H_2^{18}O$ (top right), $H_2^{17}O$ (top left), HDO (bottom left) and CH_3D (bottom right). Estimates are based on the errors on the ratios of minor to major isotopes shown in Figure 6.5 and the initial guess/*a priori* profiles based on results from CAM3 (NCAR, 2005).

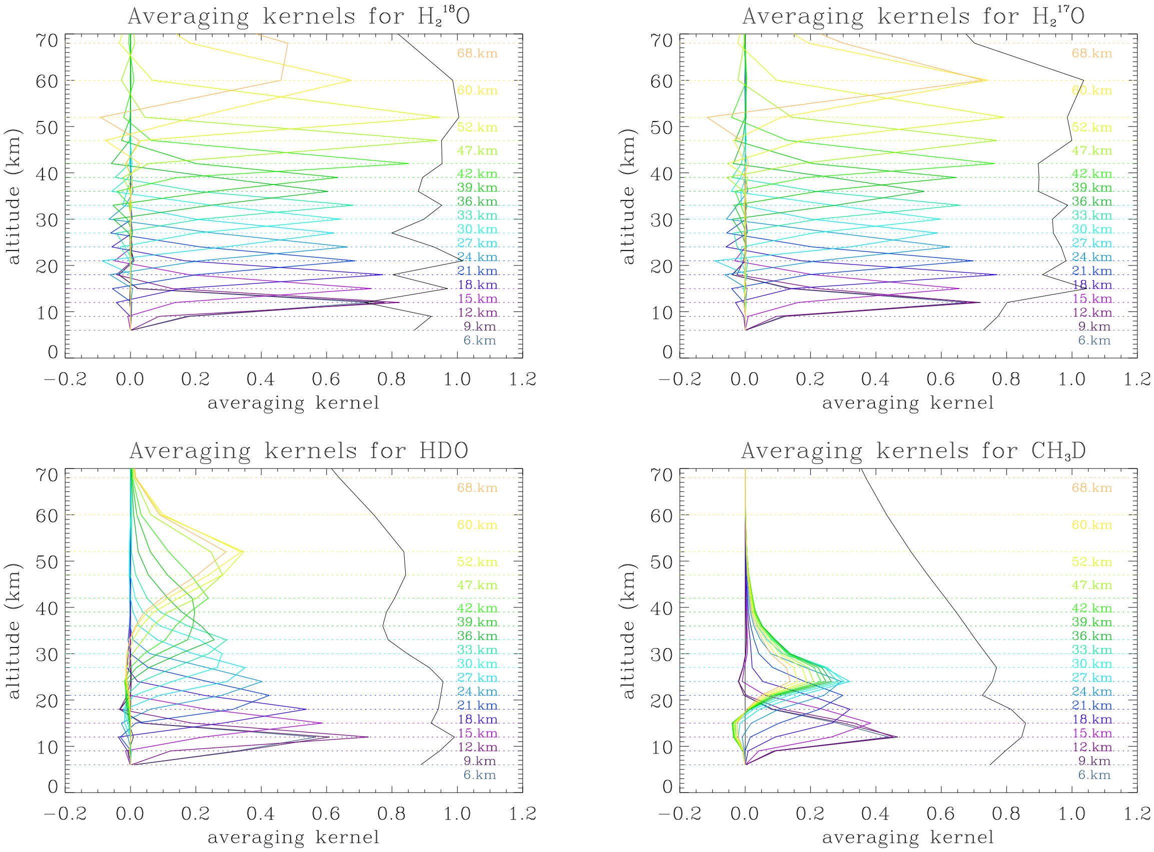

Figure 6.7: Representative averaging kernels for a single profile retrieval for $H_2^{18}O$ (top right), $H_2^{17}O$ (top left), HDO (bottom left) and CH_3D (bottom right). Coloured lines show rows of the averaging kernel matrix, while the black line shows the value of the sum of each row.

Table 6.4: Days processed for minor isotope retrievals. Processed days are shown in red.

January	01	02	03	04	05	06	07	08	09	**10**	11	12	13	14	15	16	17	18	19	**20**	21	22	23	24	25	26	27	28	29	30	31
February	**01**	02	03	04	05	06	07	08	09	**10**	11	12	13	14	15	16	17	18	**19**	20	21	22	23	24	25	26	27	28			
March	**01**	02	03	04	05	06	07	08	09	**10**	11	12	13	14	15	16	17	18	19	**20**	21	22	23	24	25	26	27	28	29	30	31
April	**01**	02	03	04	05	06	07	08	09	**10**	11	12	13	14	15	16	17	18	19	**20**	21	22	23	24	25	26	27	28	29	30	
May	**01**	02	03	04	05	06	07	**08**	09	10	11	12	13	14	15	16	**17**	18	19	20	21	22	23	24	25	26	27	28	29	30	31
June	01	02	03	04	05	**06**	07	08	09	10	11	**12**	13	14	15	16	17	18	19	**20**	21	22	23	24	25	26	27	28	29	30	
July	01	02	03	**04**	05	06	07	08	09	**10**	11	12	13	14	**15**	16	17	18	19	20	21	22	23	24	25	26	27	28	29	30	31
August	01	02	03	**04**	05	06	07	08	09	10	**11**	12	13	14	15	**16**	17	18	19	20	21	22	23	24	25	26	27	28	29	30	31
September	**01**	02	03	04	05	06	07	08	09	**10**	11	12	**13**	14	15	16	17	18	19	20	21	22	23	24	25	26	27	28	29	30	
October	**01**	02	03	04	05	06	07	08	**09**	10	11	12	13	14	15	16	17	18	19	20	21	22	23	24	25	**26**	27	28	29	30	31
November	01	**02**	03	04	05	06	07	08	09	10	**11**	12	13	14	15	16	17	18	19	20	21	**22**	23	24	25	26	27	28	29	30	
December	**01**	02	03	04	05	06	**07**	08	09	10	11	12	13	14	15	16	17	18	19	**20**	21	22	23	24	25	26	27	28	29	30	31

6.5 Retrieval results: seasonal zonal means

Since the minor isotopes of any species are much less abundant than the main isotope, the signal–to–noise ratio for isotopic lines tends to be low, and individual profile retrievals are somewhat noisy. (The estimated error budgets shown in Figure 6.5 are dominated by random error.) However, averaging of large numbers of profiles can reduce the noise.

The results shown here are presented in terms of zonal means, calculated for 10 degree latitude bands. Three days of MIPAS data were processed for each month in 2003, so each three–month "season" presented here contains nine days worth of MIPAS data. Table 6.4 shows a list of the days processed. The plan was to choose days which were evenly spaced in time, but in practice the choice of dates was also influenced by the number of available orbits of Level 1B data available at the time.

The random error on individual profiles is large. In order that the zonal means of quantities relating to the minor isotopes would not be unduly influenced by the *a priori*, quality checks were applied to profiles before they were included in the calculation of the zonal means. Points where the sum of the row of the averaging kernel was less than some threshold value were deemed to be influenced too strongly by the *a priori* and were rejected. The threshold value was set (somewhat arbitrarily) to 0.85.

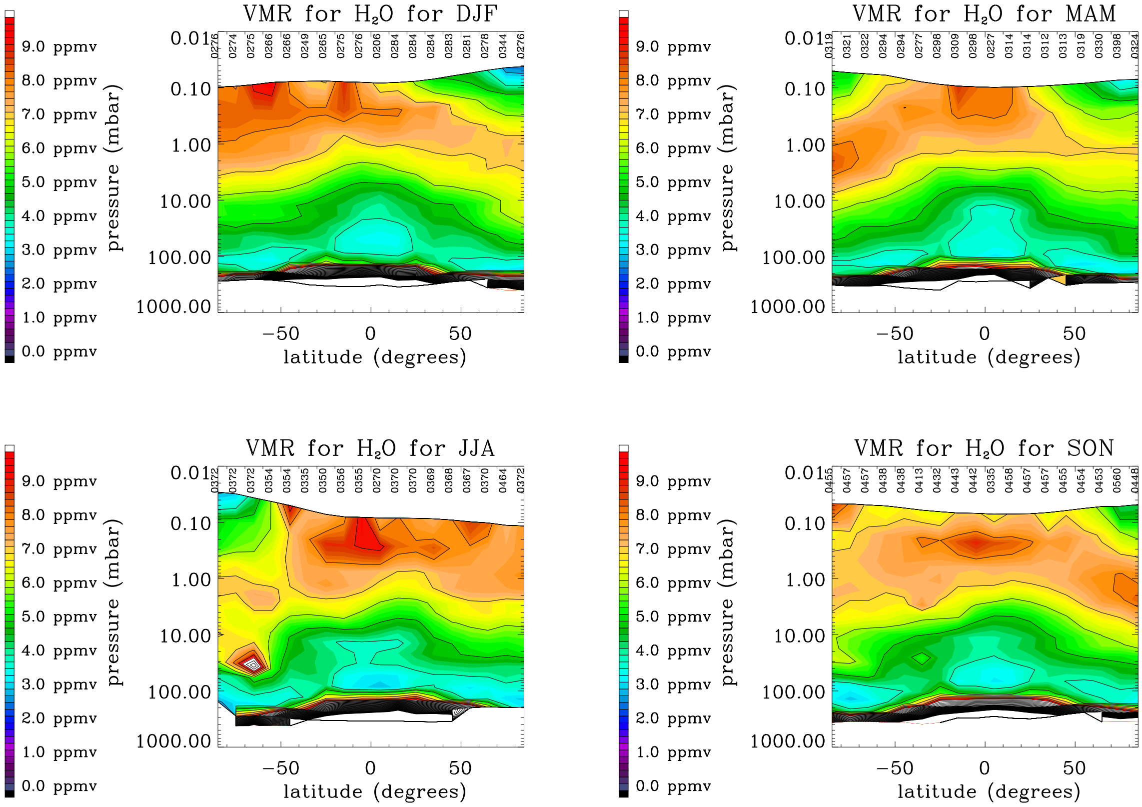

Figure 6.8: Zonal means of H_2O for December–February (top left), March–May (top right), June–August (bottom left) and September–November (bottom right). Each “season” contains nine days worth of data. The numbers at the top of each plot represent the number of profiles included in the zonal mean for each latitude band.

6.5.1 H_2O

In order to put the results of the retrievals of the minor isotopes of water vapour into context, zonal means of retrieved H_2O from the ESA operational microwindows are shown in Figure 6.8. Since there are no minor isotope lines in the ESA water vapour microwindows, the zonal mean fields of H_2O shown here are effectively fields of $H_2^{16}O$.

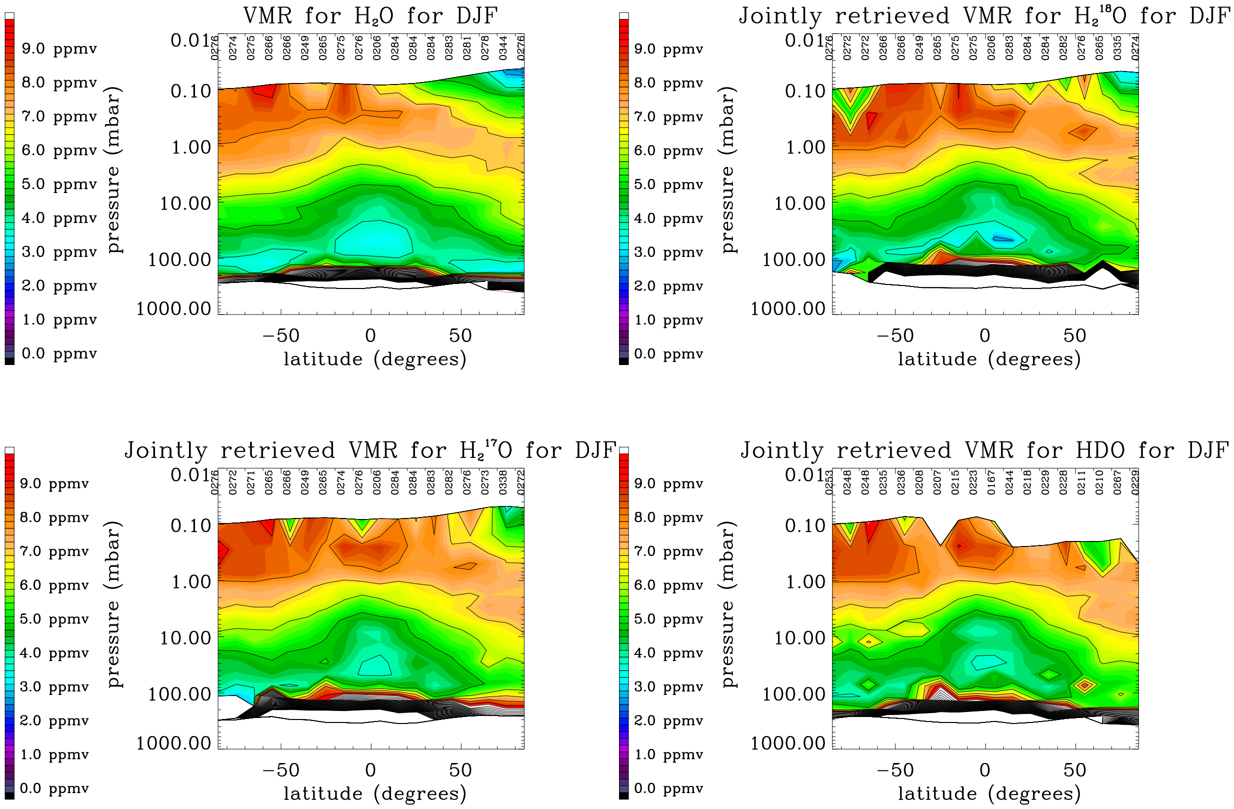

Figure 6.9: The top left plot shows zonal mean fields of $H_2^{16}O$ retrieved using the ESA operational water vapour microwindows, while the other three plots show zonal mean fields of $H_2^{16}O$ after influence from the joint retrievals of each of the minor water vapour isotopes.

6.5.2 Differences between retrievals of the main water isotope

In the retrieval approach outlined in § 6.3, the main isotopes are retrieved initially using the ESA operational microwindows. The retrieved profiles and their covariances are then used as input to the joint minor/major isotope retrievals. This may result in inconsistencies in the profiles of the main isotope used to calculate the three different minor isotopes of water vapour retrieved in this Chapter. However, since the minor isotopes were not selected with the aim of maximising the information content of the major isotope, it was expected that the minor isotope microwindows would not contain a great deal of information on the major isotopes, and so the initial retrieval result would not be adjusted by much. It was therefore expected that any inconsistencies between the main isotope retrievals would be small.

Figure 6.9 shows zonal mean fields of $H_2^{16}O$ retrieved using the ESA microwindows as well as fields of the adjusted $H_2^{16}O$ retrievals after the joint retrievals with each of the minor water vapour isotopes. There are visible differences in these fields, which could have implications for the calculation of the δ values.

6.5.3 HDO

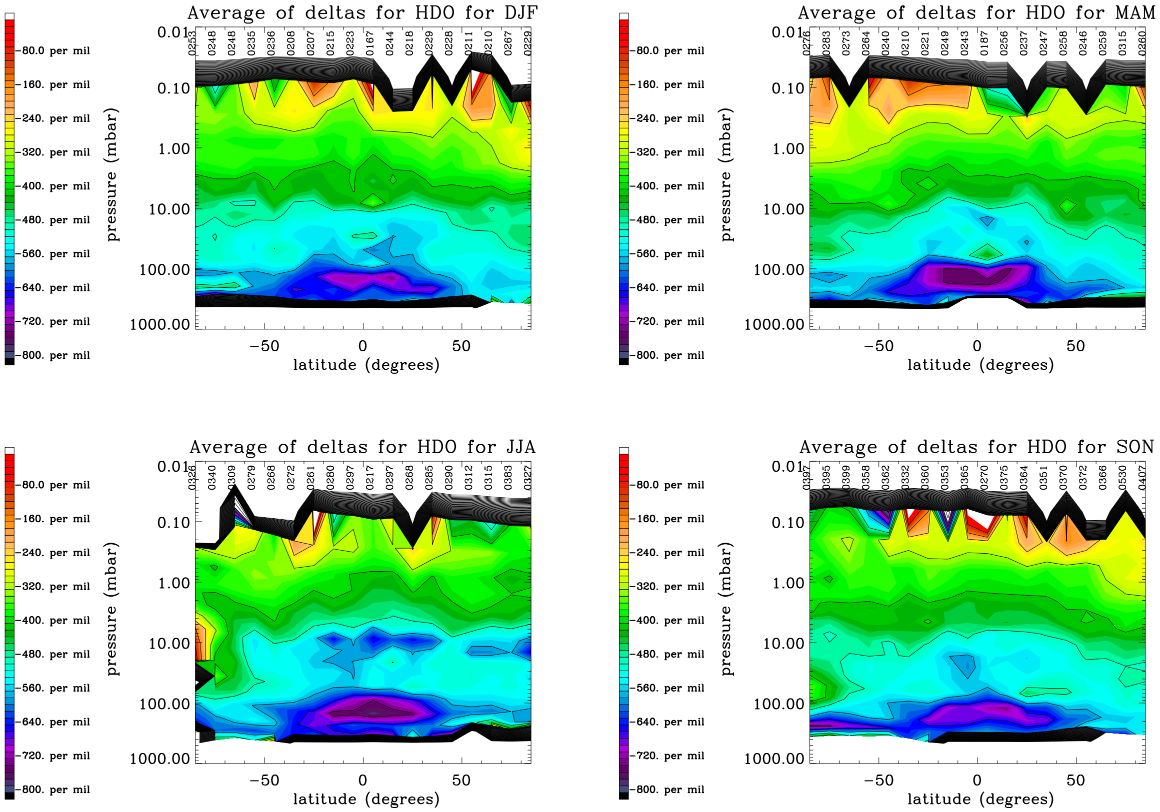

Figure 6.10: Zonal means of δD–HDO for December–February (top left), March–May (top right), June–August (bottom left) and September–November (bottom right). Each “season” contains nine days worth of data. The numbers at the top of each plot represent the number of profiles included in the zonal mean for each latitude band.

Of the minor isotopes retrieved for this Chapter, HDO is the one where the most success in retrieving recognisable features might be expected. Although it has a lower abundance (Table 6.1) than the heavy oxygen isotopes and the averaging kernels in Figure 6.7 indicate that the retrieval sensitivity is greater for the heavy oxygen isotopes, HDO shows the strongest fractionation with respect to the main isotope.

Figure 6.10 shows seasonal zonal mean fields of δD–HDO. As mentioned previously, the *a priori* profile of HDO was constructed from the H_2O profile retrieved using the operational microwindows and a HDO/H_2O ratio taken from an isotopic version of the CAM3 model. The ratio applied was kept constant across latitudes and time, so any latitudinal or temporal variation comes from the measurements.

Figure 6.10 shows various reassuring features that would have been expected from previous measurements and model results. The maximum depletions are observed in the region of the tropical tropopause. The altitude of the area of maximum depletion in Figure 6.10 is below the altitude of minimum water vapour values in Figure 6.8. In terms of time, the maximum depletions in this region correspond to the time of year (March–May) when the minimum temperatures at the tropical tropopause occur. Above the tropopause, there is a general increase in δD–HDO with altitude. This is what would be expected due to methane oxidation.

Seasonal variations in δD–HDO can be seen in polar regions. There are particularly strong depletions below 100 mbar in the Southern Hemisphere polar Spring. If polar stratospheric clouds had formed in the vortex, extremely large depletions would be expected. However, the large depletions observed in the Southern Hemisphere polar Spring are located rather low in altitude to be related to PSCs. They may be related to low temperatures in the upper troposphere. It could be interesting to perform some study of the relationship between values of δD and the occurrence of polar stratospheric clouds. Although it would not be possible to perform retrievals when PSCs are present, it could be possible to investigate the δD values before and after.

There are also hemispheric variations in δD at the uppermost end of the useful retrieval range, with HDO–rich air descending in polar regions in winter, as would be expected.

The δD–HDO shows a secondary minimum in the tropical zonal mean profiles at around 20 mbar. This secondary minimum appears to be a persistent oscillation in the δD–HDO in the tropics, particularly in the March–May season. It might be expected that there would be some kind of oscillation in the δ–values with altitude. Since the input of H_2O and its isotopes into the stratosphere is determined by the amount of convection and by the tropopause temperature, a tape–recorder effect would also be expected in the input isotopic ratio.

Figure 6.11 shows tropical zonal mean profiles of the major and minor isotopes and of the ratio between them for the four seasons. The VMR profiles of the minor isotope shown in this Figure have been scaled by the reference abundance from Table 6.1. The minor isotope profiles appear smooth. The oscillation in the ratio appears to stem from a persistent oscillation in the main isotope. It is possible that the oscillation in the main water vapour isotope stems either from a problem in capturing the temperature minimum at the tropopause (see Chapter 5) or in capturing the sharp minimum in water vapour at the hygropause. However, it is likely that there is also a signal related to the tropical tape recorder effect.

Figure 6.11 does not provide evidence of any movement of the oscillation in the ratios with time. With the number of days processed here, it is not possible to discern the tropical tape recorder effect in the retrieved water vapour, and so it is not possible to discern a tape recorder effect in the HDO/H_2O ratio. However, this might be an issue worth investigating with a larger number of processed days, spanning the full time period of the dataset rather than just 2003 data.

Supposing the VMR profiles for HDO were highly reliable, and all the problems lay in the retrieval of the main water isotope, then it might be expected that good zonal mean δ–values could be ob-

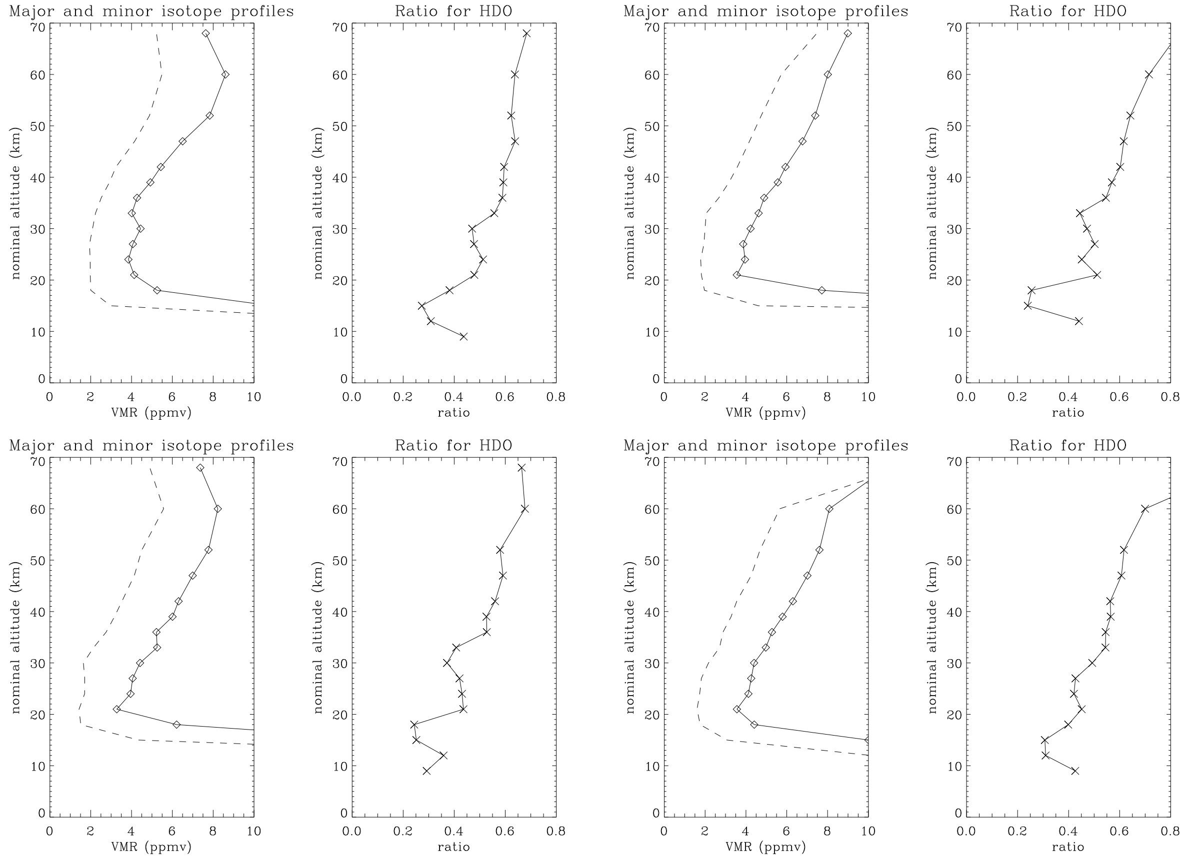

Figure 6.11: Tropical zonal mean profiles of HDO, $H_2^{16}O$ and the ratio between them for December–February (top left), March–May (top right), June–August (bottom left) and September–November (bottom right). Left–hand plots show profiles of the major isotope (solid line) alongside profiles of the minor isotope scaled by the surface abundance from Table 6.1 (dotted line). Right–hand plots show the ratio between the two profiles in the left–hand plots.

tained by calculating δ–values based on the ratio of VMR of retrieved HDO to climatological $H_2^{16}O$ from the IG2 dataset. For the sake of interest, this was done. Results from six selected latitude bands for the June–August season are shown in Figure 6.12. It can be seen from this Figure that the use of retrieved $H_2^{16}O$ results in much more sensible values of δD at lower altitudes than the use of IG2 $H_2^{16}O$. Above about 5 mbar, the effect of the high bias in the retrieved $H_2^{16}O$ with respect to the IG2 values is apparent.

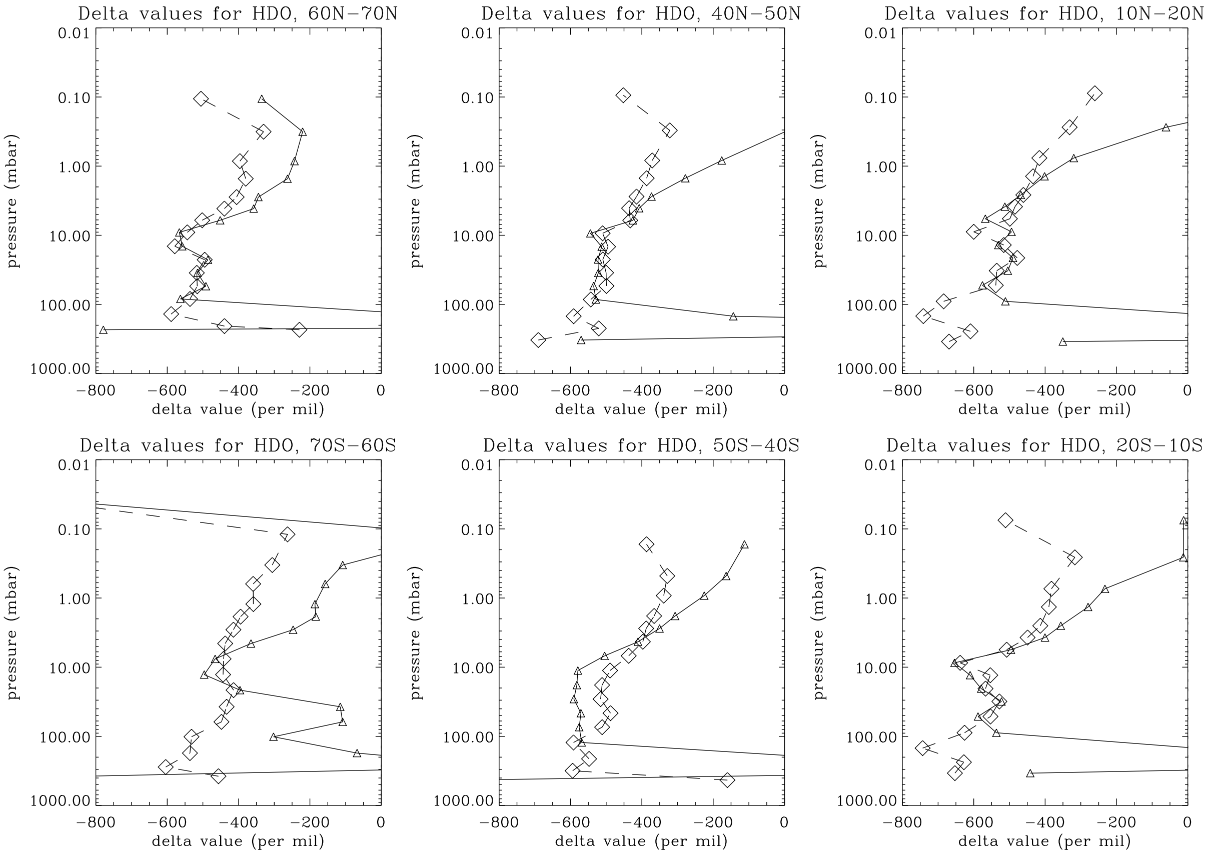

Figure 6.12: Profiles of δD–HDO calculated using retrieved $H_2^{16}O$ (squares and dotted lines) and climatological $H_2^{16}O$ (triangles and solid lines) for selected latitude bands.

6.5.4 $H_2^{18}O$

Figure 6.13 shows seasonal zonal mean distributions of $\delta^{18}O$–$H_2^{18}O$. It might be expected that these distributions would look broadly similar to those for δD–HDO shown in Figure 6.10, with the maximum depletions in $\delta^{18}O$ in the region of the tropical tropopause, and an increase in $\delta^{18}O$ with height, due to contributions from ^{18}O–enriched O_2 and possibly O_3. However, this is not the case. Figure 6.13 shows enriched values where enriched values would not be expected, and does not show a steady increase in $\delta^{18}O$ with height.

It could be argued that the maximum depletions in $H_2^{18}O$ are seen in the region of the tropical tropopause. However, there appears to be a strong persistent oscillation in the $\delta^{18}O$–$H_2^{18}O$, which

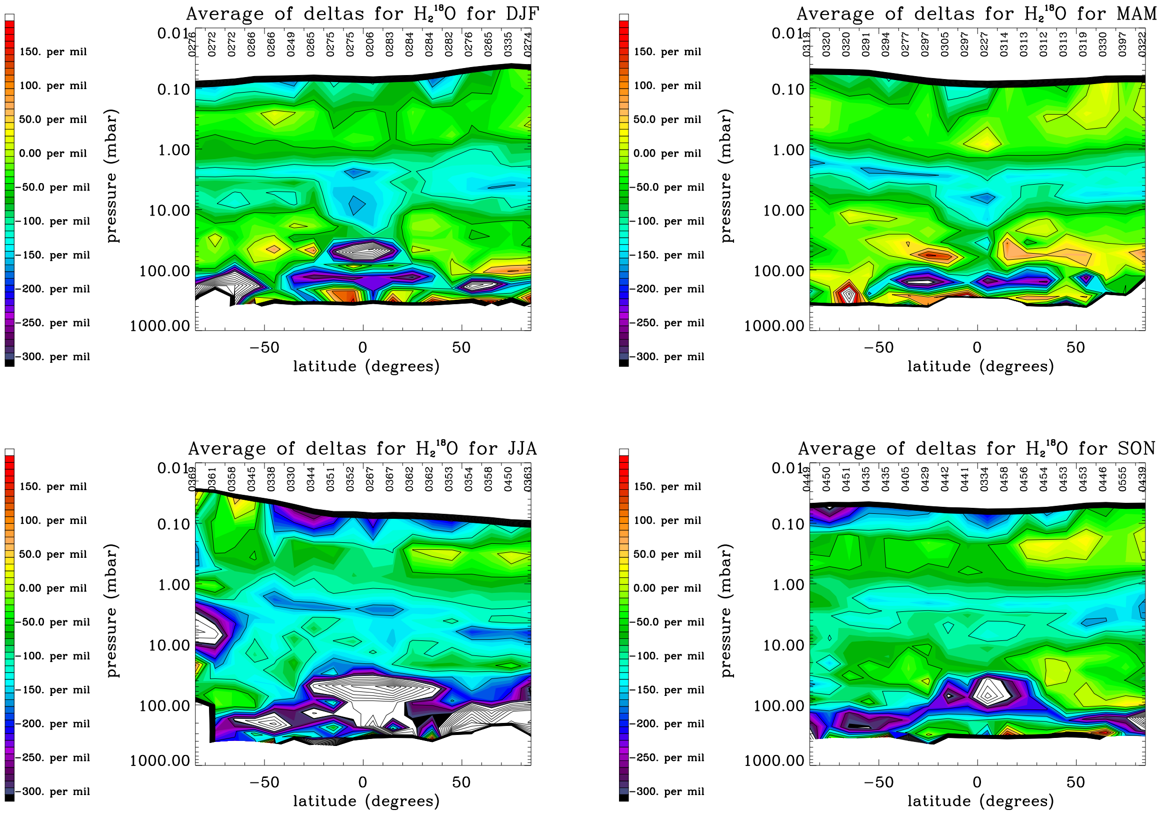

Figure 6.13: Zonal means of $\delta^{18}O$–$H_2^{18}O$ for December–February (top left), March–May (top right), June–August (bottom left) and September–November (bottom right). Each "season" contains nine days worth of data. Numbers along the top of these plots indicate the number of profiles included in the zonal mean for each latitude bin.

is not limited to the tropics. It is difficult to say how much of the structure here is real. The oscillations in $\delta^{18}O$–$H_2^{18}O$ appear to arise from persistent oscillations in the main, rather than the minor, isotope profiles (see Figure 6.14). There was a small oscillation in the *a priori* profile of δ–values which was taken from CAM model output in the tropics. It is possible that there would be some kind of oscillation in the $\delta^{18}O$ values in the tropics due to some kind of tape recorder effect. However it is assumed that the oscillations are indicative of some problem, since they are so large, they extend beyond the tropics and previous measurements and physical reasoning do not suggest that there should be such an oscillation.

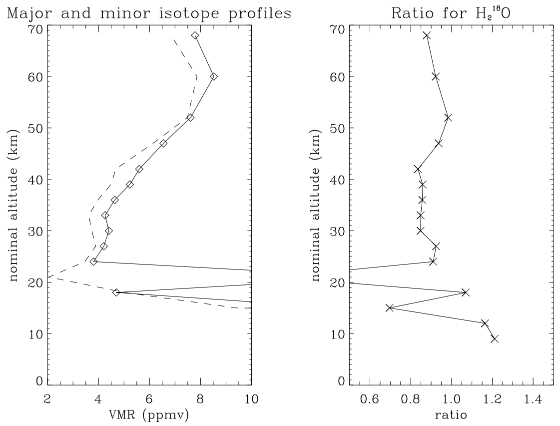

Figure 6.14: The plot on the left shows zonal mean tropical profiles of $H_2^{16}O$ (solid line) and $H_2^{18}O$, scaled by the surface abundance in Table 6.1 (dotted line). The plot on the right shows the ratio between the two.

It should be noted that the main isotope profile here is taken from the joint retrieval of major and minor isotopes, and as pointed out earlier, is slightly different for each of the minor isotopes.

Again, for the sake of interest, zonal mean δ–values were calculated using climatological $H_2^{16}O$ values. The resulting profiles are shown in Figure 6.15. As with HDO, the use of climatological $H_2^{16}O$ at lower altitudes does not result in sensible δ–values. Above 10 mbar, the use of climatological $H_2^{16}O$ does result in a profile of $\delta^{18}O$ which increases with altitude, as would be expected. It is not known how steep this increase ought to be, but the increase is certainly more marked for the $\delta^{18}O$ profiles calculated using climatological $H_2^{16}O$.

Further work would be needed on the investigation of this issue before these $H_2^{18}O$ retrievals from MIPAS could be used to infer anything about atmospheric processes.

6.5.5 $H_2^{17}O$

Figure 6.16 shows zonal mean fields of $\delta^{17}O$–$H_2^{17}O$ calculated from the $H_2^{17}O$ retrievals. Again, it might have been expected that the distribution would look broadly like a scaled version of the δD–HDO, or at least like a scaled version of the $\delta^{18}O$–$H_2^{18}O$, but it doesn't.

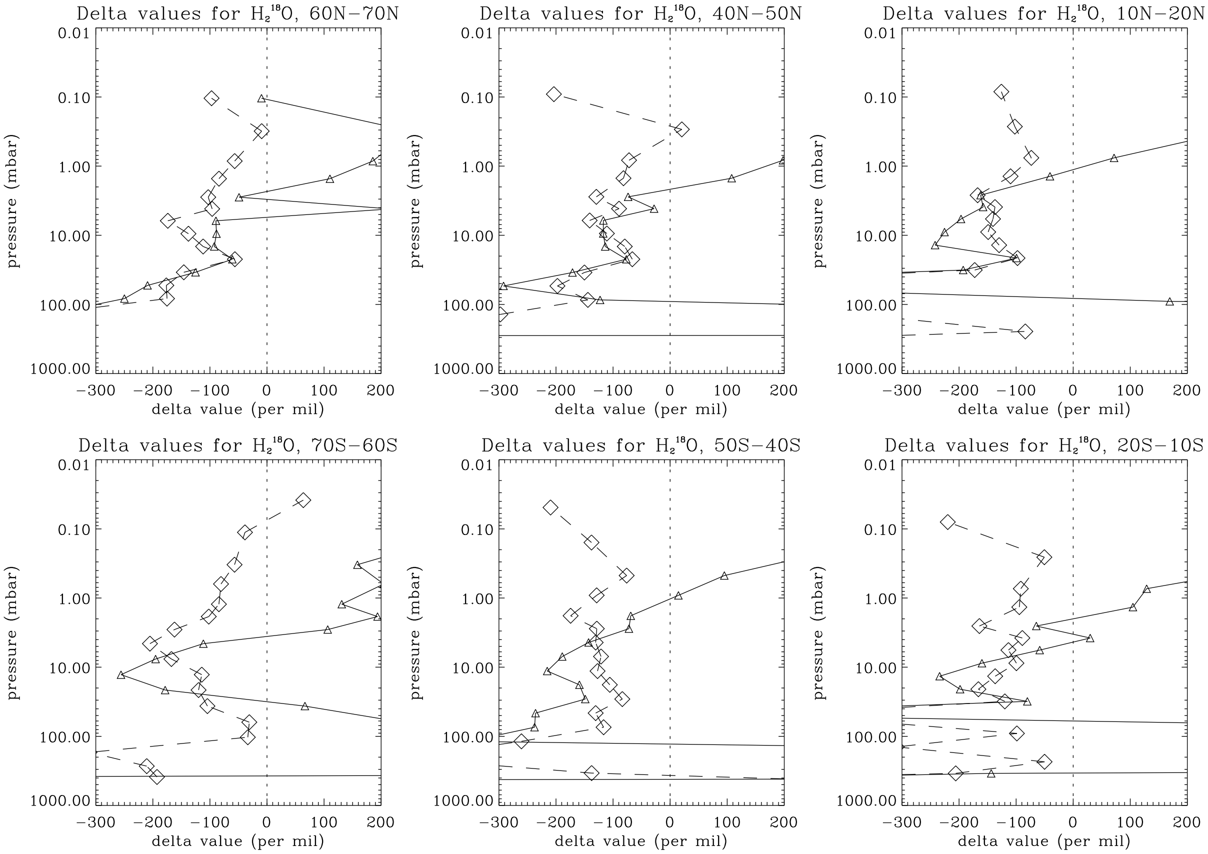

Figure 6.15: Profiles of δ^{18}O–$H_2^{18}O$ calculated using retrieved $H_2^{16}O$ (squares and dotted lines) and climatological $H_2^{16}O$ (triangles and solid lines) for selected latitude bands.

The zonal mean fields of δ^{17}O–$H_2^{17}O$ do show maximum depletion in the region of the tropical tropopause, although the values of the depletion in this region are around 250 ‰, which is somewhat larger than would be expected, based on previous measurements. The fields also show enrichment with respect to SMOW just above the area of maximum depletion, which is a not a feature that would be expected. The enriched area appears to be part of a persistent oscillation. Like the fields of δ^{18}O–$H_2^{18}O$ in Figure 6.13, the δ^{17}O–$H_2^{17}O$ zonal mean profiles in Figure 6.16 show evidence of a persistent oscillation (see also Figure 6.17) which extends further in latitude than the tropics.

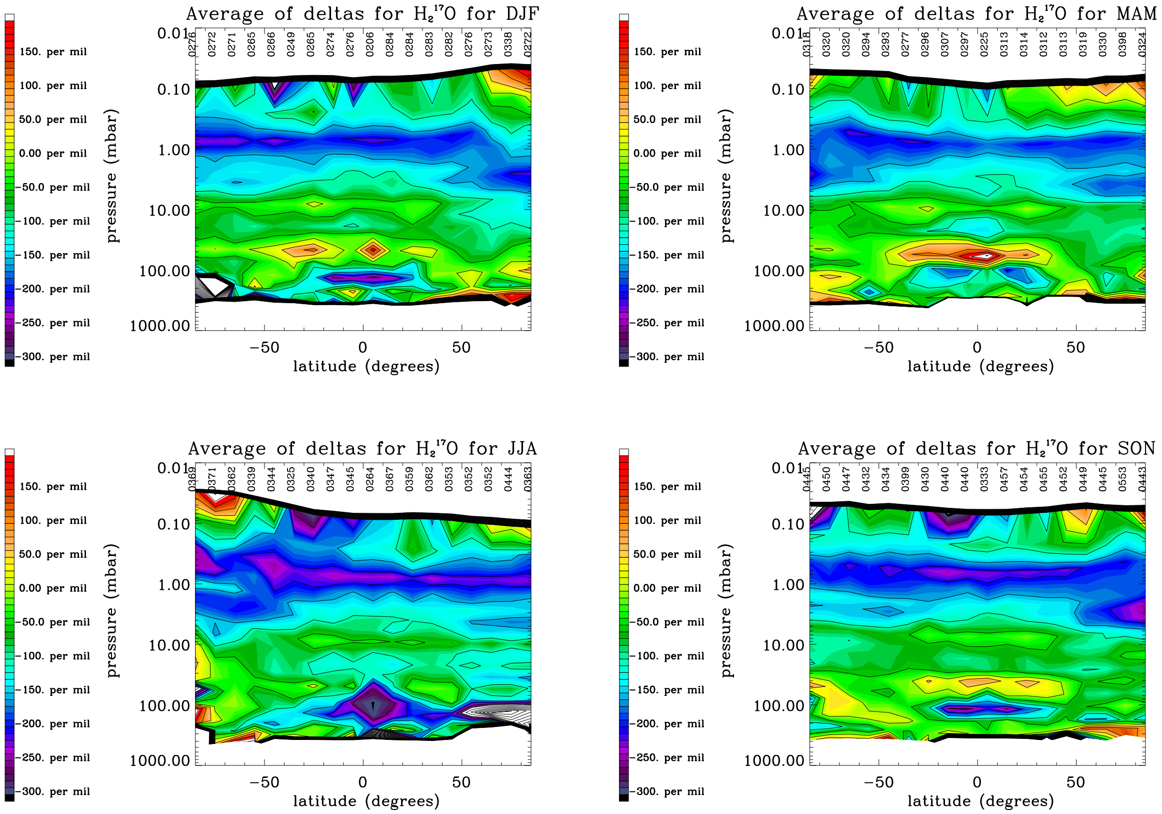

Figure 6.16: Zonal means of δ^{17}O–$H_2^{17}O$ for December–February (top left), March–May (top right), June–August (bottom left) and September–November (bottom right). Each "season" contains nine days worth of data.

Figure 6.16 shows unexpectedly large depletions, with values in the region of -200 ‰ above 10 mbar. It may be possible that there is some chemical process above this altitude which results in the depletion of δ^{17}O but not δ^{18}O. Perhaps the large depletions could be related to mass–independent fractionation in the upper stratosphere. However, it is also possible (and somewhat likely) that the large depletions are related to the observed high bias in water vapour in this altitude region, and that the greater depletions in δ^{17}O compared to δ^{18}O stem from differences in the water vapour profiles used to calculate the δ values (see § 6.5.2).

Zonal mean δ–values were calculated using climatological $H_2^{16}O$ values. The resulting profiles are shown in Figure 6.18. As with HDO and $H_2^{18}O$, the use of climatological $H_2^{16}O$ at lower altitudes

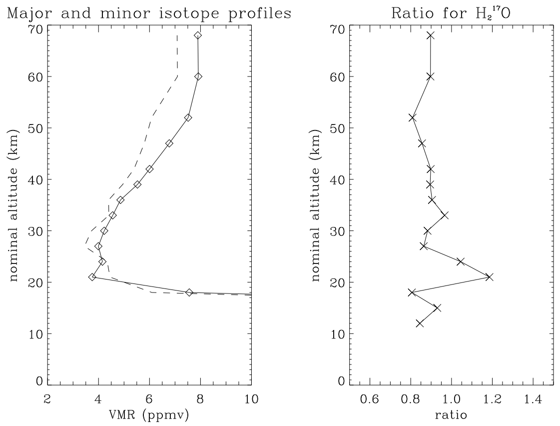

Figure 6.17: The plot on the left shows zonal mean tropical profiles of $H_2^{16}O$ (solid line) and $H_2^{17}O$, scaled by the surface abundance in Table 6.1 (dotted line). The plot on the right shows the ratio between the two.

does not result in sensible δ–values. Above 10 mbar, the use of climatological $H_2^{16}O$ does result in a profile of $\delta^{17}O$ which increases with altitude, as would be expected.

Further investigation of these issues would be required before any conclusions about atmospheric processes could be drawn from these fields of $\delta^{17}O$–$H_2^{17}O$.

6.5.6 CH_4

Figure 6.19 shows zonal mean fields of methane retrieved using MORSE and the ESA operational microwindows. Methane distributions have previously been discussed in Chapter 1. The retrieved fields are shown here in order to put the δ–values shown in the following Section into context.

6.5.7 CH_3D

Figure 6.20 shows seasonal zonal mean values of δD–CH_3D. The averaging kernels shown in Figure 6.7 indicate that retrievals of CH_3D are not useful above 21 km. This corresponds to a pressure of about 20 mbar. Previous measurements indicate that δD–CH_3D should show values in the region of -100 ‰ to -50 ‰ in the upper troposphere and that the depletion in δD should reduce with

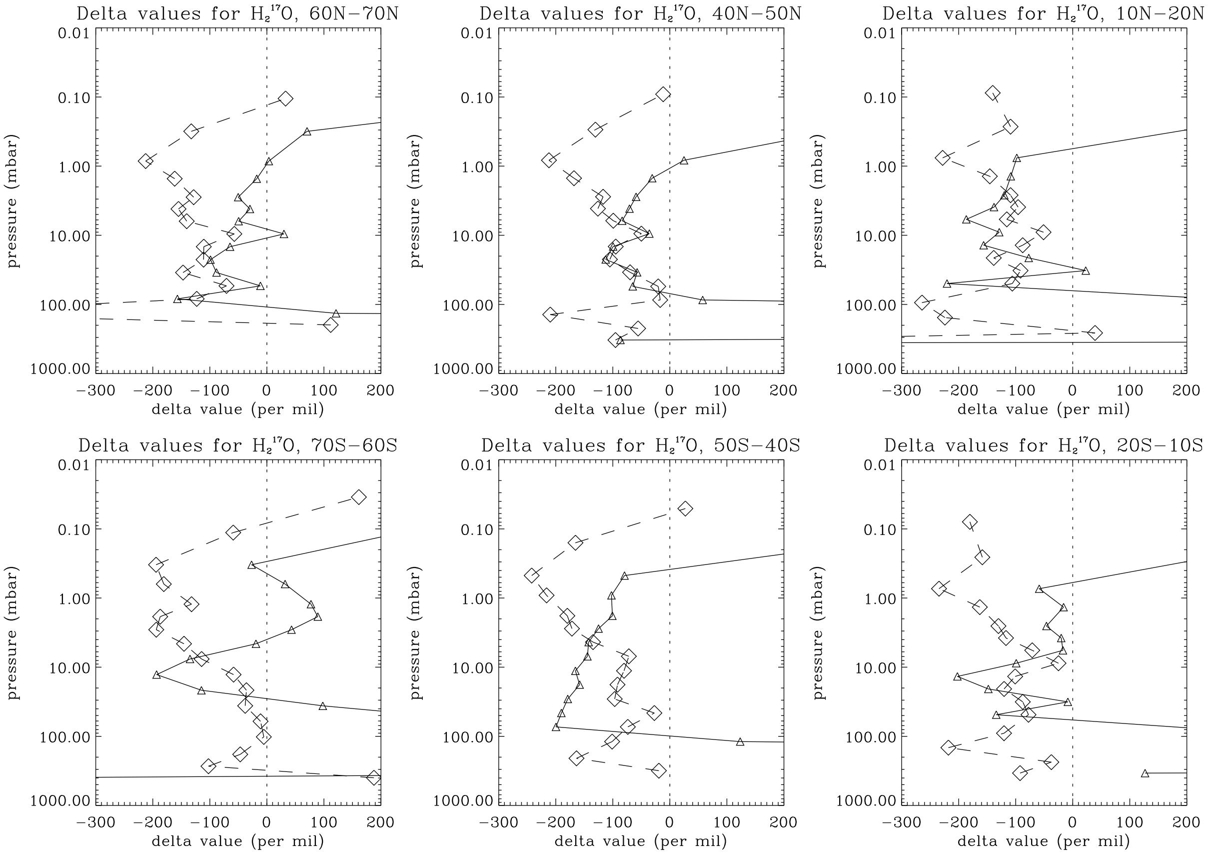

Figure 6.18: Profiles of δ^{17}O–$H_2^{17}O$ calculated using retrieved $H_2^{16}O$ (squares and dotted lines) and climatological $H_2^{16}O$ (triangles and solid lines) for selected latitude bands.

altitude, since CH_3D is expected to have a longer lifetime than CH_4. Older air is expected to be enriched in deuterium compared to younger air. By this reasoning, it would be expected that there would be greater depletion in δD–CH_3D in equatorial regions than at the poles, and that the polar vortices would show the most enriched values, due to descent of older air from higher altitudes. It cannot be argued convincingly that this is the case in Figure 6.20.

6.6 Retrieval results: correlations

In this section, relationships between H_2O, CH_4 and the minor isotopes retrieved in this section are discussed. It was hoped that viewing the seasonal zonal means shown in § 6.5 in terms of their

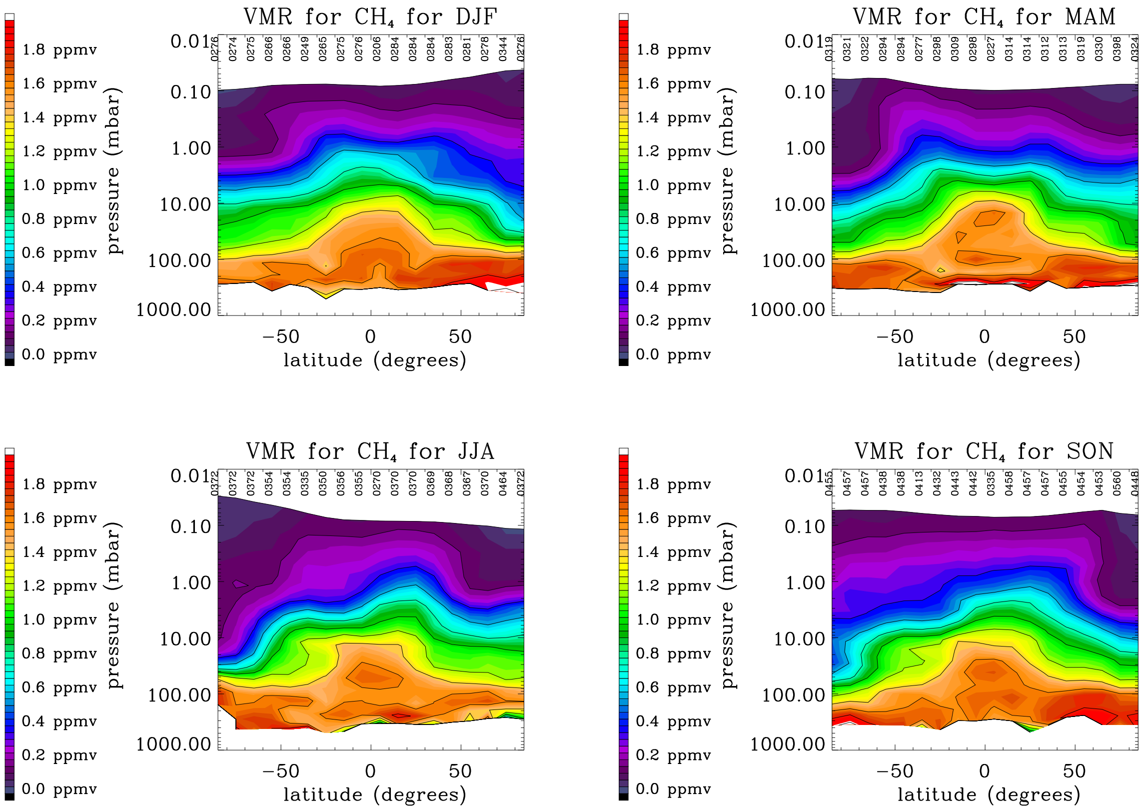

Figure 6.19: Zonal means of CH_4 for December–February (top left), March–May (top right), June–August (bottom left) and September–November (bottom right). Each “season” contains nine days worth of data. The numbers at the top of each plot represent the number of profiles included in the zonal mean for each latitude band.

relationships with each other might be a useful exercise in terms of internal consistency checks and in assessing the usefulness of the retrieved quantities in terms of making statements about atmospheric processes. Scatter plots of δ^{18}O–$H_2^{18}O$ against δ^{17}O–$H_2^{17}O$ (§ 6.6.1), δD–HDO against δ^{18}O–$H_2^{18}O$ (§ 6.6.2), δD–HDO against δ^{17}O–$H_2^{17}O$ (§ 6.6.3) and HDO against CH_3D are presented and discussed.

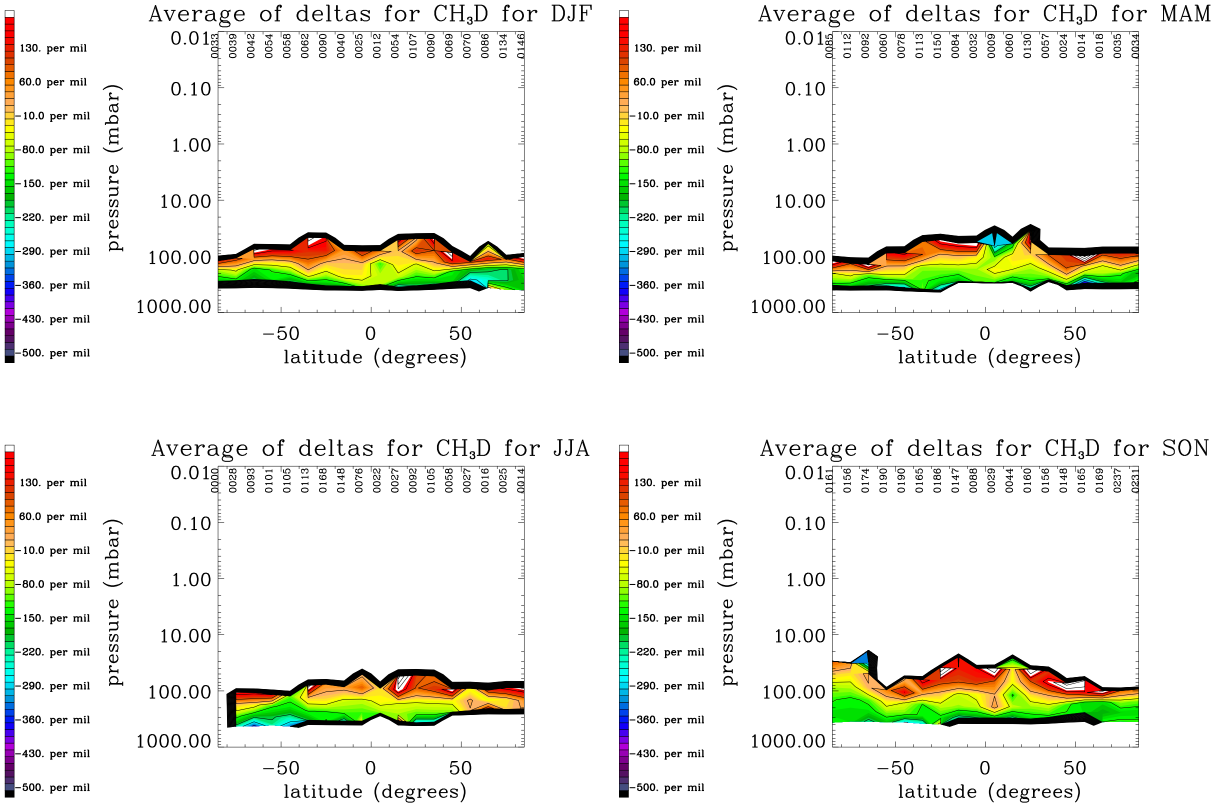

Average of deltas for CH_3D for DJF

Average of deltas for CH_3D for MAM

Average of deltas for CH_3D for JJA

Average of deltas for CH_3D for SON

Figure 6.20: Zonal means of δD–CH_3D for December–February (top left), March–May (top right), June–August (bottom left) and September–November (bottom right). Each "season" contains six days worth of data. These plots show the average of the δ–values.

6.6.1 δ^{17}O–$H_2^{17}O$ vs δ^{18}O–$H_2^{18}O$

"Mass–dependent fractionation" is expected to lead to the depletion in δ^{17}O in water vapour being less than the depletion in δ^{18}O by a factor of 0.526 (Equation 6.4). There is a mass–independent fractionation that is associated with ozone photolysis and O(^{1}D). The anomaly due to mass–independent fractionation is expected to be very small in the troposphere (Boering et al., 2004).

Figure 6.21 shows zonal mean values of δ^{17}O from the MORSE retrievals plotted against δ^{18}O. The solid line in these plots indicates the relationship expected from mass–dependent fractionation. The values in Figure 6.21 do show some correlation, and appear to be consistent with a straight line.

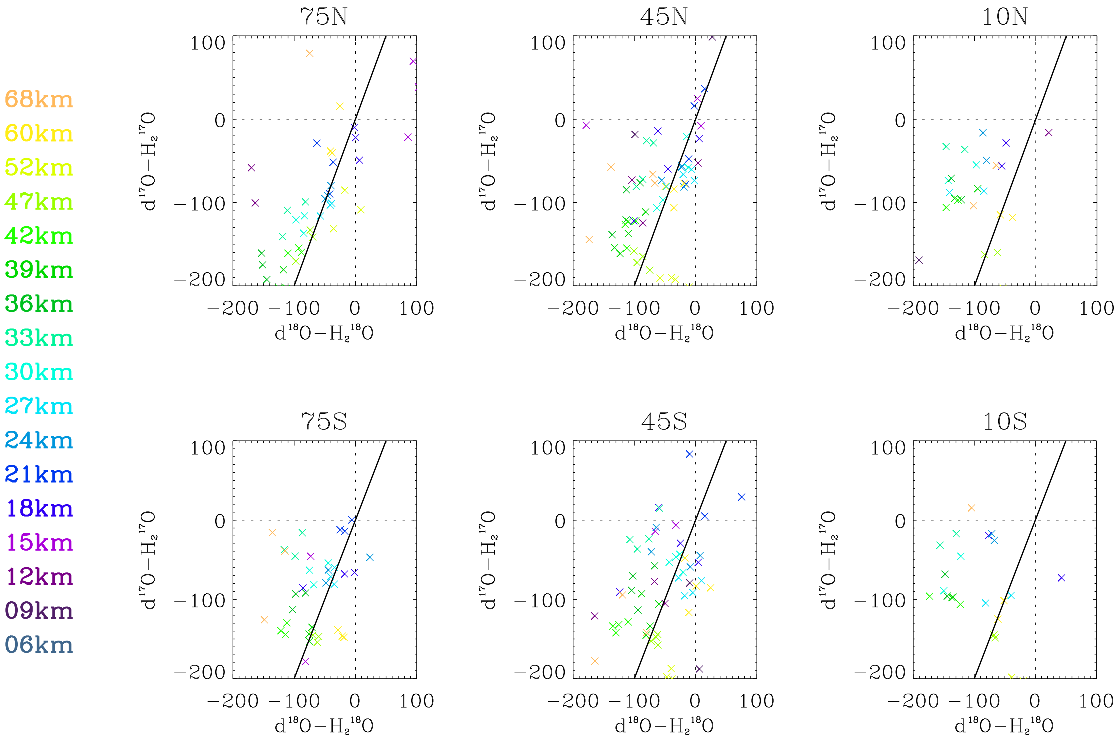

Figure 6.21: Zonal mean values of δ^{18}O–H$_2^{18}$O against δ^{17}O–H$_2^{17}$O for December–February. Different colours represent different MIPAS nominal altitudes. The solid line here represents the relationship between δ^{17}O and δ^{18}O expected from mass–dependent fractionation (Equation 6.4).

6.6.2 δD–HDO vs δ^{18}O–H$_2^{18}$O

Figure 6.22 shows seasonal zonal means of δ^{18}O–H$_2^{18}$O against δD–HDO. Also shown on these plots is the linear relationship between δ^{18}O and δD found in the tropospheric measurements of Taylor (1972) (Equation 6.3).

It is clear that the retrieved values of δ^{18}O and δD do not show a linear relationship. If anything, there is something of a C–shaped curve, with much greater depletions in the δ^{18}O than would be expected.

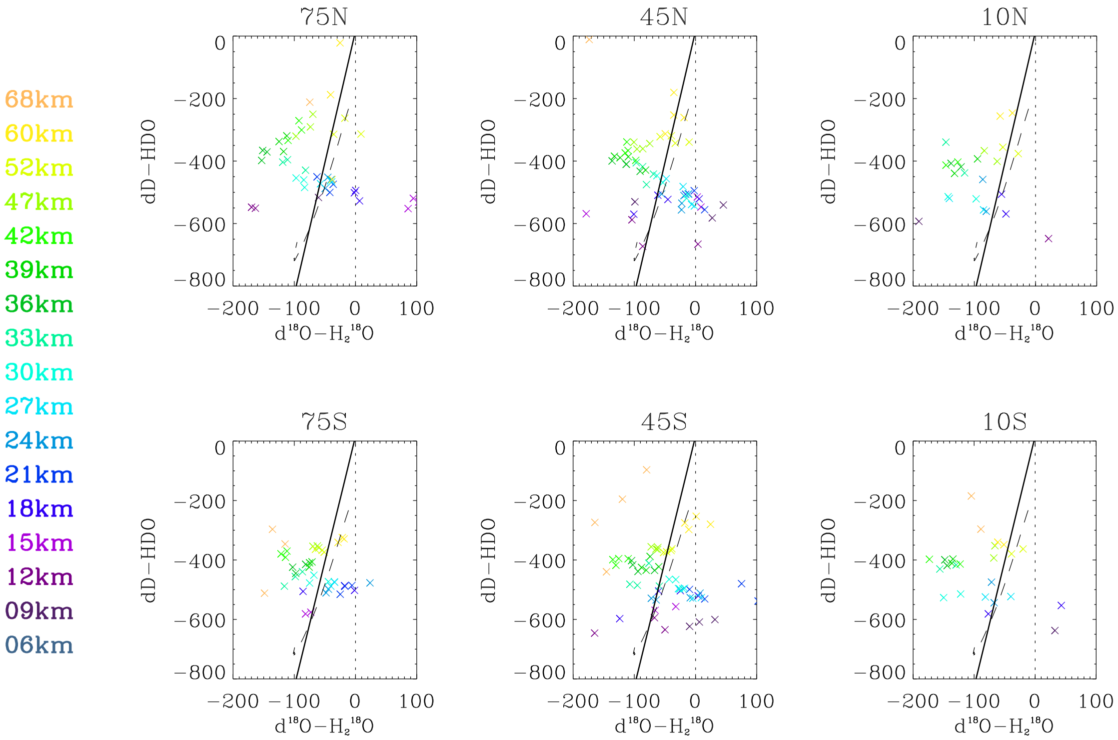

Figure 6.22: Zonal mean values of δ^{18}O–H$_2^{18}$O against δD–HDO for December–February. Different colours represent different MIPAS nominal altitudes. The solid line represents the linear relationship between δ^{18}O–H$_2^{18}$O and δD–HDO found in tropospheric measurements by Taylor (1972).

6.6.3 δD–HDO vs δ^{17}O–H$_2^{17}$O

Figure 6.23 shows seasonal zonal means of δ^{17}O–H$_2^{17}$O against δD–HDO. Also shown on these plots is a linear relationship between δ^{17}O and δD deduced from the tropospheric measurements of Taylor (1972) (Equation 6.3) and from mass–dependent fractionation (Equation 6.4.)

These plots do not show such a pronounced C–shape as the one exhibited in Figure 6.22. Instead, there is more of a linear relationship between δD and δ^{17}O, where the depletion in δ^{17}O increases as the depletion in δD decreases. This is the opposite of what would have been expected. It is not clear whether this relationship bears any truth, or is merely a symptom of systematic errors in the retrievals.

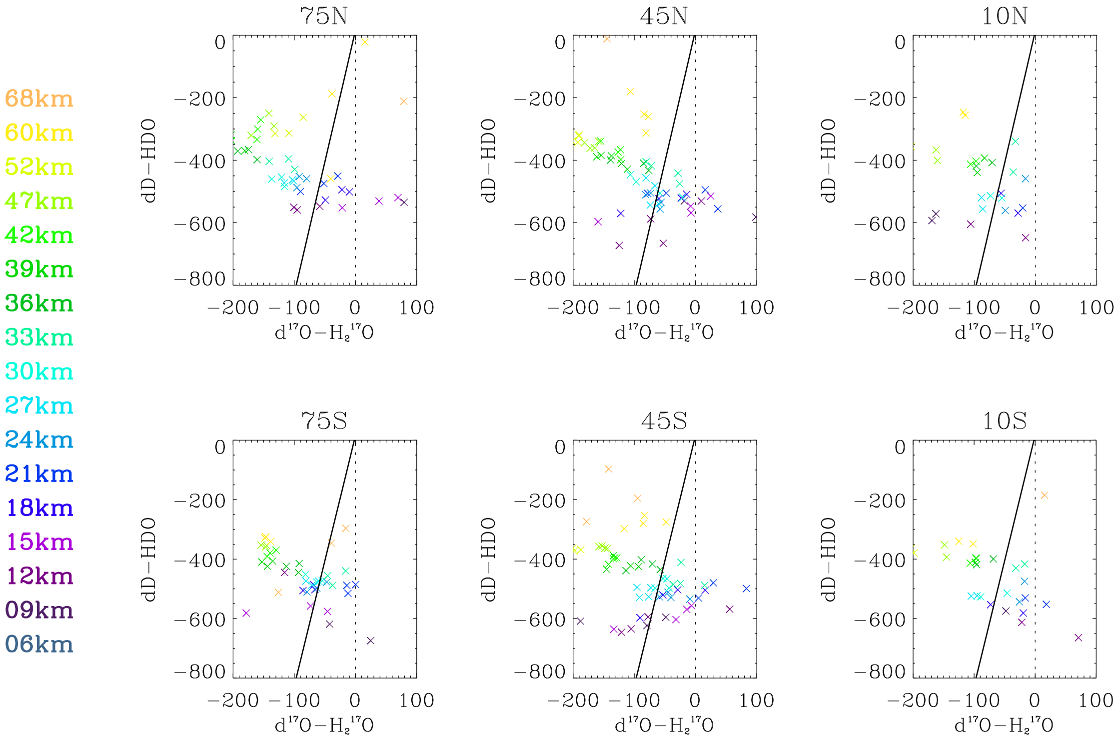

Figure 6.23: Zonal mean values of δ^{17}O–H$_2^{17}$O against δD–HDO for December–February. Different colours represent different MIPAS nominal altitudes. The solid line represents the linear relationship between δ^{17}O–H$_2^{17}$O and δD–HDO found in tropospheric measurements by Taylor (1972).

6.6.4 HDO vs CH$_3$D

The total deuterium, H$_{\text{total}}$ = HDO + CH$_3$D + HD is assumed to be constant in the stratosphere. Using ATMOS measurements of HDO and CH$_3$D, Irion et al. (1996) deduced that there was no significant change in HD with altitude. More accurate measurements have since shown that there is in fact a significant fractionation in HD, and that HDO + CH$_3$D cannot be regarded as constant with altitude.

Figure 6.24 shows zonal mean values of HDO and CH$_3$D from MIPAS. The solid lines on these plots were calculated as follows: An array of CH$_4$ values was constructed. A corresponding array of CH_3D VMR was calculated from the CH_4 array using the linear relationship between CH_4 and CH_3D deduced by McCarthy et al. (2003a). An array of HD VMR was similarly constructed using a linear relationship between CH_4 and HD deduced by McCarthy et al. (2003a). Values of D_{total} are quoted in this paper as ranging from 1.67 to 1.58 ppbv. A value of 1.63 ppbv was chosen, and an array of HDO VMR values calculated. The solid line shows HDO = D_{total} - CH_3D - HD, while the dashed line shows HDO = D_{total} - CH_3D.

Bearing in mind that the MIPAS CH_3D measurements are only useful at the lowermost altitudes, it would appear that the difference between the two scenarios would not be discernible with these MIPAS retrievals.

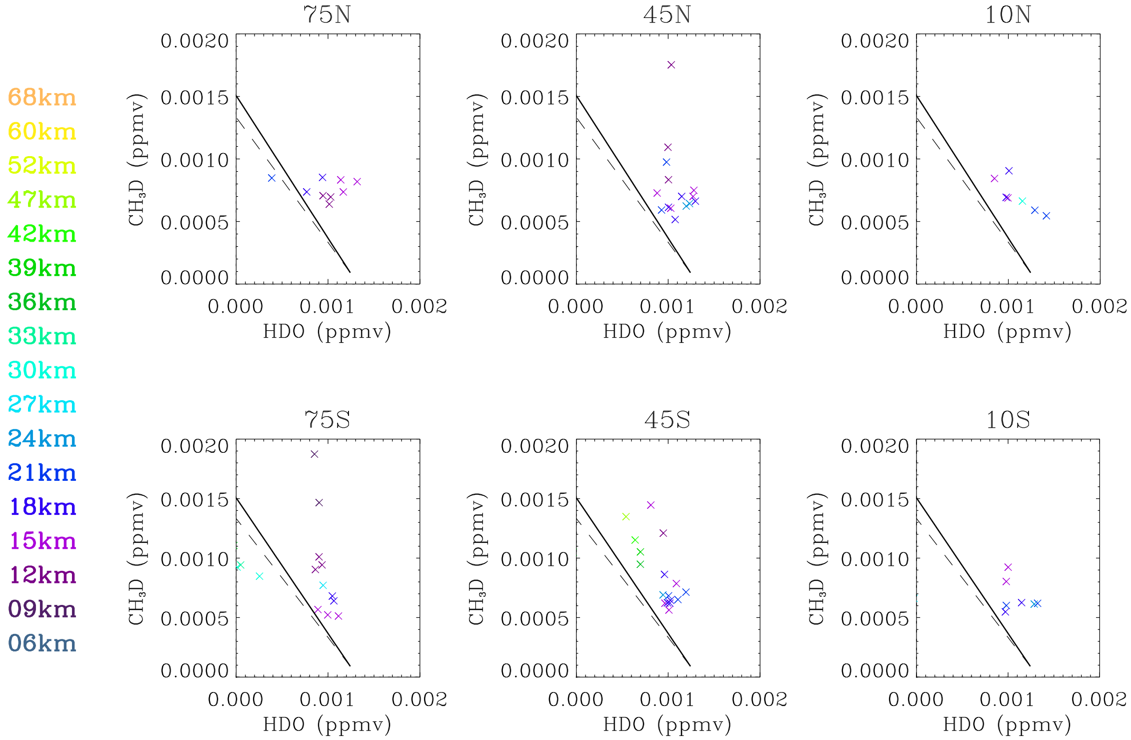

Figure 6.24: Zonal mean values of VMRs of HDO against CH_3D for December–February. Different colours represent different MIPAS nominal altitudes. The solid line represents a scenario where HDO+CH_3D = constant, as presumed by Irion et al. (1996). The dashed line represents a scenario where HDO + CH_3D + HD = constant.

6.7 Odin–SMR comparisons

The Odin–SMR instrument has previously been introduced in § 4.8. The Odin SMR measures HDO and $H_2^{18}O$ in addition to the main water vapour isotope. In this Section, zonal mean comparisons between Odin–SMR CTSO-v223 and MIPAS MORSE retrievals of $H_2^{16}O$, HDO and $H_2^{18}O$ are performed for $22^{nd}/23^{rd}$ November 2002 and 2003. Details of the coverage offered by the instruments for these days can be found in Figures 4.53 and 4.54 in § 4.8.

6.7.1 $H_2^{16}O$

Comparisons between MIPAS ESA OFL and Odin–SMR H_2O have already been shown in § 4.8. Although the MIPAS OFL processor retrieves water vapour in general, rather than $H_2^{16}O$ in particular, the operational microwindows used do not contain any minor isotope lines, so the retrieval is effectively an $H_2^{16}O$ retrieval. In the comparisons shown in this Section, the MIPAS $H_2^{16}O$ zonal means are taken from MORSE retrievals rather than from the ESA OFL data.

Figures 6.25 and 6.26 show zonal mean fields of $H_2^{16}O$ from MIPAS and the Odin–SMR respectively, while Figure 6.27 shows percentage differences between the two. The MORSE retrievals of $H_2^{16}O$ show a higher bias with respect to the Odin–SMR values than the ESA OFL retrievals above 30 km but do not show the low values at 68 km found in the ESA OFL profiles. Like the ESA OFL zonal means, the MORSE zonal means show particularly high values of H_2O in northern polar regions at about 2 mbar. As with the OFL comparisons, the MORSE H_2O shows a bias pattern with respect to the Odin–SMR H_2O which is largely consistent across latitudes and from one year to the next.

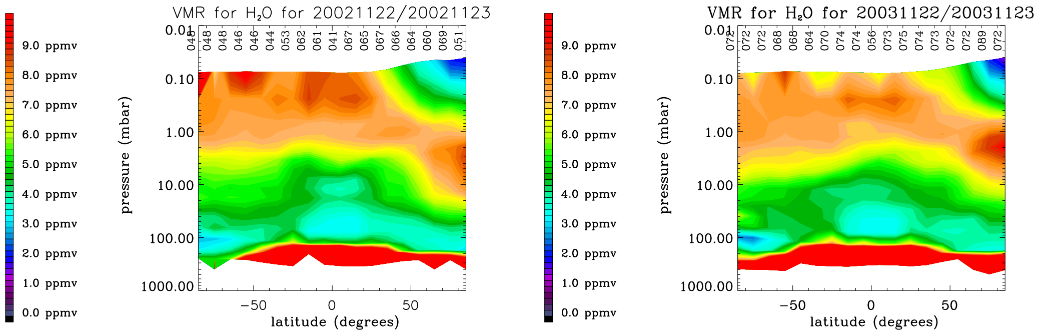

Figure 6.25: Zonal mean $H_2^{16}O$ from MIPAS MORSE retrievals for 22nd and 23rd November 2002 (left) and 2003 (right).

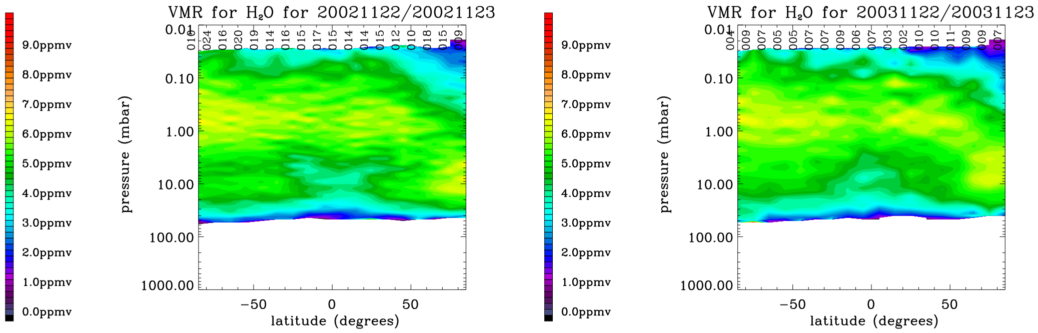

Figure 6.26: Zonal mean $H_2^{16}O$ from Odin–SMR CTSO-v223 data for 22nd and 23rd November 2002 (left) and 2003 (right).

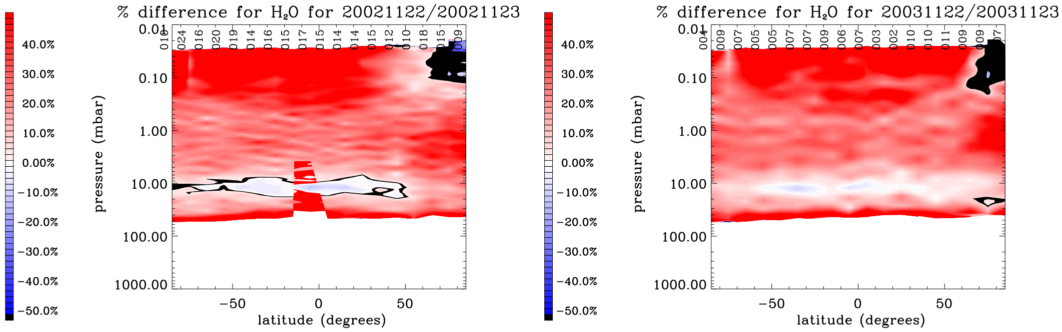

Figure 6.27: Percentage difference between zonal mean MIPAS MORSE and Odin–SMR $H_2^{16}O$ ([MIPAS-Odin]/Odin)for 22nd and 23rd November 2002 (left) and 2003 (right).

6.7.2 HDO

Figures 6.28 and 6.29 show zonal mean fields of VMR of HDO from MIPAS and the Odin–SMR respectively, while Figure 6.30 shows percentage differences between the two. Odin retrievals of HDO do not cover as large an altitude range as the $H_2^{16}O$ retrievals. In general, MIPAS values of HDO are around 10–20 % higher than Odin values. The differences are approximately the same size as the differences in the $H_2^{16}O$ retrievals within the altitude range of interest.

Figures 6.31 and 6.32 show the zonal mean fields of δD–HDO calculated from the MIPAS and Odin–SMR retrievals respectively. Both sets of data show general features which are consistent from one year to the next. Like the MIPAS distributions, Odin distributions of δD–HDO show the largest depletions in the tropics and a depletion that lessens with altitude. The Odin retrievals do not extend down to the tropopause but the maximum depletions observed in Odin at about 10 mbar, or just below, show approximately the same values of δD as the MIPAS maximum depletions just below 100 mbar. The depletions observed in the Odin data at 10 mbar seem rather large for this altitude.

6.7.3 $H_2^{18}O$

Figures 6.33 and 6.34 show zonal mean fields of VMR of $H_2^{18}O$ from MIPAS and the Odin–SMR respectively, while Figure 6.35 shows percentage differences between the two.

In general, values of $H_2^{18}O$ from MIPAS and Odin are in better agreement than values for the main water vapour isotope. MIPAS values are slightly lower than Odin between around 50 and 10 mbar, higher between 10 and 5 mbar, lower between 5 and 1 mbar, and higher between 1 and 0.1 mbar. As with the comparisons of the main isotope, the bias pattern is largely consistent across latitudes and from one year to the next.

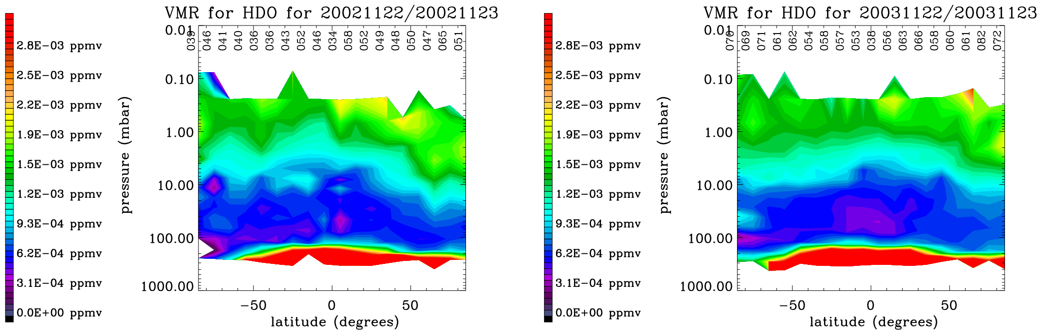

Figure 6.28: Zonal mean HDO VMR from MIPAS MORSE retrievals for 22^{nd} and 23^{rd} November 2002 (left) and 2003 (right).

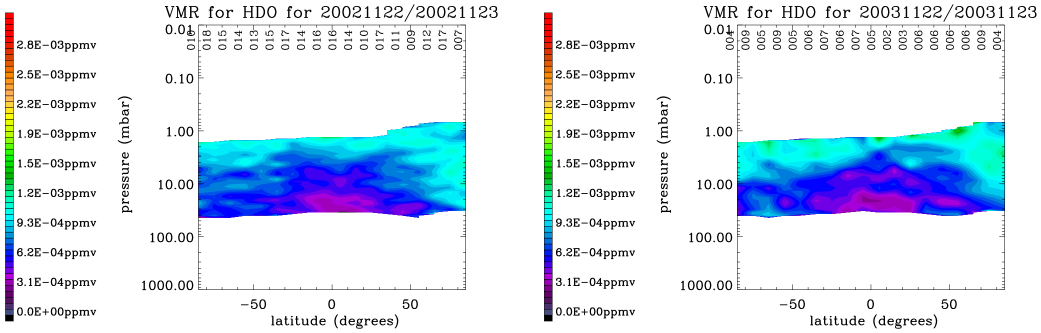

Figure 6.29: Zonal mean HDO VMR from Odin–SMR CTSO-v223 data for 22^{nd} and 23^{rd} November 2002 (left) and 2003 (right).

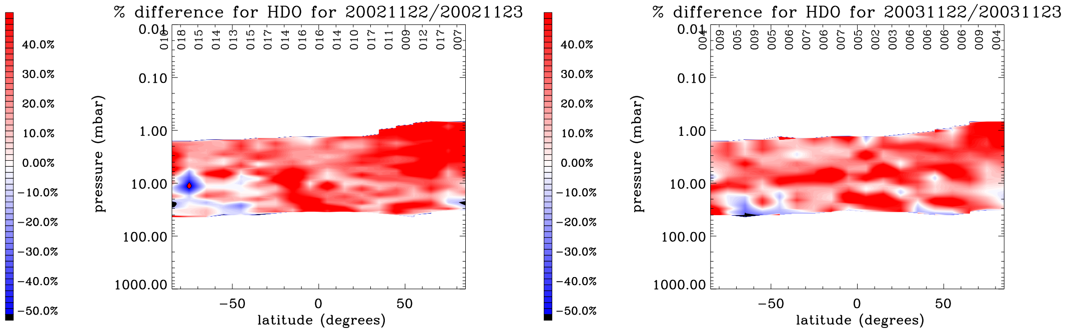

Figure 6.30: Percentage difference between zonal mean MIPAS MORSE and Odin–SMR HDO ([MIPAS-Odin]/Odin)for 22^{nd} and 23^{rd} November 2002 (left) and 2003 (right).

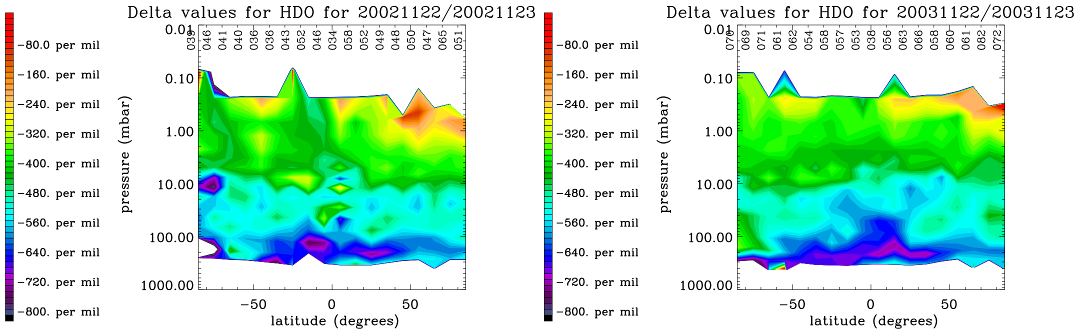

Figure 6.31: Zonal mean δD–HDO from MIPAS MORSE retrievals for 22^{nd} and 23^{rd} November 2002 (left) and 2003 (right).

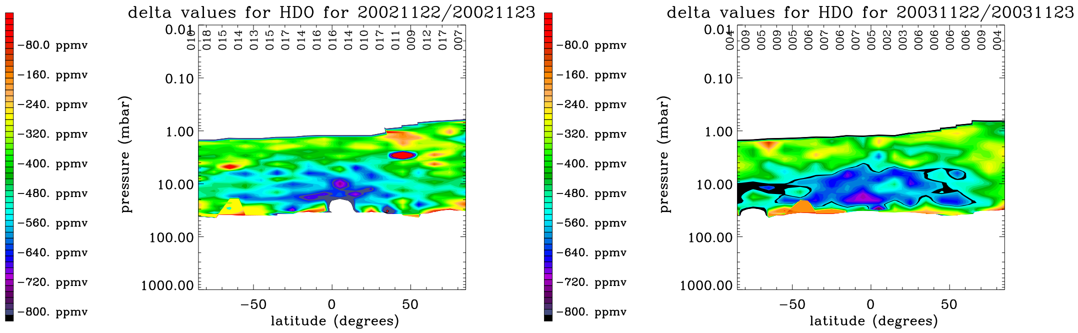

Figure 6.32: Zonal mean δD–HDO from Odin–SMR CTSO-v223 data for 22^{nd} and 23^{rd} November 2002 (left) and 2003 (right).

Figures 6.36 and 6.37 show the zonal mean fields of δ^{18}O–$H_2^{18}O$ calculated from the MIPAS and Odin–SMR retrievals. The distributions from both instruments show features which are consistent between one year and the next, but the distributions of δ^{18}O–$H_2^{18}O$ are very different for the two instruments.

Zonal mean distributions of δ^{18}O from MIPAS have already been discussed in § 6.5.4. The distributions of δ^{18}O from Odin show a maximum depletion at around 10 mbar, with a trend towards enrichment above this. Values of δ^{18}O below 10 mbar seem unrealistically enriched. It would appear that measurements of the isotopic composition of water vapour from both instruments have their problems.

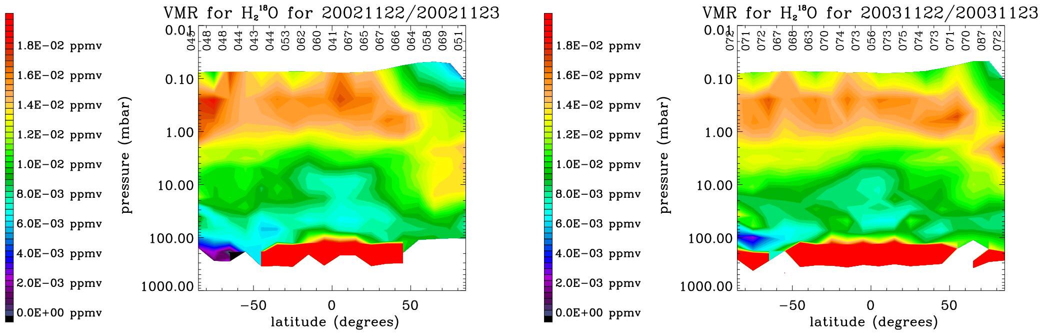

Figure 6.33: Zonal mean $H_2^{18}O$ VMR from MIPAS MORSE retrievals for 22^{nd} and 23^{rd} November 2002 (left) and 2003 (right).

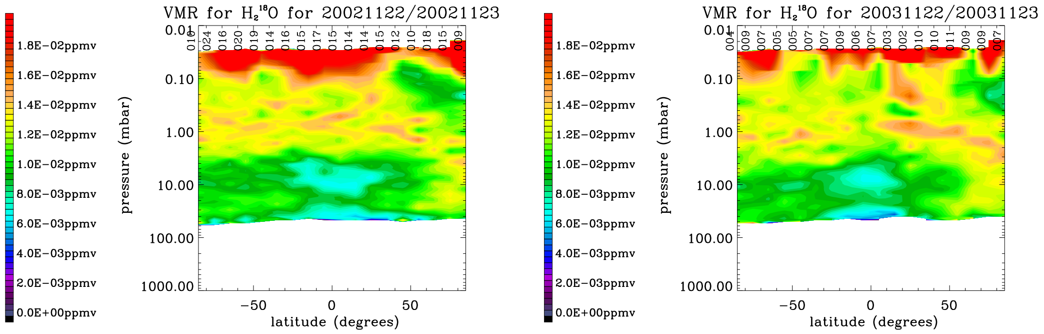

Figure 6.34: Zonal mean $H_2^{18}O$ from Odin–SMR CTSO-v223 data for 22^{nd} and 23^{rd} November 2002 (left) and 2003 (right).

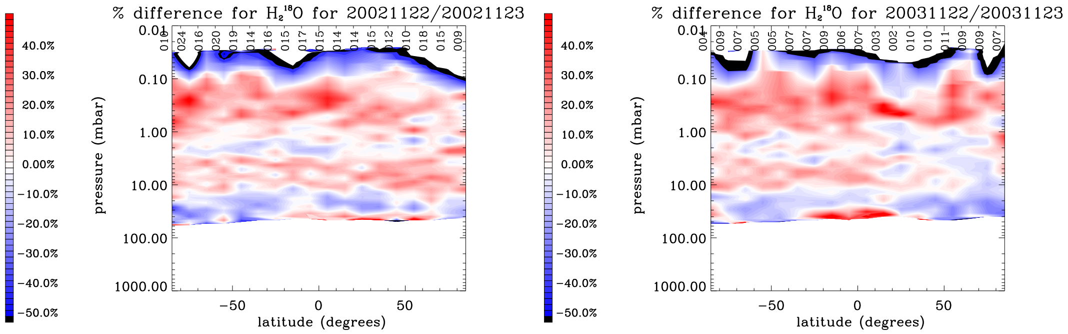

Figure 6.35: Percentage difference between zonal mean MIPAS OFL and Odin–SMR H_2O ([MIPAS-Odin]/Odin)for 22^{nd} and 23^{rd} November 2002 (left) and 2003 (right).

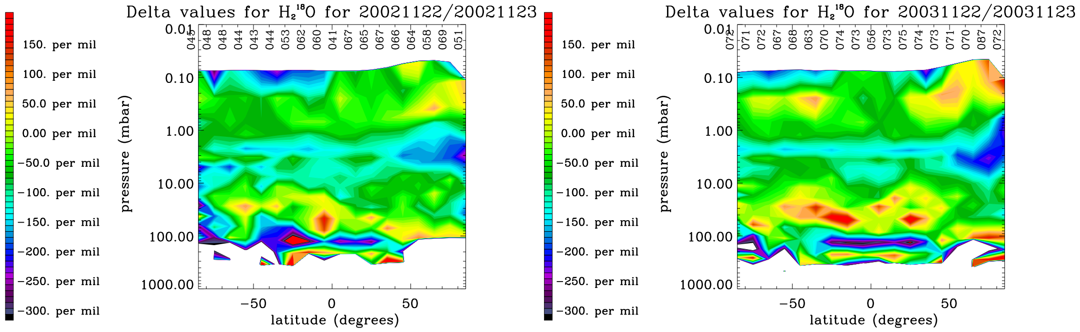

Figure 6.36: Zonal mean δ^{18}O–$H_2^{18}O$ from MIPAS MORSE retrievals for 22nd and 23rd November 2002 (left) and 2003 (right).

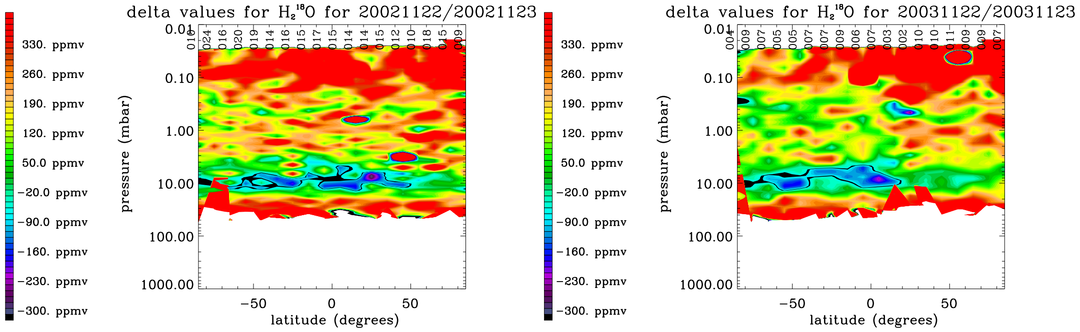

Figure 6.37: Zonal mean δ^{18}O–$H_2^{18}O$ from Odin–SMR CTSO-v223 data for 22nd and 23rd November 2002 (left) and 2003 (right).

6.7.4 Summary of Odin comparisons

In general, MORSE $H_2^{16}O$ retrievals show a high bias with respect to Odin–SMR values, with the bias increasing with altitude from around 10 % at 10 mbar to around 30 % at 0.1 mbar. The agreement between MIPAS MORSE $H_2^{16}O$ with the Odin–SMR is worse than for the MIPAS OFL H_2O.

Retrievals of volume mixing ratios of HDO and $H_2^{18}O$ from MIPAS and Odin show similar variations with latitude and altitude. Values of VMR for these minor isotopes from the two instruments are generally within ±20 %. However, distributions of δD and δ^{18}O show large discrepancies.

6.8 Summary and conclusions

Results for HDO are promising, with zonal mean distributions of δD showing maximum depletions of around -700 ‰ in the region of the tropical tropopause and a general decrease in depletion with height, as would be expected due to the formation of HDO from the oxidation of CH_3D and HD. Zonal mean distributions of δ^{18}O and δ^{17}O do, arguably, show maximum depletions in the region of the tropical tropopause. However, they do not show the expected increase in the heavy oxygen content with altitude that would be expected due to the influence of the heavy oxygen content of the reservoirs of molecular oxygen and ozone in water vapour formed through methane oxidation.

Estimates of the total error on the ratio of minor to major water vapour isotopes for single profiles are of the order of 20–30 %. The estimated error budget is dominated in all cases by random error. Assuming that enough profiles are averaged, the random error component on the zonal means should become negligible, and the precision attainable is limited by the systematic error. Assuming negligible random error, the error on the zonal mean δ–values is assumed to be in region of 50–100 ‰ for δ^{18}O and δ^{17}O, depending on altitude. The useful retrieval range for $H_2^{18}O$ and $H_2^{17}O$ is 6 to 60 km. Under the same assumption, the error on the zonal mean values of δD–HDO is around 30 ‰, rising to 100 ‰ at 52 km. The useful retrieval range for HDO is 6 to 52 km.

Profiles of δ–values for all minor isotopes of water vapour show a persistent oscillation with altitude, mainly in the tropics. This oscillation in the δ–values appears to stem mainly from structure in the zonal mean VMRs of the main isotope. The oscillations in δD are not huge and do not have a wavelength which is tied to the retrieval spacing, implying that they could be related to real atmospheric structure. However, the oscillations in δ^{18}O and δ^{17}O are rather too large to be believable and are tied to the spacing of retrieval levels.

Zonal mean comparisons of HDO and $H_2^{18}O$ from these retrievals with retrievals from the Odin–SMR show reasonable agreement between the VMRs of these minor isotopes, but poor agreement between δ–values.

Retrievals of CH_3D show an increase in the δD content with height, as would be expected, up to around 21 km. Above 21 km, there is not enough information to retrieve CH_3D. Zonal mean fields of δD–CH_3D might have been expected to show greater enrichment in areas where there is expected to be older air, but it is not clear that this is the case.

Estimates of the total error on the ratio of CH_3D to CH_4 for a single profile are also of the order of 20–30 % and are dominated by random errors. Assuming negligible random errors, the error on the zonal mean values of δD–CH_3D is around 50 ‰.

It is possible that better results could be obtained with a different approach to the microwindow selection. Microwindows were selected using assumed profiles based on scaling the IG2 climatology profiles for H_2O and CH_4 by the HITRAN surface abundances (δ–values of zero). This is a particularly bad assumption for the HDO, which shows strong depletion with respect to the main isotope. Perhaps different spectral regions would be selected if the microwindow selection program had been supplied with data based on, say, profiles from the isotopic version of the CAM3 model.

The microwindow selections for HDO, $H_2^{17}O$ and CH_3D were terminated due to reaching a somewhat arbitrarily chosen number of points (10000). Increasing the number of spectral points used could decrease the random error on the retrievals. It could therefore be worthwhile to redo the microwindow selection for these species with a larger number of points (or microwindows) allowed.

Also, systematic errors for the ratio of the minor to the major isotopes did not cancel to the extent that was expected. The microwindows for this Chapter were selected on the basis of a retrieval of one minor isotope only. Perhaps a selection of microwindows aimed specifically towards the joint retrieval of major and minor isotopes would result in lower systematic errors in the ratios. Lines of $H_2^{18}O$ and $H_2^{17}O$ are often closely spaced, and so a joint retrieval of these minor isotopes could also be beneficial.

Numerous variations on the approach to the retrieval itself could also be adopted, which could have the potential to improve the results.

There is scope for a great deal more validation work. In this chapter, MIPAS results have been compared with those from the Odin–SMR instrument. There is also potential for comparisons with aircraft and balloon measurements, such as those from the Harvard FIRS-2 instrument (*Ugo Cortesi, private communication*) and from the MIPAS balloon and aircraft instruments (*Hermann Oelhaf, private communication*). In addition, there are other satellite instruments capable of isotopic measurements. These include the Tropospheric Emission Spectrometer (TES), currently flying on the latest NASA Aura satellite, and the ACE–FTS (§ 4.7). Although neither of these satellite instruments offer measurements which overlap in time with the MIPAS 0.025 cm^{-1} dataset used here, useful comparisons could still be made.

Although the results displayed in this Chapter are far from perfect, MIPAS retrievals of minor isotopes of water vapour and methane offer potential. The results shown here were for three days per month for each month in 2003. The MIPAS Level 1B spectra provide almost continuous global coverage from July 2002 until March 2004. With improvements to the retrievals, the Level 1B dataset provides huge potential to study the distribution and variability of the isotopic composition of water vapour and methane on a global scale.

The analysis in this Chapter has been confined to zonal means, binned only according to latitude and to the MIPAS nominal altitude. Processing of larger volumes of data could allow more rigorous analysis based on pressure surfaces or on potential temperature. Variability on different spatial and time scales could be studied. MIPAS isotopic retrievals could potentially be used in conjunction with a general circulation model such as CAM3 in order to quantify the relative importance of different entry mechanisms of air and water vapour into the stratosphere, both in tropics and mid–latitudes. There is scope for much more processing and analysis of the available Level 1B data.

Chapter 7

Conclusions and Further Work

7.1 Validation of the ESA OFL data

7.1.1 H_2O

Work on the validation of ESA OFL H_2O has focused on water vapour in the stratosphere and lower mesosphere, which can generally be usefully discussed in terms of zonal means. Upper tropospheric water vapour from MIPAS has not been discussed in depth. Due to the high variability of tropospheric water vapour, zonal means are not as useful in this region. Also, comparisons with external data made in Chapter 4 have been with the IG2 climatology, which by the nature of the dataset does not capture the variability of upper tropospheric water vapour, with data from HALOE, where upper tropospheric water vapour values are known to be somewhat unreliable (HALOE, 2005) and with data from the Odin–SMR, whose measurement range for water vapour does not extend down to the upper troposphere. Further work could include the examination of spatial distributions of water vapour in the upper troposphere on, say, selected pressure levels.

Diurnal variations in stratospheric water vapour are not expected, but the MIPAS monthly means of H_2O show significant day/night differences. These day/night differences are thought to be due to a combination of a real day/night difference in the instrument pointing and non–LTE effects. There is some day/night pointing difference indicated in the MIPAS, Level 1B files, but there appear to be additional real day/night pointing differences which show up as extra day/night differences in the pressure retrievals.

Zonal mean comparisons of MIPAS OFL H_2O were performed with the IG2 climatology dataset and with data from two other satellite instruments: HALOE and the Odin–SMR. Each set of zonal mean comparisons showed a bias pattern in MIPAS with respect to the other instruments which was largely consistent with time and across latitudes.

Despite the observed biases and the unexplained day/night differences, qualitatively, monthly mean profiles of MIPAS OFL H_2O show expected the variations with altitude, latitude and time that would be expected, which in itself is an indication that the dataset is of reasonable quality.

7.1.2 CH_4

In general, monthly mean profiles of MIPAS OFL CH_4 also show the qualitative variations with altitude, latitude and time which would be expected. As with the H_2O, there are significant day/night differences in MIPAS OFL CH_4, which are thought to be caused by a combination of non–LTE effects and real day/night differences in the instrument pointing.

Zonal mean profiles of MIPAS OFL CH_4 were compared with the IG2 climatology and with data from the HALOE instrument. In general, MIPAS CH_4 is higher than both the IG2 and HALOE. However, unlike with H_2O, the vertical bias pattern is not consistent across latitudes and times.

7.1.3 General

The results of the comparisons performed for Chapter 4 would appear to support the conclusions of other validation work presented at the Atmospheric Chemistry Validation of Envisat (ACVE-2) meeting held in May 2004.

In addition to any biases, and to any individual profile oscillations (Appendix A), the comparisons performed in Chapter 4 also indicate that there is a persistent oscillation in the monthly means of methane in the region of the tropical tropopause.

Averaged residuals for the operational microwindows of both water vapour and methane show spectral features in the region of the target gas lines. The residual spectra show definite day/night differences. For some unknown reason, the residual fit is worse in summer months than in winter months, even when day/night differences are taken into account.

7.2 Investigation of problems

Possible causes of the observed biases and persistent oscillations in the MIPAS OFL H_2O and CH_4 profiles were investigated using the Oxford retrieval processor (MORSE). It could be argued that these sensitivity tests should really be performed with the ORM, as it uses the same retrieval method as the operational processor. However, tests with MORSE ought to give a reasonable idea of which issues merit further investigation.

The effects of various assumptions have been examined here in isolation. In reality, it is likely that the observed problems in the data are due to a mixture of causes.

It was established that day/night differences in the retrievals could be caused by non–LTE effects. The observed low bias in the day–time ESA OFL H_2O and CH_4 at 68 km can most probably be attributed to non–LTE effects. It has also been observed that the effects of non–LTE on day–time retrievals extend down to around 30 km, which is further down than would have been expected from the microwindow error analysis. It is therefore possible that the observed day/night differences could be at least partially attributed to non–LTE effects. It is also conceivable that variation in non–LTE effects in CH_4 with latitude could account for some of the variation in the CH_4 bias with respect to other data sources in latitude and time, although further work would be required to show conclusively that this is the case.

It was established that day/night differences in H_2O are not large enough to entirely account for the observed bias in H_2O above 30 km. Another possible candidate cause of a high bias in H_2O above 30 km is a modelled ILS which is too narrow. A modelled ILS which is too narrow would be consistent with the residual signatures in the H_2O microwindows shown in Chapter 4. Extending the continuum retrieval up to 68 rather than 30 km also appears to result in a very small reduction in the retrieved H_2O above 30 km, but residual signatures in the H_2O microwindows do not indicate a problem with the continuum.

It has already been suggested that the perceived bias in the OFL CH_4 may be partially attributed to non–LTE effects. The ILS width may also have an effect on the CH_4 bias, although this is not an effect that would be expected to result in latitudinal variations in the bias.

Biases are likely to arise through systematic errors which the retrieval can try to compensate for by changing the profile of the target species. If the retrieval is unable to better match the modelled spectra to the measurements by adjusting the profile of target species, then oscillations tend to develop. The most obvious cause of oscillations is noise. Oscillations in the retrieved profiles arising from random noise in the spectra should be random in phase, and should therefore be removed when large numbers of profiles are averaged. However, certain systematic errors may also result in oscillations which are not random in phase. An example of this is the observed differences in Level 1B radiances between forward and reverse sweeps of the MIPAS interferometer (see Appendix A), which causes oscillations in the Level 2 profiles which are distinctly anti–correlated between adjacent limb scans.

The investigations in Chapter 5 have identified a number of possible candidate causes for the persistent oscillations in CH_4 in the region of the tropical tropopause observed in the MIPAS data.

Possible causes identified are the FOV representation, the assumption that the atmosphere can be accurately represented on the retrieval grid and the assumption that the VMR varies linearly with altitude.

All these issues also affect the H_2O retrieval. Oscillations in the H_2O retrievals in the region of the tropical tropopause from real data are more complicated than those in the CH_4 retrievals, since some oscillations are expected in the tropical H_2O due to the tropical tape recorder effect. Oscillations in the tropical OFL H_2O profiles do exist, but seem to behave in a realistic way, whereas oscillations in the tropical CH_4 profiles ought not to exist.

Many of the tests performed for Chapter 5 also resulted in unexpected effects on the pressure retrieval which were different for mid–latitude and equatorial cases. These have not really been discussed here, but could be an interesting topic for further investigation.

7.3 Isotope retrievals

The isotope retrievals presented in Chapter 6 show promise, but the approaches to the microwindow selection and the retrievals adopted here could probably be improved upon. With selection of microwindows based on joint retrievals of the major and minor isotope, it may be possible to reduce the systematic error on the ratios. Different configurations of the retrieval approach might yield better results.

It is likely that a more time consuming approach to forward model calculations, (involving a more realistic FOV representation and a smaller spacing in the vertical grid) might produce better results, particularly in the upper troposphere and lower stratosphere (UTLS) region.

It would, in theory, be possible to process all of the available MIPAS Level 1B data to obtain a global dataset of the isotopic composition of water vapour (and methane) for July 2002 until

March 2004. The retrievals presented in Chapter 6 have not be subject to extensive validation, but there is scope for a great deal more validation work. Comparisons could be made with data from the ACE–FTS, TES on Aura and with further days from the Odin–SMR. Comparisons could also be made with data from a number of balloon, aircraft and ground–based instruments. Examples include the MIPAS aircraft and balloon instruments (Piesch et al., 1996; Fischer and H.Oelhaf, 1996) and the FIRS–2 instrument (Johnson et al., 2001a), both of which have flown within the time period of the MIPAS 0.025 cm^{-1} dataset.

The dataset could also be examined in conjunction with a global circulation model such as CAM3. There is potential to use this model in conjunction with MIPAS measurements to test various hypotheses on the entry of water vapour and air into the stratosphere.

The dataset could also potentially be used in conjunction with observations of polar stratospheric clouds in order to study dehydration in polar regions.

An understanding of the transfer of water vapour across the tropopause and its redistribution in the lower stratosphere is key to understanding the chemistry, radiation and dynamics of this region, which in turn are all factors which are vital to understand if atmospheric models are to make accurate predictions of future climate and climate change. Isotopic measurements from MIPAS have the potential to contribute to this area and should be a fruitful area for further research.

Appendix A

A note on systematic differences between forward and reverse interferometer sweeps

The MIPAS monthly mean profiles presented in this Chapter have been calculated from a large number of profiles. The random error on the monthly mean profiles is therefore very small, and so it is clear that any oscillations in the monthly means arise from persistent problems in the retrieval, rather than noise. There are, however, other persistent oscillations present in the MIPAS OFL profiles which are anti-correlated between adjacent scans. Although these oscillations do not show up in large–scale averages, it was felt that it would be proper to include them in a discussion of an overview of the quality of the MIPAS data.

MORSE retrievals of individual profiles from real data show some visible oscillation between adjacent retrieval levels. Oscillations can also be seen in individual profiles in the ESA OFL Level 2 products. Examination of profiles on the scale of a complete orbit reveals that these oscillations are anti–correlated between adjacent scans. To demonstrate this, average profiles of both water vapour and methane were calculated for a sample orbit (orbit 02081) from the ESA OFL Level 2 data. Separate averages were also calculated for all the “odd” and “even” scans in this orbit. Figure A.1

shows the differences of the "odd" and "even" average profiles from the average over all scans.

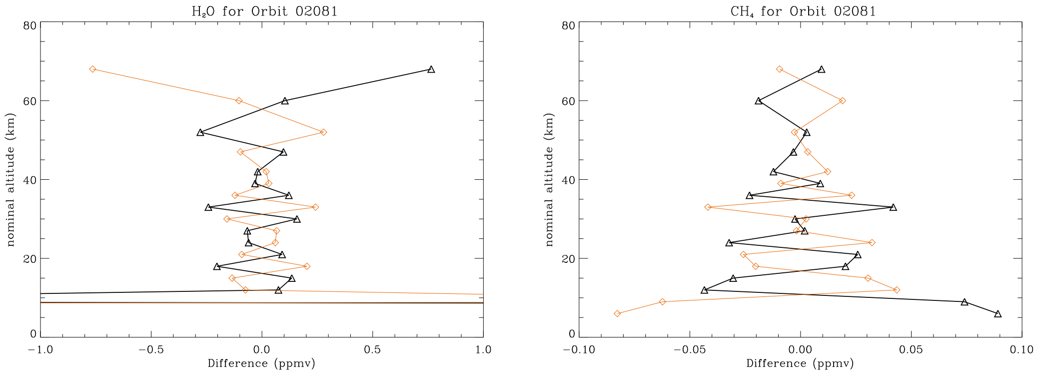

Figure A.1: Black lines (triangles) show the difference between the average over all scans and the average over even–numbered scans only for ESA OFL water vapour (left) and methane (right) profiles for orbit 02081. Red lines (squares) show the difference between the average over all scans and the average over odd–numbered scans only.

The ESA OFL retrieval uses information from the retrievals from the previous scan to set up the initial guess profiles for the next scan. However, the Oxford retrieval can be set to do this or not as the user chooses. The Oxford retrieval can therefore be used to show that the anti–correlation of profile oscillations from one scan to the next is present even when the retrieval from any one scan uses no information from previous scans. Since the pattern in the oscillations was so clearly regular, and could not be traced to any transfer of information in the Level 2 processing, it was deduced that these systematic oscillations must stem from something in the Level 1B radiances.

The spectrum measured for any one tangent altitude in any MIPAS limb scan is the result of one sweep of the MIPAS interferometer. If the moving reflectors move along the interferometer slides in one direction (call it the forward direction) for a particular sweep (tangent altitude) in a scan, then they will move in the opposite direction (the reverse direction) for the next sweep in the scan. There are 17, an odd number, of sweeps in a complete MIPAS limb scan. It was postulated that some the regular pattern in the oscillations in the Level 2 profiles could be attributed to some systematic difference in the Level 1B radiances for forward and reverse sweeps of the interferometer.

Further investigations (Ceccherini et al., 2003) revealed that forward/reverse differences in the L1B radiances were immediately apparent in bands A and AB, but not in the other bands. This led to the suggestion that perhaps the systematic differences between adjacent sweeps were related in some way to the non–linearity correction, which is applied in bands A, AB and B. Since most of the information for the p, T retrieval comes from the A band (see Figure 3.1 for locations of microwindows), it might be expected that all subsequent retrievals would be affected. Even if their microwindows were not in bands where a non–linearity correction was applied, the VMR retrievals would be expected to affected by the propogation of the effects of the oscillations in the temperature retrieval.

It was established through consultation with G.Perron (Bomem) at MIPAS Quality Working Group meetings that there was indeed a difference in the way that the non–linearity correction was applied to forward and reverse sweeps. Changes were made in the Level 1B processor to update the handling of the non–linearity correction, and the update was applied to the processor in November 2003. The correction took effect after orbit number 08762 (3rd November 2003). Subsequent tests on the Level 2 products Perron (2004) showed that the processor update resulted in an improvement in the Level 2 products. Oscillations were still present, but were smaller than before, and were smaller in amplitude than the random error component of the retrievals. Systematic differences between forward and reverse interferometer sweeps are still being investigated by the Level 1 team in the MIPAS Quality Working Group. These subsequent investigations have indicated that there also seem to be systematic forward/reverse differences in band C. The reasons for this are not yet understood.

Appendix B

Error Covariance of Ratios

Define vector $\mathbf{r}$ as the ratio of two vectors, $\mathbf{x}$, $\mathbf{y}$,

$$r_i = \frac{x_i}{y_i} \tag{B.1}$$

The total error covariance of the ratio $\mathbf{S}_r^{\mathrm{tot}}$ is obtained by adding the random and systematic components:

$$\mathbf{S}_r^{\mathrm{tot}} = \mathbf{S}_r^{\mathrm{rnd}} + \sum_k \mathbf{S}_r^k \tag{B.2}$$

where superscript k denotes different sources of systematic error.

Consider a particular source of systematic error. The absolute uncertainty (indicated by d) in each element of the ratio due to a given systematic error source will be related to the uncertainties in elements of $\mathbf{x}$ and $\mathbf{y}$ by:

$$\begin{aligned}
\mathrm{d}r_i &= \left(\frac{\partial r_i}{\partial x_i}\right)\mathrm{d}x_i + \left(\frac{\partial r_i}{\partial y_i}\right)\mathrm{d}y_i && \text{(B.3)}\\
&= \frac{1}{y_i}\mathrm{d}x_i - \frac{x_i}{y_i^2}\mathrm{d}y_i && \text{(B.4)}\\
&= \frac{x_i}{y_i}\left(\frac{\mathrm{d}x_i}{x_i} - \frac{\mathrm{d}y_i}{y_i}\right) && \text{(B.5)}
\end{aligned}$$

$$\frac{\mathrm{d}r_i}{r_i} = \frac{\mathrm{d}x_i}{x_i} - \frac{\mathrm{d}y_i}{y_i} \tag{B.6}$$

Using notation δ to represent fractional or percentage change in a quantity and labelling the error source k:

$$\delta r_i^k = \delta x_i^k - \delta y_i^k \tag{B.7}$$

$$\delta \mathbf{r}^{\mathbf{k}} = \delta \mathbf{x}^{\mathbf{k}} - \delta \mathbf{y}^{\mathbf{k}} \tag{B.8}$$

The error covariance $\mathbf{S}_x$ of $\mathbf{x}$ is defined by the expectation values of products of pairs of elements of $\delta\mathbf{x}$:

$$(S_x)_{ij} = \langle \delta x_i \delta x_j \rangle \tag{B.9}$$

$$\mathbf{S}_x = \langle (\delta\mathbf{x})(\delta\mathbf{x})^{\mathbf{T}} \rangle \tag{B.10}$$

and similarly for $\mathbf{y}$ and $\mathbf{r}$. (Note that by defining $\mathbf{S}_x$ in terms of $\delta\mathbf{x}$ rather than $\mathrm{d}\mathbf{x}$, elements of $\mathbf{S}_x$ describe fractional or percentage errors rather than absolute errors in VMR).

The systematic error covariance of the ratio is therefore given by

$$\mathbf{S}_r^{\mathrm{sys}} = \sum_k \langle (\delta\mathbf{r}^{\mathbf{k}})(\delta\mathbf{r}^{\mathbf{k}})^{\mathbf{T}} \rangle \tag{B.11}$$

$$= \sum_k \langle (\delta\mathbf{x}^{\mathbf{k}} - \delta\mathbf{y}^{\mathbf{k}})(\delta\mathbf{x} - \delta\mathbf{y})^T \rangle \tag{B.12}$$

Since the individual systematic errors k are assumed fully correlated across all the elements of $\mathbf{x}$ and $\mathbf{y}$ but independent of one another, and the random error components $\delta\mathbf{x}^{\mathrm{rnd}}, \delta\mathbf{y}^{\mathrm{rnd}}$ are also uncorrelated with anything else, Eq. B.2 becomes

$$\begin{aligned} \mathbf{S}_r^{\mathrm{tot}} = {} & \langle \left(\delta\mathbf{x}^{\mathrm{rnd}}\right) \left(\delta\mathbf{x}^{\mathrm{rnd}}\right)^T \rangle + \\ & \langle \left(\delta\mathbf{y}^{\mathrm{rnd}}\right) \left(\delta\mathbf{y}^{\mathrm{rnd}}\right)^T \rangle + \\ & \sum_k \left\langle \left(\delta\mathbf{x}^k - \delta\mathbf{y}^k\right) \left(\delta\mathbf{x}^k - \delta\mathbf{y}^k\right)^T \right\rangle \end{aligned} \tag{B.13}$$

$$
\begin{aligned}
&= \mathbf{S}_x^{\mathrm{rnd}} + \mathbf{S}_y^{\mathrm{rnd}} + \\
&\quad \sum_k \left(\delta\mathbf{x}^k - \delta\mathbf{y}^k\right)\left(\delta\mathbf{x}^k - \delta\mathbf{y}^k\right)^T \qquad \text{(B.14)} \\
&= \mathbf{S}_x^{\mathrm{rnd}} + \mathbf{S}_y^{\mathrm{rnd}} + \sum_k \mathbf{S}_{x-y}^k \qquad \text{(B.15)}
\end{aligned}
$$

where the last two equations define $\mathbf{S}_{x-y}^k$, the covariance of the difference of the systematic error k in $\mathbf{x}$ and $\mathbf{y}$. This last component is minimised if, for all (major) errors k,

$$\delta\mathbf{x}^k \simeq \delta\mathbf{y}^k \qquad \text{(B.16)}$$

i.e., if the fractional errors in $\mathbf{x}$ and $\mathbf{y}$ due to each systematic error k are equal and therefore cancel in the ratio.

Bibliography

Abbas, M. M., Gunson, M. R., Newchurch, M. J., Michelsen, H. A., Salawitch, R. J., Allen, M., Abrams, M. C., Chang, A. Y., Goldman, A., Irion, F. W., Moyer, E. J., Hagaraju, R., Rinsland, C. P., Stiller, G. P., and Zander, R. (1996). The hydrogen budget of the stratosphere inferred from ATMOS measurements of H_2O and CH_4. *Geophys. Res. Lett.*, 23:2405–2408.

Abbas, M. M., Guo, J., Carli, B., Mencaraglia, F., A.Bonetti, Carlotti, M., and Nolt, I. (1987). Stratospheric O_3, H_2O and HDO distributions from balloon–based far–infrared observations. *J. Geophys. Res.*, 92:8354–8364.

AMIL2DA (2002a). http://www-imk.fzk.de/imk2/ame/amil2da.

AMIL2DA (2002b). AMIL2DA Mid–term report. co–ordinated by T. von Clarmann.

Araguas-Araguas, L., Froelich, K., and K.Rozanski (1998). Stable isotope composition of precipitation over south–east Asia. *J. Geophys. Res*, 103:28721–28742.

BADC (2003). http://badc.nerc.ac.uk/data/haloel3.

Barath, F., Chavez, M., Colfield, R., Flower, D., Frerking, M., Gram, M., Harris, W., Holden, J., Jarnot, R., Kloezeman, W., Klose, G., Lau, G., Loo, M., Maddison, B., Mattauch, R., McKinney, R., Peckham, G., Pickett, H., Siebes, G., Slotis, F., Suttie, R., Tarsala, J., Waters, J., and Wilson, W. (1993). The Upper Atmosphere Research Satellite Microwave Limb Sounder instrument. *J. Geophys. Res.*, 98:10751–10762.

Beer, R. (1992). *Remote Sensing by Fourier Transform Spectrometry.* Wiley–Interscience.

Bernath, P. et al. (2005). Atmospheric Chemistry Experiment (ACE: mission overview. Accepted to Geophys. Res. Lett.

Bignell, K. (1970). The water vapour infrared continuum. *Q. J. R. Meteorol. Soc.*, 96:390–403.

Boering, K., Jackson, T., Hoag, K., Cole, A., Perri, M., Thiemens, M., and Atlas, E. (2004). Observations of the anomalous oxygen isotopic composition of carbon dioxide in the lower stratosphere and the flux of the anomaly to the troposphere. *Geophys. Res. Lett.*, 31:L03109. doi:1029/2003GL018451.

Boone, C., Nassar, R., Walker, K., Rochon, Y., McLeod, S., Rinsland, C., and Bernath, P. (2005). Retrievals for the Atmospheric Chemistry Experiment Fourier Transform Spectrometer. Accepted to Applied Optics.

Bracher, A., Bramstedt, K., Sinnhuber, M., Weber, M., and Burrows, J. (2004). Validation of MIPAS O_3, NO_2, H_2O and CH_4 profiles (v4.61) with collocated measurements of HALOE and SAGE II. Proceedings of the Second Workshop on the Atmospheric Chemistry Validation of ENVISAT (ACVE–2), 3–7 May 2004, ESA–ESRIN, Frascati, Italy.

Brasseur, G. and Solomon, S. (1986). *Aeronomy of the middle atmosphere*. D. Reidel, 2nd edition edition.

Brewer, A. (1949). Evidence for a world circulation provided by the measurements of helium and water vapour distribution in the stratosphere. *Q. J. R. Meteorol. Soc.*, 75:351–363.

Camy-Peret, C., Payan, S., Dufour, G., Oelhaf, H., Wetzel, G., Stiller, G., Glatthor, N., Blumenstock, T., Blom, C., Keim, C., Mikuteit, S., Engel, A., Pirre, M., Moreau, G., Catoire, V., Bracher, A., Weber, M., and Bramstedt, K. (2004). Validation of MIPAS CH_4 profiles by stratospheric balloon, aircraft, satellite and ground based measurements. Proceedings of the Second Workshop on the Atmospheric Chemistry Validation of ENVISAT (ACVE–2), 3–7 May 2004, ESA–ESRIN, Frascati, Italy.

Carlotti, M. (1988). Global-fit appraoch to the analysis of limb-scanning atmospheric measurements. *Applied Optics*, 27:3250–3254.

Ceccherini, S., Dinelli, B. M., Dudhia, A., Payne, V., Piccolo, C., Prosperi, M., Raspollini, P., and Ridolfi, M. (2003). Orm Cal Val analysis. Technical Report TN-IFAC-OST-0301.

Chipperfield, M. (1999). Multiannual simulations with a three-dimensional chemical transport model. *J. Geophys. Res*, 104:1781–1805.

Coleman, D., Risati, J., and Schoell, M. (1981). Fractionation of carbon and hydrogen isotopes by methane–oxidising bacteria. *Geochim. Cosmochim. Acta*, 45:1033–1037.

Craig, H. (1961). Standard for reporting concentrations of deuterium and oxygen–18 in natural waters. *Science*, 133:1833–1834.

Danielsen, E. (1982). A dehydration mechanism for the stratosphere. *Geophys. Res. Lett.*, 9:605–608.

Dansgaard, W. (1964). Stable isotopes in precipitation. *Tellus*, 16:436–438.

de Bievre, P., Holden, N. E., and Barnes, I. L. (1984). Isotopic abundances and atomic weights of the elements. *J. Phys. Chem. Ref. Data*, 13:809–891.

Dessler, A. (2002). The effect of deep, tropical convection on the tropical tropopause layer. *J. Geophys. Res.*, 107(D3):4033. doi:10.1029/2001JD000511.

Dessler, A., Hintsa, E., Anderson, J., and Chan, K. (1995). Mechanisms controlling water vapour in the lower stratosphere: A tale of two stratospheres. *J. Geophys. Res.*, 100:23167–23172.

Dessler, A. and Sherwood, S. (2003). A model of HDO in the tropical tropopause layer. *Atmos. Chem. Phys.*, 3:2173–2181.

Dethof, A., Geer, A., Lahoz, W., Goutail, F., Bazureau, A., Wang, D.-Y., and von Clarmann, T. (2004). MIPAS temperature validation by the MASI group. Proceedings of the Second Workshop on the Atmospheric Chemistry Validation of ENVISAT (ACVE–2), 3–7 May 2004, ESA–ESRIN, Frascati, Italy.

Dinelli, B., Magnani, L., Carlotti, M., Papandrea, E., Prevedelli, M., Ridolfi, M., and Dudhia, A. (2004). GEO–MTR: A 2–dimensional multi–target retrieval system for MIPAS/ENVISAT observations. Proceedings of the 20th Quadrennial Ozone Symposium, 1–8 June 2004, Kos, Greece.

Dinelli, B. M., Carli, B., and Carlotti, M. (1991). Measurement of stratospheric distributions of $H_2^{16}O$, $H_2^{18}O$, $H_2^{17}O$ and $HD^{16}O$ from far IR spectra. *J. Geophys. Res.*, 96:7509–7514.

Dlugokencky, E., Houweling, S., Bruhwiler, L., Masarie, K., Land, P., Miller, J., and Tans, P. (2003). Atmospheric methane levels off: Temporary pause or new steady state? *Geophys. Res. Lett.*, 30. doi:10.1029/2003GL018126.

Dudhia, A. (2003). CalVal report PO-TN-OXF-GS-0020 (REC Analysis of MIPAS Data Jul02-Feb03).

Dudhia, A. (2004a). http://www.atm.ox.ac.uk/MORSE.

Dudhia, A. (2004b). RFM Software User's Manual. Issue 4.2, http://www.atm.ox.ac.uk/RFM/sum.html.

Dudhia, A., Jay, V., and Rodgers, C. (2002a). Microwindow selection for high spectral resolution sounders. *Applied Optics*, 41:3665–3673.

Dudhia, A., Morris, P. E., and Wells, R. J. (2002b). Fast monochromatic radiative transfer calculations for limb sounding. *Journal of Quantitative Spectroscopy and Radiative Transfer*, 74:745–746.

Dudhia, A., Piccolo, C., Quijano, A., Payne, V., and Burgess, A. (2004). http://www.atm.ox.ac.uk/group/mipas.

Echle, G., von Clarmann, T., Dudhia, A., Flaud, J.-M., Funke, B., Glatthor, N., Kerridge, B., Lopez-Puertas, M., Martin-Torres, F., and Stiller, G. (2000). Optimized spectral microwindows for MIPAS–Envisat data analysis. *Applied Optics*, 39:5531–5540.

Edwards, D. P. (1992). GENLN2: a general line–by–line atmospheric transmittance and radiance model / Version 3.0 description and users guide. Technical report. Report NCAR/TN367+STR.

Engel, A., Schiller, C., Schmidt, U., Borchers, R., Ovarlez, H., and Ovarlez, J. (1996). The total hydrogen budget in the arctic winter stratosphere during the European Arctic Stratospheric Ozone Experiment. *J. Geophys. Res.*, 101:14495–14503.

Enhalt, D. (1980). In situ observations. *Phil. Trans. Ro. Soc. London*, A296:175–189.

Enhalt, D. H. (1974). Vertical profiles of HTO, HDO and H_2O in the troposphere. *Tech. Note TN/STR 100, NCAR*, 7:307–313.

Envisat (2001). http://envisat.esa.int.

Eriksson, E. (1965). Deuterium and oxygen–18 in precipitation and some other natural waters. *Tellus*, 17:498–512.

ESA (2000a). Envisat-1: Mission and system summary. Technical report, European Space Agency, Dornier Satellitensysteme GmbH, Matra Marconi Space, Thompson-CSF. ESA/SP-1229.

ESA (2000b). Envisat MIPAS - an instrument for atmospheric chemistry and climate research. Technical report, European Space Agency. ESA/SP-1229.

Ewen, G. (2005). *Infrared limb observations of cloud.* PhD thesis, University of Oxford.

Fabian, P. (1979). Simultaneously measured vertical profiles of H_2, CH_4, CO, N_2O, $CFCl_3$ and CF_2Cl_2 in the mid–latitude stratosphere and troposphere. *J. Geophys. Res.*, 84:3149.

Fischer, H. and H.Oelhaf (1996). Remore sensing of vertical profiles of atmospheric trace constituents with MIPAS limb–emission spectrometers. *Appl. Opt.*, 35:2787–2796.

Flaud, J.-M., Piccolo, C., Carli, B., Perrin, A., Teffo, L. C. J.-L., , and Brown, L. (2003). Molecular line parameters for the MIPAS (Michelson Interferometer for Passive Atmospheric Sounding) experiment. *J. Atm. and Ocean Optics*, 16:172–182.

Forster, P. and Shine, K. (1999). Stratospheric water vapour changes as a possible contributor to observed stratospheric cooling. *Geophys. Res. Lett.*, 26:3309–3312.

Forster, P. and Shine, K. (2002). Assessing the climate impact of trends in stratospheric water vapour. *Geophys. Res. Lett.*, 29(6):1086. doi:10.1029/2001GL013909.

Fricke, K., Blum, U., G.Baumgarten, Congeduti, F., Cuomo, V., Hansen, G., Mona, L., Schets, H., Stebel, K., and Stübi, R. (2004). MIPAS temperature validation by radiosonde and lidar. Proceedings of the Second Workshop on the Atmospheric Chemistry Validation of ENVISAT (ACVE–2), 3–7 May 2004, ESA–ESRIN, Frascati, Italy.

Funke, B., Payne, V., and Raspollini, P. (2005). Investigations on a possible bias in MIPAS H_2O profiles at high altitudes. ESA Technical Note in response to QWG Action Item AIL2_2.08.

Gettelman, A. and Forster, P. (2002). A climatology of the tropical tropopause layer. *J. Met. Soc. Japan*, 80(4B):911–924.

Goody, R. and Yung, Y. (1989). *Atmospheric Radiation: Theoretical Basis.* Oxford University Press, 2nd edition edition.

Gray, L. and Russell, J. (1999). Interannual variability of trace gases in the subtropical winter atmopshere. *J. Atmos. Sci*, 56:977–993.

Griffiths, P. and de Haseth, J. (1986). *Fourier Transform Infrared Spectrometry.* John Wiley and Sons.

Gunson, M., Farmer, C., Norton, R., Zander, R., Rinsland, C., and ans B.C. Gao, J. S. (1990). Measurements of CH_4, N_2O, CO, H_2O and O_3 in the middle atmosphere by the Atmospheric Trace Molecule Spectroscopy (ATMOS) experiment on Spacelab 3. *J. Geophys. Res.*, 95:13867–13882.

Guo, J., Abbas, M. M., and Nolt, I. G. (1989). Stratospheric $H_2^{18}O$ distribution from far infrared observations. *Geophys. Res. Lett.*, 16:1277–1280.

Gutnik, M. (1961). How dry is the sky? *J. Geophys. Res.*, 66:2867–2871.

HALOE (2005). http://larc.nasa.gov/haloedata.

Harries, J., Russell, J., Tuck, A., Gordley, L., Purcell, P., Stone, K., Bevilacqua, R., Gunson, M., Nedholuha, G., and Traub, W. (1996a). Validation of measurements of water vapor from the Halogen Occultation Experiment (HALOE). *J. Geophys. Res.*, 101 (D6):10205–10216.

Harries, J. E. (1997). Atmospheric radiation and atmospheric humidity. *Quart. J. Roy. Met. Soc.*, 123:2173–2186.

Harries, J. E., Ruth, S., and Russell, J. M. (1996b). On the distribution of mesospheric molecular hydrogen inferred from HALOE measurements of H_2O and CH_4. *Geophys. Res. Lett.*, 23:297–300.

Herman, R., Drdla, K., Spackman, J., Hurst, D., Popp, P., Webster, C., Romashkin, P., Elkins, J., Weinstock, E., Gandrud, B., Toon, G., Schoeberl, M., Jost, H., and Bui, E. A. T. (2003). Hydration, dehydration and the total hydrogen budget in the 1999/2000 winter Arctic stratosphere. *J. Geophys. Res.*, 108(D5):8320. doi:10.1029/2001JD001257.

Hintsa, E., Boering, K., Weinstock, E., Andersson, J., Gary, B., Pfister, L., Daube, B., Wofsy, S., Loewenstein, M., Podolske, J., Margitan, J., and Bui, T. (1998). Troposphere to stratosphere transport in the lowermost stratopshere from measurements of H_2O, CO_2, N_2O and O_3. *Geophys. Res. Lett.*, 25:2655–2658z.

Hintsa, E., Weinstock, E., Dessler, A., Ansderson, J., Loewenstein, M., and Podolske, J. (1994). SPADE H_2O measurements and the seasonal cycle of stratospheric water vapour. *Geophys. Res. Lett.*, 21:2559–2562.

HITRAN (2004). http://www.hitran.com, HITRAN database website.

Hoffman, G., Werner, M., and Heimann, M. (1998). Water isotope module of the ECHAM atmospheric general circulation model. *J. Geophys. Res*, 103:16871–16896.

Holton, J., Haynes, P., McIntyre, M., Douglas, A., Rood, R., and Pfister, L. (1995). Stratosphere–troposphere exchange. *Rev. Geophys.*, 33:403–439.

Irion, F. W., Moyer, E. J., Gunson, M. R., Rinsland, C. P., Yung, Y. L., Michelsen, H. A., Salawitch, R. J., Chang, A. Y., Newchurch, M. J., Abbas, M. M., Abrams, M. C., and Zander, R. (1996). Stratospheric observations of CH_3D and HDO from ATMOS infrared solar spectra: Enrichments of deuterium in methane and implications for HD. *Geophys. Res. Lett.*, 23:2381–2384.

Jay, V. (2000). *Remote Sounding of the Atmosphere by High Resolution Spectroscopy.* PhD thesis, University of Oxford.

Jay, V., Dudhia, A., and Rodgers, C. (2002). MIPAS error analysis using spectral signatures. Proceedings of the 10th International Workshop of Atmospheric Sounding from Space using Fourier Transform Spectrometry, Ventura, California.

Johnson, D. G., Jucks, K. W., Traub, W. A., and Chance, K. V. (2001a). Isotopic composition of stratospheric water vapour: implications for transport. *J. Geophys Res*, 106:12219–12226.

Johnson, D. G., Jucks, K. W., Traub, W. A., and Chance, K. V. (2001b). Isotopic composition of stratospheric water vapour: measurements and photochemistry. *J. Geophys Res*, 106:12211–12217.

Jones, R., Pyle, J., Harries, J., Zavody, A., Russell, J., and Gille, J. (1986). The water vapour budget of the stratosphere studied using LIMS and SAMS data. *Q. J. R. Meteorol. Soc.*, 112:1127–1143.

Jouzel, J., Russel, G. L., SUozzo, R. J., Koster, R., White, J., and Broeker, S. (1987). Simulations of the HDO and $H_2^{18}O$ atmospheric cycles using the NASA GISS general circulation model; The seasonal cycle for present–day conditions. *J. Geophys. Res.*, 92:14739–14760.

Juckes, M. (2004). http://home.badc.rl.ac.uk/mjuckes/gallery/talks/mnj_darc_0411.pdf.

Kaye, J. A. (1987). Mechanisms and observations for isotope fractionation of molecular species in planetary atmospheres. *Rev. Geophys.*, 25:1609–1658.

Kaye, J. A. (1990). Analysis of the origins and implications of the ^{18}O content of stratospheric water vapour. *J. Atm. Chem.*, 10:39–57.

Kennaugh, R., Ruth, S., and Gray, L. (1997). Modelling quasi–biennial variability in the semi–annual double peak. *J. Geophys. Res.*, 102:16169–16187.

Kiyosu, Y. (1983). Hydrogen isotopic compositions of hydrogen and methane from some volcanic areas in northeastern Japan. *Earth. Planet. Sci. Lett.*, 62:41–52.

Kley, D., Stone, E., Henderson, W., Drummond, J., , Harrop, W., Schmeltekopf, A., Thompson, T., and Winkler, R. (1979). *In situ* measurements of the mixing ratio of water vapor in the stratosphere. *J. Atmos. Sci*, 36:2513–2524.

Lachance, R. (1999). MIPAS level 1B algorithm technical baseline document: an overview. *Proceedings of the European Symposium on Atmospheric Measurements from Space*, 1:51–63.

Lahoz, W., Geer, A., Swinbank, R., Jackson, D., Thornton, H., Dethof, A., and Fonteyn, D. (2004). Modelling and assimilation: Evaluation of MIPAS water vapour data. Proceedings of the Second Workshop on the Atmospheric Chemistry Validation of ENVISAT (ACVE–2), 3–7 May 2004, ESA–ESRIN, Frascati, Italy.

Le Texier, H., Solomon, S., and Garcia, R. R. (1988). The role of molecular hydrogen and methane oxidation in the water vapour budget of the stratosphere. *Q. J. R. Meteorol. Soc.*, 114:281–295.

Lopez Puertas, M. and Taylor, F. (2001). *Non–LTE radiative transfer in the atmosphere.* World Scientific Publishing.

Lopez Puertas, M., von Clarmann, T., Dudhia, A., Flaud, J.-M., Funke, B., Garcia Comas, M., Gil Lopez, S., Glatthor, N., Grabowski, U., Jay, V., Kiefer, M., Lopez Valverde, M. A., Perron, G., and Stiller, G. (2003). Non–LTE studies for the validation of MIPAS L2 products. Proceedings of the Envisat Validation Workshop, ESA–SP531, Noordwijk.

Lopez-Puertas et al, M. (1996). Evaluation of non–LTE effects in MIPAS pressure, temperature and volume mixing ratio retrievals. ESA final report, ESTEC PO 151625.

Mastenbrook, M. and Oltmans, S. (1990). Stratospheric water vapour variability for Washington DC and Boulder, Colorado, 1964–1982. *J. Atmos. Sci*, 40:2157–2165.

Mauersberger, K., Lammerzahl, P., and Krankowsky, D. (2001). Stratospheric ozone isotope enrichments — revisited. *Geophys. Res. Lett*, 28:3155–3158.

McCarthy, M. C., Boering, K., Rahn, T., Eiler, J., Rice, A., Tyler, S., Schauffler, S., Atlas, E., and Johnson, D. G. (2003a). The hydrogen isotopic composition of water vapor entering the stratosphere inferrred from high–precision measurements of δD–CH_4 and δD–H_2. *J. Geophys. Res.*, 109:D07304. doi:10.1029/2003JD004003.

McCarthy, M. C., Boering, K., Rice, A., Tyler, S., Connell, P., and Atlas, E. (2003b). The carbon and hydrogen isotopic compositions of stratospheric methane: Part 2: 2-D model results and implications for kinetic isotope effects. *J. Geophys. Res.*, 108(D15):4461.

McHugh, M., Magill, B., Walker, K., Boone, C., Bernath, P., and Russell, J. (2005). Comparison of atmospheric retrievals from ACE and HALOE. Accepted to Geophys. Res. Lett.

McIntyre, M. and Palmer, T. N. (1983). Breaking planetary waves in the stratosphere. *Nature*, 305:593–594.

Mote, P., Rosenlof, K., Holton, J., Harwood, R., and Waters, J. (1995). Variations of water vapour in the tropical lower stratosphere. *Geophys. Res. Lett.*, 22:1093–1096.

Mote, P., Rosenlof, K. H., McIntyre, M., Carr, E., Gille, J., Holton, J., Kinnersley, J., Pumphrey, H., Russell, J., and Waters, J. (1996). An atmospheric tape recorder: The imprint of tropical tropopase temperatures on stratospheric water vapour. *J. Geophys. Res.*, 101:3989–4006.

Moyer, E. J., Irion, F. W., Yung, Y. L., and Gunson, M. R. (1996). ATMOS stratospheric deuterated water and implications for stratosphere–troposphere transport. *Geophys. Res. Lett.*, 23:2385–2388.

Murtagh, D., Frisk, U., Ridal, M., Jonsson, A., Stegman, J., Witt, G., Eriksson, P., Jiminez, C., Megie, G., de la Noe, L., Ricaud, P., abd J.R. Pardo, P. B., Hauchcorne, A., Llewellyn, E., Degenstein, D., Gattinger, R., Lloyd, N., Evans, W., McDade, I., Haley, C., Sioris, C., von Savigny, C., abd J.C. McConnell, B. S., Strong, K., Richardson, E., Leppelmeier, G., Kyrola, E., Auvinen, H., and Oikarinen, L. (2002). An overview of the Odin satellite mission. *Canadian Journal of Physics*, 80:309–319.

NCAR (2005). The community atmosphere model (CAM). http://www.ccsm.ucar.edu/models/atm-cam.

Newell, R. and Gould-Stewart, S. (1981). A stratospheric fountain? *Geophys. Res. Lett.*, 38:2789–2796.

Norton, R. H. and Beer, R. (1977). New apodizing functions for Fourier spectrometry. *J. Opt. Soc. Am.*, 66:259–264.

Oelhaf, H., Fix, A., Schiller, C., Chance, K., Gurlit, W., Ovarlez, J., Renard, J.-B., Rohs, S., Wetzel, G., von Clarmann, T., Milz, M., Wang, D.-Y., Remedios, J., and Waterfall, A. (2004). Validation of MIPAS–Envisat version 4.61 operational data with balloon and aircraft measurements: H_2o. Proceedings of the Second Workshop on the Atmospheric Chemistry Validation of ENVISAT (ACVE–2), 3–7 May 2004, ESA–ESRIN, Frascati, Italy.

Oltmans, S., Vömel, H., Hofman, D., Rosenlof, K., and Kley, D. (2000). The increase in stratospheric water vapor from balloonborne, frostpoint hygrometer measurements at Washington DC and Boulder, Colorado. *Geophys. Res. Lett.*, 27:3453–3456.

Pappalardo, G., Colavitto, T., Congeduti, F., Cuomo, V., Dueber, B., Kämpfer, N., Iarlori, M., Mona, L., and Rizi, V. (2004). Validation of MIPAS water vapour products by ground based measurements. Proceedings of the Second Workshop on the Atmospheric Chemistry Validation of ENVISAT (ACVE–2), 3–7 May 2004, ESA–ESRIN, Frascati, Italy.

Park, J., Russell, J., Gordley, L., Drayson, R., Benner, D., McInerney, J., Gunson, M., Toon, G., Sen, B., Blavier, J.-F., Webster, C., Zipf, E., Erdman, P., Schmidt, U., and Schiller, C. (1996). Validation of Halogen Occultation Experiment CH_4 measurements from the UARS. *J. Geophys. Res.*, 101 (D6):10183–10203.

Payne, V., Dudhia, A., and Piccolo, C. (2003). Analysis of monthly mean profiles of water vapour and methane from mipas. Proceedings of ASSFTS-11, Bad Wildbad, Germany, 8-10 October 2003.

Perron, G. (2004). MIPAS level 1b: Changes and status. Proceedings of the Second Workshop on the Atmospheric Chemistry Validation of ENVISAT (ACVE–2), 3–7 May 2004, ESA–ESRIN, Frascati, Italy.

Persky, M. (1995). A review of spaceborne infrared Fourier transform spectrometers for remote sensing. *Rev. Sci. Instrum.*, 66:4763–4797.

Piesch, C., Blom, C., Fischer, H., Friedl-Vallon, F., Gulde, T., Sartorius, C., Seefelder, M., and Wolfel, M. (1996). Design of a MIPAS instrument for high–altitude aircraft. Proceedings of the 2nd International Airborne Remote sensing Conference and Exhibition, ERIM, Ann Abbor.

Plumb, R. A. (2002). Stratospheric transport. *J. Met. Soc. Japan*, 80(4B:793–809.

Pollock, W., Heidt, L. E., Lueb, R., and Enhalt, D. H. (1980). Measurement of stratospheric water vapour by cryogenic collection. *J. Geophys. Res.*, 85:5555–5568.

Press, W. H., Flannery, B. P., Teukolsky, S. A., and Vetterling, W. T. (1987). *Numerical Recipes: The art of scientific computing.* Cambridge University Press.

Quay, P., Stutsman, J., Wilbur, D., Snover, A., Dlugokencky, E., and Brown, T. (1999). The isotopic composition of atmospheric methane. *Glob. Biogeochem. Cycl.*, 13:445–461.

Rabier, F., Fourriè, N., Chafaï, D., and Prunet, P. (2001). Channel selection methods for infrared atmospheric sounding interferometer radiances. *Q. J. R. Meteorol. Soc.*, 128:1011–1027.

Rahn, T., Eiler, J., Wennberg, P., M.C.McCarthy, Boering, K. A., Tyler, S., and Atlas, E. (2003). Extreme deuterium enrichment in stratospheric molecular hydrogen and its signifigance for the global atmospheric budget of H_2. *Nature*, 424:918–921.

Randel, W., Wu, F., Russell, J., Roche, A., and Waters, J. (1998). Seasonal cycles and QBO variations in stratospheric CH_4 observed in UARS HALOE data. *J. Atmos. Sci.*, 55:163–185.

Randel, W. J., Wu, F., Gettelman, A., Russell, J. M., Zawodny, J. M., and Oltmans, S. J. (2001). Seasonal variation of water vapor in the lower stratosphere observed in Halogen Occultation Experiment data. *J. Geophys. Res.*, 106:14313–14325.

Remedios, J. J. (1999). Extreme atmospheric constituent profiles for MIPAS. *Proceedings of the European Symposium on Atmospheric Measurements from Space*, 2:779–783.

Rice, A., Tyler, S., McCarthy, M. C., Boering, K., and Atlas, E. (2003). The carbon and hydrogen isotopic compositions of stratospheric methane: Part 1: High–precision observations from the NASA ER–2 airgraft. *J. Geophys. Res.*, 108(D15):4460.

Rice, A. L., Tyler, S., McCarthy, M., and Boering, K. (2001). Measurements of the D/H and $^{13}C/^{12}C$ isotope ratios in stratospheric CH_4 from the POLARIS, STRAT and SOLVE campaigns. *EOS Trans. AGU*, 82(47).

Ridolfi, M., Carli, B., Carlotti, M., von Clarmann, T., Dinelli, B., Dudhia, A., Flaud, J.-M., Höpfner, M., Morris, P. E., Raspollini, P., Stiller, G., and Wells, R. J. (2000). Optimised forward model and retrieval scheme for MIPAS near–real–time data processing. *Applied Optics*, 39:1323–1340.

Rinsland, C., Gunson, M., Foster, J., R.A.Toth, Farmer, C., and R.Zander (1991). Stratospheric profiles of heavy water isotopes and CH_3D from analysis of the ATMOS Spacelab 3 infrared spectra. *J. Geophys. Res.*, 96:1057–1068.

Rinsland, C. P., Goldman, A., Malathy-Devi, V., Fridvich, B., Snyder, D., Jones, G., Murcray, F., Murcray, D., Smith, M., Seals, R., Coffey, M., and Mankin, W. (1984). Simultaneous stratospheric measurement of H_2O, HDO and CH_4 from balloon–borne and aircraft infrared solar absorption spectra and tunable laser diode laboratory spectra of HDO. *J. Geophys. Res.*, 89:7259–7266.

Roche, A., J.B.Kumer, Mergenthaler, J., Ely, G., Uplinger, W., Potter, J., James, T., and Sterrit, L. (1993). The Cryogenic Limb Array Etalon Spectrometer (CLAES) on UARS — Experiment description and performance. *J. Geophys. Res.*, 98:10763–10775.

Röckmann, T., Rhee, T., and Engel, A. (2003). Heavy hydrogen in the stratosphere. *Atmos. Chem. Phys.*, 3:2015–2023.

Rodgers, C. (1976). Retrieval of atmospheric temperature and composition from remote measurements of thermal radiation. *Reviews of Geophysics and Space Physics*, 14:609–624.

Rodgers, C. (1996). Information content and optimisation of high spectral resolution measurements. In: Optical Spectroscopic Techniques and Instrumentation for Atmospheric and Space Research II, Proc. SPIE 2830, eds P.B. Hayes and J. Wang.

Rodgers, C. (1998). Information content and optimisation of high spectral resolution measurements. *Adv. Space Research*, 21:361–367.

Rodgers, C. (2000). *Inverse Methods for Atmospheric Sounding: Theory and Practice.* World Scientific.

Roscoe, H. (2005). The lower stratospheric water vapour trend, 1950s to 1970s, revisited. Proceedings of Water Vapour in the Upper Troposphere and Lower Stratosphere Workshop, Lancaster University, UK, 5–7 July 2005.

Rosenlof, K. (2001). Stratospheric water vapor increases over the past half–century. *Geophys. Res. Lett.*, 28(7):1195–1198.

Rosenlof, K., Tuck, A., and Kelly, K. (1997). Hemispheric asymmetries in water vapour and iferences about transport in the lower stratosphere. *J. Geophys. Res.*, 102:13213–13324.

Rosenlof, K. H. (2003). How water enters the stratosphere. *Science*, 302:1691–1692.

Rozanski, K. and Sonntag, C. (1982). Vertical distribution of deuterium in atmospheric water vapour. *Tellus*, 34:135–141.

Russell, J., Gordley, L. L., and Park, J. (1993). The Halogen Occultation Experiment. *J. Geophys. Res.*, 98:10777–10797.

Ruth, S., Kennaugh, R., Gray, L., and Russell, J. (1997). Seasonal, semiannual and interannual variability seen in measurements of methane made by the UARS Halogen Occultation Experiment. *J. Geophys. Res.*, 102 (D13):16189–16199.

Schiegl, W. E. and Vogel, J. (1970). Deuterium content of organic matter. *Earth. Planet. Sci. Lett.*, 7:307–313.

Schmidt, U. (1974). Molecular hydrogen in the atmosphere. *Tellus*, 26:78.

Schoell, M. (1980). The hydrogen and carbon isotopic composition of methane from natural gases of various origins. *Geochim. Cosmochim. Acta*, 44:649–661.

Shannon, C. E. and Weaver, W. (1949). *The mathematical theory of communication*. University of Illinois Press, 8th edition edition.

Sherwood, S. and Dessler, A. (2000). On the control of stratospheric humidity. *Geophys. Res. Lett.*, 27:2513–2516.

Smith, R. B. (1992). Deuterium in North Atlantic storm tops. *J. Atmos. Sci.*, 49:2041–2057.

Spang, R., Remedios, J., and Barkley, M. (2004). Cloud indices for the detection and differentiation of cloud type for infra–red limb emission spectra. *Advances in Space Research*, 33(7):1041–1047.

Taylor, C. (1972). The vertical variations of isotopic concentrations of tropospheric water vapour over continetal europe, and their relationship to tropospheric structure.

Thiemens, M. H. (1999). Mass–independent isotope effects in planetary atmospheres and the early solar system. *Science*, 283:341–345.

Tikhonov, A. and Arsenin, V. (1977). *Solutions of ill-posed problems.* Winston.

Urban, J., Lautiè, N., Murtagh, D., Kasai, Y., Dupuy, E., de la Nöe, J., El Amraoui, L., Eriksson, P., Frisk, U., Jimènez, C., Le Flochmoën, E., Olberg, M., and Ricaud, P. (2004). Odin/SMR observations of stratospheric water vapour and its isotopes: requirements on spectroscopy. Proceedings of the International Workshop on Critical Evaluation of mm–/submm–wave Spectroscopic Data for Atmospheric Observation, Mito, Japan.

Vaughan, G., Price, J. D., and Howells, A. (1994). Transport into the troposphere in a tropopause fold. *Quart. J. Roy. Meteor. Soc.*, 120:1085–1103.

von Clarmann, T., Ceccherini, S., Doico, A., Dudhia, A., Funke, B., Grabowski, U., Hilgers, S., Jay, V., Linden, A., Lopez-Puertas, M., Martin-Torres, F. J., Payne, V., Reburn, J., Ridolfi, M., Schreier, F., Schwarz, G., Siddans, R., and Steck, T. (2003). A blind test retrieval experimment for limb emission spectrometry. 4746, doi:10.1029/2003JD003835.

von Clarmann, T. and Echle, G. (1998). Selection of optimized microwindows for atmospheric spectroscopy. *Applied Optics*, 37:7661–7660.

Wang, P., Minnis, P., McCormick, M., Kent, G., and Skeens, K. (1996). A 6–year climatology of cloud occurence frequency from Stratospheric Aerosol and Gas Experiment II observations (1985–1990). *J. Geophys. Res.*, 101:29407–29429.

Waterfall, A., Remedios, J., Spang, R., and Sembhi, H. (2004). Validation of the MIPAS level 2 products using reference atmospheres. Proceedings of the Second Workshop on the Atmospheric Chemistry Validation of ENVISAT (ACVE–2), 3–7 May 2004, ESA–ESRIN, Frascati, Italy.

Waters, J., Read, W., Froidevaux, L., Jarnot, R., Colfield, R., Flower, D., Lau, G., Pickett, H., Santee, M., Wu, D., Boyles, M., Burke, J., Lay, R., Loo, M., livesey, N., Lungu, T., Manney, G., Nakamura, L., Perun, V., Ridenoure, B., Shippony, Z., Siegel, P., Thurstans, R., Harwood, R., Pumphrey, H., and Filipiak, M. (1999). The UARS and EOS microwace limb sounder (MLS) experiments. *J. Atmos. Sci*, 56:194–218.

Wayne, R. (1996). *Chemistry of Atmospheres.* Oxford Science Publications, 2nd edition.

Weber, M., Bracher, A., Bramstedt, K., Bazureau, A., and Goutail, F. (2004). Overview on validation of MIPAS h$_2$o vapour by comparison with independent satellite measurements. Proceedings of the Second Workshop on the Atmospheric Chemistry Validation of ENVISAT (ACVE–2), 3–7 May 2004, ESA–ESRIN, Frascati, Italy.

Webster, C. and Heymsfield, A. (2003). Water isotope ratios D/H, O-18/O-16, O-17/O-16 in and out of clouds map dehydration pathways. *Science*, 302:1742–1745.

WMO (1982). The stratosphere 1981, theory and measurements, global ozone research and monitoring project. WMO Rep. 11, WMO/NASA.

WMO (2000). Stratospheric Processes and their Role in Climate (SPARC) assesment of upper tropospheric and stratospheric water vapour. SPARC Rep. 2, WCRP-113, WMO/TD-1043, Geneva.

Wood, A. and Andrews, D. (1997). A spectral model for simulation of tides in the middle atmosphere. I: Formulation. *J. Atmos. Terrest. Phys*, 59:31–51.

Zhou, X., Geller, M., and Zhang, M. (2001). Tropical cold point tropopause characteristics derived from ECMWF reanalyses and soundings. *J. Clim.*, 14:1823–1838.